INFORMATION TO USERS

This manuscript has been reproduced from the microfilm master. UMI films the text directly from the original or copy submitted. Thus, some thesis and dissertation copies are in typewriter face, while others may be from any type of computer printer.

The quality of this reproduction is dependent upon the quality of the copy submitted. Broken or indistinct print, colored or poor quality illustrations and photographs, print bleedthrough, substandard margins, and improper alignment can adversely affect reproduction.

In the unlikely event that the author did not send UMI a complete manuscript and there are missing pages, these will be noted. Also, if unauthorized copyright material had to be removed, a note will indicate the deletion.

Oversize materials (e.g., maps, drawings, charts) are reproduced by sectioning the original, beginning at the upper left-hand corner and continuing from left to right in equal sections with small overlaps. Each original is also photographed in one exposure and is included in reduced form at the back of the book.

Photographs included in the original manuscript have been reproduced xerographically in this copy. Higher quality 6" x 9" black and white photographic prints are available for any photographs or illustrations appearing in this copy for an additional charge. Contact UMI directly to order.

UMI

A Bell & Howell Information Company
300 North Zeeb Road, Ann Arbor MI 48106-1346 USA
313/761-4700 800/521-0600

EFFECT OF THERMOMECHANICAL PROCESSING ON MICROSTRUCTURE, TEXTURE, AND ANISOTROPY IN TWO Nb MICROALLOYED STEELS

by

ABBAS AKBARZADEH

A Thesis Submitted to the Faculty of Graduate Studies and Research in Partial Fulfillment of the Requirements of the Degree of Doctor of Philosophy

Department of Mining and Metallurgical Engineering

McGill University

Montreal, Canada

February 1997

Abstract

The process parameters that affect the anisotropy of mechanical properties of two Nb microalloyed linepipe steels (grades X-70 and X-80) were examined by controlled rolling and accelerated cooling on a pilot mill. The rolling schedules were first simulated by multi-pass torsion testing so as to determine the critical temperatures, such as T_{nr} and Ar_3. Using the torsion test results, two finish rolling temperatures were chosen so as to be above and below the Ar_3 (in the $\gamma + \alpha$ region). Two reheat temperatures were selected to study the effect of prior austenite grain size. The properties of air cooled samples are compared with those of specimens cooled at two different rates; in each case, cooling was interrupted at one of three different temperatures. The textures were measured by x-ray diffractometry and are presented in the form of ODF plots and skeleton lines. The yield strengths were measured by carrying out tensile tests along directions inclined at increasing angles to the rolling direction.

The state of the pancaked austenite before transformation was characterized in terms of the effective interfacial area. It is shown that this parameter determines the sharpness of the transformation texture because it accounts for both the amount of pancaking strain applied to the austenite before transformation and the austenite grain size. Another important factor affecting texture development during transformation is the rate of cooling, as it determines the dislocation density present on each active slip system. The results of hardness testing, texture measurement, and mechanical testing showed that a moderate cooling rate and a medium cooling interruption temperature lead to the best combination of a fine microstructure and a desirable texture. It is shown that accelerated cooling increases both the yield strength and the planar anisotropy of the yield strength, the latter property rising to a maximum in the samples associated with the lowest cooling interruption temperature. Comparison between the experimental results and model predictions of the yield strength ratio indicates that the pancake and lath models are in the best agreement with the measured values.

Résumé

Les paramètres influençant l'anisotropie des propriétés mécaniques de deux aciers microalliés au Nb (X-70 et X-80) pour conduits ont été étudiés par laminage contrôlé et refroidissement accéléré sur un laminoir-pilote. Les températures critiques, telles que T_{nr} et Ar_3, ont au préalable été déterminées au moyen de tests de torsion multipasses. Les résultats obtenus ont décidé le choix de deux températures de fin de laminage, une supérieure à Ar_3 et l'autre inférieure (dans la région $\gamma + \alpha$). Deux températures de recuit ont également été selectionnées afin d'étudier l'effet de la taille de grain austénique initiale. De plus, les propriétés des échantillons refroidis à l'air libre ont été comparées à celles des échantillons obtenus au moyen de deux différentes vitesses de refroidissement. Cette comparaison s'est faite à trois températures différentes, à chacune desquelles le refroidissement fut interrompu. Les textures furent mesurées par diffraction de rayons X et sont présentées sous forme d'ODFs et de lignes de fibres. Les limites d'élasticité furent déterminées par des tests de traction effectués selon différents angles par rapport à la direction de laminage.

L'état de l'austénite aplatie avant la transformation a été caractérisé en termes de surface interfaciale effective. L'influence de ce paramètre, qui prend en compte à la fois la quantité de déformation appliquée à l'austenite aplatie avant la transformation et la taille de grain austenitique, sur l'intensité de la texture de transformation a été montrée. Par ailleurs, l'effet de la vitesse de refroidissement sur le developpement de la texture s'est également avéré important, puisque cette dernière détermine la densité de dislocation présente sur tous les systèmes de glissement actifs. Les résultats des tests de dureté, des mesures de textures ainsi que des tests mécaniques ont montré qu'une vitesse de refroidissement modérée ainsi qu'une température d'interruption du refroidissement intermédiaire permettent d'obtenir à la fois une microstructure satisfaisante ainsi que la texture désirée. De plus, il s'est avéré que plus la vitesse de refroidissement est élevée, plus la limite d'élasticité est grande ainsi que son anisotropie planaire, cette dernière atteignant un maximum dans les échantillons associés aux températures d'interruption les plus basses. Enfin, la comparaison entre les résultats

expérimentaux et les valeurs modélisées des rapports des limites d'élasticité a montré que le modéle 'pancake' et le modéle 'lath' mènent à des valeurs qui concordent le mieux avec celles mesurées.

Acknowledgments

I would like to express my thanks to my thesis supervisor Professor John J. Jonas, for his patience and stimulating discussions. The successful completion of this thesis was due to his guidance and constant encouragement throughout the course of this research.

I am also indebted to Professors S. Yue and T. Maccagno for their very useful help in performing the TEM and mechanical tests, respectively. The administrative and technical help of Mrs. L. Mello and Mr. E. Fernandez is also very much appreciated.

I would like to thank Research Associates Drs. J. Savoie, L. Kestens, and Y. Zhou, who kindly shared their room with me, for the very useful discussions and debates we had. I am also grateful to my fellow graduate students, from all around the world, who participated in the indelible memories I will retain from these years.

Financial support received from IPSCO Inc. was very much appreciated. In particular, I would like to thank Drs. M. Kostic and L.E. Collins from IPSCO Inc. for their interest in this work. I also thank Dr. G.E. Ruddle and the technical staff of the MTL laboratory at CANMET for performing the rolling trials.

The author is grateful to the Ministry of Culture and Higher Education of Iran for granting him a postgraduate scholarship. He also thanks the Ministry for its patience regarding the delay in the completion of this work due to the late start of the experiments.

Last, but not at least, I would like to express my sincere appreciation to my wife, who sacrificed her academic life for the completion of this study, and my mother, for their support and patience throughout this work.

Figure Page

CHAPTER 2

CHAPTER 3

CHAPTER 4

CHAPTER 5

CHAPTER 6

Table Page

CHAPTER 3

CHAPTER 4

CHAPTER 5

CHAPTER 6

CHAPTER 1

Introduction

During the past two decades, thermomechanical processing (TMP) has played an important role in plate technology, particularly with regard to the production of high strength steels with superior low temperature toughnesses, such as steel for line pipes. This was important because it eliminated the need for subsequent heat treatment and therefore was more economical. This process covers a wide range of decision-making areas, such as material (alloy) selection, as well as design of the controlled rolling and run-out table cooling processes.

From a metallurgical point of view, TMP improves the strength and toughness of rolled niobium steels by means of three distinct processes: *i*) grain refinement of the ferrite, *ii*) control of the γ-to-α transformation, and *iii*) the precipitation of Nb-base particles. Grain refinement is achieved by means of the static or dynamic recrystallization of austenite and by the application of pancaking deformation. The transformation and precipitation processes

are also under the direct influence of the deformation and cooling conditions. Each of these processes is in turn controlled by the TMP parameters.

It is well known that during the transformation, the crystallographic texture developed by heavy deformation (pancaking) of the austenite is inherited by the ferrite. The orientation distribution functions obtained from the new texture analysis methods provide a quantitative measure of the texture developed by the transformation. Furthermore, an understanding of the way in which texture is formed is important in accounting for the microstructural characteristics and properties of the final product.

Preferred orientations or textures are the primary cause of the anisotropy of mechanical properties in metals. The detailed aspects of their influence on the final properties of steel have been the subject of much research. Also, much consideration has been given to modeling the plastic anisotropy of polycrystalline materials by introducing grain interaction models. Many of these models are based on the observation that the grains are not equiaxed, but rather flattened (pancaked) or elongated (lath-shaped).

For the manufacture of spiral welded pipe from skelp, it is desirable to have higher strengths in the hoop rather than in the longitudinal direction. For this purpose, knowledge of the influence of the processing parameters on the anisotropy of mechanical properties is required. In fact, all the processing parameters affecting the texture influence the planar anisotropy of the plates.

In this research, the effect of the thermomechanical processing conditions on the microstructure, texture, and planar anisotropy of the mechanical properties was investigated by carrying out systematic experiments to determine the influence of the most important parameters. Some of these were chosen to simulate the rolling conditions at IPSCO. The evolution of the microstructure, texture, and mechanical properties during

thermomechanical processing was studied in four separate sets of experiments. These were associated with:

I- Thermomechanical processing

II- Microscopic observations

III- Texture measurement

IV- Mechanical testing

In this program of tests, controlled rolling of the plate was carried out on the pilot mill at the MTL laboratory of CANMET in Ottawa. This process was designed so that the effect of the rolling conditions on texture development and on the mechanical properties could be studied at the McGill laboratories.

In Chapter Two, the effects of thermomechanical processing parameters on the microstructure and texture of Nb microalloyed steels will be reviewed briefly, as based on a survey of the literature. Some consideration will also be given to the anisotropy of mechanical properties.

In Chapter Three, the materials used will be introduced, after which the above four stages of the experimental work will be described. The processing conditions mainly include:

1) the reheat temperature (this affects the initial austenite grain size and the amount of niobium in solution)
2) the finishing temperature
3) the amount of austenite pancaking (determined by the rolling schedule and the T_{nr})
4) the cooling rate
5) the cooling interruption temperature.

The results obtained in this investigation concerning the effects of the process conditions on microstructural evolution, both before and after transformation, will be presented and discussed in Chapter Four. The characteristics of the microstructures will be examined with the aid of observations by both electron microscopy and hardness testing.

In Chapter Five, the influence is examined of the processing conditions on the transformation textures of the pancaked austenite. In this regard, the microstructural evolution must also be taken into account. Here, some possible relations between texture evolution and the phase transition are discussed. The texture predictions obtained from some variant selection criteria proposed for the modelling of transformation textures will also be compared with the experimental results.

In Chapter Six, the effects of the processing parameters, described in Chapter Three, on the anisotropy of the strength will be discussed. The relations between texture, presented in Chapter Five, microstructure, described in Chapter Four, and the plastic anisotropy of the yield strength will also be considered. The experimental results of the tensile tests are compared with models for predicting the anisotropy in the last section. Some data regarding the anisotropy of the fracture properties gathered as part of this investigation are not presented here because of space limitations.

CHAPTER 2

Literature Review

2.1 Introduction

Thermomechanical processing (TMP) has mostly been concerned with the manufacture of flat rolled products, such as steel for line pipes, in relatively high tensile form. This process covers a wide range of decision-making areas, such as material (alloy) selection, as well as design of the controlled rolling and run-out table cooling processes. Four metallurgical events during thermomechanical treatment, i.e. deformation, recrystallization, precipitation, and transformation govern microstructural and texture development in microalloyed steels. The detailed aspects of these mechanisms and their influence on the final properties of the steel have been the subject of much research. In this section, the effects of thermomechanical processing parameters on the microstructure and texture of Nb microalloyed steels will be briefly surveyed and consideration will also be given to the anisotropy of mechanical properties.

2.2 Texture Representation

Polycrystalline materials consist of a large number of crystallites, all of which may have the same structure as a single phase, as in pure metals, or contain several structures, as in multiphase alloys. In both cases, the orientations of the crystallites will tend to cover a considerable range. The orientation of an individual crystallite is specified in terms of the relation between the crystal coordinate system, K_C, and the sample coordinate system, K_S, Fig. 2.1 [1]. In the case of cubic materials, the crystal axes are referred to as [100], [010], and [001]. The sample coordinate system of rolled materials is also a Cartesian reference frame (X,Y,Z) of the axes parallel to the rolling (RD), transverse (TD), and normal (ND) directions, respectively. The orientation distribution function (ODF), i.e. the texture of the material, can then be defined by specifying the relative volumes of crystals of orientation g within the limits dg:

$$f(g) = \frac{dV/V}{dg} \tag{2.1}$$

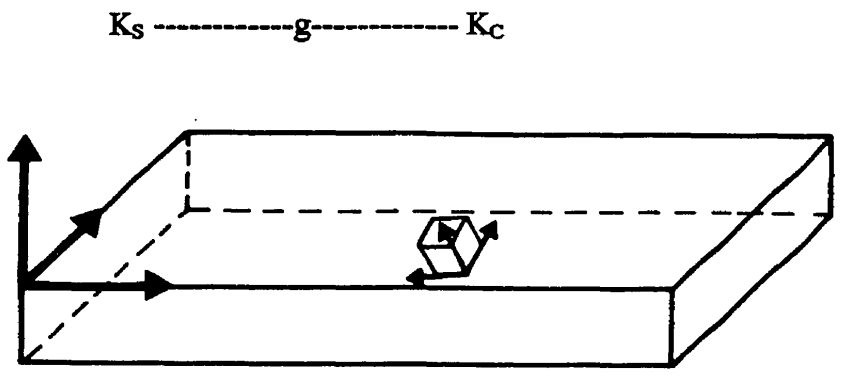

Figure 2.1 Orientation g of crystal coordinate system K_C with respect to sample coordinate system K_S.

The crystal orientation g is determined by the transformation matrix relating the sample and crystal coordinate systems, K_S and K_C, to each other.

$$K_C = g.K_S \quad ; \quad g = [g_{ik}] \tag{2.2}$$

Usually, this transformation rotation is specified by the Euler angles:

$$g = \{\varphi_1, \phi, \varphi_2\} \tag{2.3}$$

or by the Miller indices (metallurgical representation),

$$g = (hkl)[uvw] \tag{2.4}$$

The latter indicates that the crystal plane (hkl) is parallel to the rolling plane and that the crystal direction [uvw] is parallel to the rolling direction, Fig. 2.1.

Euler angles are the most commonly used rotation parameters, and are represented in three dimensions in Fig. 2.2 [2]. The ODF is approximated as a continuous function f(g), where g is a point in Euler space representing the rotations required to make the reference (specimen) axes coincide with those of the crystal. This function can be expanded into a series of generalized spherical harmonics and in this way provide a numerical representation of the texture [3]:

$$f(g) = \sum_{l=0}^{\infty} \sum_{m=-l}^{l} \sum_{n=-l}^{l} C_l^{mn} T_l^{mn}(g) \tag{2.5}$$

In practice, specimen and crystal symmetries lead to a reduction in the extent of summation, and a finite series truncation $l=L$ is used. The value of this limit depends on the actual texture and on the eventual use of the coefficients.

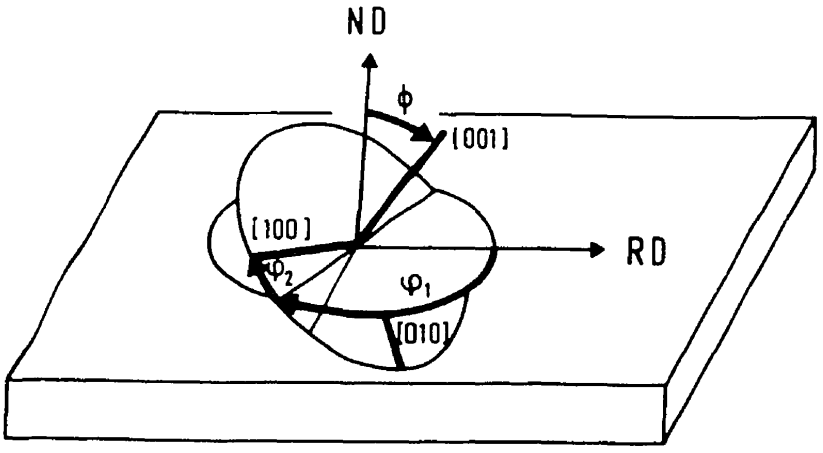

Figure 2.2 Description of orientation g by the Euler angles φ_1, Φ, φ_2 [4].

2.2.1 Fibres

The three dimensional representation of an ODF provides a powerful tool for quantifying and characterizing the texture. For practical purposes, however, this can be further simplified by expressing the orientation densities along selected fibres in the form of diagrams. As the textures in steels are frequently made up of fibres, this type of texture representation does not lead to a loss of essential information. An overview of the key texture fibres found in steels and their positions in Euler space is provided in Fig. 2.3. The orientations along the RD fibre are important for hot and cold rolled steels as well as for recrystallization textures, whereas the TD fibre components are mostly developed in hot rolled products. In deep drawing steels, the intensities along the ND fibre characterize the recrystallization texture. The surface texture of hot rolled products can be described in terms of the ζ fibre [5].

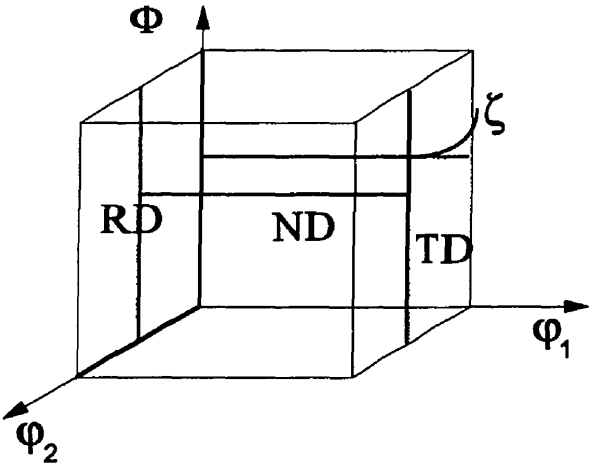

Figure 2.3 Main texture fibres in steel sheets presented in Euler space.

2.3 Hot Rolling Textures in Steels

In all processes such as recrystallization, deformation, and transformation, changes in the orientations of the grains take place, which lead to the development of texture. The latter is the main cause of the planar anisotropy of rolled sheets and plates. Depending on the TMP parameters, the texture development can be varied through modification of the above mentioned three processes.

During the recrystallization of austenite and the γ-to-α transformation, the texture is normally formed in two separate stages: both of these involve nucleation and growth of the product phase. To date, little is known about the governing mechanisms of nucleation and growth and of the role of the TMP parameters on these processes. By contrast, the deformation texture results from the rotation of grain orientations due to slip. Thus, the deformation texture depends solely on the previously recrystallized texture (or the

concurrently developing texture due to dynamic recrystallization) and the current strain path. Stable orientations are produced by deformation and the intensity of the associated ideal texture components is influenced by the amount of deformation in the absence of recrystallization.

2.3.1 Recrystallization Textures

In the roughing stage of controlled rolling, a series of high temperature rolling steps is carried out at temperatures above the no-recrystallization temperature (T_{nr}). The usual pass intervals and strains at this stage lead to the completion of static recrystallization, which in turn results in a fairly uniform grain size [6].

When austenite recrystallizes before transformation, a fairly weak transformed ferrite texture develops [7]. It has been reported that in the recrystallization range of austenite (above the T_{nr} temperature), the textures of plain carbon and Nb (0.034 wt.%) microalloyed steels are similar [8,9]. Since the deformation texture is not retained, the main components are the {001}<110> and {110}<110>, which are derived from the recrystallization texture components present in the γ, i.e. the cube {100}<001> and its twin {122}<212> [8].

2.3.2 Precipitation of Particles

The precipitation of particles during rolling makes a considerable contribution to texture formation in steels. First, the precipitation of carbides and nitrides retards the static recrystallization of austenite, leading to more pancaking by raising the T_{nr} [10,11]. And, secondly, strain induced precipitation prevents dynamic recrystallization. Consequently, the deformation texture is sharpened which , in turn, results in a sharper transformation texture in the ferrite. The size, distribution and orientation relationships of the precipitates with respect to the matrix are important characteristics of the precipitates in this regard. Strain-

induced precipitation is also influenced by the chemical composition of the steel and the deformation temperature [12].

The orientation relationship between precipitate and matrix also has an effect on the nucleation and growth modes [13] and can determine the morphology of the precipitates [14]. Hosford and Zeisloft's [15] analysis of the crystal plasticity of Al-Cu alloys has shown that the influence of oriented semi-coherent precipitates, such as θ', depends on both the shape and habit plane of the precipitates.

2.3.3 Deformation Textures

In controlled rolled steels, depending on whether deformation was carried out above or below the T_{nr} (or even below the Ar_3) and on the amount of deformation, the sharpness of the crystallographic texture of the ferrite is drastically changed [16-21]. This is explained in terms of changes in the austenite texture before transformation or by the effect of ferrite rolling in the two phase region. In Nb steels, the development of strong transformation textures can be expected, since the precipitation of NbC or Nb(CN) particles results in the formation of sharper austenite deformation textures because of the suppression of recrystallization.

It has been reported that the rolling of niobium microalloyed steels below the no-recrystallization temperature of the austenite (T_{nr}) leads to the formation of the copper {112}<111> and brass {110}<112> components of the fcc deformation texture [22,24]. The intensities of these components are increased by the amount of deformation imposed below the T_{nr}. Ray *et al.* [25] tried to simulate the austenite texture by cold rolling a Ni-Co alloy with a stacking fault energy close to that of austenite. They also found that the copper and brass, as well as the S, {123}<634>, are the main orientations in the deformed austenite.

The strain path also has an important role to play in the development of austenite deformation textures. For instance, in areas close to the surface of rolled plates, the plastic deformation occurring during hot rolling takes the form of simple shear. In this case, the RD fibre texture is not involved and a {110}<uvw> type of ferrite texture (the ζ fibre) is developed instead [5,21]. By contrast, deformation of the austenite along the mid-section is performed in plane strain, which usually leads to formation of the RD, TD and ND fibres in the ferrite after transformation.

2.3.4 Transformation Textures

Because of the crystallographic relationship between the product phase (e.g. bct martensite) and parent phase (e.g. fcc austenite), martensite inherits some texture from the austenite during transformation. Frequently, orientation relationships between parent and product phases in a transformation are expressed by parallelism between planes and/or directions in the two phases:

$$\begin{cases} (hkl) \| (h'k'l') \\ [uvw] \| [u'v'w'] \end{cases} \tag{2.6}$$

The transformation from fcc austenite to bcc ferrite is generally described in terms of the Kurdjumov-Sachs relationship [26]:

$$\begin{cases} (1\,1\,1)_\gamma \| (1\,1\,0)_\alpha \\ [1\,\bar{1}\,0]_\gamma \| [1\,\bar{1}\,1]_\alpha \end{cases} \tag{2.7}$$

Since the ODF has a definite mathematical form, the mechanism of the orientation transition, i.e. the transformation, can be investigated quantitatively. For this purpose, it is

possible to compare the experimental data with that obtained on the basis of the orientation transformation.

Experiments have shown that the preferred orientations in transformed Nb microalloyed steels with varied transformation products are the {332}<113> and {113}<110> [9, 22, 27-30]. Although the major orientations in the product phase, i.e. the {113}<110> and {332}<113>, are independent of the natures of the transformation products, such as ferrite-pearlite or ferrite-bainite or acicular ferrite, the texture sharpness and the fibre intensities are different among the various products. Yutori and Ogawa reported that, even with the same conditions of rolling, the intensity of the texture differs depending on the transformation products that are present, Fig. 2.4 [29].

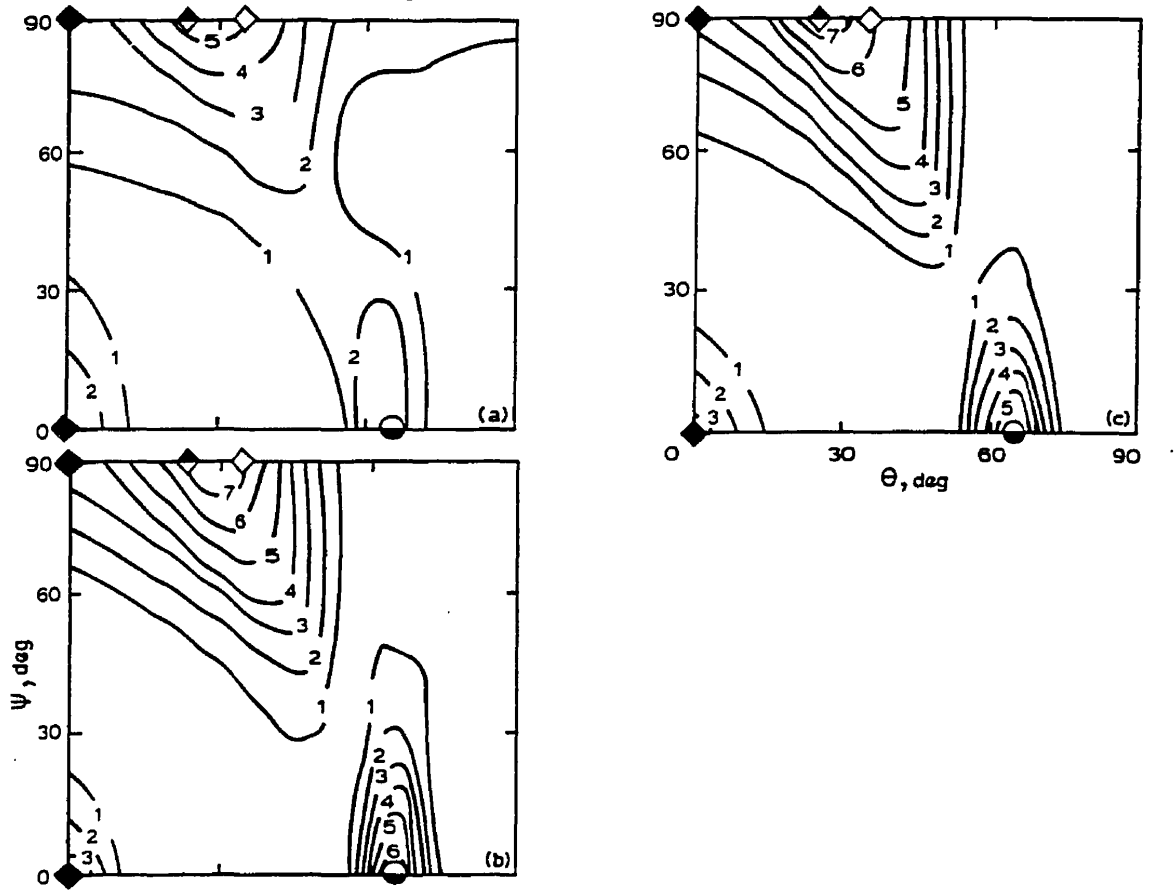

Figure 2.4 Φ=45° (Roe notation) ODF sections, showing the transformation textures of steels with various structures; a) polygonal ferrite, b) acicular ferrite, and c) martensite [29].

Because the texture of samples does not depend on the diffusion mode of transformation, even with changes in grain size and the presence of banded microstructures, it can be concluded that ferrite nucleation and growth as occurs in the diffusion mode of transformation does not have a major effect on texture development. Similarly, there is not much difference between the textures of air cooled acicular ferrite and water quenched martensite, both of which contain a sharp {332}<113> component. The shear mode of transformation or a mixed mode of transformation seems to be accompanied by an increase in the intensity of the {332}<113>, Fig. 2.5 [29].

The origin of the transformation texture and its relation to the microstructure have been discussed by many workers [22, 23, 27, 31-34]. Inagaki [21] showed that, depending on the thermomechanical processing parameters, the austenite deformation texture components, i.e. the copper {112}<111> and brass {110}<112> components, will be converted into the {113}<110> and {332}<113> components during the $\gamma \rightarrow \alpha$ transformation. Further rolling will convert these into other bcc texture components.

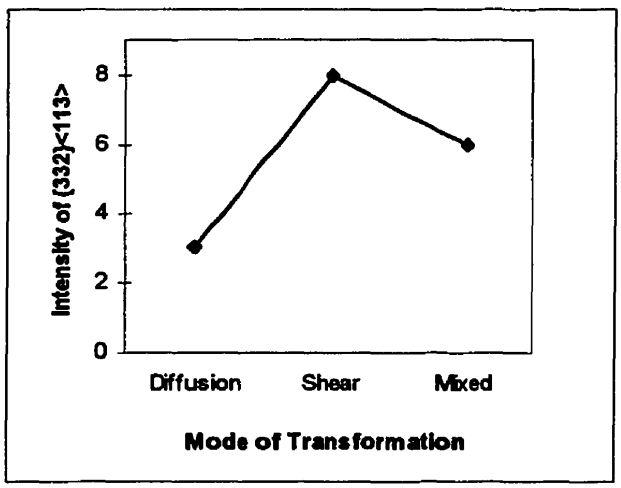

Figure 2.5 Relationship between the intensity of the {332}<113> orientation and the mode of transformation.

A more systematic study of the transformation components derived from various fcc rolling and recrystallization orientations according to the KS relationship has shown that more than one parent γ orientation can produce the same bcc orientation [33, 34]. From this it has been concluded that it is not possible to determine, unambiguously, the origin of some transformation texture components. In a more detailed discretization analysis, Butron-Guillen et al. [35] also considered the frequencies of occurrence of particular product orientations from a single parent. Their results for the most important fcc orientations are illustrated in the form of an ODF diagram in Fig. 2.6.

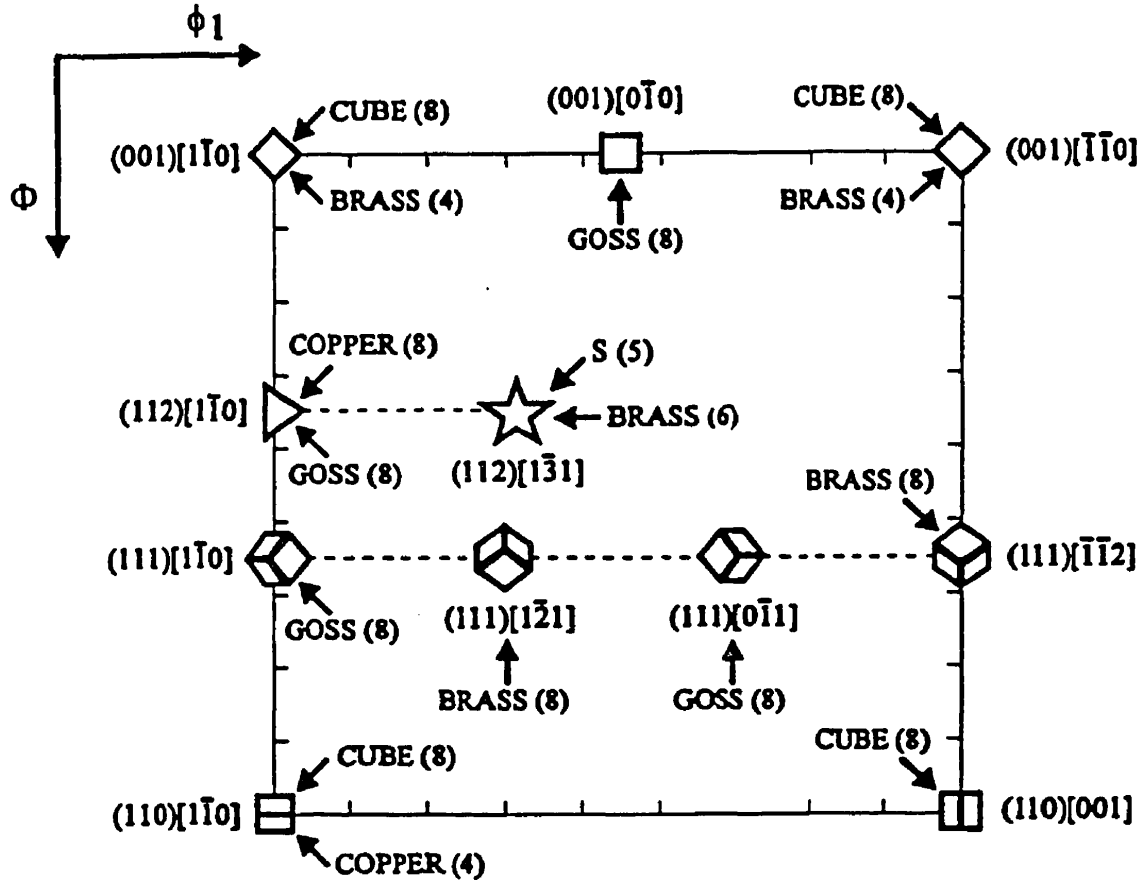

Figure 2.6 Selected bcc product orientations in the $\varphi_2 = 45°$ section, showing the major fcc parent orientations from which they originate [9].

Generally, there are two approaches to transformation textures. 1- All variants are operative to an equal degree (Kurdjumov-Sachs or the Nishiyama-Wassermann orientation relationship); their frequencies are independent of the transformation behaviour and the product texture after transformation is inherited from the Cu type austenite rolling texture [22, 27]. 2- Variant selection is utilized to describe the transformation mechanism applicable to deformed austenite and the orientation relationship between the parent and product phases is modified in this way [28, 29, 36-38].

2.3.4.1 Variant Selection

On the transformation of austenite to ferrite, the texture of the ferrite formed from pancaked austenite differs sharply from that observed when the austenite is recrystallized. Experiments have shown that, in hot rolled plain carbon and microalloyed steels, when the austenite is recrystallized between passes, similar textures are developed [8]. By contrast, sharp textures form when microalloyed steels are finish rolled below the T_{nr}. At high cooling rates, martensite generally forms by a change in volume and a transformation shear. Any elastic and plastic deformations that result from these phenomena can therefore affect the transformation.

The difference between the shear and diffusional growth processes as first-order transformation mechanisms is clear at the atomic level. Diffusional growth essentially involves the uncoordinated jumping of individual atoms by diffusion (which is motivated by chemical potential gradients) towards or away from advancing interface boundaries. Some areas of the boundary with sufficient atomic disorder make the atomic jumps energetically feasible. Shear, on the other hand, is a coordinated glide-type process, which can occur without significant thermal activation. In shear, each atom in the matrix phase has a destination site in the product phase and moves towards that position in a shuffle-like action. Growth by shear requires glide by partial transformation dislocations or unit vector

dislocations [39]. The high dislocation densities induced by accelerated cooling provide the required conditions for shear to occur.

Texture inheritance after transformation has been studied by both experiment and modelling. It is generally observed that when all possible variants have equal weights in the calculation, the predicted transformation textures are weaker than the experimental ones. For this reason, it is generally accepted in the literature that variant selection takes place [23, 28,2 9, 38].

The texture of martensite is said to be essentially a nucleation texture, which is solely determined by variant selection during transformation [34]. The other possible explanation for the differences between the observed and simulated textures in an acicular ferrite microstructure was first introduced by Inagaki as the selective growth of some transformed orientations [22]. A semi-quantitative work by Savoie et al. on variant selection also showed that when ferrite transformed from austenite at higher temperatures, the selective growth of some ferrite orientations seemed to occur [33].

Generally, the existing variant selection models fail to explain fully the observed experimental textures in a quantitative way. A detailed description of this approach can be found in Ref. 23. Recently, a cumulative variant selection model composed of three criteria was introduced by Jonas and co-workers [38]. In this model, a slip activity criterion, which takes into account the relative shears on the fcc slip systems that were active in the austenite during prior rolling, is utilized to explain the nucleation texture [37].

Two other criteria deal with the selective growth of some of the orientations whose nucleation is called for by the slip activity model. A planar growth criterion is introduced to consider the grain aspect ratio of the pancaked austenite grains as favouring growth along the rolling direction [38]. This rule favours growth of the {113}<110> and {112}<110> transformed copper orientations. A residual stress criterion also acts so as to favour those

variants which reduce the residual stresses in the matrix surrounding a given parent grain [36]. They showed that, using a combination of these three criteria in transformation texture calculations, good agreement can be obtained between predicted textures and experimental results.

2.4 Thermomechanical Processing

As mentioned in the previous sections, texture evolution occurs during TMP in parallel with the microstructural changes. The sharpness of the texture in the ferrite phase is directly influenced by the severity of the texture of the austenite phase prior to transformation. Therefore, all the parameters that affect the mechanisms of deformation, recrystallization, precipitation, and transformation contribute to texture development. In order to understand the effect of thermomechanical processing on the final ferrite texture, three important parameters of TMP, i.e. the chemical composition, and the controlled rolling and accelerated cooling schedules, are reviewed in the sections that follow.

2.4.1 Chemical Composition of Microalloyed Steels

To improve the weldability and toughness, the use of pearlite free steels was first proposed by Duckworth *et al.* [42]. Later, low carbon HSLA steels were developed [40, 41], which eliminated the need for extra tempering and also led to good weldability. For the last two decades, low carbon (0.03-0.06 wt% C) and extra low carbon (0.01-0.03 wt% C) microalloyed steels with different amounts of various microalloying elements have been introduced so as to provide better balances of strength and toughness.

From a texture point of view, it has been shown that transformation textures are generally strengthened by increasing the content of alloying elements such as Mn, Ni, Cr, and Mo [7, 24]. For instance, in C-Mn steels, increasing the Mn content strengthens the texture [7]. This is because the γ-to-α transformation takes place at lower temperatures and

deformation bands also become active sites for the nucleation of ferrite, in addition to the γ grain boundaries. This change in texture is accompanied by a change from a ferrite-pearlite to a fine acicular ferrite microstructure [7]. Higher manganese and molybdenum levels result in fully acicular ferrite microstructures at all cooling rates [29]. When the Mn_{eq} is more than about 2.5, bainite and acicular ferrite form on cooling, which leads to higher intensities of the {332}<113> component in the product phase [29]. Inagaki reported that the α transformation texture component {332}<113> is more sensitive to the amount of Mn than the {113}<110> component [7]. He also observed that the maximum intensity of the {113}<110> occurred in a lower Mn steel. Other alloying elements, such as Ni, Mo, Cr etc., which also act as austenite stabilizers, retard the transformation of γ in the same manner as Mn [7, 23].

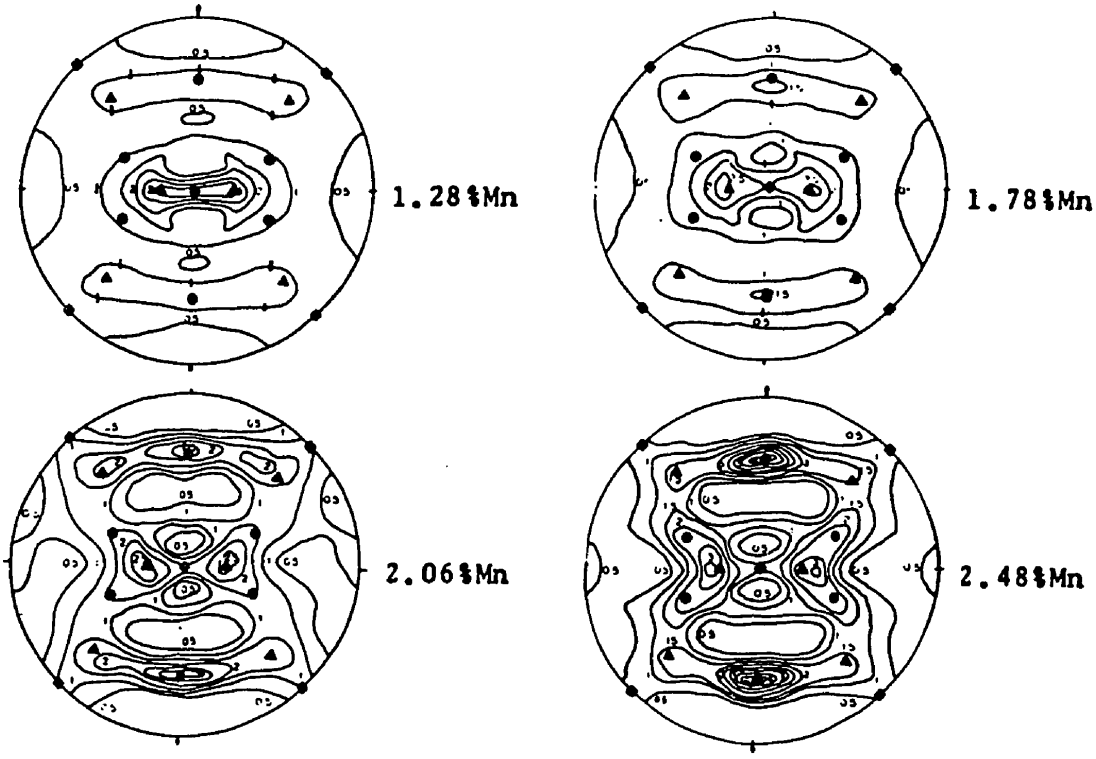

Figure 2.7 Effect of Mn on transformation texture, (200) pole figures [24].

If Nb is not added, textures such as those shown in Fig. 2.7 cannot be formed, irrespective of the Mn content. Thus, retarding recrystallization of the γ phase by the precipitation of Nb(C,N) affects the transformation texture. This is because strain accumulation prior to transformation depends on the effect of Nb in retarding the recrystallization of austenite. Many investigations [8, 21, 43, 44] have shown that the addition of Nb or V sharpens the texture in microalloyed steels. The texture of a plain carbon steel is compared with that of a Nb microalloyed steel in Fig. 2.8. Niobium affects the texture by increasing the T_{nr}, either as a substitutional element by contributing to solute drag [11] or by the precipitation of fine dispersions of NbC [45-47].

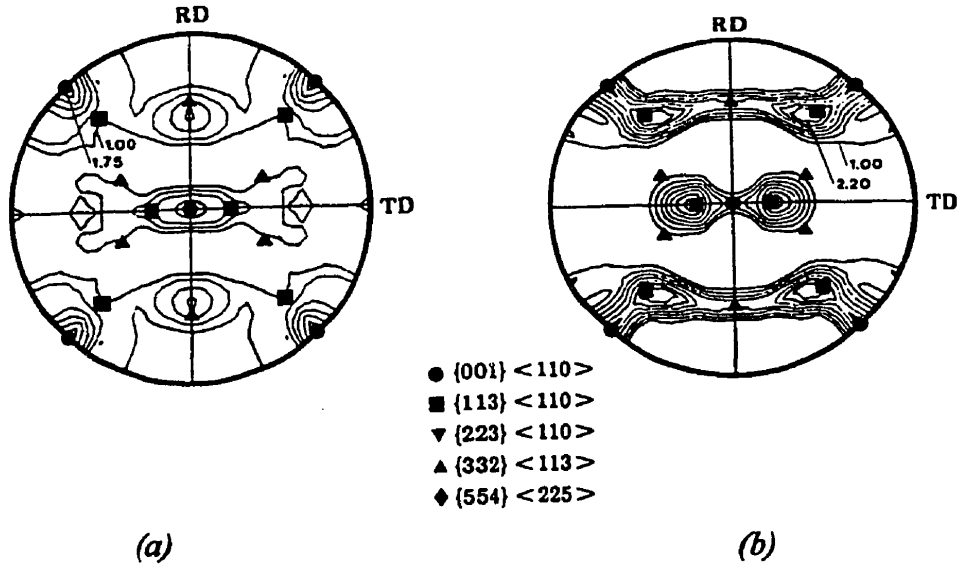

Figure 2.8 (200) pole figures of *(a)* a plain C steel and *(b)* a Nb steel finish rolled in the unrecrystallized austenite region.

2.4.2 Controlled Rolling

In controlled rolling, heavy reductions of the austenite in the no-recrystallization temperature range increase the surface area of the austenite grain boundaries; concurrently, high densities of deformation bands are introduced into the matrix. Both of these interfaces provide preferential nucleation sites for ferrite and therefore contribute to grain refinement.

2.4.2.1 Reheat Temperature

Generally, in order to promote grain refinement, the reheat temperature is selected so as to produce a fine and uniform γ grain structure [48]. Dissolution of the NbC or Nb(CN) particles during reheating is an important requirement so as to provide for the possibility of the Nb precipitation that is required to retard recrystallization. A good review of the different techniques for calculating precipitate dissolution temperatures can be found in Ref. 49. Using atom probe analysis, Palmiere *et al.* [49] presented the following relation for the solubility limit of Nb and C in austenite:

$$\log [Nb][C] = 2.06 - 6700/T \qquad (2.8)$$

Here T is the temperature in Kelvin and [Nb] and [C] are the niobium and carbon concentrations in weight percent, respectively. They also suggested that the grain coarsening temperature of austenite (T_{GC}) is 125 °C below the dissolution temperature of NbC (T_{DISS}):

$$T_{GC} = T_{DISS} - 125^{\circ}C \qquad (2.9)$$

This means that reheating below the T_{GC} promotes the presence of a fine and uniform hot rolled γ grain structure, while reheating above the T_{DISS} provides the greatest potential for precipitation in either the γ or the α during subsequent processing.

Inagaki has reported that sharper textures were developed when low reheating temperatures were used [24], which also entails finer γ grain sizes. This might arise because of the influence of the grain size on the rolling texture through its effect on the deformation and recrystallization textures [50]. He also showed that the {113}<110> is rather insensitive to a decrease in soaking temperature (or the initial austenite grain size), whereas the {332}<113> is noticeably strengthened when the soaking temperature is decreased [24], Fig. 2.9. Yutori and Ogawa reported that decreasing the prior austenite grain size increased the intensity of the {332}<113> in the shear or mixed mode of transformation but not in the diffusion mode [29].

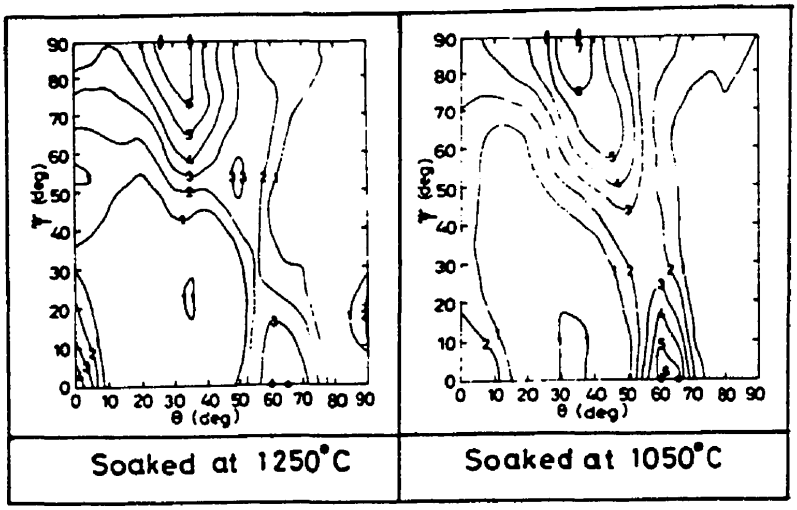

Figure 2.9 Effect of soaking temperature on the martensite texture of a low C-Mn-Nb steel, ϕ=45° sections [24].

2.4.2.2 Finish Rolling Temperature

The major purpose of controlled rolling is to enhance the strength and toughness of steel by grain refinement. Refinement of the ferrite structure is mainly achieved through refinement of the γ structure by choosing the appropriate rolling conditions, such as the amount of deformation and the finishing temperature [16,51,52]. In fact, the grain structure of α is determined by the recrystallized γ grain size before deformation in the no-recrystallization region and the amount of reduction in that region or in the subsequent γ + α region. Tanaka *et al.* described the controlled rolling process as consisting of the following three stages: (*i*) deformation in the γ recrystallization region (above the T_{nr}), (*ii*) deformation in the no-recrystallization region (below the T_{nr} and above the Ar_3), and (*iii*) deformation in the intercritical γ + α two-phase region, Fig. 2.10 [52].

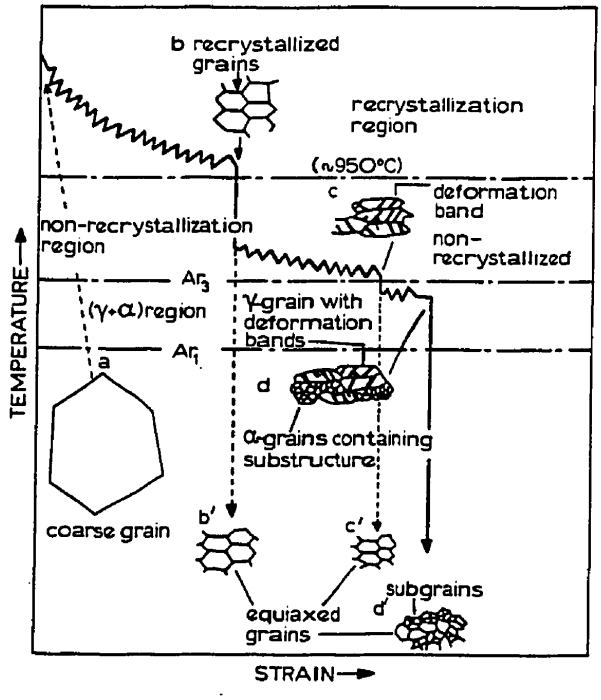

Figure 2.10 Schematic illustration of the three stages of controlled rolling.

2.4.2.2.1 Rolling in the Region above the T_{nr}

In this region, repeated recrystallization of the coarse austenite refines the γ structure which transforms to relatively coarse ferrite. When the steel is rolled in the region above the T_{nr}, the austenite is fully recrystallized [22]. Such recrystallization is responsible for the presence of orientations such as the {100}<011>, which originate from the {100}<001> austenite recrystallization texture [8, 27,43, 50, 53].

2.4.2.2.2 Rolling in the Unrecrystallized γ Region (below the T_{nr})

Deformation in the unrecrystallized γ region decreases the ferrite grain size by pancaking the austenite before transformation. Pancaking takes place because recrystallization is retarded by elements such as niobium [11, 45, 47]. The deformation of austenite below its recrystallization temperature introduces deformation bands in addition to elongated austenite grains. These divide an austenite grain into several blocks, and are equivalent to austenite grain boundaries with regard to the potential for ferrite nucleation. In niobium steels, the deformation bands are observed to occur at temperatures as high as 950 to 1000 °C because of the retardation of recrystallization by Nb [6]. The density of deformation bands depends primarily on the reduction and is only slightly affected by temperature and the strain rate of deformation [54].

By rolling between the no-recrystallization temperature of the austenite and the Ar_3, the intensity of the transformation texture derived from austenite rolling texture is increased. This texture contains maxima at {332}<113> and {113}<110> [22]. Fig. 2.11 [7] shows the effect of finishing temperature on the densities of these two components. In this region, the transformation texture is sharpened by decreasing the finishing temperature and increasing the reduction [24]. At a fixed finishing temperature, the intensity of the

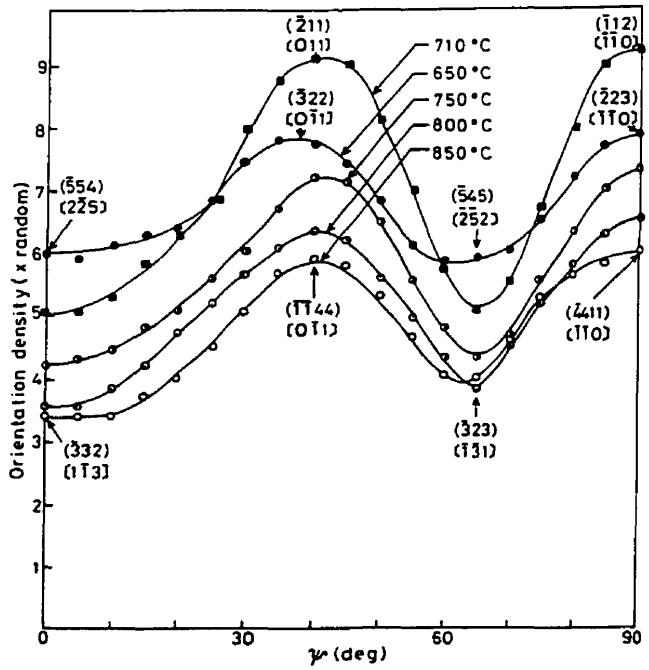

Figure 2.11 Variation of orientation density along the skeleton lines of a Nb-V steel in samples finish rolled at different temperatures [21].

{332}<113> increases with the amount of reduction; it is less sensitive than the {113}<110> to finishing temperature.

2.4.2.2.3 Rolling in the γ + α Region

Deformation in the intercritical range produces a mixed microstructure consisting of equiaxed α grains and elongated ferrite grains with hardened subgrains. In the deformed ferrite, recrystallization is very sluggish. This is partly because of the stabilization of the α sub-boundary network by the strain induced precipitation of Nb(C,N) [10, 19, 55]. Deformation in the two phase region has a substantial effect on the microstructure and mechanical properties. While deformation of the γ produces a structure of soft ferrite

grains, deformation in the two-phase region produces a duplex structure of soft polygonal and hard subgrain-containing ferrite grains. The latter component is responsible for increasing the yield and tensile strengths and decreasing the impact energy [6].

If controlled rolling is finished in the $\gamma + \alpha$ range, the following processes occur concurrently :

i- crystal rotation of the parent phase

ii- transformation of the parent phase

iii-crystal rotation of the product phase

Thus, the resultant texture is complex and the amount of deformation (and consequently the rate of transformation and the characteristics of variant selection) affects this texture. The following crystal rotations about <110> || TD for {332}<113> and about <110> || RD for {113}<110> are produced by rolling in this region [56]:

$$\{332\}\langle 113\rangle \rightarrow \{554\}\langle 225\rangle \rightarrow \{111\}\langle 112\rangle$$

$$\{113\} \sim \{112\}\langle 110\rangle \rightarrow \{223\}\langle 110\rangle$$

Inagaki also made a distinction between finishing in the upper or lower $\gamma + \alpha$ region [56]. In Nb-V steels finished in the upper intercritical region, most of the {332}<113> formed after the final pass. The {332}<113> component is relatively stable during rolling [57], so that the remainder of this component does not undergo any significant change during intercritical rolling.

In the lower range, the ferrite grains accumulate further deformation, because they have already transformed at higher temperatures. This results in a sharpening of the texture of the α phase and some orientations are modified. Orientations in the range {332}<113> to {554}<225> rotate towards {554}<225>, while orientations between {100}<011> and {113}<110> rotate towards {223}<110>. However, the theoretical calculations of Toth et al. [58], which were based on crystal plasticity using the relaxed constraint method for

simulating grain rotations during rolling, showed that the {112}<110> orientation is too stable to rotate toward the ND fibre. From this they concluded that TD fibre components are more desirable for deep drawability as they are converted into ND fibre components on further deformation.

2.4.3 Accelerated Cooling

Until 1962, air cooling was the most rapid cooling rate used during the industrial processing of hot rolled steels. In low carbon microalloyed steels, additional ferrite grain refinement can be achieved by the use of accelerated cooling to compensate for the loss in strength caused by the lower carbon content. Tanaka [59] considered accelerated cooling as an additional stage that can compensate for the disadvantages of controlled rolling such as mixed grain structures. In fact, controlled rolling increases the density of ferrite nucleation sites and accelerated cooling enhances the ferrite nucleation rate.

The advantages of the combination of controlled rolling and accelerated cooling can be summarized in terms of three concepts: *i*) more refinement of the transformed microstructure, *ii*) increased homogeneity of the grain structure, and *iii*) a decrease in the cost of alloying [60]. Interrupted accelerated cooling has been established as superior to continuous cooling since it provides an optimum degree of supercooling and thereby enhances α nucleation. Furthermore, interrupted accelerated cooling helps to preserve the flatness of the plate.

Accelerated cooling affects the transformation texture through variant selection [29]. When the transformation occurs at lower temperatures, the ferrite nucleation rate is increased and at the same time growth is limited. In this way, the cooling rate and cooling interruption temperature are very effective in influencing the conditions of nucleation and growth.

2.4.3.1 Cooling Rate

When the cooling rate is increased during transformation, a much finer microstructure is produced due to the fact that the transformation occurs at lower temperatures. This suggests that there is only limited growth of the ferrite nuclei. As mentioned above, for steels finish rolled in the unrecrystallized γ region, the preferred orientations of the transformation texture are the {113}<110> and {332}<113>. Figures 2.12 and 2.13 show the effect of Mn_{eq} and cooling rate, respectively, on the orientation densities. It can be seen that, even with low levels of Mn or of other alloying elements (Mn_{eq} = 1.27), the intensity of the {332}<113> is increased significantly when a cooling rate of 80 °C s^{-1} is employed. This intensity increase is accompanied by a change in microstructure from polygonal ferrite-pearlite to martensite.

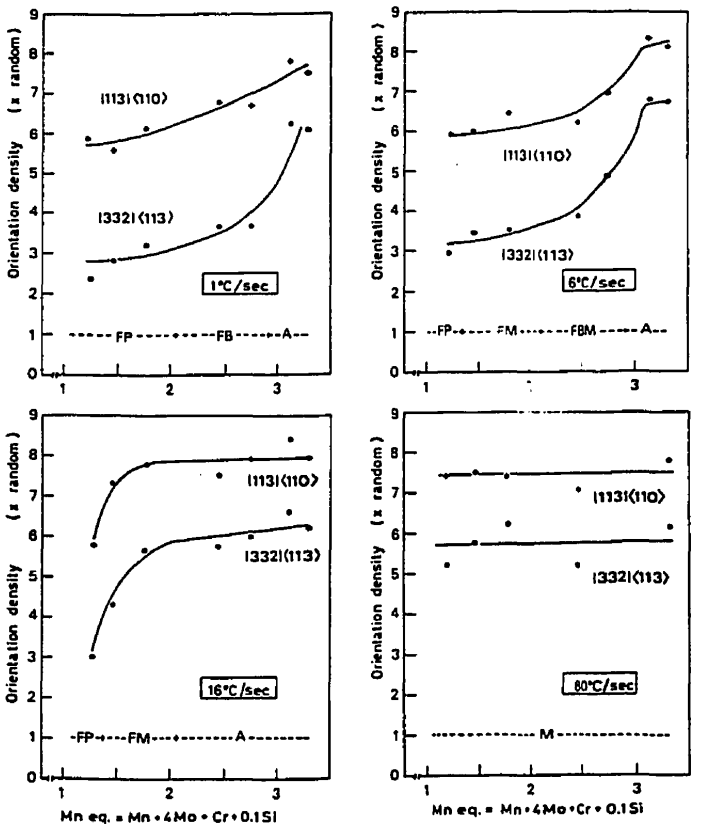

Figure 2.12 Change in orientation density as a function of content of alloying elements and increasing cooling rate [29].

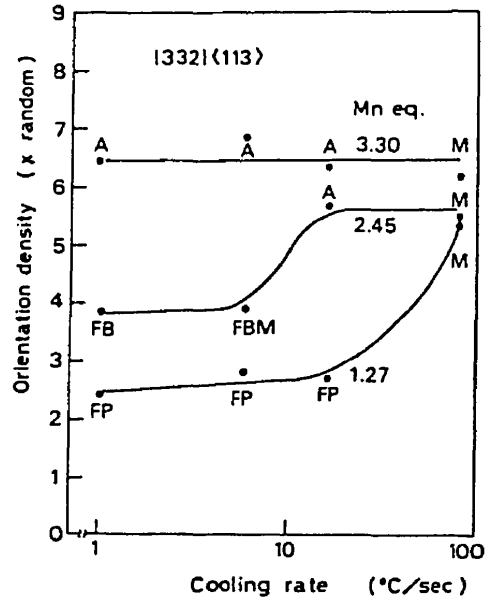

Figure 2.13 Change in orientation density as a function of cooling rate [29].

The fact that these components are dominant is independent of the cooling rate and the nature of the transformation products. However, the sharpness of the texture and the intensities of these orientations are obviously different among the various phase transformation products [29]. For example, the textures in both martensite and acicular ferrite are stronger than in polygonal ferrite-pearlite. This is, obviously, due to the effect of cooling rate on variant selection during nucleation of the product phase as well as its limited growth.

2.4.3.2 Cooling Interruption Temperature

Accelerated cooling influences the high and low temperature transformation products by affecting the nature, amount and distribution of the various phases and microconstituents. This is why it is used to control the microstructure and to optimize the final properties. Such effects are the most pronounced in the case of interrupted accelerated cooling during both isothermal and continuous cooling. Although the morphological and cementite

precipitation characteristics of the different types of bainite and martensite developed by interrupted cooling have been studied by numerous researchers [40, 61, 62], less attention has been paid to the effect of cooling interruption temperature on texture development. The salient features of this process with respect to the texture are studied in the present work.

2.5 Microstructural Development

2.5.1 Grain Refinement

The prediction of ferrite grain size from austenite grain size and shape is a difficult task. This is because, in addition to nucleation, the impingement and coalescence of the ferrite units must also be considered. In addition, coalescence can be strongly influenced by the strain-induced precipitation of microalloy carbides. In spite of these difficulties, it is clear that if the ferrite nucleation rate is increased, the resulting grain size is reduced. Most commercial controlled rolling processes for refining the ferrite grain size therefore concentrate on increasing the ferrite nucleation rate by increasing the value of S_V (grain boundary area per unit volume). This can be done by refining the recrystallized austenite grain size or by pancaking the unrecrystallized austenite so as to provide a larger number of heterogeneous nucleation sites [63]. In the section that follows, the characteristics of the acicular ferrite structure formed from pancaked austenite is studied in more detail.

2.5.2 Acicular Ferrite and Bainite

Acicular ferrite HSLA steels were developed by the Climax Molybdenum Company [64]. The idea is to use a low carbon (<0.06 wt%) Mn-Mo-Nb steel, which transforms to upper bainite from undeformed or conventionally hot rolled γ; it can also transform to acicular ferrite when the transformation is accelerated by controlled cooling. The acicular ferrite structure is illustrated in Fig. 2.14 together with the bainitic structure [6]. The acicular ferrite phase consists of fine non-equiaxed ferrite dispersed with cementite and

martensite islands. This constituent is defined as a highly substructured, non-equiaxed phase that forms on continuous cooling by a mixed diffusion and shear mode of transformation at temperatures slightly above the upper bainite transformation range [64] Acicular ferrite differs from bainitic ferrite with respect to the prior γ grain boundary network and the cementite and martensite morphologies.

In the bainitic structure, the prior γ boundary network is retained and plate-like cementite is formed at coarse lath boundaries as well as at the prior grain boundaries. By contrast, in the acicular ferrite structure, the prior grain boundary network is completely eliminated because of the presence of a fine grained structure, and small cementite and martensite islands are scattered throughout the matrix instead (see Fig. 2.14). Such a difference in structure is accompanied by a distinct difference in the facet unit (effective grain size). In the bainitic structure, the effective grain size is almost equal to the prior γ grain size, but in acicular ferrite, the facet unit is much smaller than the prior γ grain. This can make a difference in the mechanical properties. For instance, the acicular ferrite structure results in a lower ductile-to-brittle transition temperature.

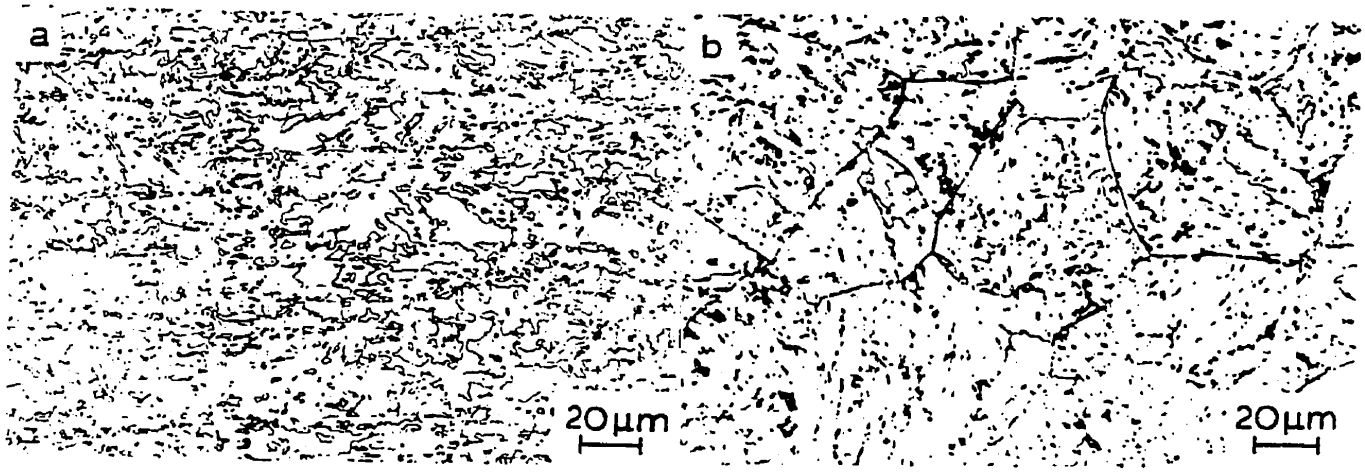

Figure 2.14 (a) Acicular ferrite and (b) upper bainite structures in a 0.06C, 0.2Si, 1.96Mn, 0.42Mo, and 0.06Nb steel [6].

A fully acicular ferrite structure exhibits high strength but poor toughness. The introduction of a proportion of fine polygonal ferrite, up to 15 %, by lowering the finishing temperature and increasing the amount of deformation in the austenite no-recrystallization region, can improve the toughness [6]. Continuous yielding followed by rapid work hardening is another feature of acicular ferrite [65]. Acicular ferrite steels, produced by controlled rolling and transformation hardening, allow the plate thickness to be increased without the loss of toughness at the midsection. This is particularly useful for linepipe service in severe arctic environments.

2.6 Anisotropy of Mechanical Properties

The most important metallurgical characteristics affecting the mechanical properties are: *i*) the size and shape of the grains of the transformation products, *ii*) the size and volume fraction of the precipitates, *iii*) the dislocation density, and *iv*) the texture. These effects are normally taken into account in the expanded Hall-Petch equation [40, 61].:

$$YS = YS_0 + \Delta YS_s + \Delta YS_T + \Delta YS_P + \Delta YS_D + k_y d^{-1/2} \qquad (2.10)$$

Here, YS_0, the lattice friction stress, is a constant for a given structure. ΔYS_S, the solid solution strengthening, varies approximately linearly with the solute content in dilute solutions [40, 66]. The texture component (ΔYS_T) is related to the Taylor factor and varies with the nature and sharpness of the crystallographic texture of the ferrite grains [67]. Whereas the square root of the volume fraction of precipitates increases the precipitation hardening increment, the precipitate size affects it inversely [41]. The yield strength contribution attributable to dislocation hardening (ΔYS_D) varies with the square root of the dislocation density [68].

In the literature, although the contribution of texture to the strength of hot rolled steels has been reported as only of the order of a few percent [41], its influence on the formability and deep drawability of cold rolled and annealed steels and on the through-thickness ductility of plate, i.e. on the phenomenon of splitting, have been the subjects of considerable interest and concern [69-73]. Some researchers have discussed the influence of the texture developed by controlled rolling on the strength and toughness and their anisotropies [21, 74-77]. One example of high yield and ultimate tensile strength anisotropy in a sample with a sharp {001}<110> texture is illustrated in Fig. 2.15.

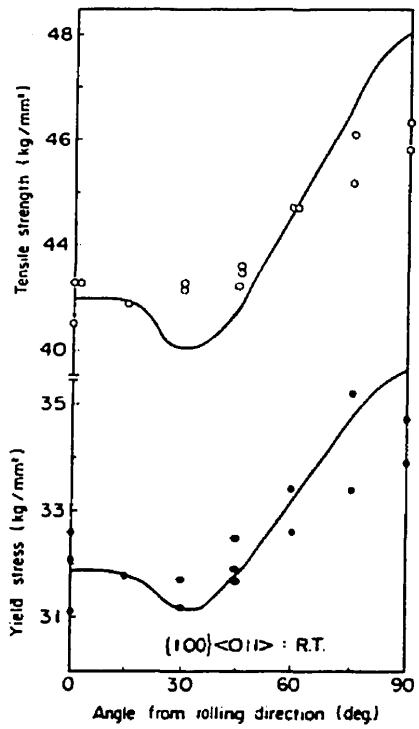

Figure 2.15 Anisotropies of yield and tensile strength for {001}<011> specimens tested at room temperature. Solid curves are the theoretical curves, which were fitted to the experimental results at the rolling direction [74].

The texture developed in the unrecrystallized γ region and/or below the A_{r3} temperature consists mainly of three fibres: *i*) A partial fibre covering the range of orientations between {001}<110> and {111}<110>, which have their <110> axes parallel to the rolling direction (RD or α fibre). (This partial fibre contains the {113}<110> and {112}<110> components that contribute most to the planar anisotropy of the mechanical properties [74].) *ii*) The TD fibre, consisting of orientations such as the {332}<113>, which have their <110> axes parallel to the transverse direction. *iii*) The so-called γ fibre (or ND fibre) for which {111} is parallel to the rolling plane. This third fibre is not as intense as the other two fibres. The ND and TD fibres lead to more isotropy of the mechanical properties [18, 23, 74].

2.6.1 Plastic Anisotropy Models

In bcc crystals, <111> is the slip direction. The {110}, {112} and {123} planes have been reported as potential slip planes. For simplicity, however, the "pencil glide" model has been used for the prediction of deformation textures [78]. In the PG model, all planes containing the <111> direction are considered as potential slip systems. It has also been shown that the {110} and {112] planes are sufficient to describe plastic flow accurately in bcc metals [79]. There exists an asymmetry of glide along the {112} planes, the twinning direction being the direction of easier glide; moreover there is no reason for the critical resolved shear stresses (CRSS's) to be the same on the {110} and {112] planes. Therefore, by assigning various values to the ratios:

$$\alpha_s = \frac{\tau_{\{112\}}\text{twinning}}{\tau_{\{110\}}} \tag{2.11}$$

and

$$\alpha_s = \frac{\tau_{\{112\}}\text{antitwinning}}{\tau_{\{110\}}} \tag{2.12}$$

different situations, such as the possibility of glide exclusively on the {110} or {112} planes, the asymmetry of {112} slip, etc. can be readily simulated [80].

Flow stresses can be predicted using the Sachs [81] average or the Taylor [82] and Bishop and Hill [83] approaches. The Sachs average assumes that the stress direction in each grain in the aggregate is the same but that they deform independently. Then the averaged flow stress of the whole specimen can be calculated as the average of the Schmid factor of each crystallite.

Taylor assumed that each crystallite undergoes the same deformation as the polycrystalline specimen. In general, five independent slip systems are necessary to allow the deformation to proceed. Among all possible combinations of five slip systems, the combination which minimizes the deformation energy will be active. Bishop and Hill showed that the Taylor least total shear concept is equivalent to their maximum work principle, and described the analytical procedures required to evaluate the flow stress for a textured polycrystalline aggregate.

Certain assumptions used in the Taylor theory permit the local plastic work on the active slip system, $\dot{W}_q(g)$, to be defined [84]:

$$M_q(g) = \frac{\dot{W}_q(g)}{\tau_{\{110\}}} = \sum_{i=1}^{n_{\{110\}}} b_{\lambda_i} + \alpha_S \sum_{j=1}^{n_{\{112\}S}} b_{\lambda_j} + \alpha_H \sum_{k=1}^{n_{\{112\}H}} b_{\lambda_k} \qquad (2.13)$$

Here the b_λ's are the amounts of shear on the {110} and/or {112} planes, and α_S and α_H were defined in *eqs.* (2.11) and (2.12).

The $M_q(g)$ functions can be developed as a series using cubic/orthorhombic generalized spherical harmonics, $T(g)$, by numerical integration through Euler space. This leads to the definition of the following coefficients [3]:

$$m_l^{\mu\nu}(q) = (2l+1)\oint_{Euler} M_q(g)\dot{T}_l^{\mu\nu}(g)dg \tag{2.14}$$

This mathematical formalism readily permits an averaging procedure to be applied to the Taylor factor [3].

$$\overline{M}_q = \oint_{Euler} M_q(g)f(g)dg \tag{2.15}$$

Therefore, for a test performed at an angle θ to the rolling direction, we can obtain:

$$\overline{M}_q(\theta) = \sum_{l=0}^{\infty}\sum_{\mu=l}^{M(l)}\sum_{\nu=l}^{N(l)} \frac{m_l^{\mu\nu}(q)C_l^{\mu\nu}}{2l+1}\cos 2(\nu-1)\theta \tag{2.16}$$

Daniel and Jonas accomplished the minimization of $\overline{M}_q$ by a polynomial regression method [85]. The corresponding minimum value of $\overline{M}_q$ represents the yield stress σ_θ/τ per unit CRSS on the {110} plane.

Models intermediate to those of Sachs and Taylor-Bishop-Hill have been introduced by a number of researchers [58, 86-89]. Some workers have proposed a modified version of the Taylor model in which certain components of the strain rate tensor are relaxed in the grains. All relaxed constraint models are based on the observation that the grains are not polygonal, but rather flattened (pancaked, as in the rolling process) or elongated in one direction (as in wire drawing).

As a result, misfits near the type C boundaries (Fig. 2.16a) only affect a very small volume fraction of the grains; thus the shear rate $\dot{\varepsilon}_{13}$ can be relaxed (Fig. 2.16b). The next component to be relaxed is the shear rate $\dot{\varepsilon}_{23}$, causing misfits near the type B boundaries.

These are two possible RC models in addition to the FC (full constraints or Taylor) model [87]. Note that when:

(*i*) $\dot{\varepsilon}_{13}$ is relaxed, four geometric constraints, pertaining to the four activated slip systems, are left in the Taylor-Bishop-Hill theory. This has been called the lath model [87].

(*ii*) both $\dot{\varepsilon}_{13}$ and $\dot{\varepsilon}_{23}$ are relaxed, as in the pancake model, three active slip systems are called for. This model, which was first introduced by Honneff and Mecking [86], has been employed by many researchers for the prediction of rolling textures.

Another relaxed constraint model, referred to as the RC2 model, in which $\dot{\varepsilon}_{12}$, $\dot{\varepsilon}_{13}$ and $\dot{\varepsilon}_{23}$ are relaxed, was used by Tavard and Royer [89] for the prediction of r-value in fcc metals. All these models can be employed in the calculation of R-values and in predicting the anisotropy of the yield stress.

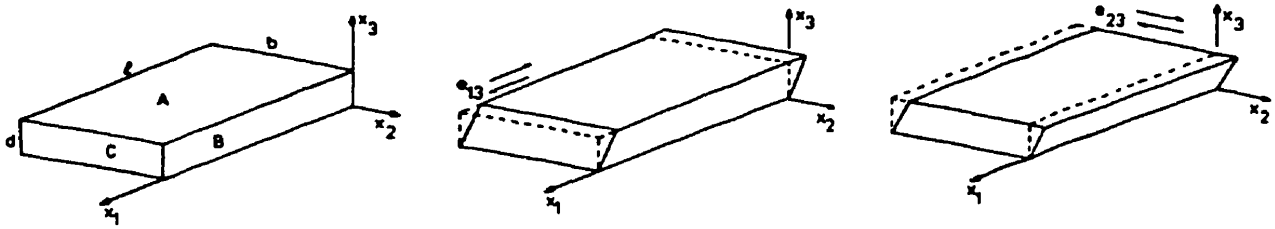

Figure 2.16 Schematic representation of a flat grain in a rolled sheet. x_1 is the rolling direction, x_3 is the sheet plane normal [87].

CHAPTER 3

Experimental Work

3.1 Introduction

The effect of the thermomechanical processing conditions on texture development and on the anisotropy of mechanical properties was investigated by carrying out systematic experiments to determine the influence of the most important parameters. Some of these parameters were chosen to simulate the rolling conditions at IPSCO. The evolution of the microstructure, texture, and mechanical properties during thermomechanical processing was studied in four separate sets of experiments. These were associated with:

I- Thermomechanical processing

II- Microscopic observations

III- Texture measurements

IV- Mechanical testing

In this program of tests, the controlled rolling of plate was simulated on the pilot mill scale at the MTL laboratory of CANMET in Ottawa. This process was designed so that the effect of the rolling conditions on texture development and on the mechanical properties could be studied at the McGill laboratories. In the sections below, the materials used will be introduced, after which the above four stages of the experimental work will be described.

3.2 Materials

The materials used in this investigation were two niobium microalloyed pipeline steels, designed to satisfy the requirements for the X-70 and X-80 grades. They were provided by IPSCO from continuously cast slabs which had been produced on a commercial scale. The chemical compositions of these steels are shown in Table 3.1.

This list is based on microprobe analysis carried out on a sample prepared from the center of the slab. The slab was cut into six pieces, each 150mm long, which were labeled A to F. The pieces were then cut into eleven blocks, each of which was 150mm wide, Fig. 3.1. All the blocks were machined on their tops and bottoms to reduce the slab thickness from 200mm to 150mm.

Table 3.1 Chemical compositions of the continuously cast steel slabs, wt.%.

El. / Steel	C	Mn	Si	Nb	Cu	Ni	Cr	Mo	Ti	Al	S	P	N
X-70	0.041	1.66	0.26	0.065	0.25	0.12	0.05	0.20	0.026	0.043	-	-	0.009
X-80	0.038	1.84	0.28	0.091	0.42	0.13	0.06	0.25	0.017	0.045	0.003	0.011	0.0092

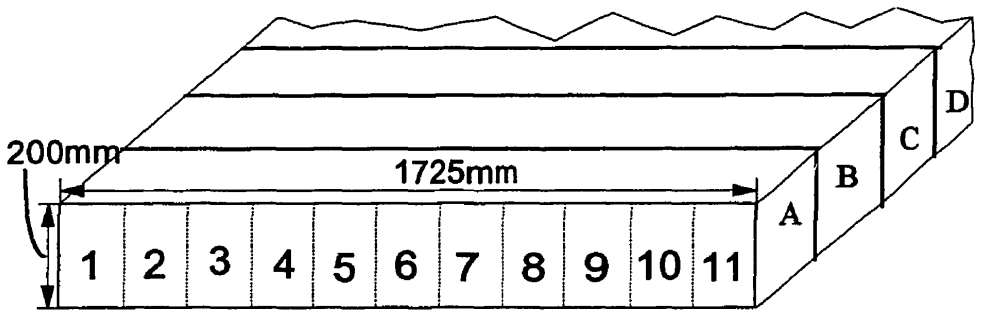

Figure 3.1 Material preparation from the slab.

3.3 Thermomechanical Processing

In this work, thermomechanical treatment includes both controlled rolling and accelerated cooling after rolling. The controlled rolling was designed to investigate the effects of prior austenite grain size, amount of austenite pancaking, and ferrite rolling in the two phase region on the anisotropy. The effect of the γ-to-α transformation texture on the anisotropy of mechanical properties was studied by accelerated cooling of the plates after rolling. This was performed by water spraying on the run-out table after rolling. For each controlled rolling condition, one sample was also air cooled for the sake of comparison. Fig. 3.2 illustrates the general TMP schedule employed.

For purposes of controlled rolling design, it was necessary to determine the exact T_{nr} (recrystallization stop temperature) of the austenite, Ar_3 (the γ-to-α transformation start temperature), and Ar_1 (the γ-to-α transformation finish temperature) temperatures for the steels. This was done both by using the empirical equations available in the literature [90,91], which are based on chemical composition considerations, and by using the laboratory torsion test method developed at McGill [92,93].

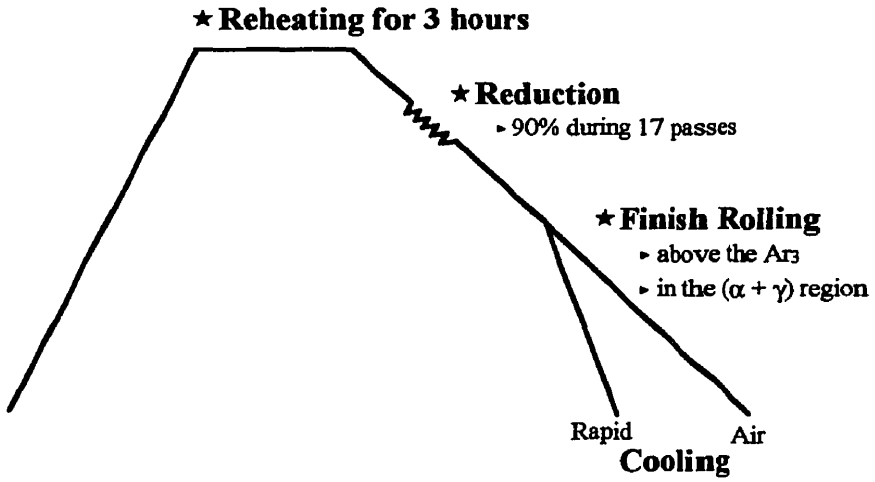

Figure 3.2 TMP schedule employed for the experimental work.

3.3.1 Measuring the Critical Temperatures

The critical temperatures associated with the hot deformation of austenite have been measured by a diverse range of laboratory techniques. For instance, multi-pass torsion testing [92] and compression tests [94] have been utilized to characterize the recrystallization behaviour of niobium steels. The γ-to-α transformation temperature (Ar_3) has also been determined by thermal analysis [95], dilatometry [96], continuous cooling compression testing [97], and even by texture measurements [98]. In this study, simulation of the rolling conditions in the pilot mill was achieved by using multi-pass torsion testing as a good technique for measuring both the T_{nr} and the Ar_3. The data obtained from the torsion tests were then used to design the controlled rolling experiments. Torsion tests were performed on both the X-70 and X-80 pipeline grades, the chemical compositions of which were presented in Table 3.1.

3.3.1.1 Torsion Test Technique

The torsion tests were carried out on a servo-hydraulic instrumented torsion testing machine, which is mounted on a lathe base and is used for the simulation of hot rolling. On this machine, the specimen is connected to the rotating hydraulic actuator at one end and is fixed into a grip at the other end. The rotational displacement of the actuator is measured by a potentiometer and is provided to the computer controller as the feedback signal. A torque cell is located next to the grip at the other end of the specimen to measure the developed torque. The specimen was located in a quartz chamber and was heated up in a four-element radiant furnace. An Electromax process controller, which was coupled to a process programmer, was used to control the temperature. The temperature was detected by a K-type Chromel-Alumel shielded thermocouple, which was in contact with the specimen on the gauge length close to one shoulder.

A TestStar workstation interface of the MTS system was used to record the twist and torque as well as the temperature. A microcomputer was connected to the digital controller of the TestStar to acquire the data and execute the test. The computer programs used for running the tests were designed using the MTS TestWare S/X application software, which provides a set of procedures that are put together into a series of logical steps to perform the test. The controller channels employed, command signals generated and the data acquisition activities performed are determined by the various steps of the program.

3.3.1.2 Torsion Test Method for Determining the Critical Temperatures

In multi-pass torsion tests, time is usually the controller channel that provides the command signals to the machine [92]. In the series of torsion tests that were performed in this study, for the first time, a temperature control program was utilized instead of the interpass time control program to make sure that the deformation at each pass is performed at the temperature shown in Table 3.2. In the program template, temperature was chosen as

the control channel. In this way, it was possible to simulate more precisely the temperature schedule of rolling at the pilot mill.

The conditions of pilot mill rolling (which represent in turn the rolling conditions at IPSCO) were simulated by employing a 17 pass torsion test. Since the amount of spread during each rolling pass was negligible, a von Mises factor of 1.155 was used to represent the strain under the plane strain conditions. The rolling deformation schedule and the simulated multi-pass torsion schedules are presented in Table 3.2. Standard torsion specimens, Fig. 3.3 , were used for the torsion tests.

From the twist angle, torque, and temperature data acquired by the data file, the equivalent stresses and strains were calculated according to the following equations:

$$\varepsilon_{eq} = \frac{D\theta}{2\sqrt{3}l} \tag{3.1}$$

$$\sigma_{eq} = \frac{\sqrt{3}(3+m+n)}{2\pi r^3} M \tag{3.2}$$

where D is the gauge diameter, θ is the rotation angle (in radians), l is the gauge length, and M is the developed torque. m and n are two test parameters that were given constant values, of 0.17 and 0.13, respectively, according to usual laboratory practice [99]. The mean flow stress (MFS) at each pass was taken to be the area under each σ-ε curve divided by the strain:

$$MFS = \frac{1}{\varepsilon_b - \varepsilon_a} \int_{\varepsilon_a}^{\varepsilon_b} \sigma_{eq} d\varepsilon_{eq} \tag{3.3}$$

where $(\varepsilon_b - \varepsilon_a)$ is the equivalent strain of the pass of interest. A curve of mean flow stress versus inverse absolute temperature was then drawn and the critical temperatures were determined from the points of slope change on the curve.

Table 3.2 Simulation of the rolling schedule by means of torsion testing.

	Torsion Schedule			X-70		X-80			
	Rolling Schedule		Twist Angle	Reheat Temperature, °C					
				1225		1275		1150	
Pass No.	Red., %	ε_{eq}	(radians)	High FRT	Low FRT	High FRT	Low FRT	High FRT	Low FRT
1	8	0.10	1.16	1160	1160	1185	1180	1145	1140
2	11	0.13	1.60	1140	1140	1160	1150	1130	1115
3	11	0.13	1.61	1120	1120	1135	1120	1120	1090
4	11	0.13	1.62	1110	1110	1110	1090	1110	1065
5	11	0.14	1.68	1080	1080	1090	1060	1090	1040
6	11	0.14	1.68	1065	1065	1070	1030	1070	1020
7	12	0.15	1.76	1050	1050	1050	1001	1050	1000
8	12	0.15	1.76	1030	1030	1030	990	1030	980
9	13	0.15	1.86	1010	1010	1010	970	1010	960
10	13	0.17	2.00	990	990	990	950	990	940
11	14	0.17	2.08	970	970	970	930	970	920
12	13	0.17	2.00	950	950	950	900	950	900
13	17	0.21	2.58	930	860	900	820	900	820
14	18	0.23	2.80	890	820	870	790	870	790
15	20	0.25	3.05	860	780	840	760	840	760
16	18	0.23	2.77	820	740	810	730	810	730
17	20	0.25	3.05	790	700	780	700	780	700

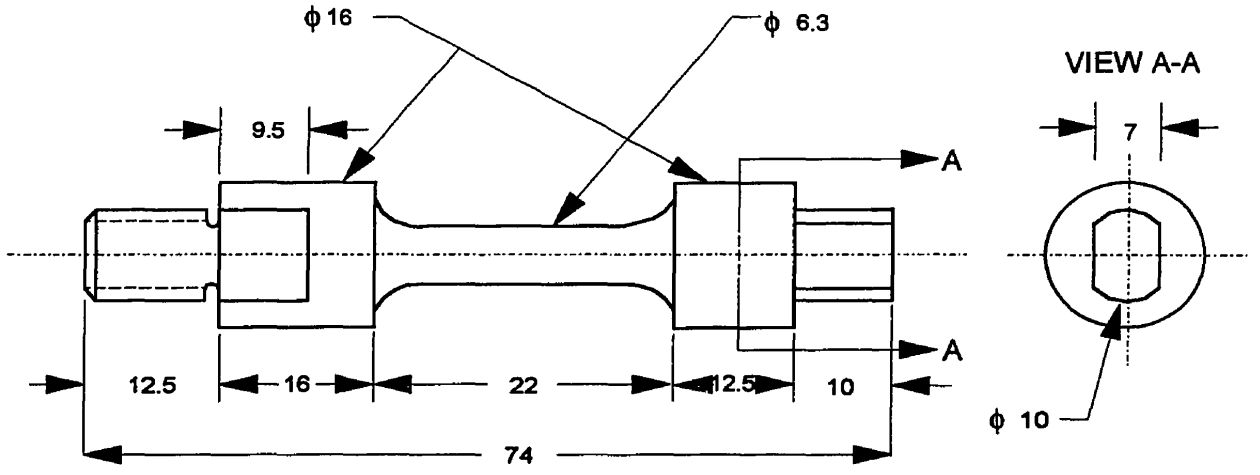

Figure 3.3 Geometry of the standard torsion specimen (all dimensions in mm).

3.3.2 Controlled Rolling

The controlled rolling was performed on a two-high, single stand, reversing mill. A general view of the pilot mill is presented in Figure 3.4. A Park Thermal programmable heating furnace with a maximum temperature of 1275 °C was used to soak the blocks for three hours before rolling. The rolling trials were operated at 1 m s^{-1} (45 rpm) roll speed with 470 mm diameter and 457mm length working rolls. Computerized data acquisition for load, torque, voltage, current, speed, roll gap, temperature, and time was employed for almost all the rolling trials.

Monitoring of the temperature during the rolling tests was done using thermocouples inserted into the bodies of the blocks. A 3.2 mm diameter hole was drilled almost 5 cm deep

into the side of each block at its mid-plane. Before loading the block into the furnace, a 3.2 mm diameter stainless steel pin was inserted into that hole. On removal of the slab from the reheating furnace, the pin was replaced by a K-type Chromel-Alumel thermocouple. A schematic sketch of the thermocouple position is illustrated in Fig. 3.5. The thermocouple was directly connected to an electrical sensor for temperature data acquisition by the computer. During the first rolling pass, the thermocouple was pressed and firmly embedded into the side of the block; it then continued to give a direct measure of the block-plate temperature during the controlled rolling and subsequent cooling process.

The position of the thermocouple at the exact mid-section of the plate and near the lateral centre of the block ensured that the readings were uniform in all the samples. Moreover, from their study of the through-thickness cooling gradient, Ruddle et al. [100] concluded that the temperature recorded at the center-thickness is representative of that throughout the plate thickness except for the near-surface regions.

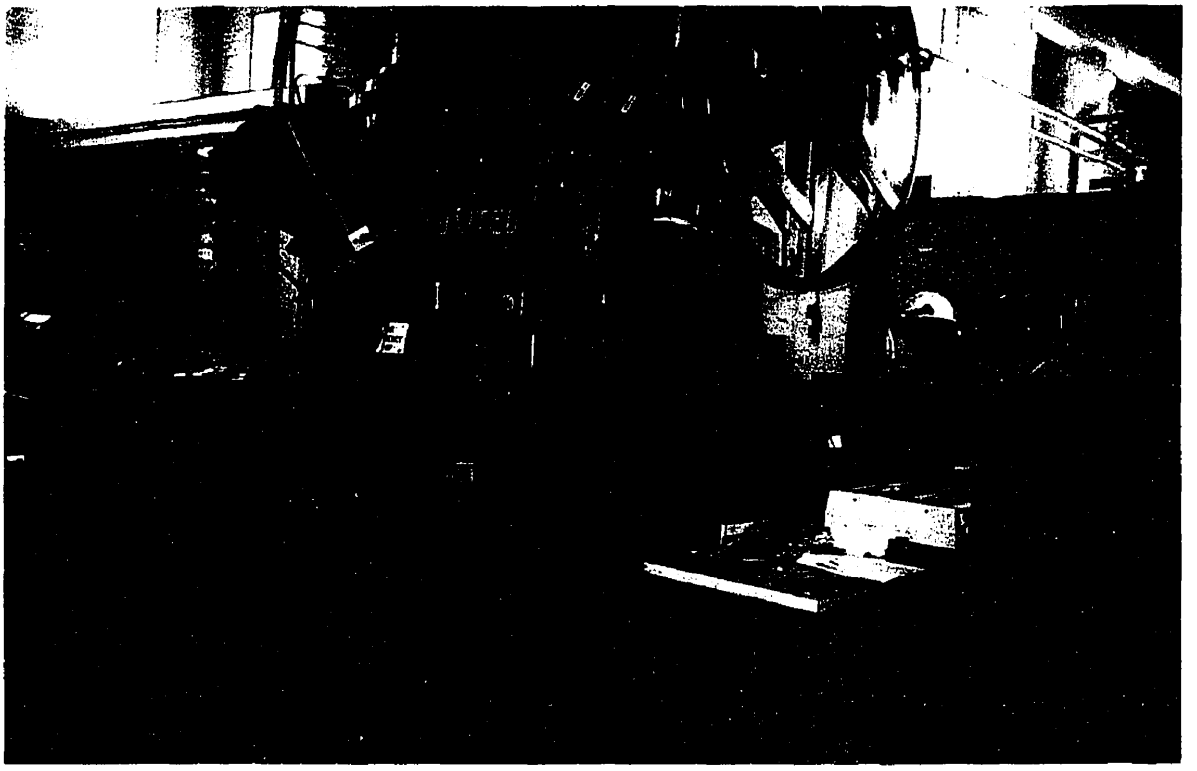

Figure 3.4 A general view of the pilot mill at CANMET.

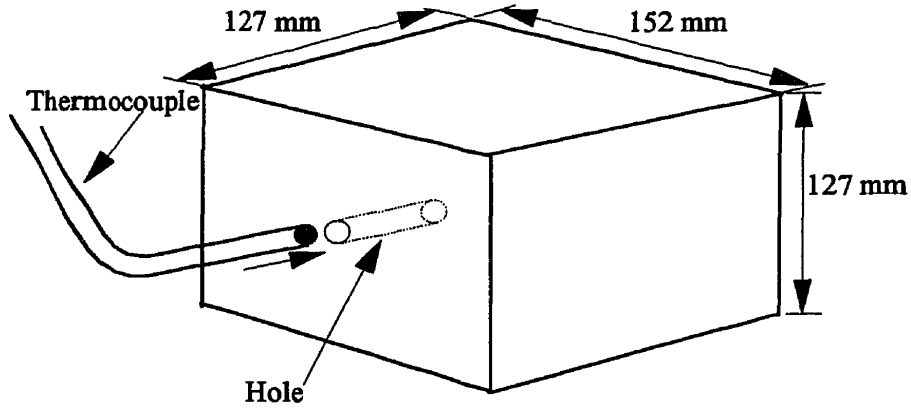

Figure 3.5 Schematic illustration of the position of the thermocouple in the block.

The controlled rolling conditions consist primarily of the soaking temperature, the strains, strain rates and interpass times associated with the individual passes, and the finish rolling temperature. To simulate the industrial operation, the number of passes and the amount of reduction per pass were kept the same as employed in the draft schedule of the IPSCO mill. These were presented in Table 3.2. Interpass times of 15 to 30 seconds for roughing and 40 seconds for finishing were used, which were based on a cooling rate of 1 °C s^{-1} for the plate. To investigate the effects of above rolling parameters, two reheat temperatures and two finish rolling temperatures were chosen, as already described above.

3.3.2.1 Reheat Temperature

The following two considerations played a role in selecting the appropriate reheat temperature:

- the effect of niobium in solution on retarding recrystallization;
- the effect of austenite grain size before rolling.

Reheat temperatures were therefore chosen based on existing empirical equations for the dissolution temperatures of niobium carbide and niobium nitride in niobium steels. The solubilities of NbC, NbN, and Nb(CN) are given by equations (3.4), (3.5) [101], and (3.6) [102], respectively.

$$\log[Nb][C]^{0.87} = 3.40 + \frac{-7920}{T} \tag{3.4}$$

$$\log[Nb][N]^{0.87} = 2.86 + \frac{-7920}{T} \tag{3.5}$$

$$\log([Nb][C + \frac{12}{14}N]) = \frac{-6770}{T} + 2.26 \tag{3.6}$$

The estimated dissolution temperatures for NbC, NbN, and Nb(CN) in the X-70 and X-80 steels along with the reheat temperatures chosen for each case are shown in Table 3.3. The soaking times (almost three hours for all cases) in the furnace were selected to produce almost uniform austenite grain sizes.

Table 3.3 Reheat temperatures chosen based on the estimated dissolution temperatures of NbC, NbN, and Nb(CN).

Steel	Estimated Dissolution Temperature, °C			Reheat Temperature, °C	
	Nb(CN)	**NbC**	**NbN**		
X-70	1149	1090	1085	1225	
X-80	1186	1025	1023	1150	1275

3.3.2.2 Finish Rolling Temperature

The amount of pancaking of the austenite and ferrite phases has a great influence on sharpening the texture, either during transformation or by the development of further deformation textures during ferrite rolling. The choice of finishing temperature is therefore an important parameter in the design of controlled rolling schedules. Here, to investigate the effect of finish rolling temperature, the first temperature was selected to be above the Ar_3 but below the T_{nr} (the no-recrystallization temperature), and the second was placed in the (γ + α) intercritical region. To fulfill these conditions, one high FRT at 790 °C and one low FRT at 730 °C were chosen for the X-70 steel. The finish rolling temperatures for the X-80 steel were selected as 780 °C and 690 °C.

3.3.2.3 Rolling Schedules

The total reduction employed on all the plates was about 90%, which is equal to a von Mises strain (equivalent strain) of 2.8. The number of passes and the amount of reduction per pass were also the same for all plates, see Table 3.4. The strain rate at each pass was calculated using the following equation [103]:

$$\bar{\dot{\varepsilon}} = \frac{\upsilon_r}{\sqrt{Rh_0}}\sqrt{r}\left(1+\frac{r}{4}\right) \qquad (3.7)$$

where $\upsilon_r = 2\pi Rn$, n is the revolutions per second (rps), and $r = \left(h_0 - h_f\right)/h_0$. The roll radius and rolling speed were R=235 mm and n=400 (rpm) or 9.6 (rps).

To determine whether rolling took place under plane strain conditions, i.e. with minimum spread, the amount of spread at each pass was calculated using eq. 3.8, in which L_p was estimated as $L_p = \sqrt{R\Delta h}$ [103]:

$$S = \frac{L_p / w_0}{1 + L_p / w_0} \qquad (3.8)$$

where R and Δh are the roll radius and amount of reduction at each pass, respectively. w_0 is the width of the plate before each pass. The results obtained in this way are illustrated in Table 3.4. As can be seen, after pass number 8, which is above the T_{nr} of the X-70 and X-80 steels, the amount of spread is about 8%. This confirms that the pancaking deformation of the plates was performed under plane strain conditions.

Table 3.4 Schedule of pass strains and strain rates.

Pass No.	Mill Setting, mm	Reduction Per Pass, %	True Strain	Equivalent Strain	Spread (*S*)	Strain Rate, s^{-1}
1	116.8	8	0.08	0.10	0.28	2
2	104.1	11	0.12	0.13	0.26	2
3	92.7	11	0.12	0.13	0.25	2
4	82.5	11	0.12	0.13	0.25	3
5	73.1	11	0.12	0.14	0.17	3
6	64.8	11	0.12	0.14	0.23	3
7	57.1	12	0.13	0.15	0.16	3
8	50.3	12	0.13	0.15	0.15	3
9	44	13	0.13	0.15	0.07	4
10	38.1	13	0.14	0.17	0.08	4
11	32.8	14	0.15	0.17	0.08	5
12	28.4	13	0.14	0.17	0.08	5
13	23.6	17	0.19	0.21	0.07	6
14	19.3	18	0.20	0.23	0.03	7
15	15.5	20	0.22	0.25	0.03	8
16	12.7	18	0.20	0.23	0.03	8
17	10.2	20	0.22	0.25	0.03	10

Initial thickness of the plate: 127 mm Total Strain: 2.90

Final thickness of the plate: 12.5 mm

Table 3.5 Rolling and cooling schedule for the X-70 *high* FRT samples.

TMP Schedule			**Cooling Rate, °C s^{-1}**	
Reheating at 1225°C Finish Rolling at 790°C		**Air**		
Pass No	**Desired Pass Temperature**	**Cooled**	**20**	**6**
		Actual Rolling Temperature, °C		
1	1160	1200	1194	1199
2	1140	1139	1140	1139
3	1120	1121	1121	1120
4	1110	1100	1100	1100
5	1080	1078	1081	1080
6	1065	1065	1065	1064
7	1050	1050	1050	1051
8	1030	1029	1030	1030
9	1010	1010	1010	1010
10	990	988	990	991
11	970	969	960	970
12	950	939	930	950
13	930	913	914	928
14	890	884	890	888
15	860	860	860	860
16	820	822	818	818
17	790	785	788	792
			Actual Cooling Conditions	
Cooling Start Temperature, °C			770	770
Cooling Stop Temperature, °C			625	620
Cooling Rate, °C s^{-1}			25	5

Table 3.6 Rolling and cooling schedule for the X-70 *low* FRT samples.

TMP Schedule		**Air**	**Cooling Rate, °C s^{-1}**	
Reheating at 1225°C Finish Rolling at 730°C				
Pass No	**Desired Pass Temperature**	**Cooled**	**20**	**6**
		Actual Rolling Temperature, °C		
1	1160	1198	1190	1196
2	1140	1141	1141	1140
3	1120	1120	1121	1120
4	1110	1100	1100	1100
5	1080	1079	1080	1079
6	1065	1065	1065	1064
7	1050	1050	1050	1050
8	1030	1030	1030	1030
9	1010	1009	1010	1009
10	990	989	990	990
11	970	970	969	969
12	950	950	949	950
13	870	870	869	868
14	830	830	831	830
15	800	800	801	797
16	760	759	761	760
17	730	731	734	729
		Actual Cooling Conditions		
Cooling Start Temperature, °C			730	715
Cooling Stop Temperature, °C			600	620
Cooling Rate, °C s^{-1}			21	6

Table 3.7 Rolling and cooling schedule for the X-80 *high* RT and *high* FRT samples.

TMP Schedule			**Cooling Rate**					
Reheating at 1275°C Finish Rolling at 780°C		**Air Cooled**	**40 °C s^{-1}**			**20 °C s^{-1}**		
Pass No.	**Desired Pass Temperature**		**Cooling Interruption Temperature, °C**					
			620	**520**	**420**	**620**	**520**	**420**
		Actual Rolling Temperature, °C						
1	1185	1210	1200	1197	1175	1175	1190	1210
2	1160	1160	1161	1160	1160	1160	1159	1160
3	1135	1135	1135	1135	1135	1136	1135	1135
4	1110	1111	1110	1110	1110	1110	1110	1110
5	1090	1090	1090	1090	1090	1090	1090	1090
6	1070	1070	1070	1070	1070	1070	1070	1070
7	1050	1050	1050	1049	1050	1050	1050	1050
8	1030	1030	1031	1030	1030	1030	1030	1030
9	1010	1011	1009	1010	1010	1010	1009	1011
10	990	990	986	990	990	1000	990	990
11	970	970	967	970	971	971	971	972
12	950	951	948	950	950	945	951	951
13	900	899	900	899	900	901	900	900
14	870	869	870	870	870	871	871	871
15	840	841	840	840	842	841	840	840
16	810	810	810	810	810	810	810	810
17	780	781	779	781	779	780	780	780
			Actual Cooling Conditions after Rolling					
Cooling Start Temperature, °C			771	767	765	770	768	765
Cooling Stop Temperature, °C			623	530	435	615	510	435
Cooling Rate, °C s^{-1}			43	47	47	22	19	19

Table 3.8 Rolling and cooling schedule for the X-80 *low* RT and *high* FRT samples.

TMP Schedule		**Air Cooled**	**Cooling Rate**					
Reheating at 1150°C Finish Rolling at 780°C			**40 °C s^{-1}**			**20 °C s^{-1}**		
Pass No.	**Desired Pass Temperature**		**Cooling Interruption Temperature, °C**					
			620	**520**	**420**	**620**	**520**	**420**
		Actual Rolling Temperature, °C						
1	1145	1148	1145	1150	1155	1150	1146	1136
2	1130	1130	1130	1130	1140	1131	1131	1130
3	1120	1120	1121	1120	1130	1120	1120	1120
4	1110	1110	1110	1110	1120	1110	1110	1110
5	1090	1090	1090	1090	1090	1090	1090	1090
6	1070	1070	1070	1070	1085	1070	1069	1070
7	1050	1050	1050	1050	1050	1050	1050	1050
8	1030	1030	1031	1030	1030	1030	1030	1030
9	1010	1011	1010	1011	1010	1009	1010	1010
10	990	990	990	991	990	981	990	989
11	970	970	969	971	970	970	970	970
12	950	951	946	950	950	949	948	949
13	900	899	901	900	900	900	901	899
14	870	869	870	870	870	869	870	870
15	840	841	840	839	838	840	841	839
16	810	810	810	811	810	810	810	810
17	780	781	780	784	781	779	782	779
			Actual Cooling Conditions after Rolling					
Cooling Start Temperature, °C			760	770	763	770	766	768
Cooling Stop Temperature, °C			610	518	430	650	520	390
Cooling Rate, °C s^{-1}			37	55	55	26	27	20

Table 3.9 Rolling and cooling schedule for the X-80 *high* RT and *low* FRT samples.

TMP Schedule		**Air Cooled**	**Cooling Rate**					
Reheating at 1275°C Finish Rolling at 690°C			**40 °C s^{-1}**			**20 °C s^{-1}**		
Pass No.	**Desired Pass Temperature**		**Cooling Interruption Temperature, °C**					
			620	**520**	**420**	**620**	**520**	**420**
		Actual Rolling Temperature, °C						
1	1180	1175	1183	1186	1198	1180	1180	1192
2	1150	1150	1151	1150	1155	1150	1150	1150
3	1120	1120	1120	1120	1120	1120	1120	1120
4	1090	1090	1090	1090	1090	1090	1090	1090
5	1060	1060	1060	1060	1060	1060	1060	1060
6	1030	1030	1030	1029	1030	1030	1030	1030
7	1001	1010	1010	1010	1009	1010	1008	1010
8	990	990	990	990	990	990	990	990
9	970	970	968	970	969	970	970	970
10	950	950	950	950	950	950	950	950
11	930	929	930	930	930	930	929	931
12	900	898	899	900	900	901	900	900
13	850	850	849	836	851	850	850	850
14	810	810	810	810	810	810	810	810
15	770	770	769	770	770	770	769	770
16	730	730	730	730	730	729	731	730
17	690	691	692	690	691	691	691	690
			Actual Cooling Conditions after Rolling					
Cooling Start Temperature, °C			691	686	691	690	689	689
Cooling Stop Temperature, °C			597	510	450	613	510	400
Cooling Rate, °C s^{-1}			37	49	50	28	28	18

Table 3.10 Rolling and cooling schedule for the X-80 *low* RT and *low* FRT samples.

TMP Schedule		**Air Cooled**	**Cooling Rate**					
Reheating at 1150°C Finish Rolling at 690°C			**40 °C s^{-1}**			**20 °C s^{-1}**		
Pass No.	**Desired Pass Temperature**		**Cooling Interruption Temperature, °C**					
			620	**520**	**420**	**620**	**520**	**420**
		Actual Rolling Temperature, °C						
1	1140	1140	1150	1150	1145	1070	1138	1146
2	1115	1114	1115	1115	1116	1067	1116	1115
3	1090	1090	1090	1090	1090	1062	1090	1088
4	1065	1065	1065	1064	1066	1059	1065	1065
5	1040	1040	1040	1040	1040	1040	1040	1040
6	1020	1020	1020	1020	1020	1019	1020	1020
7	1000	1000	1000	1000	1000	1000	1000	1000
8	980	980	980	980	980	980	980	980
9	960	960	960	960	960	960	961	960
10	940	939	939	941	940	940	940	940
11	920	913	919	920	920	920	920	902
12	900	886	899	900	900	898	900	874
13	850	849	850	849	850	850	847	849
14	810	810	810	810	811	809	810	808
15	770	769	770	770	769	769	771	769
16	730	731	730	730	730	731	731	730
17	690	691	689	690	690	691	688	691
			Actual Cooling Conditions after Rolling					
Cooling Start Temperature, °C			689	690	689	688	683	689
Cooling Stop Temperature, °C			610	550	445	630	500	420
Cooling Rate, °C s^{-1}			39	40	37	9	12	13

3.3.3 Accelerated Cooling

Accelerated cooling was performed on the MTL on-line accelerated cooling (OLAC) system at CANMET. This system was designed to operate in conjunction with controlled rolling operations on the pilot mill. After the final rolling pass, the steel plates destined for accelerated cooling were fed into the cooling chamber of the OLAC system along a series of small conveyor rollers. At the same time, the water flow was commenced immediately. A means was used to oscillate the steel plate back and forth to achieve uniform cooling of the steel plates.

A schematic diagram of the OLAC system is shown in Fig. 3.6. In Figure 3.7, the spray nozzles (Fig. 3.7a) and their schematic layout (Fig. 3.7b) are illustrated. The cooling system consisted of top and bottom double banks of spray nozzles, which provided angularly directed fan shaped water sprays inclined at 45° to the plate. In the chamber, cooling water was delivered to the top and bottom surfaces of the horizontal plate at a full flow rate through the conical-spray nozzles, which provided turbulent-flow cooling, Fig. 3.7b. The cooling rates in the plate were controlled by appropriate selection of the nozzle sizes, i.e. by the rate of water flow through the nozzles.

The procedure from the last pass to the onset of cooling required about 14 s during which heat was lost at air cooling rates of less than 1 °C s^{-1}. For all the rapidly cooled plates, the cooling start temperature was therefore almost 15° below the finish rolling temperature.

In this work, another important parameter that affects the morphology of the bainite and other products of accelerated cooling, i.e. the cooling interruption temperature, was also studied. By monitoring the temperature of the plate through the embedded thermocouple, the plate was withdrawn from the water spray at an appropriate time to achieve the desired

interruption temperature. After the interruption of accelerated cooling, the plates were allowed to cool by natural air convection to ambient temperature.

From the continuous cooling temperature (CCT) diagrams applicable to the X-70 and X-80 steels, which were determined by dilatometry [106, 107], cooling rates and cooling interruption temperatures were chosen as listed in Table 3.11. These were the cooling conditions applicable to each case of controlled rolling illustrated in Table 3.2. Each interruption condition was expected to lead to different percentages of the product phases, together with different morphologies, crystallographic features, and textures. By means of this experimental procedure, it was possible to study the relationships between the different microstructures, textures, and mechanical properties.

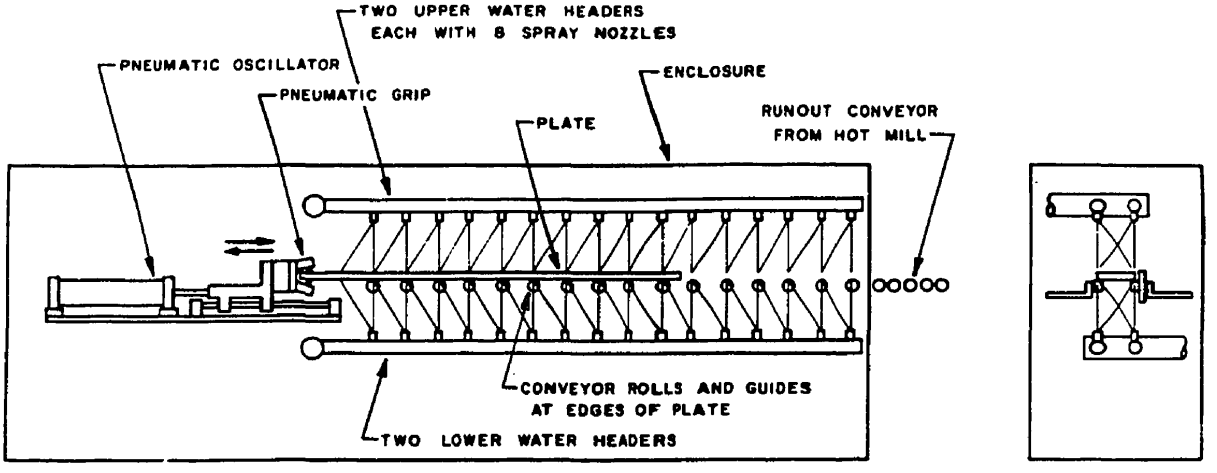

Figure 3.6 Schematic diagram of the OLAC system at CANMET [104].

Table 3.11 Cooling conditions of the plates after controlled rolling

Steel	Cooling Rate (CR), °C s^{-1}	Cooling Interruption Temperature (CIT), °C
X-70	Air Cooled	-
	6	620
	20	620
X-80	Air Cooled	-
	20	620
		520
		420
	40	620
		520
		420

Cooling rates were measured between the cooling start and stop temperatures by interpolation on the cooling curves. The cooling curves were obtained from both multi-pen charts and computer data recordings of the thermocouple readings.

Since the water spray cooling system was controlled manually, it was difficult to reproduce desired conditions of accelerated cooling with regard to both the cooling rate and cooling interruption temperature. A spread of ±8 °C/s was therefore considered acceptable for each cooling rate and ±30 °C for each cooling interruption temperature.

(a)

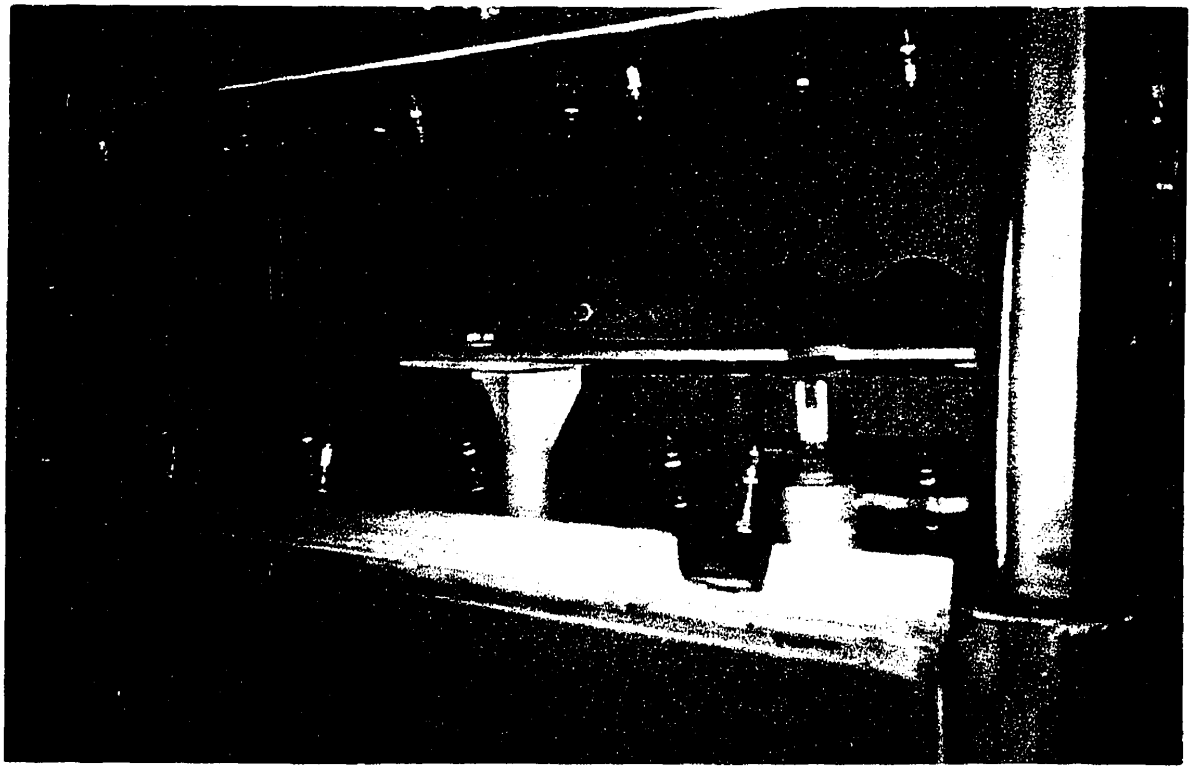

(b)

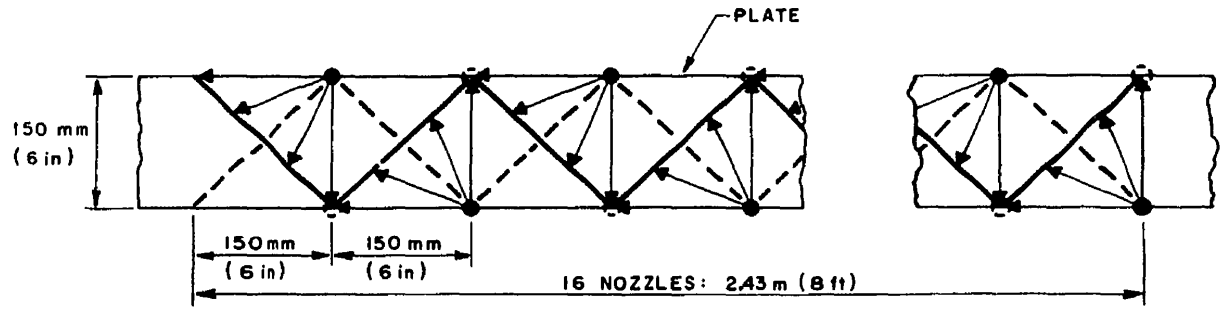

	NOZZLES	SPRAY PATTERN
TOP OF PLATE	●	———
BOTTOM OF PLATE	○	- - - -

NOZZLE ELEVATION APPROX. 9in FROM TOP AND BOTTOM OF PLATE
WATER SPRAY AT ANGULAR INCIDENCE TO PLATE SURFACE

Figure 3.7 *(a)* General view of the positions of the nozzles in the OLAC system, (b) schematic plan view of the locations of the upper and lower spray nozzles and of the pattern of impingement of the water on the plate

3.4 Microscopy

The microstructures of the materials produced by controlled rolling and accelerated cooling were analyzed by optical and electron microscopy. Generally, very fine microstructures developed in the rapidly cooled samples composed of various transformation products. In most cases, although acicular ferrite was the dominant phase in the microstructure, bainite and martensite, whose volume fractions depended on the cooling stop temperature and cooling rate, were also present. The characteristics of these microconstituents were studied by both scanning and transmission electron microscopy.

3.4.1 Sample Preparation

After rolling and cooling to ambient temperature, samples for microscopy (both optical and electron) were selected from the plate mid-width close to the position of the thermocouple, Fig. 3.8. Piece 1 was used for texture measurement and the sample preparation for that portion will be described in the relevant section below. Piece 2 was cut using a band saw so as to provide the longitudinal section (parallel to the rolling direction); it was then ground using 120, 240, 480, and 600 grit silicon carbide grinding papers. Next, each sample was polished using 6 and 1 micron diamond pastes on a rotary plate. Polishing using a suspension of alumina powder was performed as the final preparation stage before etching. The same sample was used for scanning electron microscopy.

In some cases, a combination of three micrographs taken along the rolling, transverse, and normal directions was used to provide a three-dimensional view of the microstructure. For this purpose, piece 3 in Fig. 3.8 was prepared using the same method as for piece 2, albeit on the transverse section parallel to the transverse direction of the plate. Piece 4 was also machined on the normal plane (parallel to the rolling plane) by milling

down to a thickness 0.3mm thicker than the half thickness of the plate. Then it was ground and polished to the exact half thickness within ± 0.1 mm.

For transmission electron microscopy, thin foils were prepared from slices about 400 μm thick taken from the mid-section of the plate. These had been machined by milling from piece 5, Fig. 3.8, parallel to the rolling plane from the top and bottom sides. The slices were first ground to a thickness of 120 to 150 μm using the 480 and 600 grit silicon carbide papers. They were then cut into disks of 3mm diameter with the aid of a punch. At this stage, a Struers Tenupol-2 jet-electropolisher was employed to produce perforations at the centres of each disk. An electrolyte solution of 10% perchloric acid and 90% methanol was used at temperatures of less than 30 °C. For the steels studied here, a potential of 30V, a high photosensitivity setting of the perforation detector, and a medium flow rate of electrolyte were found to provide the optimum thinning conditions.

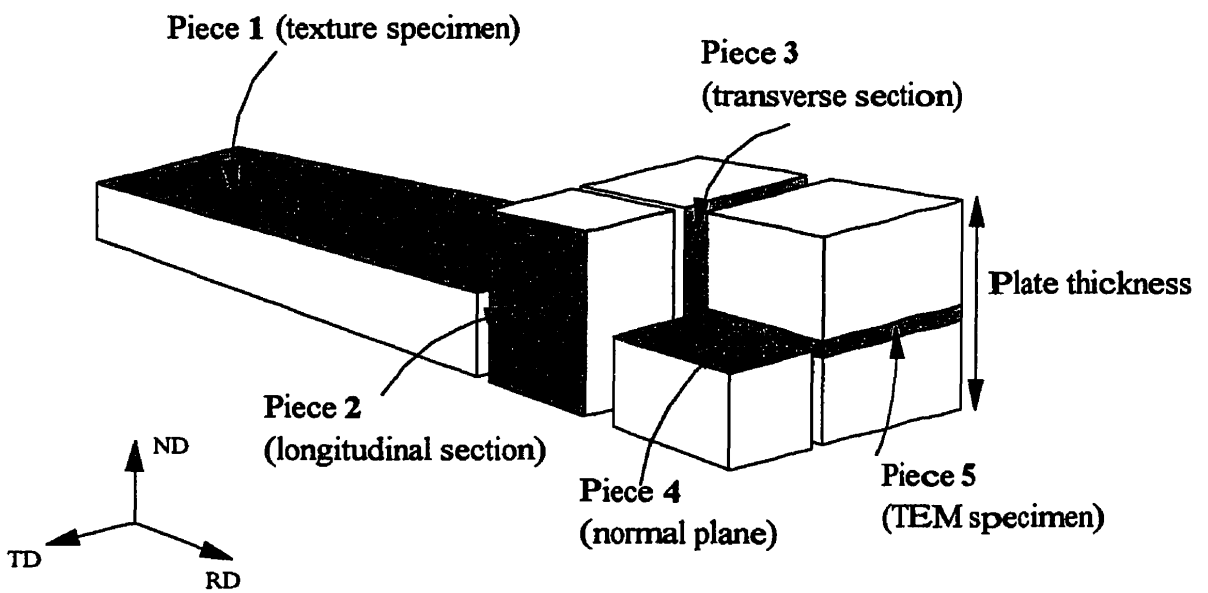

Figure 3.8 Schematic view of plate sections employed for preparation of the texture and microscopy specimens.

3.4.2 Optical Microscopy

The samples polished on the longitudinal cross section were chemically etched with a solution of 2% nital. As a result, the ferrite grain boundaries in the air cooled plates and almost all the acicular ferrite grain boundaries in the rapidly cooled plates were revealed. In this way, it was possible to compare qualitatively the general microstructures of the plates processed under the present wide range of TMP conditions. This was done using a NEOPHOT 21 optical microscope, which was connected to a computer so that the images could be saved as graphics files. Due to the typical morphology of acicular ferrite, it was not possible to have a quantitative measure of the ferrite grain size, except for the air cooled samples, in which a high percentage of polygonal ferrite had developed.

3.4.3 Scanning Electron Microscopy (SEM)

For SEM metallography, the longitudinal section samples used for optical microscopy were further etched with nital to provide more contrast. A JEOL JSM-840A scanning electron microscope was utilized to obtain better resolution of microconstituents such as bainite and acicular ferrite. The secondary electron mode with 20 kV accelerating voltage and a medium working distance were employed in almost all cases. However, in some cases, the working distance was reduced to increase the contrast.

3.4.4 Transmission Electron Microscopy (TEM)

Metallographic examination by transmission electron microscopy was carried out in order to characterize the bainitic microstructures in the rapidly cooled samples. Two transmission electron microscopes were used for this purpose: a JEOL-100 CXII transmission microscope with a maximum accelerating voltage of 100 kV and a Phillips CM20 with an accelerating voltage of up to 200 kV.

3.5 Texture Measurements

In order to study the relationship between the microstructural characteristics of the thermomechanically treated plates and the orientation densities of the grains, texture measurements were performed by the x-ray reflection method. All the texture measurements were carried out using a Siemens D-500 x-ray goniometer. A description of the x-ray goniometer is given in Ref. 9. Using the back reflection method, pole figures were measured on the samples prepared from the mid-sections of the rolled plates on a surface parallel to the rolling plane. The same location was used for all samples for consistency.

3.5.1 Sample Preparation

Texture specimens were machined from samples at the centers of the plates. For all plates, piece 1, Fig. 3.8, was machined by milling down to the half thickness plus 0.3mm. Then it was ground gradually with the aid of 120, 240, 480, and 600 grit silicon carbide papers and polished using 6 and 1 micron diamond pastes. Finally, electropolishing was performed to remove any material deformed during polishing. The optimum conditions for producing shiny surfaces were: a current of 1.5 A, a voltage of 20 V, and a time period of 80 seconds. By means of this method, almost 50 μm of the material was removed from the top surface, leaving the sample section within ± 0.1 mm of the exact half thickness of the plate.

3.5.2 Pole Figure Measurement

The pole figure measurements were performed by x-ray diffraction using the back-reflection technique. Three incomplete pole figures, which are normally based on the (110), (200), and (211) reflections for bcc materials, were measured using Mo-K_α x-ray radiation. ODF's were calculated from the experimental pole figure data by the series expansion

method. A user-friendly software [107] was used for the texture calculations and plotting the graphs.

3.6 Mechanical Testing

As mentioned in Chapter Two, it is well known that the relatively large directionalities of strength and toughness observed in control-rolled HSLA steels are closely related to their textures. For the purposes of the present investigation, a semi-quantitative relationship was therefore established between the texture and the anisotropy of strength and impact strength of the acicular ferrite containing HSLA steels. This was done by measuring the yield strengths of the thermomechanically processed plates along different directions with respect to the rolling direction. The yield strength was measured by the 0.2 % offset method because almost all the samples appeared to display continuous yielding due to their acicular microstructures. The impact test results are not presented in this thesis, so that experimental methods employed for these tests are not described here.

3.6.1 Sample Preparation

All samples for mechanical testing were prepared from the area shown in Fig. 3.9 to ensure reasonable uniformity of conditions such as the strain state and temperature during thermomechanical treatment. For this purpose, 35 cm of the tail and head of the plate were discarded, together with 2cm from the edges. Flat samples were machined from the top and bottom sides of the plate to a thickness of 5 mm at its centre.

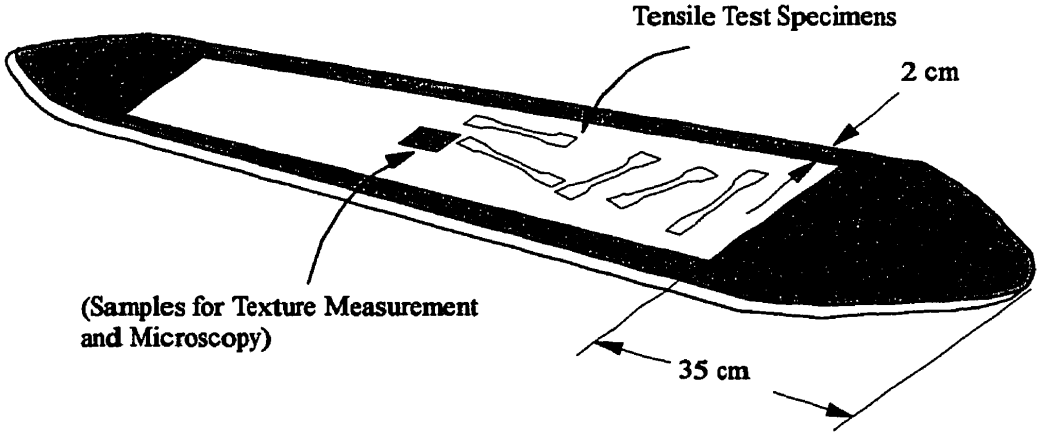

Figure 3.9 Preparation of mechanical testing samples from the central regions of the plate.

In order to investigate the strength anisotropy, tensile test samples were machined from the plates along inclinations of 0°, 22.5°, 45°, 67.5°, and 90° with respect to the rolling direction. Three to five tensile samples were prepared for each direction. The dimensions of the subsize flat samples machined according to ASTM standard E8M are shown in Fig. 3.10.

As allowed by ASTM E8M, a taper of nearly 1% was fashioned along the gauge length of each sample toward the center so as to induce a weaker cross section within the gauge length and to ensure that the sample broke within the gauge length. The shoulders of the specimens were arbitrarily extended to 3 cm length in order to increase the contact surface with the grips. The tensile tests were carried out on an instrumented MTS machine. A special MTS extensometer was used for measuring the elongation precisely.

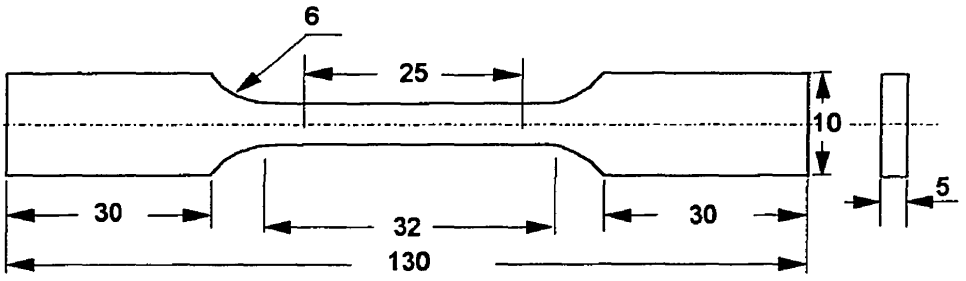

Figure 3.10 ASTM subsize flat tensile specimen [108] (all dimensions in mm).

3.6.2 Tensile Testing

3.6.2.1 Tensile Test Technique

A closed-loop servo-hydraulic MTS machine with a capacity of 100 kN was used for tensile testing. Displacement of the actuator was measured from the output of a linear variable differential transformer (LVDT) with a total linear range of ±50mm. Loads were measured using a 50 kN (10^5 lb.) load cell at its full range. Data acquisition and control were performed by means of a personal computer coupled to the MTS TestStar workstation interface. The TestStar workstation includes the TestStar software, a load unit control panel, and a digital controller, Fig. 3.12. The TestStar software was run on the OS/2 operating system on the PC, and employed to provide a graphical user interface for overall system control. The digital controller acted as an interface between the computer and the rest of the system. The digital controller controlled test command generation, the servo control functions, data acquisition and signal conditioning. The load unit control panel (LUC) helped the operator to control the hydraulics of the load unit, Fig. 3.12.

A template in the Testware-SX software, which is a set of written commands, consists of all the logical steps required to perform a digitally controlled test. All the tensile tests were performed at room temperature. In addition to the displacement records, a special MTS extensometer with a 25 mm gauge length was used to record the precise elongation of the gauge length. The extensometer was also connected to the controller and elongation data (mm/mm) were acquired directly by the data file. Time, displacement, and force were the other data which were acquired every 2 seconds and transferred to the data file. These data were then analyzed using the Windows Excel software.

3.6.2.2 Tensile Testing Method

Tensile properties such as the yield strength and the uniform elongation were obtained from the true stress-true strain curves. However, the ultimate tensile strength was obtained from the engineering stress-strain curve, as defined by eq. (3. 9) [103]:

$$\sigma_{UTS} = \frac{F_{max}}{A_0} \tag{3.9}$$

where F_{max} is the maximum tensile force and A_0 is the initial cross section of the specimen. From the data acquired by the MTS machine for the tension force and the elongation of the gauge length, the true stresses and true strains were calculated using the following equations:

$$\sigma = S(1+e) \tag{3.10}$$

$$\varepsilon = \ln(1+e) \tag{3.11}$$

where $S = F/A_0$ and $e = \Delta L/L_0$ are the nominal (engineering) stress and strain, respectively. ΔL is the change in gauge length and L_0 is the initial gauge length. The yield strength was measured by the 0.2% offset method on the true stress-true strain curve.

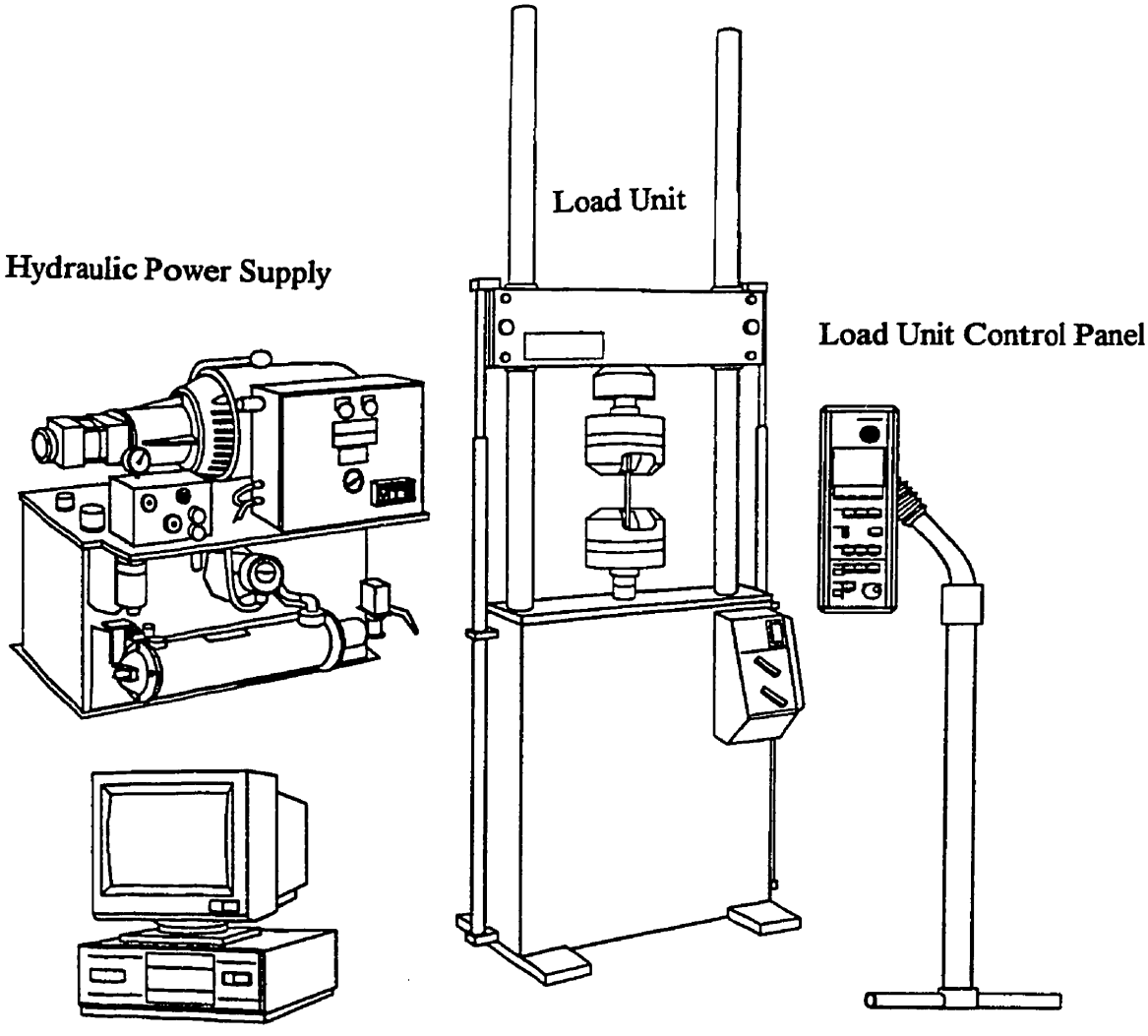

Figure 3.12 The main components of the TestStar materials testing workstation.

CHAPTER 4

Microstructural Evolution during Thermomechanical Processing

4.1 Introduction

From a metallurgical point of view, TMP improves the strength and toughness of rolled niobium steels by means of three distinct processes: *i*) grain refinement of the austenite, *ii*) control of the γ-to-α transformation, and *iii*) the precipitation of Nb-base particles. Grain refinement is achieved by means of the static or dynamic recrystallization of austenite and by the application of pancaking deformation. The transformation and precipitation processes are also under the direct influence of the deformation and cooling conditions. Each of these processes is in turn controlled by the TMP parameters. In this chapter, the results obtained in this investigation concerning the effect of process conditions

on microstructural evolution before and after transformation will be presented and discussed. The processing conditions mainly include:

1) the reheat temperature (this affects the initial austenite grain size and the amount of niobium in solution)
2) the amount of austenite pancaking (determined by the T_{nr})
3) the finishing temperature
4) the cooling rate
5) the cooling interruption temperature.

High strength steels can be based on a microstructure of acicular ferrite because in this case controlled rolling and accelerated cooling produce an extremely fine grained structure. The evolution of this structure through recrystallization, deformation and transformation was studied for the steels used in this work, which develop an acicular microstructure. The characteristics of the microstructures will be examined and discussed with the aid of results obtained by both electron microscopy and hardness testing.

4.2 Experimental Results

The results of torsion test simulations of the rolling operation are presented first. From these, the amount of austenite pancaking taking place in the no-recrystallization region before transformation was calculated for each processing condition. The microstructures were then examined using optical microscopy; further information obtained using electron microscopy will be presented and analyzed in the discussion section.

4.2.1 Thermomechanical Processing

4.2.1.1 Torsion Test Simulations

As mentioned in Chapter Three, the 17-pass deformation and temperature schedule was simulated by means of a temperature controlled multi-pass torsion test. A typical set of stress-strain curves obtained in this way is presented in Fig. 4.1. From these data, mean flow stress (MFS) versus inverse absolute temperature curves were drawn on which the critical temperatures were determined from the slope change points. The results of tests covering all the rolling conditions applicable to the X-70 and X-80 steels are illustrated in Figs. 4.2 to 4.4 and were also presented in Table 3.2.

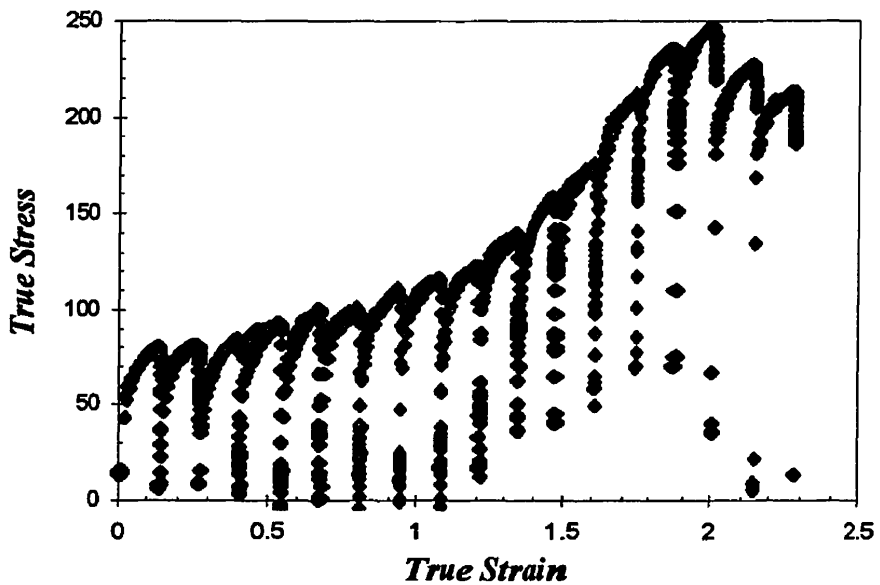

Figure 4.1 A typical set of curves showing the flow stresses generated during each pass of a 17-pass torsion test performed on one X-80 sample.

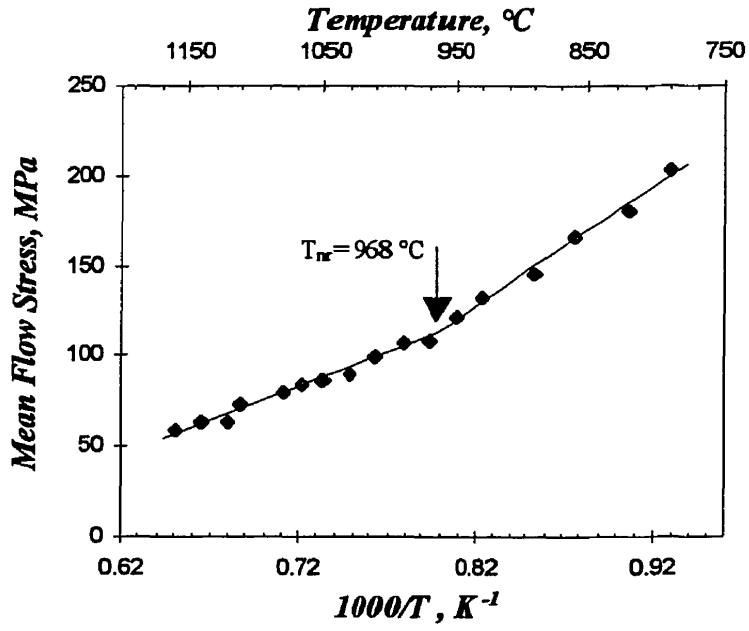

(a)

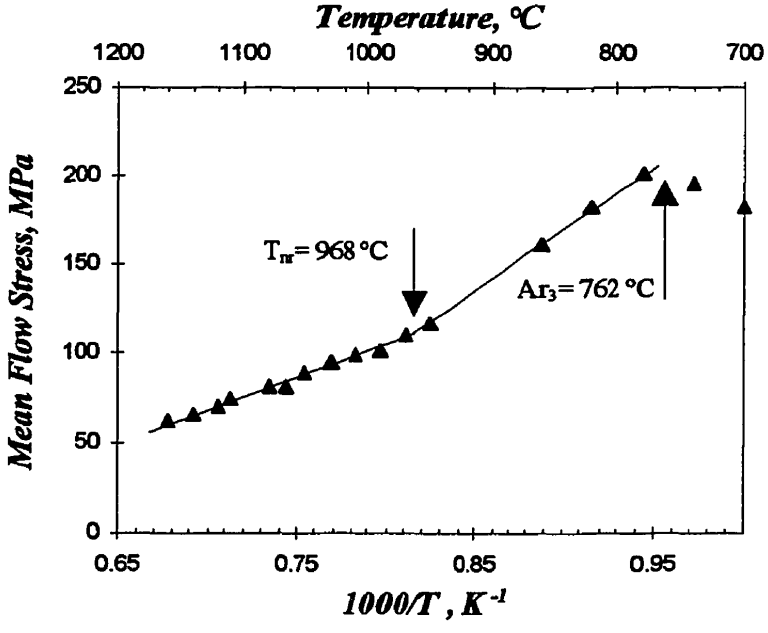

(b)

Figure 4.2 Mean flow stress versus temperature behaviour of the X-70 steel during the multi-pass torsion tests; *(a)* high and *(b)* low finishing temperature schedules, respectively.

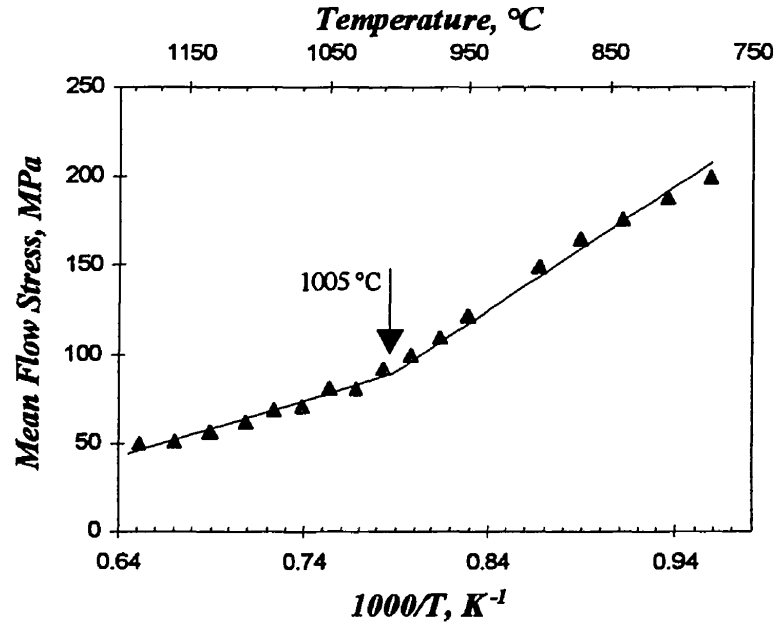

(a)

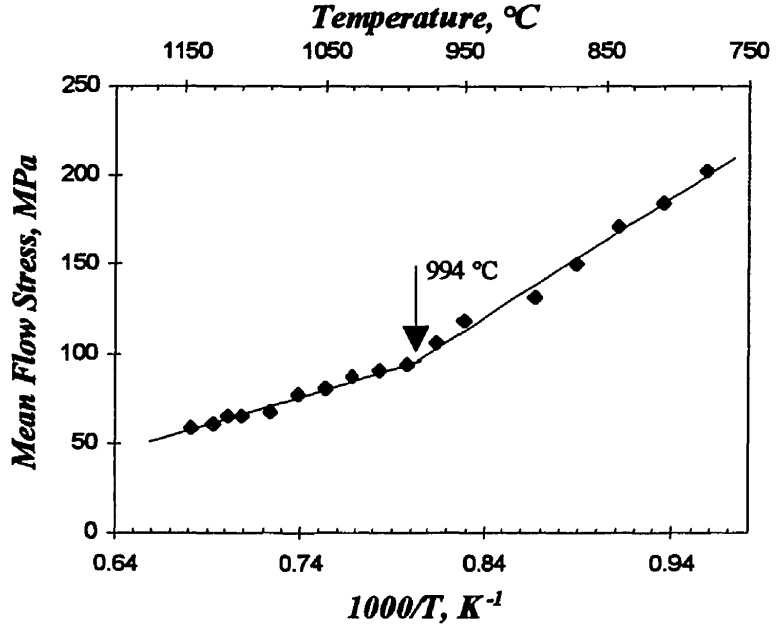

(b)

Figure 4.3 Mean flow stress versus temperature behaviour of the X-80 steel determined using the *high* finishing temperature schedule; *(a)* high and *(b)* low reheat temperatures, respectively.

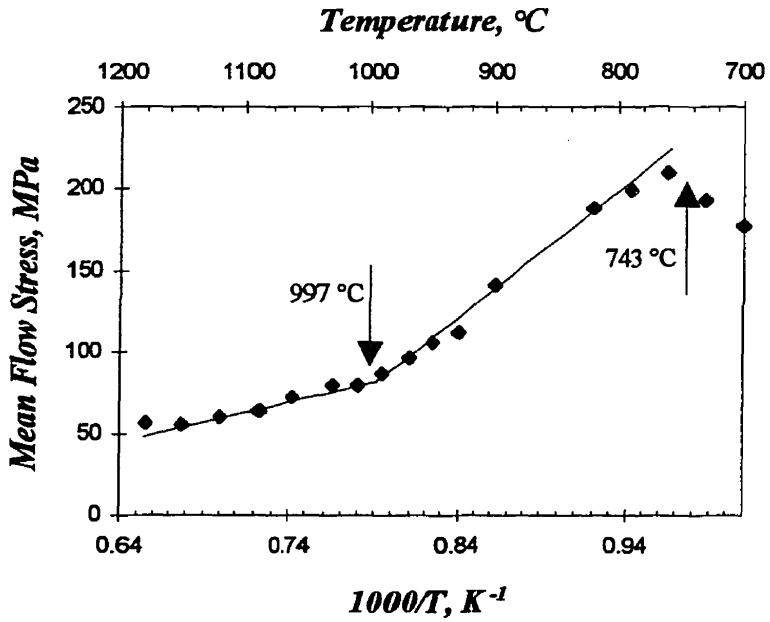

(a)

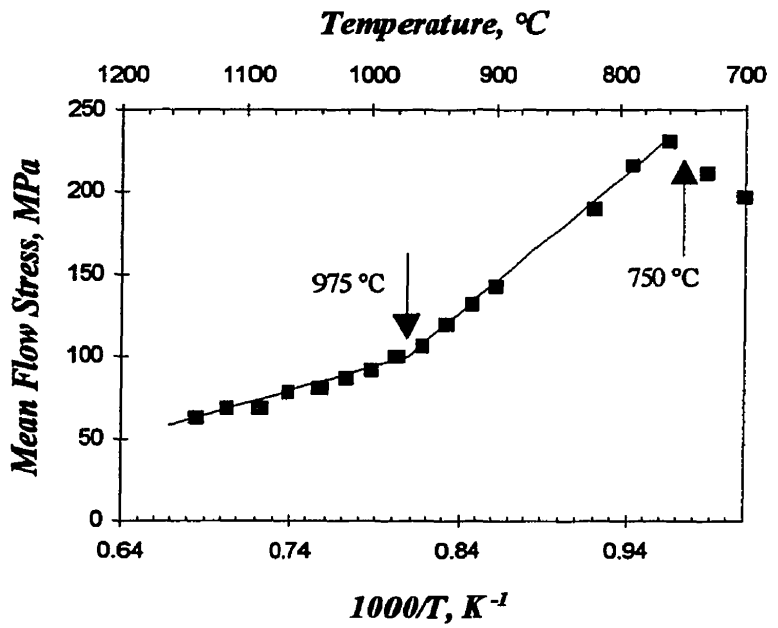

(b)

Figure 4.4 Mean flow stress versus temperature behaviour of the X-80 steel determined using the *low* finishing temperature schedule; *(a)* high and *(b)* low reheat temperatures, respectively.

The following empirical equation, which was obtained using serial multi-pass torsion tests on various Nb microalloyed steels [109], was used to calculate the T_{nr}'s.

$$T_{nr} = 173.9\log([Nb][C]) + 1444 \qquad (4.1)$$

The T_{nr}'s determined experimentally by means of the torsion test simulations are compared in Table 4.1 with those predicted using empirical equation 4.1. The Ar_3 results obtained from the torsion tests are also compared in Table 4.1 with the temperatures calculated using equation 4.2 [91], which is mainly based on the chemical composition of the steel. The measured T_{nr} values were determined on high reheat temperature plates which were finish rolled above the Ar_3. The measured Ar_3's in Table 4.1 also apply to plates reheated at the higher temperature; however, in this case, they were finish rolled below the Ar_3.

$$Ar_3 = 910 - 310C - 80Mn - 20Cu - 15Cr - 80Mo + 0.35(t-8) \qquad (4.2)$$

As mentioned above, different reheat temperatures and rolling schedules were employed in the simulations so that the effects of initial austenite grain size and accumulated strain could be determined. This is one reason why the values calculated using the empirical equations, which do not allow for the above-mentioned parameters, differ somewhat from the measured values presented in Table 4.1.

It is of interest to note that the Ar_3 temperatures were also measured using the effect of recalescence on the cooling curve (see Fig. 4.5); resulting slope changes agree very well with the torsion test data. The cooling curves illustrated in Fig. 4.5 pertain to two X-80 plates which were air cooled after finish rolling to below the Ar_3; the upper and lower curves apply to high and low reheat temperatures, respectively. These observations are in better agreement with the results of the torsion tests than with the predictions obtained from eq.

4.2. This indicates that the torsion simulation of rolling schedules leads to highly accurate predictions of the "critical temperatures" pertaining to steel rolling.

The T_{nr} 's and Ar_3 's measured using the torsion tests are listed in Table 4.2. It can be seen that when the low reheat temperature is employed, the recrystallization stop temperature is decreased. This is because some of the Nb(CN) precipitates remained undissolved in the austenite and the recrystallization retarding effect of Nb was weakened. The same reason, i.e. less Nb in solution, can explain the lower T_{nr} of the X-70 steel (which has a lower Nb content) compared with that of the X-80 steel.

Table 4.1 Comparison between the measured and calculated T_{nr}'s and Ar_3's.

Steel Grade	**T_{nr} , °C**		**Ar_3 , °C**	
	Measured	**Calculated**	**Measured**	**Calculated**
X-70	968	990	762	746
X-80	1005	1016	750	725

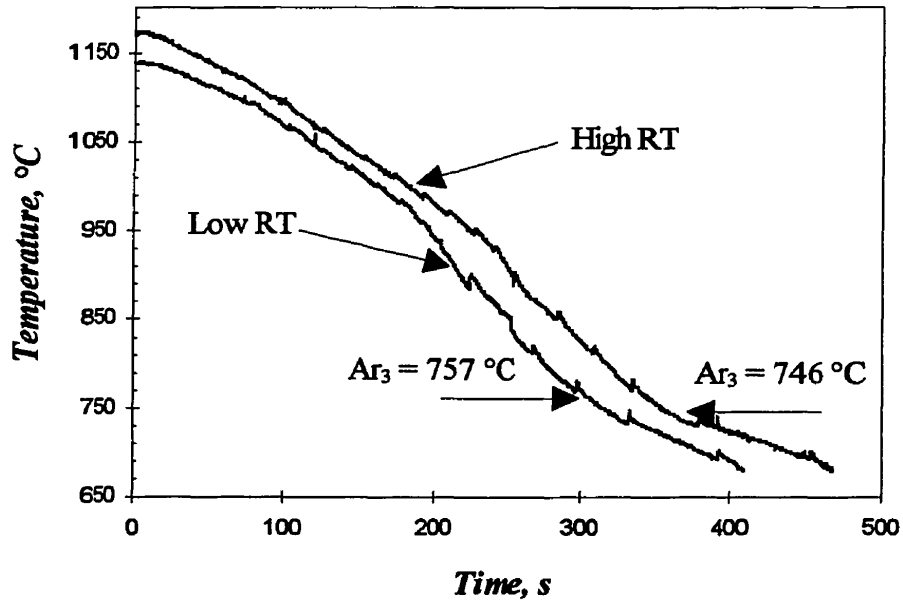

Figure 4.5 Air cooling curves applicable to two controlled rolled plates of X-80 steel that were reheated to high (1275 °C) and low (1150 °C) reheat temperatures.

It should be pointed out that the T_{nr} 's obtained from the low finishing temperature schedules are lower than those that correspond to the high FRT schedules. This can be linked to the longer interpass times, Tables 3.9 and 3.10, an observation that is in agreement with the work of Bai et al. [110], which indicates that longer interpass times lead to decreases in the T_{nr}.

Table 4.2 The measured critical temperatures and the calculated pancaking strains for each set of the controlled rolling conditions.

Steel Grade	Reheat Temperature, °C	Finish Rolling Temperature, °C	T_{nr}, °C	Ar_3, °C	Pancaking Strain between the T_{nr} and Ar_3	Pancaking Strain below the Ar_3
X-70	1225	790	966	-	1.34	-
		730	966	762	0.86	0.48
X-80	1275	780	1005	-	1.68	-
		690	997	743	1.50	0.48
	1150	780	994	-	1.68	-
		690	975	750	1.50	0.48

4.2.2 Microstructural Examination

The microstructures of an air cooled X-70 and a rapidly cooled X-80 sample are displayed in Fig. 4.6; here three-dimensional views are employed. The air cooled X-70 specimen of Fig. 4.6a was finish rolled in the austenite region; the rapidly cooled X-80 example of Fig. 4.6 b was reheated at 1275 °C and finish rolled below the Ar_3. The cooling rate applied to this sample was 20 °C s^{-1} and accelerated cooling was interrupted at 520 °C.

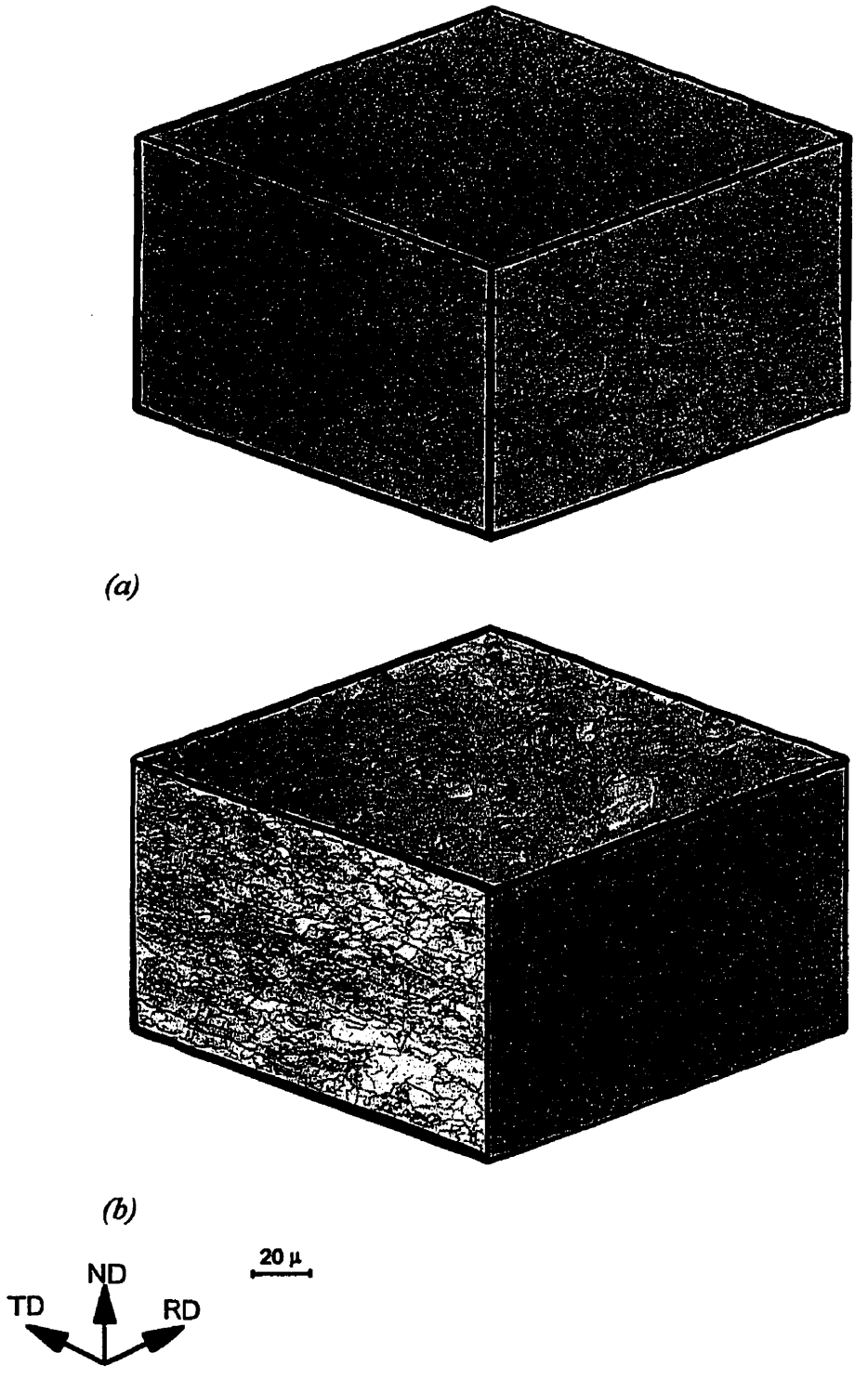

Figure 4.6 Microstructures of *(a)* an air cooled X-70 plate and *(b)* a rapidly cooled X-80 plate reheated at high temperature and finish rolled below the Ar_3.

The grain sizes of the air cooled samples, which generally displayed polygonal ferrite microstructures, were measured using the intercept method. The results obtained in this way are illustrated in Table 4.7. By contrast, in the case of the rapidly cooled samples, it was not possible to obtain meaningful measurements of ferrite grain size because there were too many extraneous boundaries present associated with the acicular ferrite substructures and other microstructural features. Nevertheless, it was evident that the grain sizes were quite fine; these were estimated to be below ASTM 11.5 (average grain diameter of 7 μm).

4.2.2.1 Low Niobium (X-70) Steel

The microstructures developed in the X-70 steel processed under the conditions presented in Tables 3.5 and 3.6 are illustrated in Figs. 4.7 and 4.8. A banded structure of polygonal ferrite and non-lamellar pearlite (or in some places bainite) was developed in the air cooled sample that was finish rolled in the unrecrystallized austenite region, Fig. 4.7 c. As can be seen in micrographs (a) and (b) of Fig. 4.7, accelerated cooling increased the proportion of the bainitic substructure. Use of a low finishing temperature introduces elongated (pancaked) ferrite grains and the banded structure is maintained, Fig. 4.8.

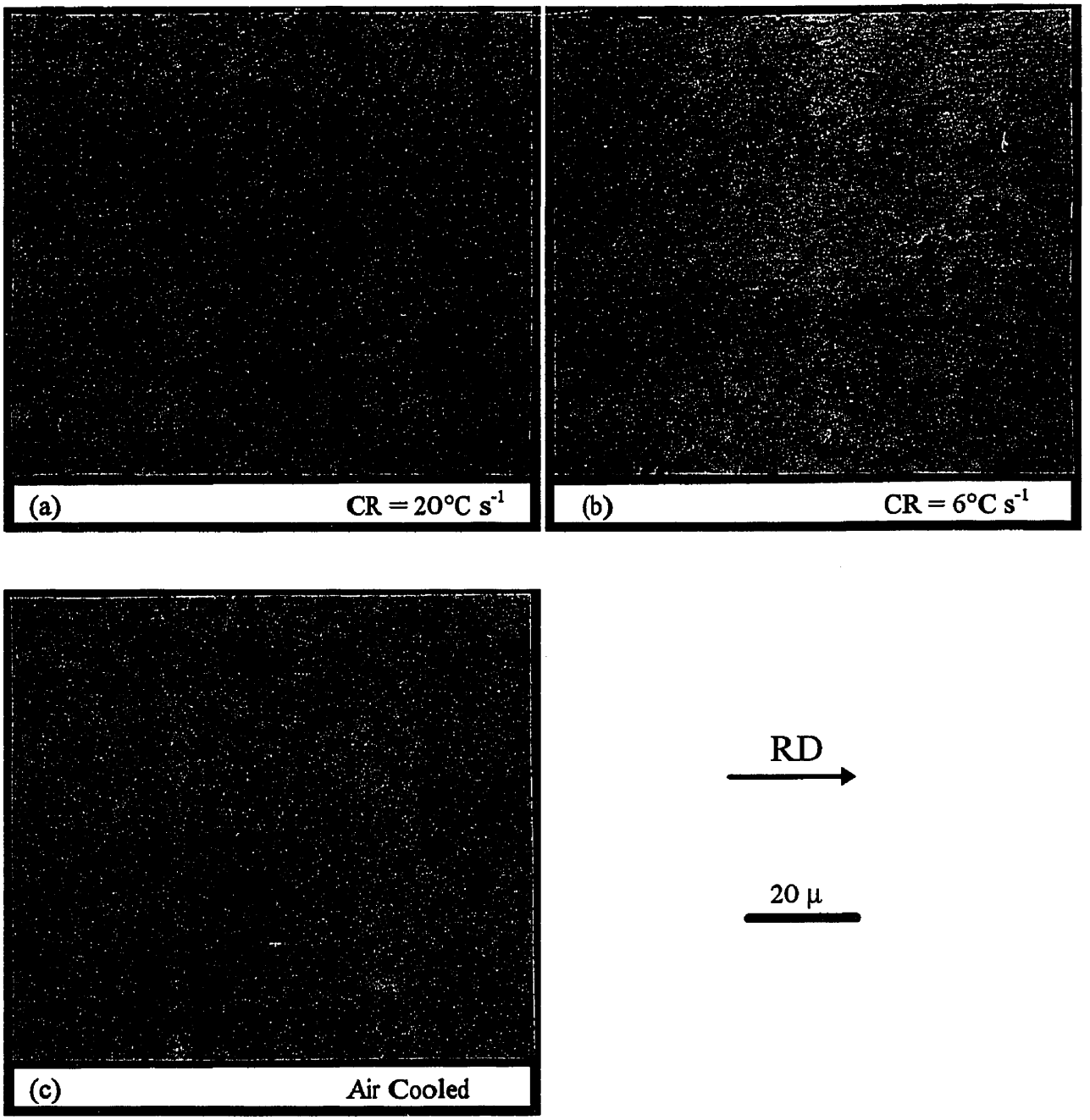

Figure 4.7 Optical microstructures of the X-70 plates reheated at 1225°C and finish rolled at 790°C; accelerated cooling was interrupted at 620°C.

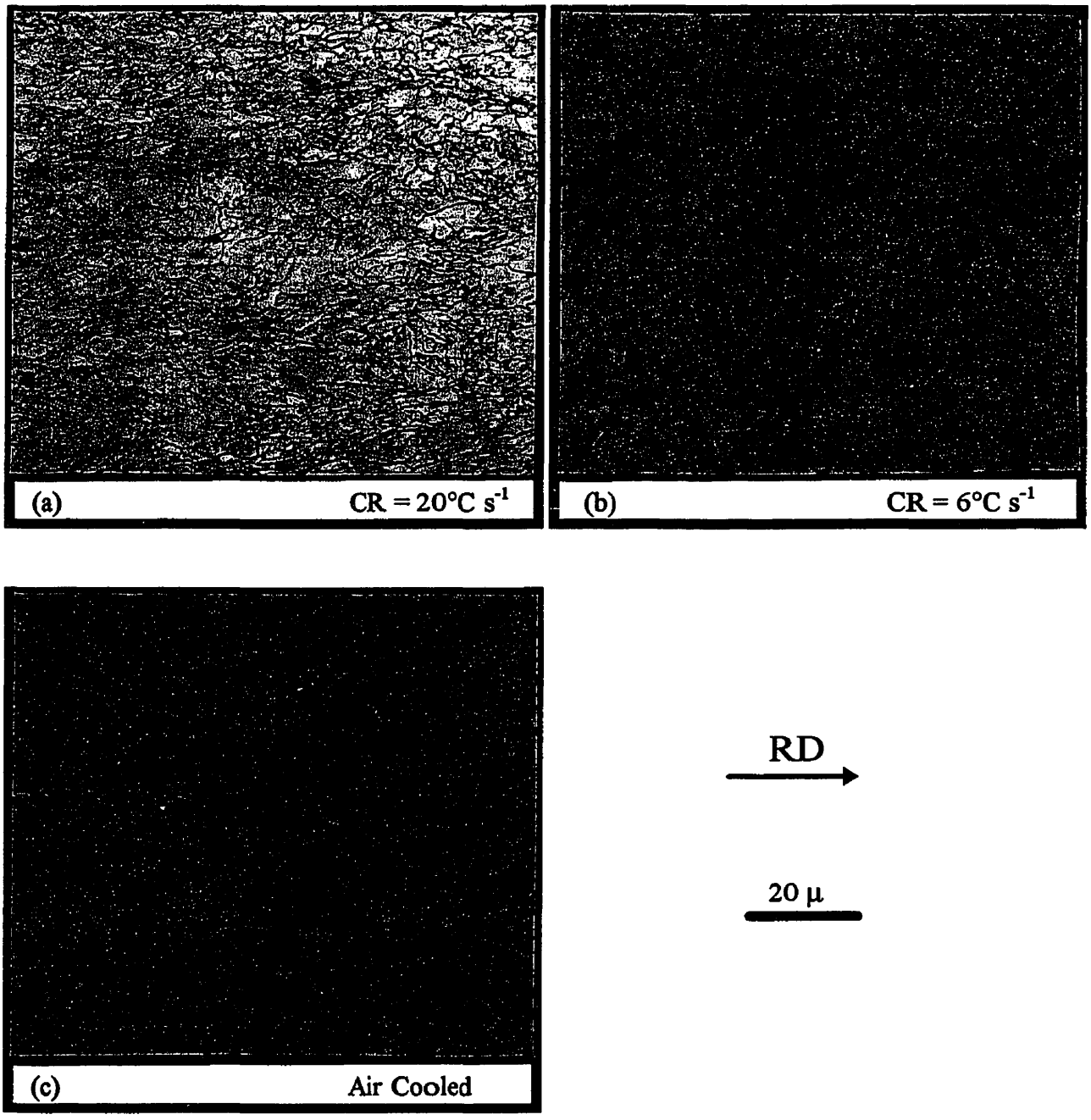

Figure 4.8 Optical microstructures of the X-70 plates reheated at 1225°C and finish rolled at 730°C; accelerated cooling was interrupted at 620°C.

4.2.2.2 High Niobium (X-80) Steel

4.2.2.2.1 Finishing in the Austenite Region

The microstructures of the X-80 plates finish rolled above the Ar_3 are illustrated in Figs. 4.9 and 4.10 for the cases of high (1275 °C) and low (1150 °C) reheat temperature, respectively. The banded structures of ferrite and acicular ferrite (or bainite) associated with air cooling can be seen in Figs. 4.9g and 4.10g. In most cases, accelerated cooling resulted in acicular ferrite structures along with some discontinuous bands of finer substructures. It seems that for the samples reheated at both 1275 °C and 1150 °C, Figs. 4.9 and 4.10, the finest microstructures are associated with the medium cooling rate, i.e. 20 °C s^{-1}. Generally, the highest cooling interruption temperature also resulted in the coarsest acicular ferrite.

4.2.2.2.2 Finishing in the ($\gamma + \alpha$) Region

Complex microstructures of pancaked ferrite, polygonal ferrite, and acicular ferrite (or bainite) were observed in the X-80 plates finish rolled in the two phase region, Figs. 4.11 (RT= 1275 °C) and 4.12 (RT= 1150 °C). Although it was hard to measure the sizes of these microconstituents, their finenesses were evidently influenced by the rate of accelerated cooling and by the cooling interruption temperature, as can be seen in Figs. 4.11 and 4.12.

In the discussion section of this chapter, the characteristics of these microconstituents will be analyzed in more detail and related to the results of the microhardness tests.

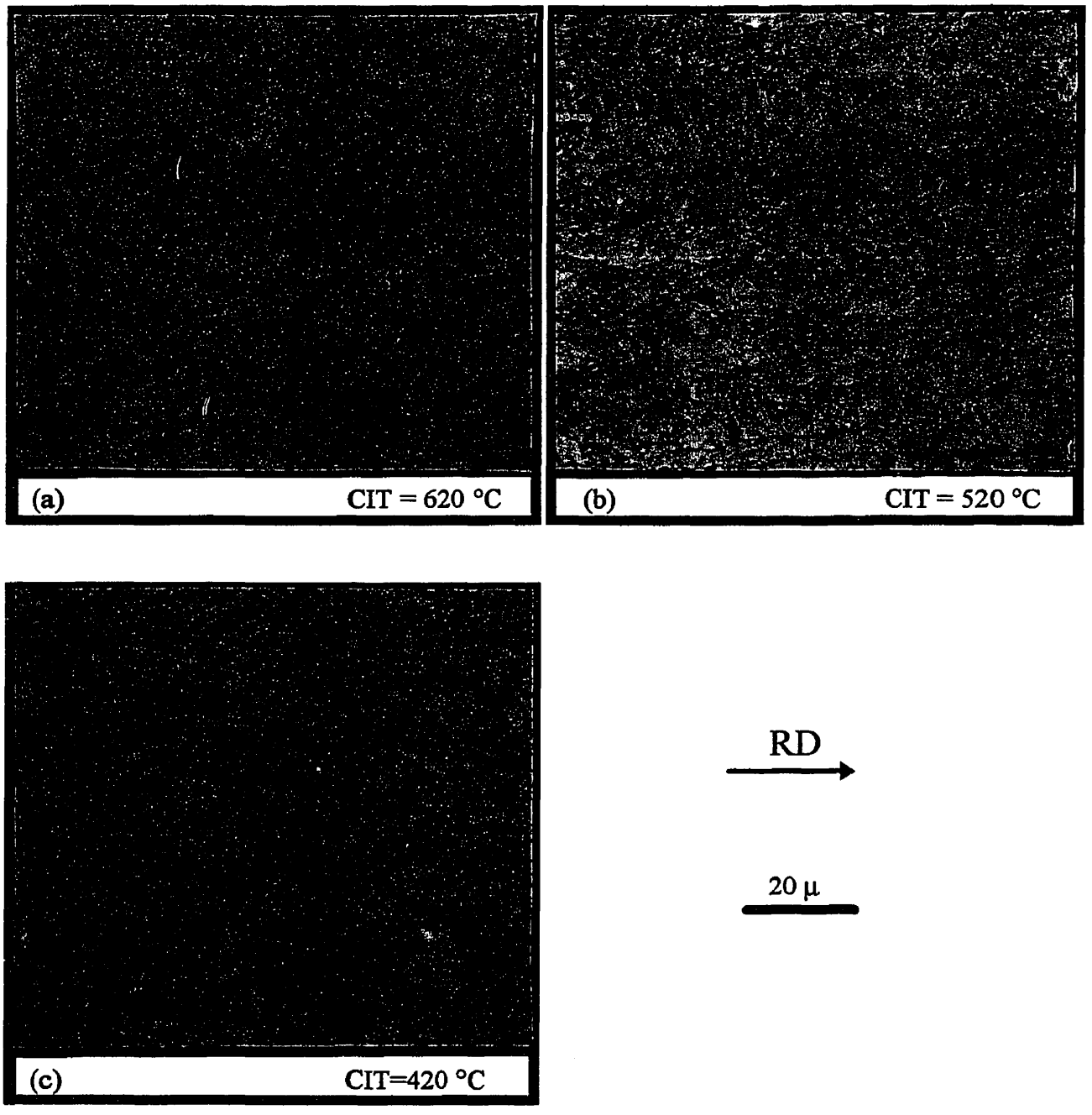

Figure 4.9 Optical microstructures of the X-80 plates reheated at 1275°C and finish rolled at 780°C; (a) to (c) CR=40°C s^{-1},

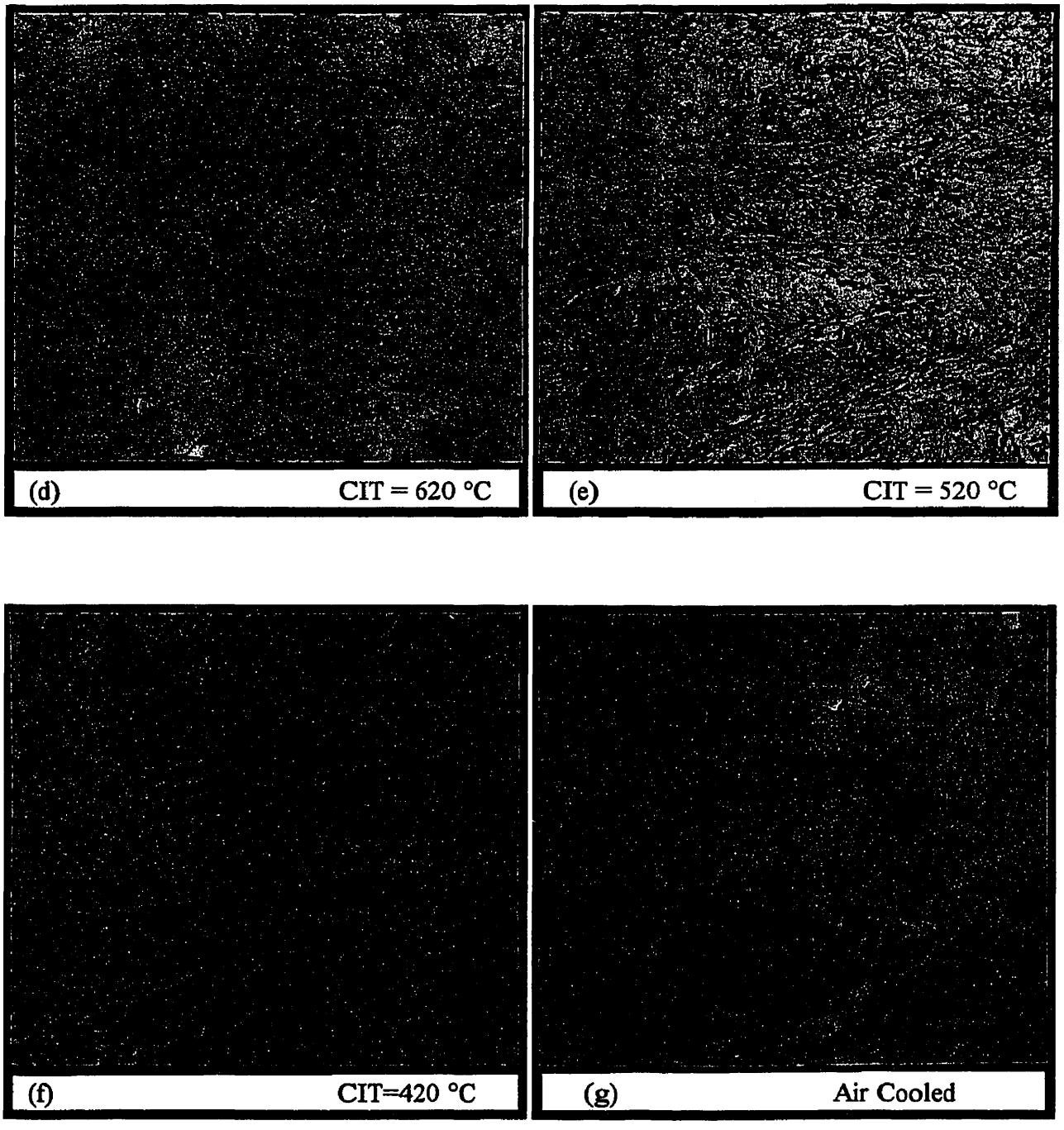

Figure 4.9 (continued) (d) to (f) CR=20°C s^{-1}, and (g) air cooled.

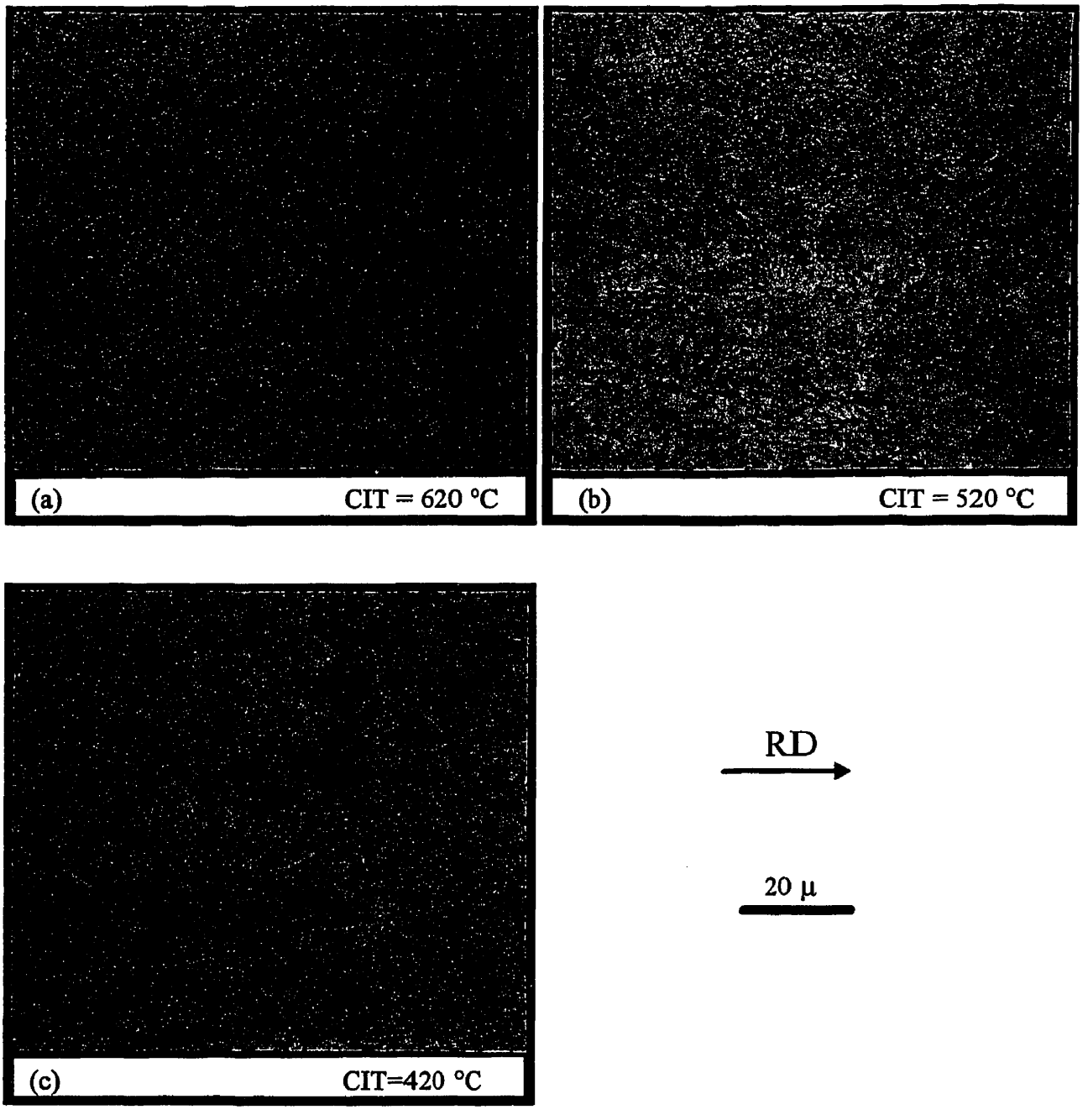

Figure 4.10 Optical microstructures of X-80 plates reheated at 1150°C and finish rolled at 780°C; (a) to (c) CR=40°C s^{-1},

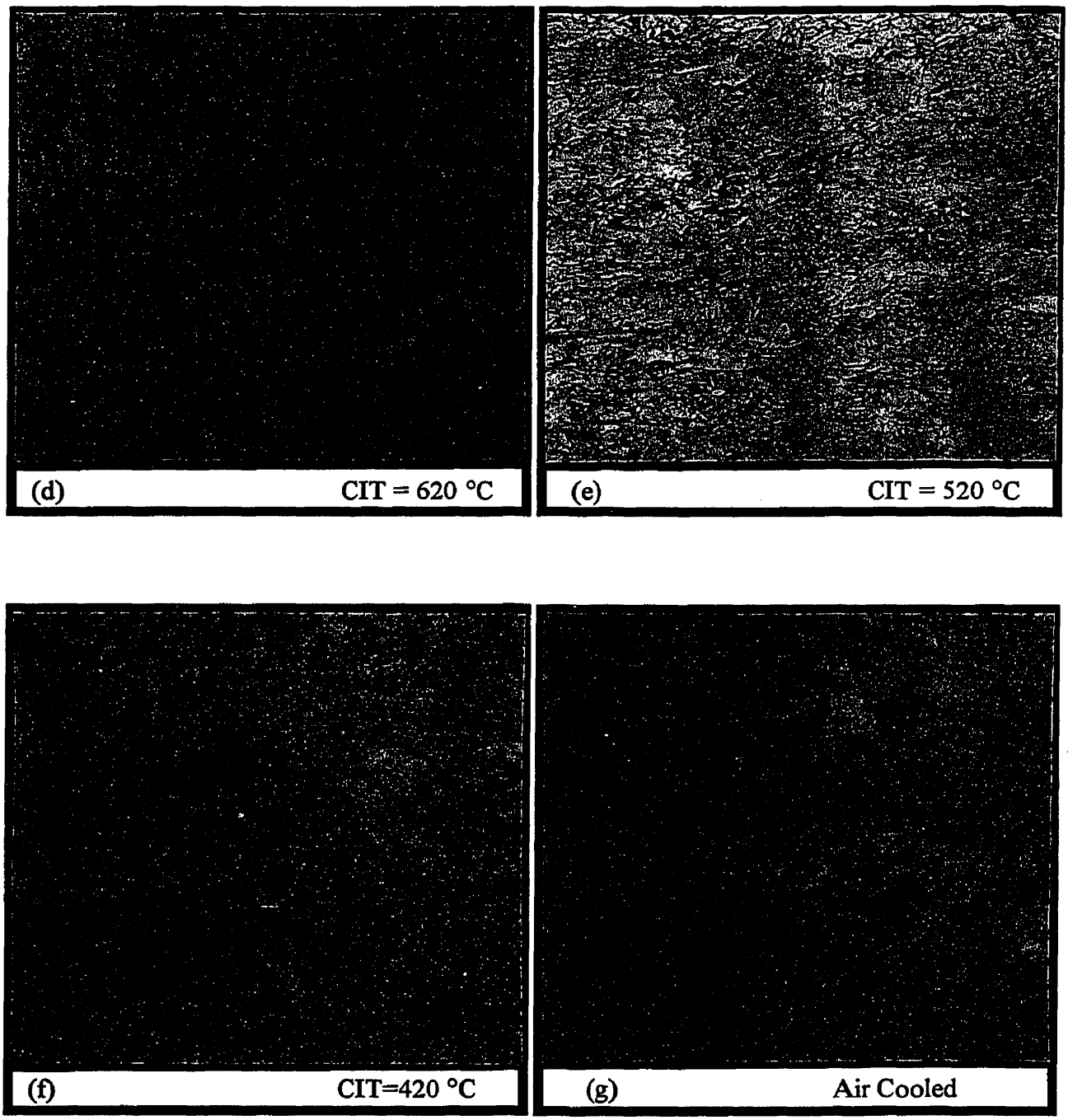

Figure 4.10 (continued) (d) to (f) CR=20°C s^{-1}, and (g) air cooled.

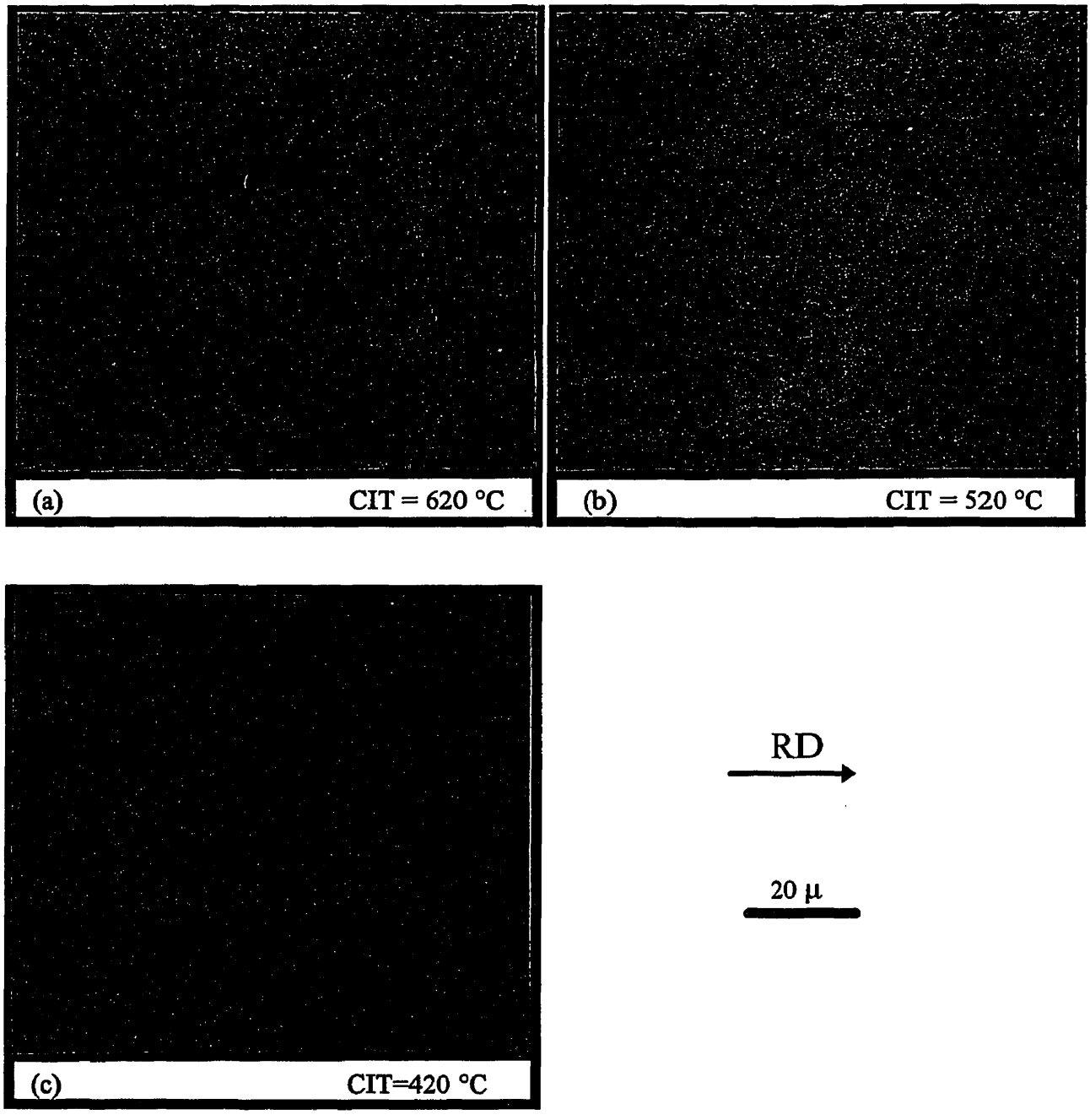

Figure 4.11 Optical microstructures of X-80 plates reheated at 1275°C and finish rolled at 690°C; (a) to (c) CR=40°C s^{-1},

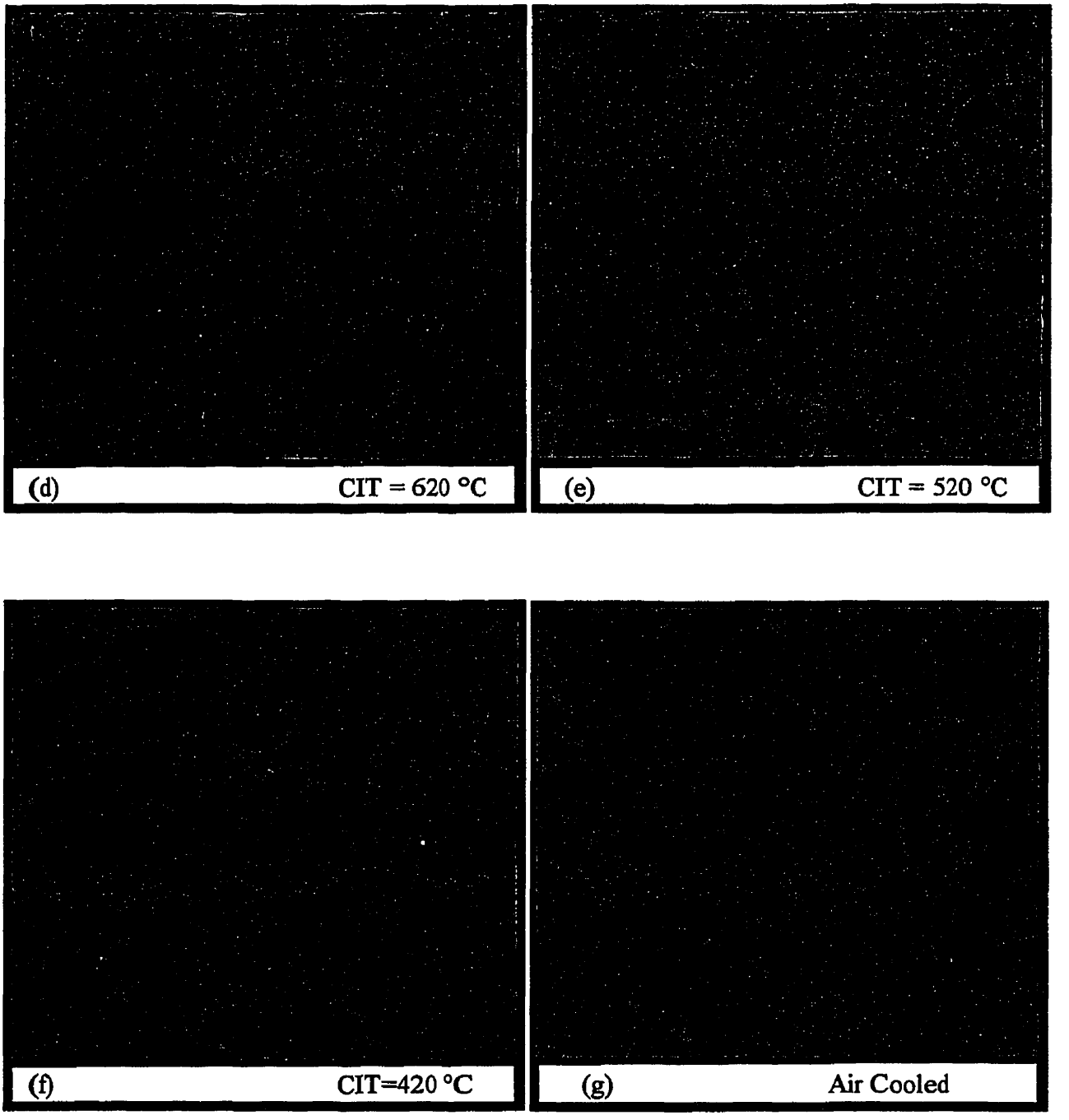

Figure 4.11 (continued) (d) to (f) CR=20°C s^{-1}, and (g) air cooled.

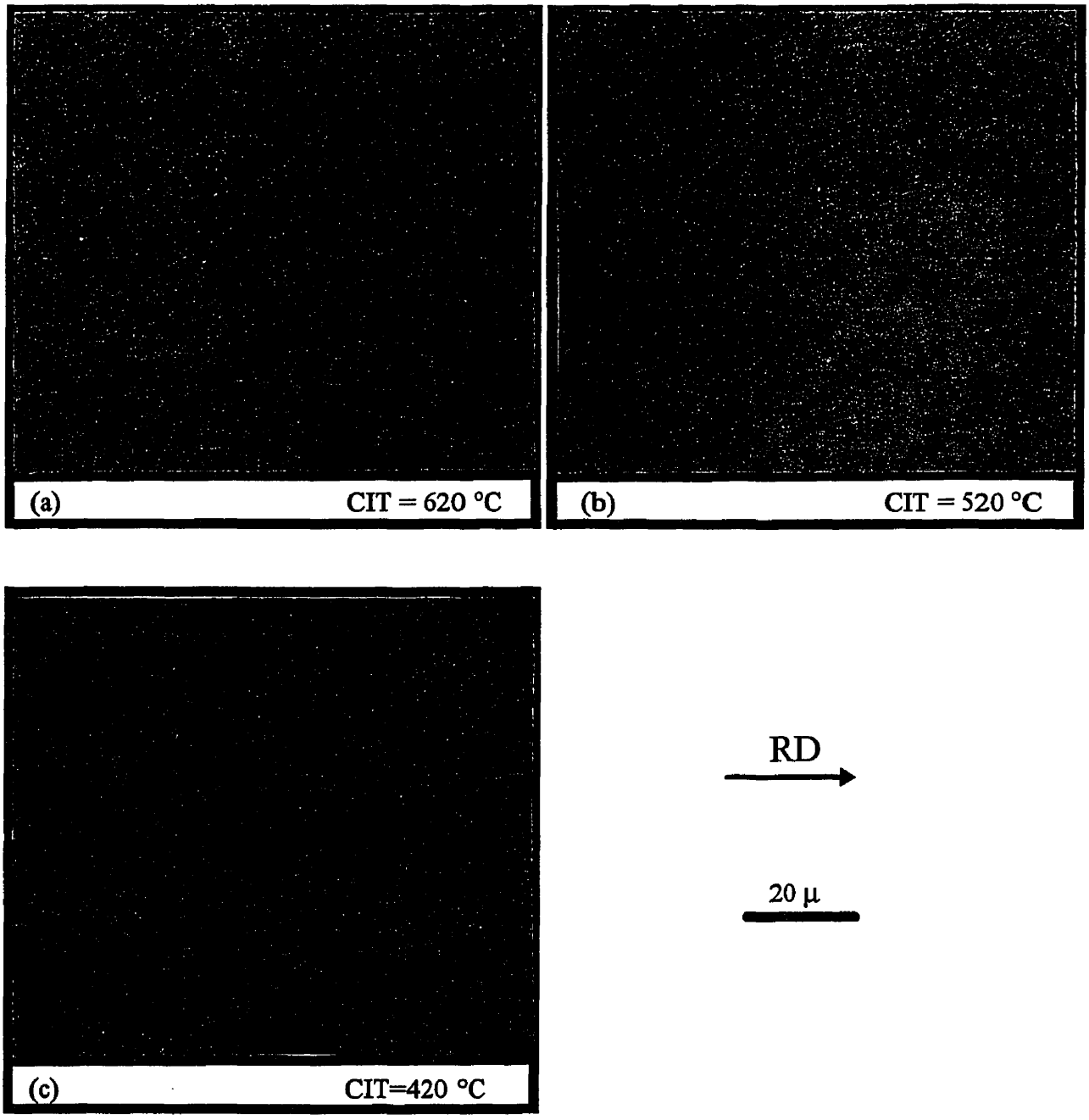

Figure 4.12 Optical microstructures of X-80 plates reheated at 1150°C and finish rolled at 690°C; (a) to (c) CR=40°C s^{-1},

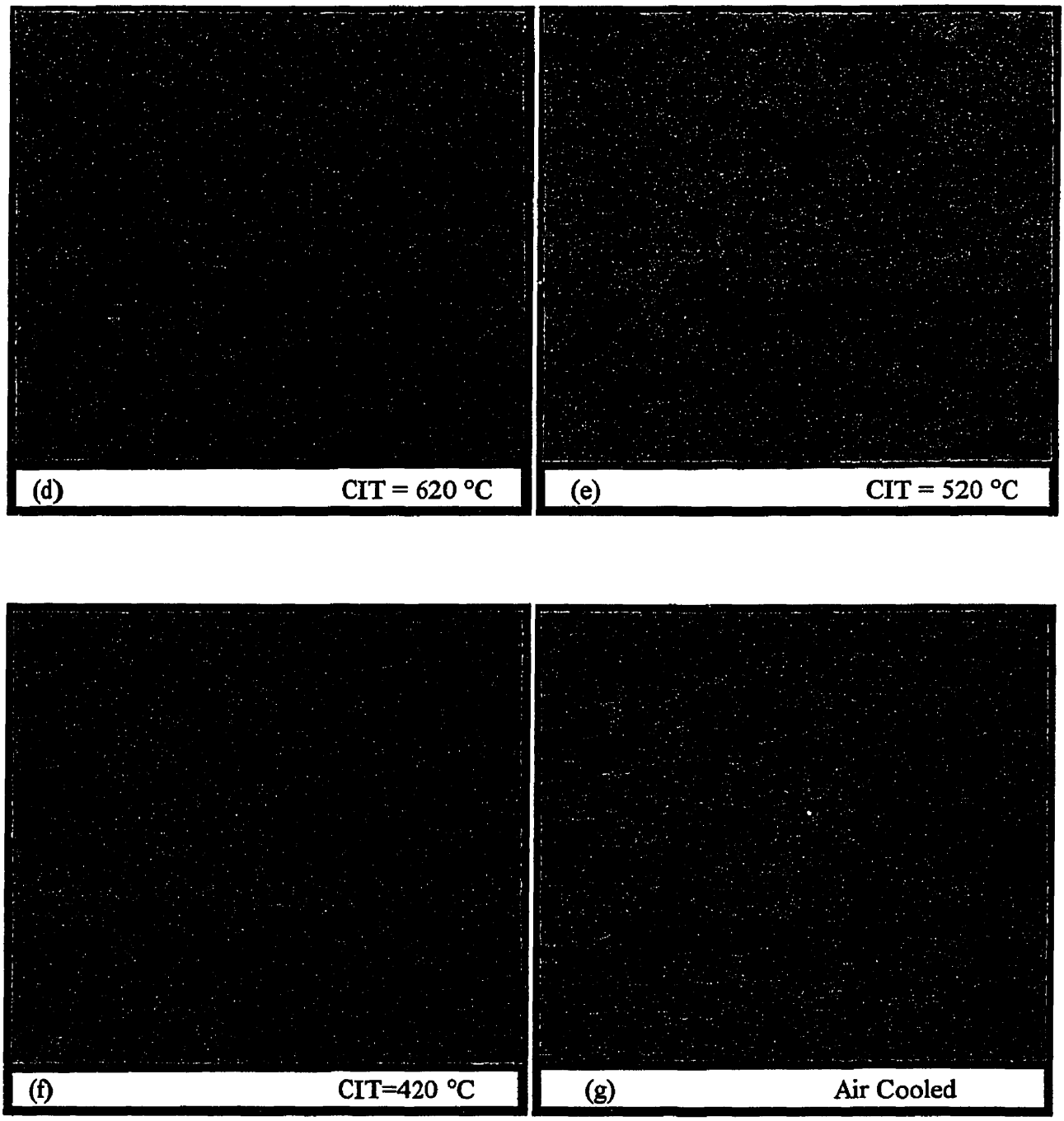

Figure 4.12 (continued) (d) to (f) CR=20°C s^{-1}, and (g) air cooled.

4.3 Hardness

The bulk Vickers hardnesses of the X-70 and X-80 steels are presented in Tables 4.3 and 4.4.

Table 4.3 Hardnesses of the X-70 steel plates.

Finish Rolling Temperature, °C	**Cooling Rate, °C s^{-1}**	**Hardness, H_V**
790	**Air Cooled**	181
	6	218
	20	227
730	**Air Cooled**	215
	6	219
	20	234

Table 4.4 Hardnesses of the X-80 steel plates.

Finish Rolling Temperature °C	Reheat Temperature °C	Cooling Rate, °C s^{-1}	Cooling Interruption Temperature °C	Hardness, H_V
780	1275	Air Cooled	-	220
		20	620	229
			520	241
			420	238
		40	620	225
			520	238
			420	239
	1150	Air Cooled	-	202
		20	620	225
			520	231
			420	226
		40	620	231
			520	246
			420	231
690	1275	Air Cooled	-	240
		20	620	249
			520	261
			420	256
		40	620	245
			520	241
			420	252
	1150	Air Cooled	-	228
		20	620	235
			520	254
			420	254
		40	620	243
			520	240
			420	237

4.4 Analysis and Discussion

In multi-pass rolling, the effect of an intermediate pass depends on the grain size determined by the preceding passes. Because long interpass times promote the occurrence of both static recrystallization (SRX) and strain-induced precipitation under conventional controlled rolling conditions, the alternative possibility that strain accumulation could lead to dynamic recrystallization (DRX) was also investigated. This was done by analyzing the evolution of grain size during multi-pass rolling above the T_{nr}. The amounts of austenite and ferrite pancaking and the effective austenite interfacial areas were also calculated. By comparison with the hardnesses of the final product, it was possible to come to some conclusions regarding the evolution of the microstructure before and after transformation.

4.4.1 Microstructural Evolution Before Transformation

4.4.1.1 Recrystallization of Austenite

Since Nb in solution retards static recrystallization and promotes the accumulation of strain, there is a possibility that dynamic recrystallization can be initiated in this way. If DRX occurs during hot rolling, it should be possible to produce finer austenite grain sizes than in the case where SRX is the only operative recrystallization process. In the present work, the possible occurrence of DRX was studied by modifying the spreadsheet of Ref. [111], which was developed for the rod rolling of C-Mn steels, so that it applies to the plate rolling of high Nb steels.

As a first step, the peak strain, ε_P, was calculated using the equation modified for high Nb steels by Minami et al. [112]:

$$\varepsilon_p = (1+20[Nb])/1.78\times 2.8\times 10^{-4} d_0^{0.5}\{\dot{\varepsilon}\exp(375000/RT)\}^{0.17} \qquad (4.3)$$

Here, d_0 is the austenite grain size at the entry of each pass and [Nb] represents the Nb concentration. Then, the critical strain (ε_c) required to initiate DRX was determined as:

$$\varepsilon_C = C\varepsilon_p \tag{4.4}$$

where C is a constant equal to 0.6 for Nb steels. It is well known that DRX is initiated when the accumulated strain exceeds ε_c. If DRX is not initiated, conventional SRX remains the operative softening mechanism. Otherwise, metadynamic recrystallization, MRX (or post-dynamic recrystallization) is the governing static mechanism and the related empirical equations are used for grain size calculations. The fraction X of recrystallized material present after a given pass can be specified by the following Avrami equation:

$$X = 1-\left[-\ln Y\left(t_{ip}/t_Y\right)^n\right] \tag{4.5}$$

where the Avrami exponent n=1, and t_{ip} and t_Y represent the interpass time and the time for a fractional softening of Y, respectively. The times for 25% static recrystallization were calculated using equations 4.6 and 4.7 [113]. Here, equation 4.7 corresponds to the situation where strain-induced precipitation becomes effective.

$$\text{T>990°C}, \quad t_{0.25} = 1.5\times10^{-18} d_0^{\,2} (\varepsilon - 0.025)^{-2.8} \exp(30[Nb]) \exp(300000/RT) \tag{4.6}$$

$$\text{T<990°C}, \quad t_{0.25} = 1.0\times10^{-42} d_0^{\,2} (\varepsilon - 0.025)^{-2.8} \exp(30[Nb]) \exp(880000/RT) \tag{4.7}$$

The grain sizes observed in a number of steels after full static recrystallization have been shown to be a function of strain and initial grain size (in μm) as follows [114]:

$$d = D\varepsilon^{-0.67} d_0^{\,0.67} \tag{4.8}$$

The following equation given by Hodgson et al. [115] for Nb steels was used to calculate the extent of grain coarsening after recrystallization is complete:

$$d^{4.5} = {d_{SRX}}^{4.5} + 4.1\times10^{23}(t_{ip} - 4.32\times t_{0.5})\exp(-435000/RT) \qquad (4.9)$$

The critical strain calculations revealed that the accumulated or effective strain at each pass was far below the limit for the initiation of DRX. As a result, it was concluded that no DRX occurred under the processing conditions of this work. The final recrystallized austenite grain size for each controlled rolling condition is illustrated in Table 4.5. A typical spreadsheet used for calculation of the recrystallized grain size of a plate reheated at 1275 °C and finish rolled in the austenite region is presented in Table 4.6.

It is of interest that, despite large differences in initial austenite grain size, the final recrystallized grain sizes are close to each other. This is because the deformation conditions corresponding to the various simulations were quite similar (see Table 3.4 for the strains and strain rates). Nevertheless, the higher Nb content of the X-80 steel resulted in coarser recrystallized grain sizes due to the greater retardation of recrystallization. The latter, in turn, led to recrystallization at higher temperatures.

Table 4.5 Microstructural features of the austenite before transformation together with the associated austenite and ferrite pancaking strains.

Steel Grade	RT, °C	FRT, °C	Initial Austenite Grain Size, μm	Final Recrystallized Austenite Grain Size, μm	Pancaking Strain of Austenite	Pancaking Strain of Ferrite
X-70	1225	790	65	41	1.32	-
		730	65	41	1.24	0.07
X-80	1275	780	110	50	1.65	-
		690	110	55	1.87	0.05
	1150	780	80	48	1.65	-
		690	80	46	1.73	0.05

Table 4.6 Example of the spreadsheet used for calculation of the recrystallized austenite grain size. Here, the sample was reheated at 1275 °C and finish rolled in the austenite region.

pass	Grain size (d) entry (μm)	temp. ° C	ε rate (s^{-1})	interpass time (s)	ε calc.	ε_a	ε_c	$\varepsilon_a > \varepsilon_c$?
F 1	110.0	1200	1.9	39	0.09	0.09	0.56	--
F 2	120.8	1161	2.3	26	0.12	0.16	0.71	--
F 3	95.5	1135	2.5	25	0.12	0.14	0.70	--
F 4	89.1	1110	2.6	20	0.12	0.16	0.75	--
F 5	79.3	1090	2.8	20	0.13	0.18	0.78	--
F 6	68.7	1070	3.0	20	0.13	0.17	0.80	--
F7	65.5	1050	3.3	19	0.14	0.20	0.85	--
F 8	63.2	1031	3.5	22	0.14	0.20	0.88	--
F 9	61.1	1009	3.8	4	0.14	0.21	0.94	--
F10	58.2	986	4.2	19	0.16	0.33	1.06	--
F11	44.1	967	4.6	19	0.17	0.21	0.97	--
		948	4.9		0.16			

Continued...

t_{50} (s)	X	Grain size (d) if X>0.95	Grain size (d) after time t (μm)	Grain size (d) after new t	Grain size (d) if X>0.95		coarsening after	
					MRX	SRX	MRX	SRX
40.84	0.48	132.3	120.8	155.0	22.8	132.3	79.7	120.8
8.84	0.87	91.7	95.5	113.2	20.2	91.7	78.2	95.5
14.24	0.70	86.3	89.1	100.9	18.6	86.3	62.5	89.1
11.76	0.69	74.9	79.3	85.7	17.2	74.9	54.4	79.3
10.10	0.75	65.1	68.7	75.0	16.0	65.1	49.2	68.7
13.04	0.65	60.8	63.5	68.2	14.9	60.8	42.8	63.5
11.03	0.70	53.0	56.2	59.4	13.8	53.0	38.6	56.2
13.28	0.68	48.8	51.1	54.1	12.7	48.8	35.0	51.1
15.12	0.17	44.1	50.0	44.9	11.6	44.1	39.5	50.0
6.52	0.87	31.7	34.1	36.4	10.6	31.7	27.1	34.1
46.08	0.25	33.3	33.9	35.7	9.8	33.3	24.5	33.9

4.4.1.2 Pancaking of the Austenite

The amount of pancaking strain for each TMP condition was calculated using the experimental rolling temperatures listed in Tables 3.5 to 3.10. In these tables, the passes applied in the unrecrystallized austenite region and above the Ar_3 are shaded for identification purposes. For the low FRT schedules, the effective amount of austenite pancaking was calculated using the following relation:

$$\varepsilon_\gamma(pancaking) = \varepsilon_{\gamma_1} V_{\gamma_1} + \varepsilon_{\gamma_2} V_{\gamma_2} + \varepsilon_{\gamma_3} V_{\gamma_3} \qquad (4.10)$$

where ε_{γ_1} is the strain accumulated in the unrecrystallized γ region above the Ar_3, and ε_{γ_2} and ε_{γ_3} are the strains accumulated in each of the two passes applied below the Ar_3, see Table 3.5. $V\gamma_1$, $V\gamma_2$, and $V\gamma_3$ represent the volume fractions of austenite present during each of the above-mentioned stages of rolling. These were determined from the CCT curves applicable to these steels, Fig. 4.13. The same type of equation was used to calculate the effective pancaking strain applicable to the ferrite:

$$\varepsilon_\alpha(pancaking) = \varepsilon_{\alpha_1} V_{\gamma_1} + \varepsilon_{\alpha_2} V_{\gamma_2} + \varepsilon_{\alpha_3} V_{\gamma_3} \qquad (4.11)$$

Here, $\varepsilon_{\alpha_1} = \varepsilon_{\gamma_2} - \varepsilon_{\gamma_1}$ and $\varepsilon_{\alpha_2} = \varepsilon_{\gamma_3} - \varepsilon_{\gamma_2}$ and $\varepsilon_{\alpha_3} = 0$. The volume fractions of the transformed austenite and ferrite at each pass in the two phase region are identical; $V\alpha_1 = V\gamma_1$, $V\alpha_2 = V\gamma_2$, and $V\alpha_3 = V\gamma_3$.

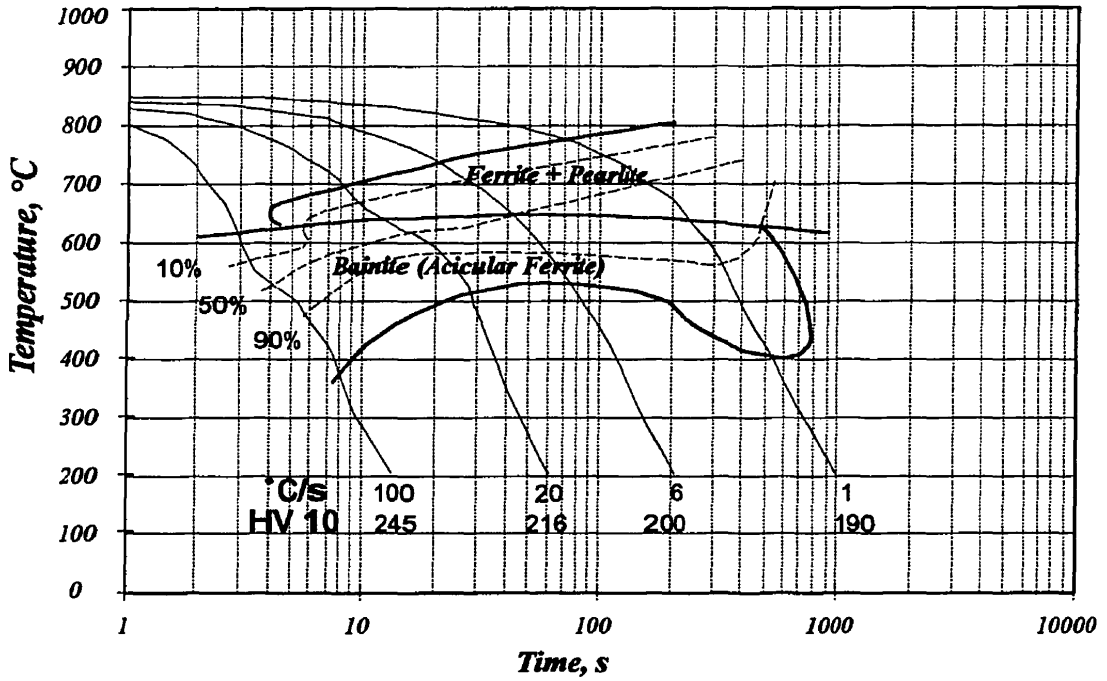

(a)

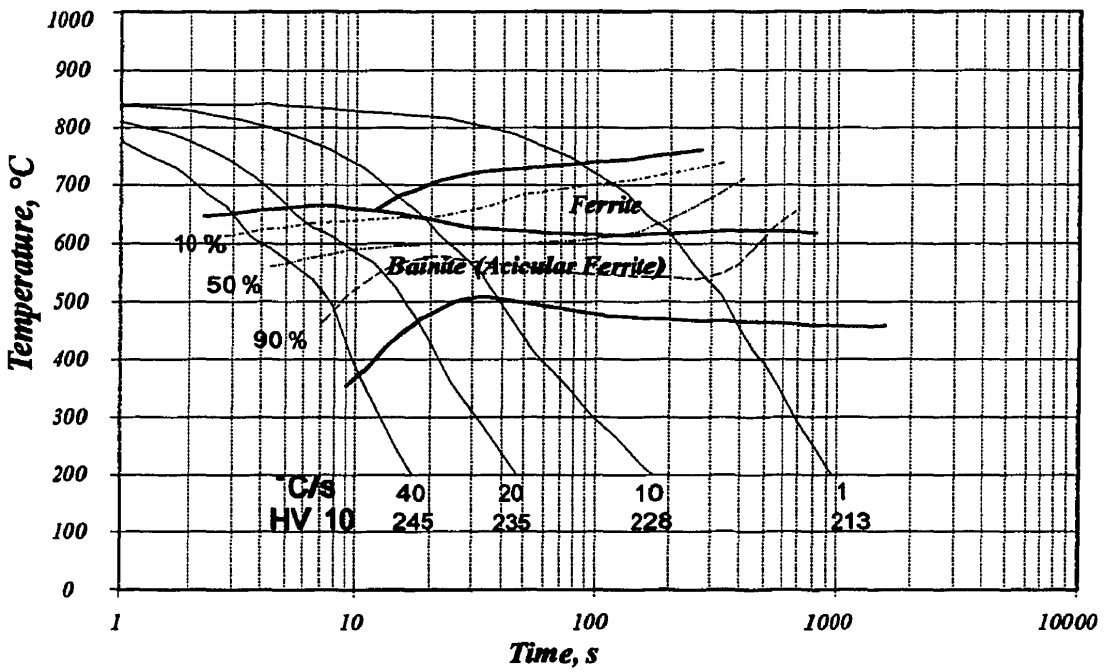

(b)

Figure 4.13 CCT diagrams for the (a) X-70 [105] and (b) X-80 [106] niobium microalloyed steels.

4.4.2 Transformation of Austenite to Ferrite

4.4.2.1 Effective Austenite Interfacial Area (S_V)

The microstructural features developed by deformation below the T_{nr} are the elongated austenite grain boundaries and the introduction of deformation bands. The importance of deformation bands lies in that they are effective nucleation sites for ferrite in addition to the γ grain boundaries. The metallurgical state of the austenite that results from hot rolling can be described by the parameter S_V, which refers to the effective austenite interfacial area [54, 63, 116, 117]. In this regard, the higher the S_V, the more effective has the austenite conditioning been during processing. Previous workers have shown that there are three factors which contribute to S_V, and all these have been considered in eq. 4.12 [60] so as to provide a proper measure of the state of the austenite before transformation:

a: initial grain boundary area per unit volume of equiaxed grains prior to pancaking;
b: increase in initial grain boundary area due to a change in grain shape by pancaking; and
c: formation of intragranular crystalline defects such as deformation bands during rolling.

$$S_v(mm^2/mm^3) = \{1.67(\varepsilon - 0.10) + 1.0\}(2/d_\gamma) + 63(\varepsilon - 0.30) \qquad (4.12)$$

Here, d_γ is the final recrystallized γ grain diameter and ε is the amount of strain in the unrecrystallized γ region. Ouchi [60] has shown that both S_V and increasing cooling rates result in finer ferrite grain sizes, Fig. 4.14.

The results of S_V calculations for the air cooled samples are compared with the measured ferrite grain sizes in Table 4.7. It can be seen that, generally, higher calculated S_V's are associated with finer ferrite grain sizes.

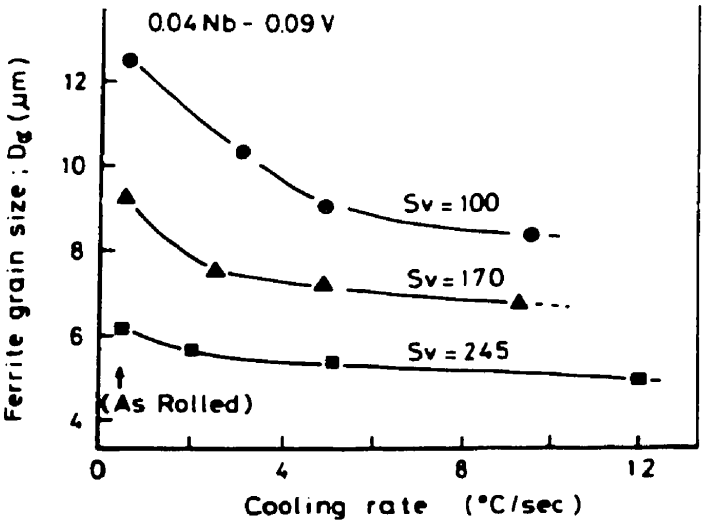

Figure 4.14 Effect of S_V and cooling rate on the ferrite grain size [60].

Table 4.7 Grain sizes of air cooled samples compared to the calculated S_V's for each case.

Steel Grade	RT, °C	FRT, °C	Effective Austenite Interfacial Area S_V (mm^{-1})	Final Ferrite Grain Size, μm
X-70	1225	790	213	10
		730	200	8
X-80	1275	780	228	7
		690	242	4
	1150	780	237	6
		690	252	4

4.4.2.2 Nucleation Rate

The complex situation of nucleation followed by growth and combined with the precipitation of microalloy carbides has not been successfully modelled quantitatively. This issue is still more complex when the transformation occurs upon continuous cooling. Nevertheless, at an early stage of transformation, the transformation rate can be taken to be expressed by $N_\alpha \times S_V$, where N_α is the nucleation rate per unit boundary area.

For continuous accelerated cooling processes, the ambiguity and difficulty of the calculations lies in the heterogeneous nature of nucleation and of the morphology of the transformed product phase. To simplify the effect of temperature on nucleation rate, the homogeneous nucleation of a particle of radius r can be considered [59, 118, 119]. The free energy of the $\gamma \rightarrow \gamma + \alpha$ reaction of a particle is given by:

$$\Delta G = (4/3)\pi r^3 \Delta G_V + 4\pi r^2 \sigma + (4/3)\pi r^3 \varepsilon \qquad (4.13)$$

where ΔG_V is the free energy difference between α and γ, σ is the interfacial energy at the γ/α interface, and ε is the strain energy. ΔG^* is calculated as the maximum energy at a critical size of r^*:

$$r^* = 2\sigma/(\Delta G_V + \varepsilon)$$
$$\Delta G^* = 16\pi\sigma^3/\{3(\Delta G_V + \varepsilon)^2\} \qquad (4.14)$$

From the thermodynamic definition of the equilibrium temperature, $\Delta G_V = 0 = \Delta H - T_e \Delta S$, the following relation is obtained:

$$\Delta G_V = \Delta H \cdot \Delta T / T_e \qquad (4.15)$$

This implies that ΔG_V increases in a linear manner with the amount of supercooling ΔT, which, in turn, strongly decreases the activation energy ΔG^* associated with the formation of a nucleus. Since the embryos grow and shrink by the addition or loss of atoms that move by diffusion, there are two activation energies to be considered in homogeneous nucleation [119]:

$$N_\alpha = K \cdot \exp\left(-\Delta G^*/kT\right) \cdot \exp\left(-\Delta G_D/kT\right) \qquad (4.16)$$

Here K is a proportionality factor, ΔG_D is the activation energy for diffusion, and k is the Boltzmann constant. When ΔT approaches zero, ΔG^* approaches infinity and N_α approaches zero. When ΔT becomes very large, i.e. T is very low, ΔG^* approaches zero and N_α approaches the level governed by $\exp(-\Delta G_D/kT)$. Since T is low, this value is small and the nucleation rate at large ΔT is small. Thus, N_α is small at very small and very large ΔT's; by contrast, it displays its maximum values at intermediate values of ΔT. As will be discussed in the following sections, a condition of moderate supercooling is expected to result in finer microstructures by increasing the nucleation rate during transformation.

4.4.3 Transformed Austenite

The precise microconstituents present depend, of course, upon the pertinent CCT diagram and cooling rate. The bainite transformation temperature, B_s, is the most meaningful parameter in transformation during continuous cooling. The empirical equation that follows [120] predicts the bainite transformation start temperature of the X-70 and X-80 steels to be 645 °C and 625 °C, respectively, under air cooling conditions.

$$B_s = 830 - 270[C] - 90[Mn] - 37[Ni] - 70[Cr] - 83[Mo] \qquad (4.17)$$

This is in agreement with the CCT diagrams of these steels illustrated in Fig. 4.13. Since the cooling stop temperatures of all the rapidly cooled plates were below B_s, bainitic (acicular ferrite) substructures were expected, as can be seen from Figs. 4.7 through 4.12. In the following sections, the effect of the processing conditions on the characteristics of the bainite phase will be discussed.

4.4.3.1 Low Niobium Steel (X-70)

The microstructure of the X-70 steel under air cooling conditions consisted of polygonal ferrite, non-lamellar pearlite and bainite, Fig. 4.7c. This is consistent with the CCT diagram for this material, Fig. 4.13a [105]. In some cases, a clear distinction between the non-lamellar pearlite and bainite could not be made because a nearly continuous range of morphologies was present, Fig. 4.15. Accelerated cooling, however, increased the volume fraction of acicular ferrite at cooling rates of both 6 and 20 °C s^{-1}, Figs. 4.7a and 4.7b. In Fig. 4.16, the bulk hardnesses of the X-70 samples are illustrated. The higher hardnesses of the samples cooled at the higher rates indicate that the characteristics of the acicular phase have changed. The main cause of this observation could be that higher dislocation densities are induced when the cooling rate is increased. (Measurements of the volume fraction of the harder phase were not possible because of the difficulty of revealing its presence by etching.)

The microhardnesses of the pearlite and bainite in the X-70 steel plates, Fig. 4.17, confirmed that the second phase (pearlite or bainite) in rapidly cooled samples is harder than in air cooled plates. This indicates that the proportion of bainite increases when higher cooling rates are employed.

Figure 4.15 SEM micrograph of an X-70 plate, FRT=790 °C and CR= 6°C s^{-1}.

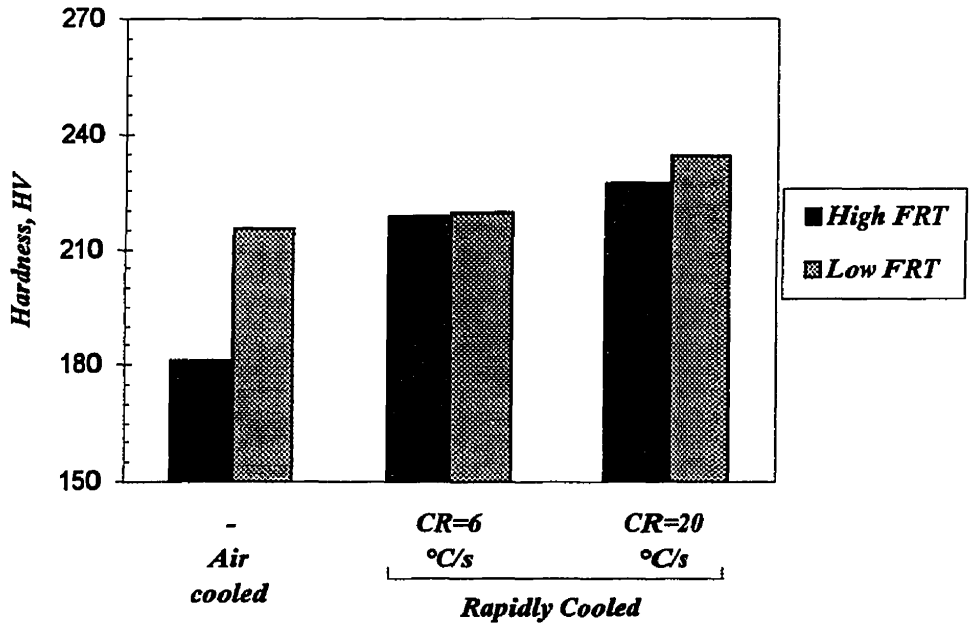

Figure 4.16 Hardnesses of the X-70 plates.

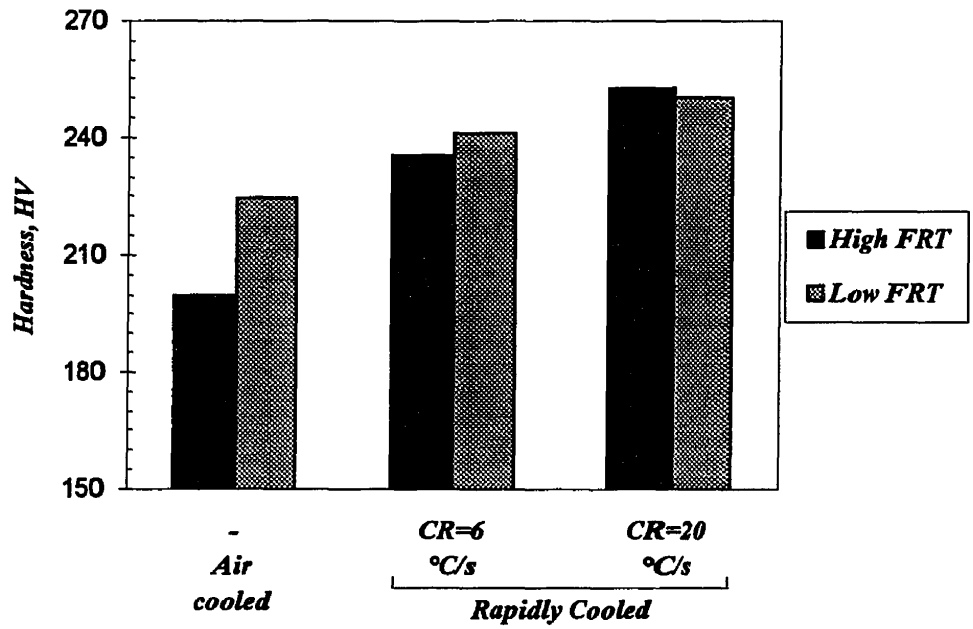

Figure 4.17 Microhardnesses of the bainite phase corresponding to the cases shown in Fig. 4.16.

4.4.3.2 High Niobium Steel (X-80)

4.4.3.2.1 Air Cooled Plates

The banded structures of ferrite and bainite (or acicular ferrite) observed in the air cooled plates, Figs. 4.9g and 4.10g, display a proportion of 4:1, as expected from the CCT curve, Fig. 4.13b. It is clear from these micrographs that the ferrite phase is not truly polygonal with respect to the character of its grain boundaries. The nature of the grain boundary seems to change from high-angle to low-angle, the observed shapes of the boundaries are irregular, and the etched lines are discontinuous. For this reason, the type of ferrite present in the air cooled samples has been called "quasi-polygonal" [121].

The hardnesses of the X-80 air cooled samples, Fig. 4.18, show that lower hardnesses are observed in the plates reheated at the lower temperature. This is because less Nb was put into solution in these plates, which resulted in less strain-induced precipitation of Nb-containing particles. It can also be seen that, due to the ferrite rolling of samples finish rolled in the two phase region, the hardnesses of the samples with the lower FRT have increased considerably. This can be attributed to the greater amount of precipitation, to more austenite pancaking before transformation, Table 4.6, and to the increased dislocation density attributable to ferrite pancaking. The other cause in this regard may be the finer ferrite grain sizes of samples finish rolled below the Ar_3, Table 4.7.

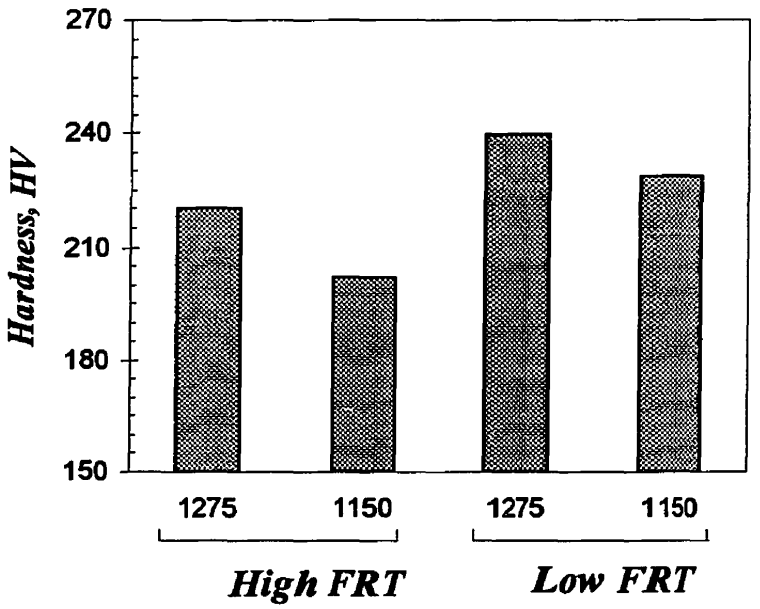

Figure 4.18 Hardnesses of the air cooled X-80 plates.

4.4.3.2.2 Accelerated Cooling

Microstructures

Due to the fine grain sizes and the natures of the acicular ferrite structures in the rapidly cooled plates, differences in microstructure were scarcely detectable by means of optical microscopy. This was most difficult when samples with different cooling interruption temperatures were to be compared to each other. By contrast to the air cooled plates, in the rapidly cooled samples, the structures were almost entirely acicular, Figs. 4.9 and 4.10 (a) through (f). In these microstructures, some discontinuous banded substructures of the fine sheaf-like bainite or acicular ferrite are also observed, which formed at heavily deformed shear bands. Although the final grain sizes could not be measured quantitatively,

it is clear from the micrographs of Figs. 4.9 and 4.10 that the samples associated with a high CIT exhibit coarser grains (thicker lath sheaves) than the medium and low CIT plates.

The grain boundaries of this substructure have "irregular and jagged" characteristics and consist of plates pointing along many directions. According to several previous workers [121-123], this phase is called acicular ferrite because of its sheaf-like morphology. A more general definition of this morphology can be bainite-like [122] or carbide-free bainite [124]. The SEM and optical micrographs of two rapidly cooled samples in Fig. 4.19 reveal the uneven and discontinuous nature of the etched boundary lines of acicular ferrite substructures orientated along different directions.

The other clear feature of this substructure is that no prior γ grain boundaries are observed. This is consistent with the findings of other workers [6, 122]. A typical TEM micrograph of the same sample is shown in Fig. 4.20. It can be seen that there is no sign of carbide precipitation and that the substructure contains a relatively high density of dislocations. Diffraction patterns revealed that some dark areas are either retained austenite or martensite. Figure 4.21 provides a schematic view of the morphology of acicular ferrite in comparison with those of polygonal ferrite and bainitic microstructures.

According to Babu and Bhadeshia [123], acicular ferrite and bainite are both formed by a mechanism that involves displacive growth without diffusion, except that the morphology of acicular ferrite differs in the sense that physical impingement between the plates nucleated intragranularly prevents full development of the sheaf morphology [124]. After growth stops at a temperature where the carbon concentration of the austenite reaches a definite amount, the partitioning of carbon starts [125]. This is known as the incomplete reaction phenomenon. It has also been shown that the acicular sheaves tend to form and grow on planes parallel to the maximum shear stress at approximately 45 degrees to the compressive stress axis [125].

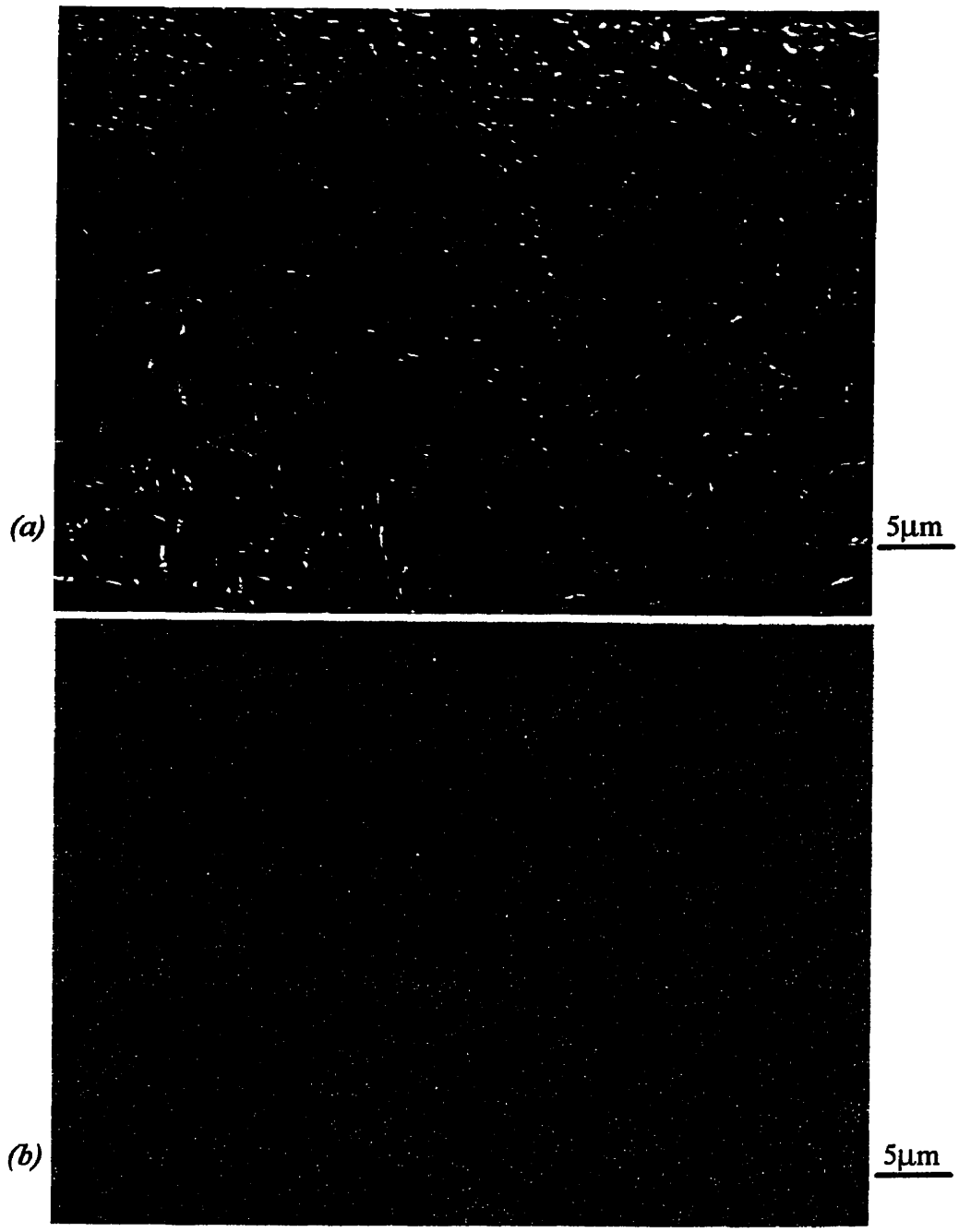

Figure 4.19 Microstructures of two X-80 plates finish rolled above the Ar_3 and rapidly cooled at 20 °C s^{-1}; (a) RT= 1275 °C (SEM micrograph), (b) RT= 1150 °C (optical micrograph).

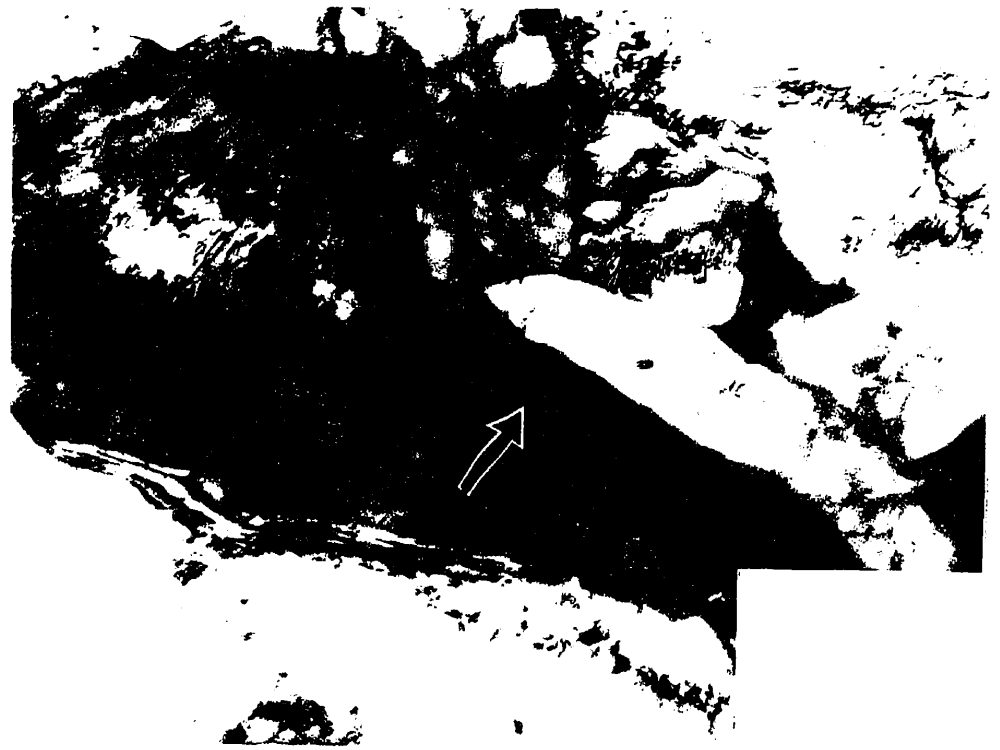

Figure 4.20 TEM micrograph of the X-80 sample of Fig. 4.19a. The arrow indicates retained austenite or martensite.

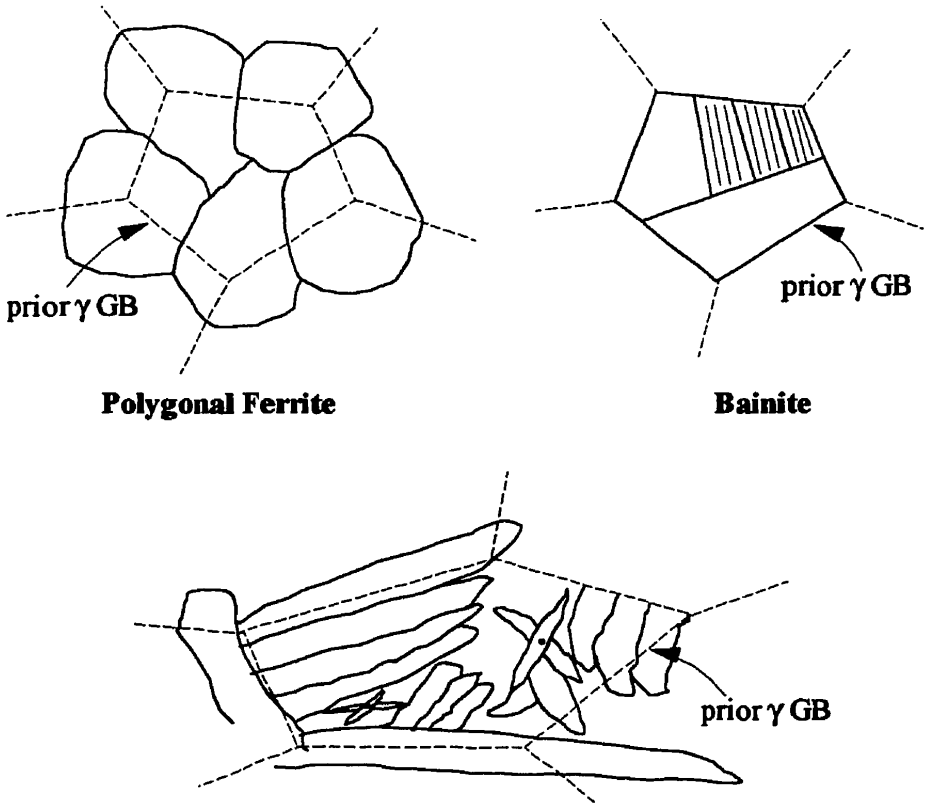

Figure 4.21 Schematic illustration of the microstructural features of different austenite transformation products.

Two typical SEM and optical micrographs showing acicular ferrite sheaves at 45 degrees are illustrated in Fig. 4.22. It should be noted that this was found mostly in samples finish rolled below the Ar_3 where the austenite underwent more pancaking strain before transformation. Traces of such characteristics can be found in the optical micrographs of samples finish rolled in the two phase region, Figs. 4.9 to 4.12. These observations support the displacive mechanism for the growth of acicular ferrite [123].

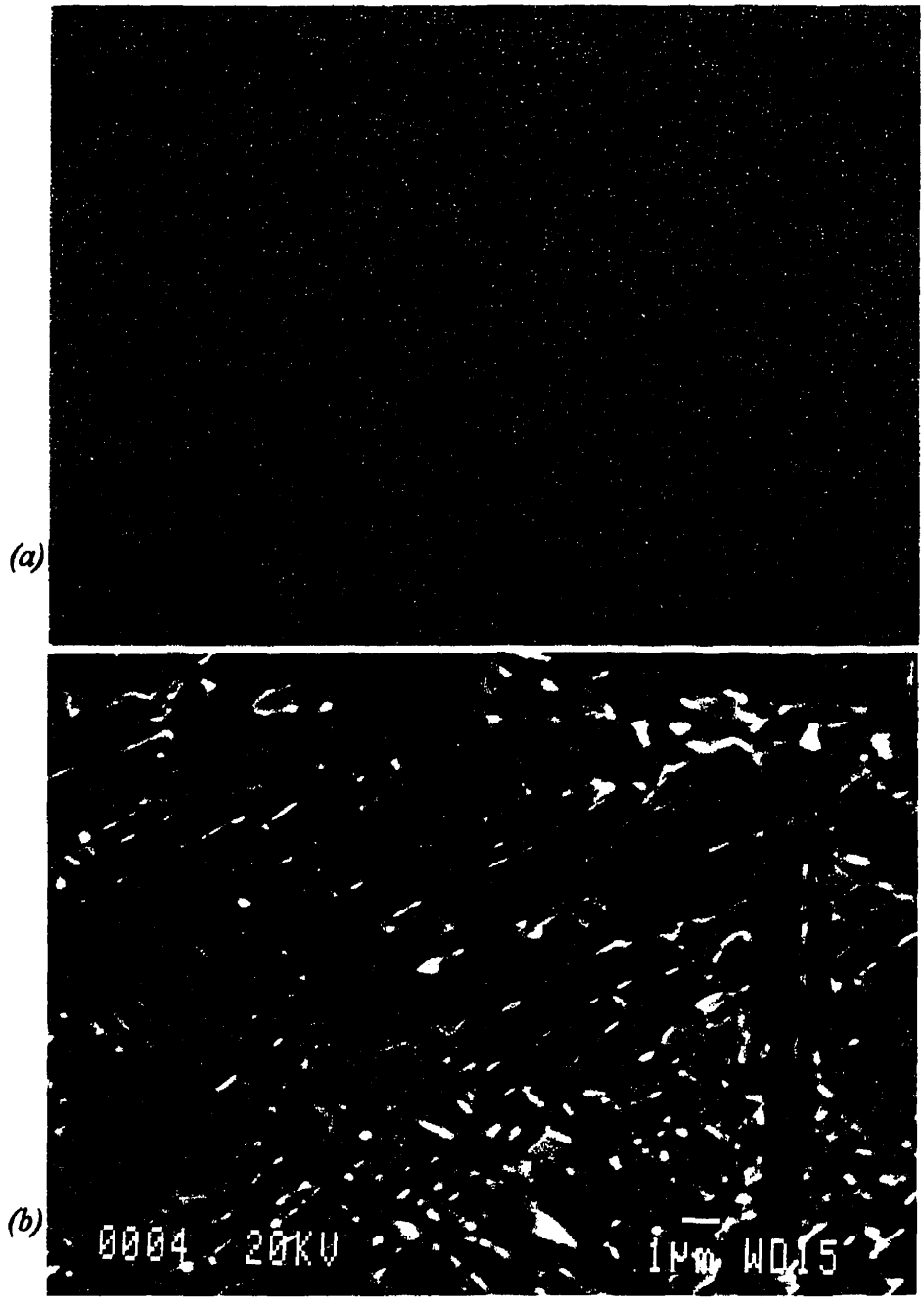

Figure 4.22 Microstructures of two X-80 plates finish rolled below the Ar_3 and rapidly cooled at 20 °C s^{-1}; (a) CIT= 520 °C (optical micrograph), (b) CIT= 420 °C (SEM micrograph).

Hardness

The results of the hardness tests on the rapidly cooled X-80 samples are illustrated in Figs. 4.23 and 4.24. A comparison with the hardnesses of the X-70 samples in Fig. 4.16 reveals that for all comparable cases the hardnesses are increased in the X-80 samples. This is mainly because of the greater amount of Nb(CN) precipitation in the X-80 steels. Comparison with the *air cooled* X-80 samples, Fig. 4.18, indicates that accelerated cooling increases the hardness. These increases are attributed to increases in the volume fraction of acicular ferrite and the dislocation density as well as to refining the grain size.

It is of interest to note that the hardnesses of the rapidly cooled high FRT samples are lower than those of the corresponding low FRT samples. This is despite the fact that nearly fully acicular structures are developed in these samples. Part of the hardness increase can obviously be attributed to the higher dislocation densities in the pancaked ferrite, as was postulated for the equivalent differences in the air cooled samples. However, the microhardness results associated with the acicular substructures, Fig. 4.25, indicate that the acicular ferrite in the low FRT samples is much harder than in the high FRT material. It should be noted that the microhardness testing of the high FRT samples was performed on the finest parts of the acicular substructure. These hardness increases can again be attributed to more precipitation and to the enhanced dislocation density associated with ferrite pancaking.

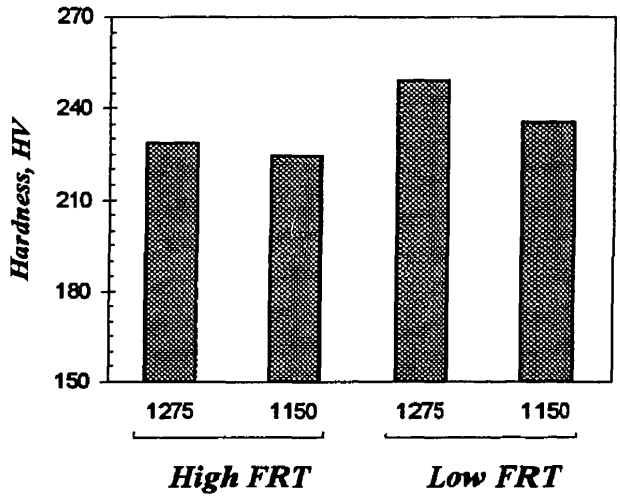

(a) CIT= 620 °C

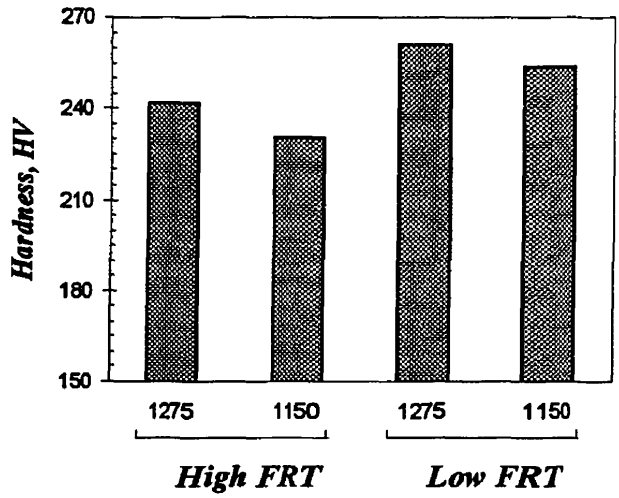

(b) CIT= 520 °C

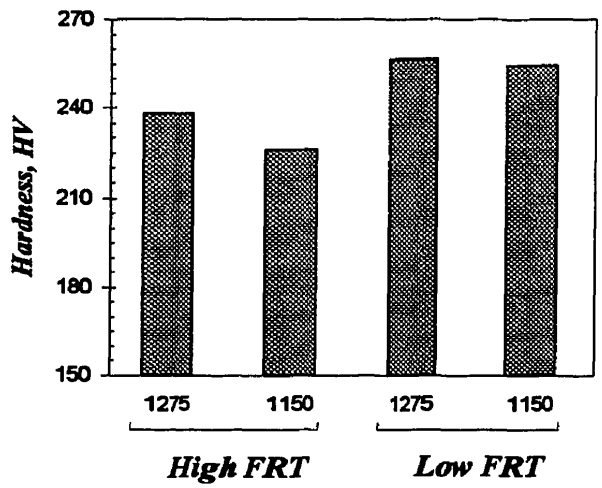

(c) CIT= 420 °C

Figure 4.23 Hardnesses of the X-80 plates rapidly cooled at 20 °C s^{-1}.

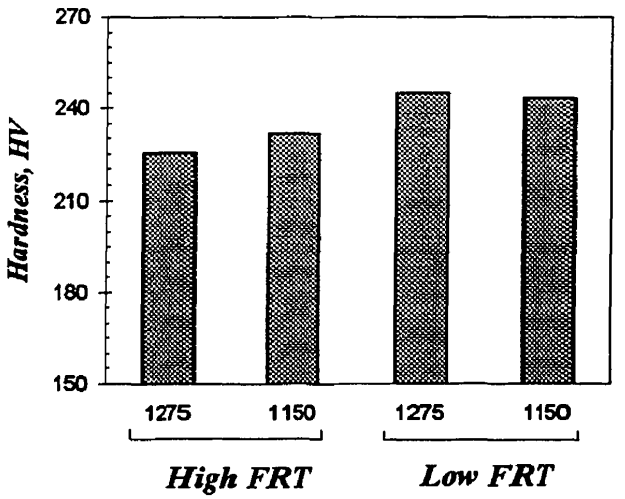

(a) CIT= 620 °C

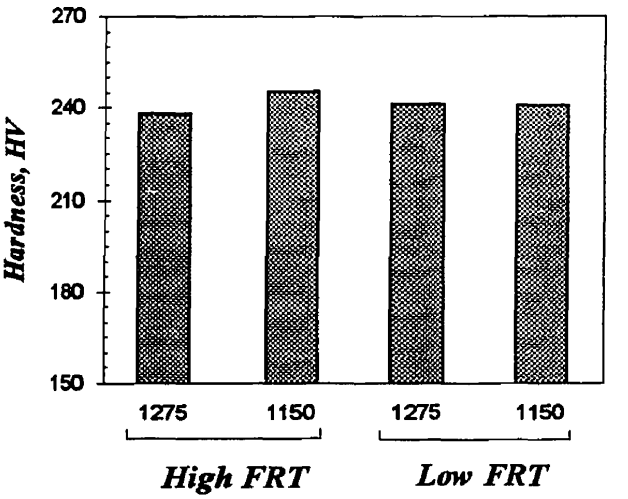

(b) CIT= 520 °C

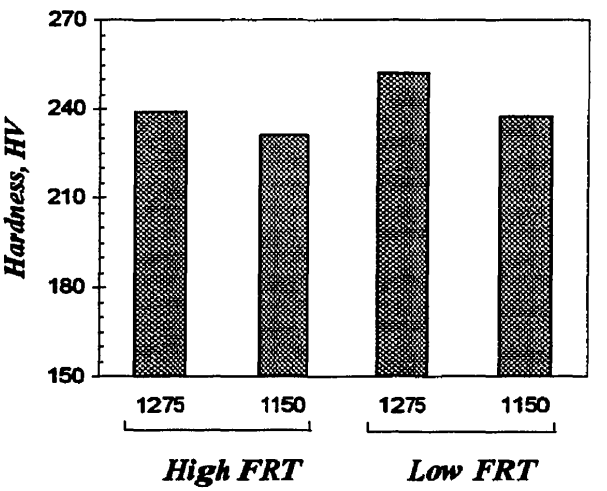

(c) CIT= 420 °C

Figure 4.24 Hardnesses of the X-80 plates rapidly cooled at 40 °C s^{-1}.

4.4.3.2.3 Effect of Cooling Interruption Temperature

Accelerated cooling during the γ-to-α transformation effectively keeps the precipitates fine or prevents precipitation during the transformation [126]. On the other hand, accelerated cooling and especially the use of a lower CIT decreases the grain size of the bainite or acicular ferrite. As mentioned earlier, it is hard to detect the differences in the microstructures developed in samples for which cooling was interrupted at 520 °C and 420 °C. The microhardnesses of samples with different cooling interruption temperatures are compared in Fig. 4.25. It can be seen that when a low FRT is employed, a lower CIT results in higher hardness. This is due to the finer acicular ferrite and/or bainite formed from the more pancaked austenite phase with the higher S_V. However, for the case of finishing in the austenite region, the hardness is at a maximum when a medium CIT (520°C) is employed. This is also evident in Figs. 4.23 and 4.24, where the bulk hardnesses of the same samples characterized in Fig. 4.18 are illustrated.

These observations are consistent with the finding of Ouchi et al. [126] that when accelerated cooling was interrupted at too low temperature or when cooling rates above 15 °C s^{-1} were employed, larger amounts of coarse bainite were formed and the toughness of the steel was deteriorated. Although the grain size of such acicular ferrite is not easy to measure, this observation can be attributed to the higher nucleation rate applicable to transformation during moderate supercooling, as discussed in section 4.4.2.2. Moderate supercooling may also lead to finer precipitate dispersions in the transformation products. Such an effect will be discussed again in Chapter Six, where the yield strengths of these materials will be presented and analyzed. The scatter obtained in the present study for some samples rapidly cooled at 40 °C s^{-1} may in fact result from the more inhomogeneous dislocation structures produced.

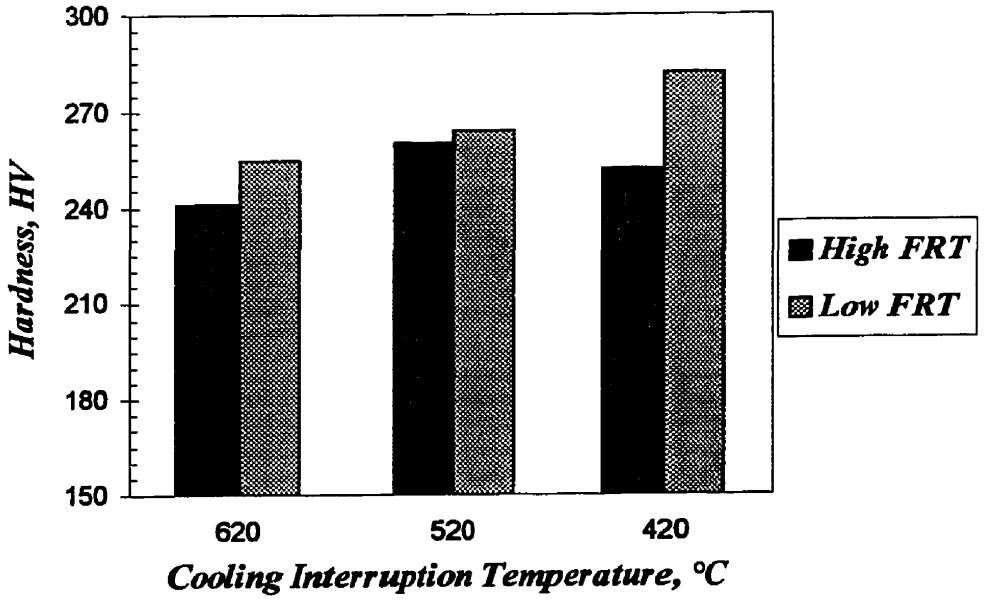

(a)

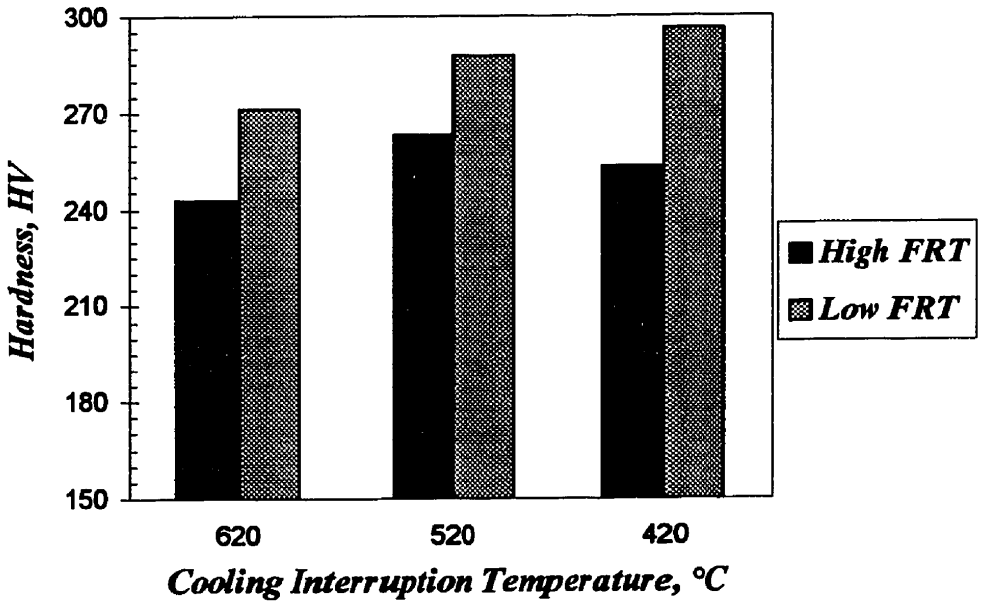

(b)

Figure 4.25 Microhardnesses of the fine acicular phase in samples reheated at 1275 °C; (a) CR= 40 °C s^{-1}, (b) CR= 20 °C s^{-1}.

CHAPTER 5

Texture Development during the γ-to-α Transformation

5.1 Introduction

As discussed in the previous chapter, the pancaked state of the austenite before transformation and the cooling rate during transformation determine whether the mode of transformation is mixed or shear in the case of acicular ferrite or bainite. It is well known that during the transformation, the crystallographic texture developed by heavy deformation (pancaking) of the austenite is inherited by the ferrite. The orientation distribution functions obtained from the new texture analysis methods provide a quantitative measurement of texture development during the transformation. Furthermore, an understanding of the way in which texture is formed is important in accounting for the microstructural characteristics and properties of the final product.

At all stages of the thermomechanical processing described in the previous chapter, textures are formed and transformed. The formation of the RD and TD fibers (or the {113}<110> and {332}<113> components as the most intense orientations in those fibers) from the pancaked austenite has been reported by many investigators [7, 22, 24, 31, 128, 129]. However, the sharpness and relative intensities of these fibers depend on the characteristics of processing in ways that are not fully understood.

In the present part of this work, the influence of the processing conditions on the transformation textures of the pancaked austenite is examined. In this regard, the microstructural evolution must also be taken into account, which was discussed in the previous chapter. Here, some possible relations between the texture evolution and the phase transition will be discussed. The texture predictions obtained from some variant selection criteria proposed for the modelling of transformation textures will also be compared with the experimental results.

5.2 Textures

In the following sections, the textures calculated from the experimental pole figures are presented in the form of ODF (Orientation Distribution Function) diagrams in the same order of description of the samples and their processing conditions as employed in Tables 3.5 to 3.10. As the $\varphi_2 = 45°$ ODF section includes most of the important fibers and ideal orientations, Fig. 5.1, it is used below to represent the textures.

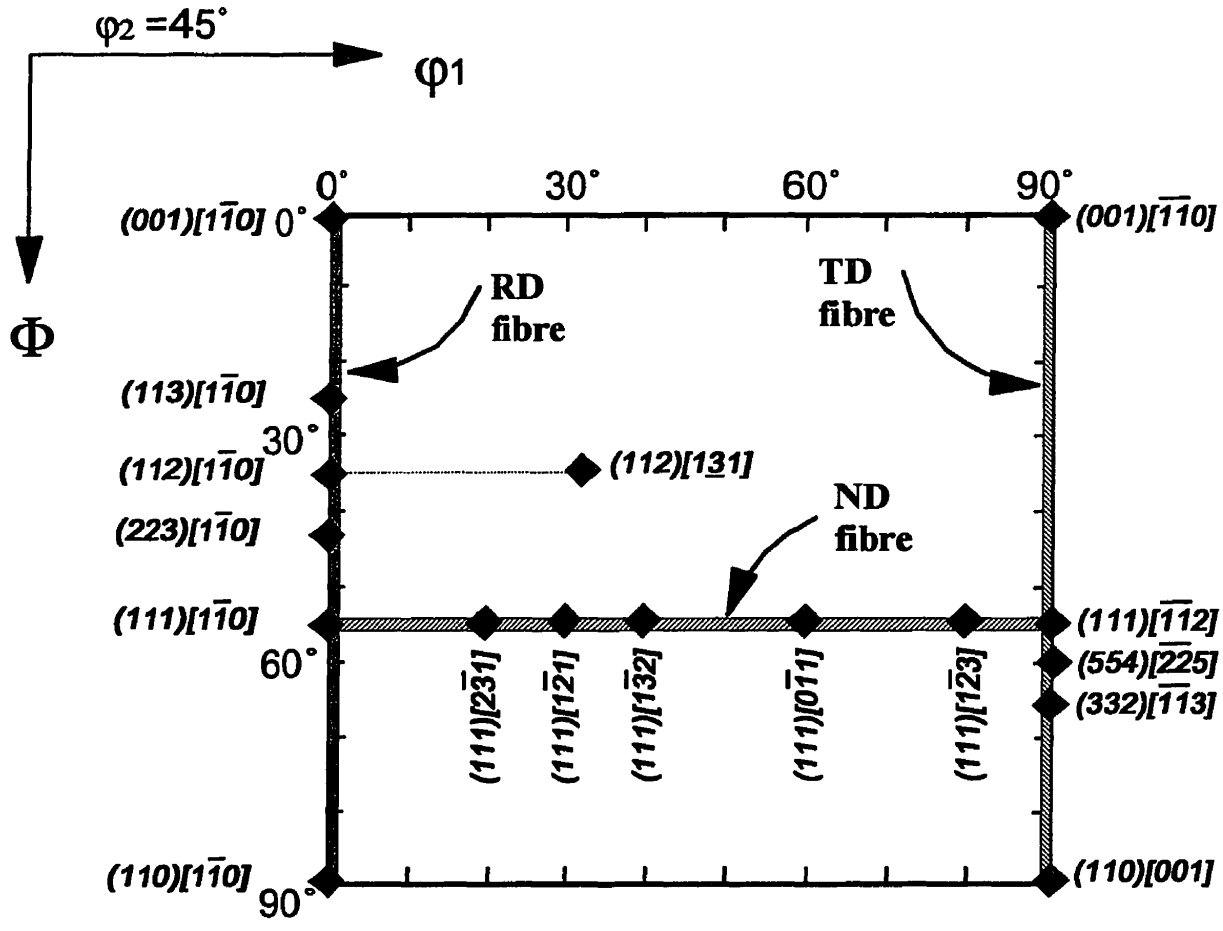

Figure 5.1 φ_2 = 45° ODF section showing the positions of the ideal orientations and the RD, TD, and ND fibers in the ferrite texture.

5.2.1 Low Niobium Steel (X-70)

The textures of the X-70 steel reheated at 1225 °C are illustrated in Figs. 5.2 and 5.3. Figure 5.2 includes the ODF's of the samples finish rolled in the austenite region. It is evident from these figures that sharper textures are developed by accelerated cooling after rolling. Finish rolling in the two phase region, Fig. 5.3, increased the sharpness of the textures slightly when accelerated cooling was employed.

Comparison of these figures with the $\varphi_2 = 45°$ ODF section illustrated in Fig. 5.1 reveals that the three partial fibers identified in this figure are largely formed by the transformation. These fibers are:

i) the RD fibre, which includes components having their <110> directions parallel to the rolling direction;
ii) the TD fibre, which consists of components having their <110> directions parallel to the transverse direction.
iii) the ND fibre, which contains the components having their <111> directions parallel to the normal direction.

In Figure 5.4, the effects of the processing conditions on texture development are shown in the form of skeleton lines; this provides a clearer presentation of the ideal orientations and their intensity values along each fibre.

It can be seen from Fig. 5.4 that accelerated cooling increased the intensities of all three fibers, the most pronounced effect being on the TD fibre. It is evident that in the samples finish rolled below the Ar_3, the peak intensities of the RD fibers are broadened. In Fig. 5.4 (c), it can be observed that, although accelerated cooling generally increases the intensity of the ND fibre, the {111}<112> is favoured in comparison to the {111}<110>.

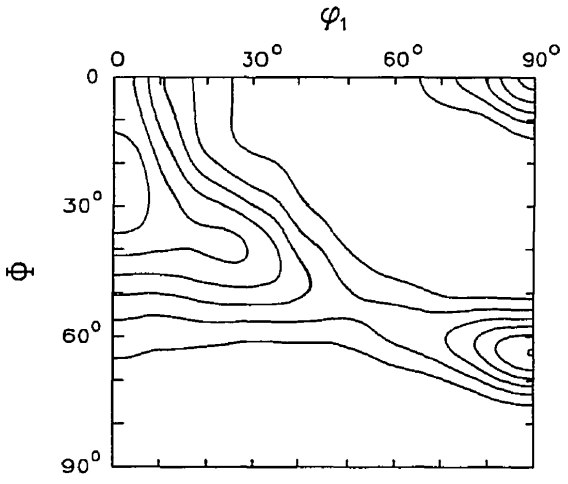

Max : 6.9

(a) CR=20°C s^{-1}

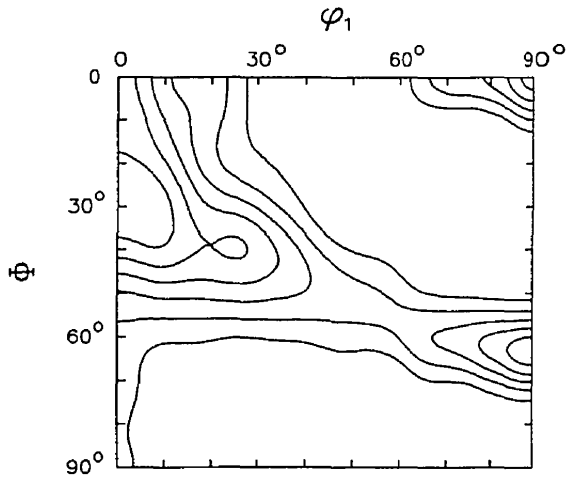

Max : 6.7

(b) CR=6°C s^{-1}

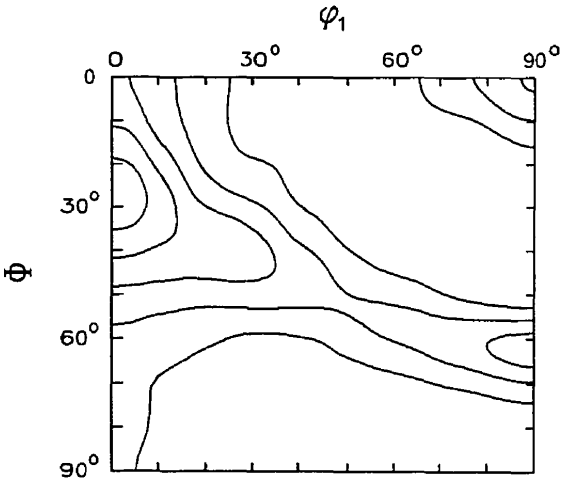

Max : 5.7

(c) Air cooled

Figure 5.2 $\varphi_2 = 45°$ ODF sections; the X-70 plates reheated at 1225°C and finish rolled at 790°C; accelerated cooling was interrupted at 620°C. Contour levels: 1, 2, 3, 4, 5, 6.

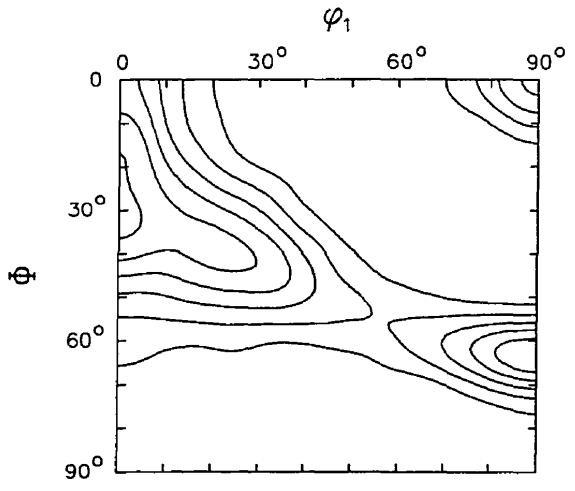

Max : 6.3

(a) CR=20°C s^{-1}

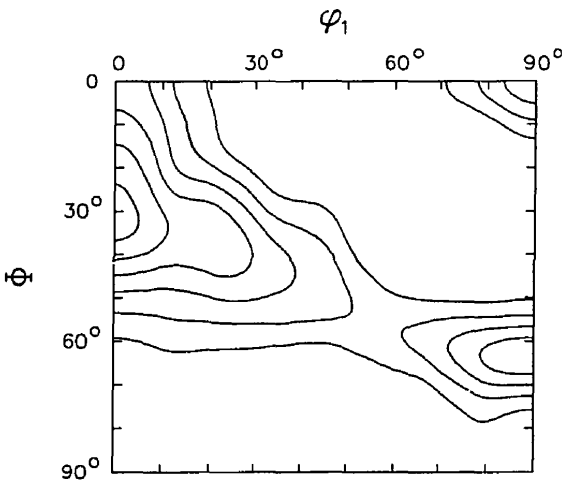

Max : 6.4

(b) CR=6°C s^{-1}

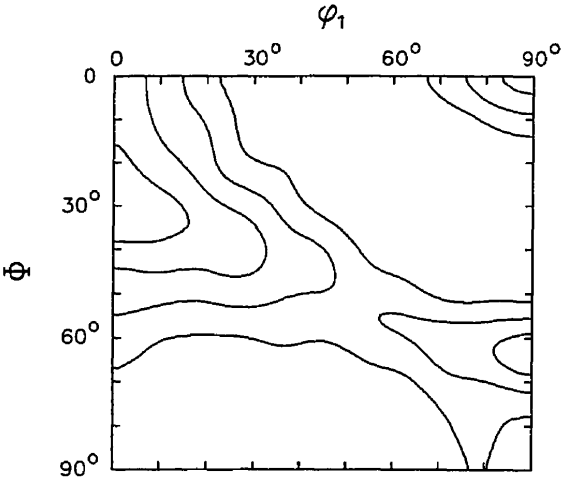

Max : 4.7

(c) Air cooled

Figure 5.3 φ_2 = 45° ODF sections; the X-70 plates reheated at 1225°C and finish rolled at **730°C**; accelerated cooling was interrupted at 620°C. Contour levels: 1, 2, 3, 4, 5, 6.

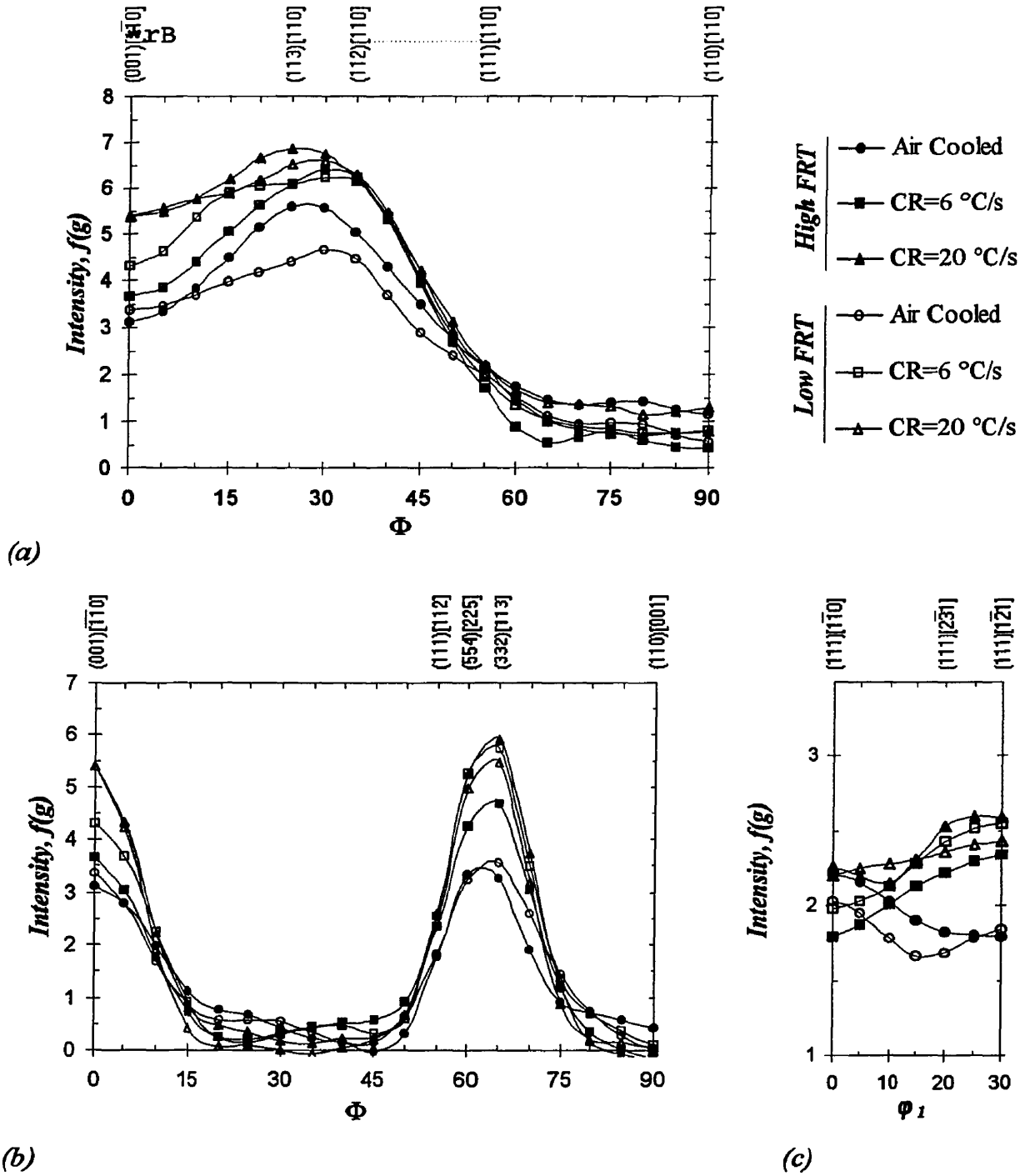

Figure 5.4 The intensity curves of the *(a)* RD, *(b)* TD, and *(c)* ND fibres for the X-70 plates reheated at 1225 °C; accelerated cooling was interrupted at 620 °C.

5.2.1.1 Through-Thickness Inhomogeneity of the Texture

Since there was a strain gradient through the thickness of the rolled plates, an inhomogeneity of the texture was expected to develop from the surface to the mid-plane of the plates. The shear strain applied at and near the surface of the plate modifies the type of texture and it no longer corresponds to plane strain conditions through the thickness. In order to investigate the texture gradients, six more texture measurements were carried out on one air cooled and one rapidly cooled plate of the X-70 steel. For each case, three cuts at the surface (R=0), R=1/6, and R=1/3 ($R = (t_0 - t)/t_0$) were prepared for texture measurement in addition to the mid-plane texture measurements. Here, t is the thickness of the plate after each cut and t_0 is the initial thickness which was about 12 mm. The ODF sections of these textures are shown in Figs. 5.5 and 5.6. Because of the monoclinic symmetry of the shear texture developed at the surface, the ODF sections are drawn in Figs. 5.5a and 5.6a over the range φ_1 = 0 to 180°. These are typical shear textures with {110}<uvw> orientations [5]. The maximum intensity lies at (110)[$\bar{1}$ 11] in the case of the rapidly cooled sample, Fig. 5.6a. Comparison of Fig. 5.5 with Fig. 5.2c and Fig. 5.6 with Fig. 5.3a shows that the shear texture is present down to about 2 mm below the surface of the plate. In both cases, no texture gradient was observed within about 5 mm of the mid-plane of the 12 mm thick plate.

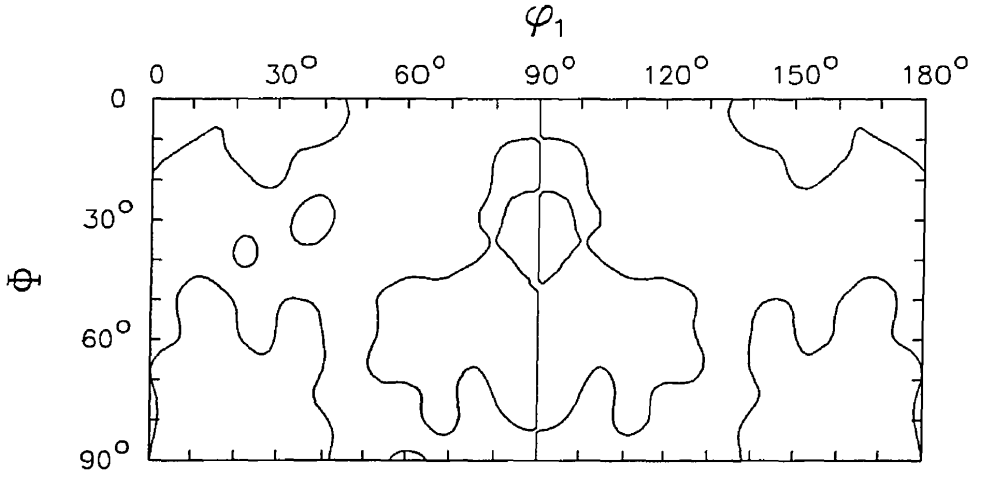

Max= 2.3

(a) R=0

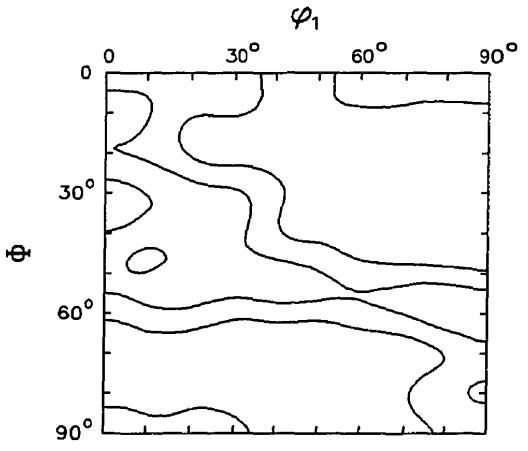

Max= 3.7

(b) R=1/6

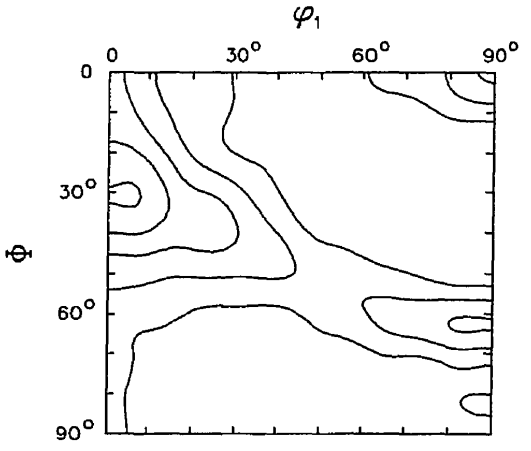

Max= 5.1

(c) R=1/3

Figure 5.5 $\varphi_2 = 45°$ ODF sections of an *air cooled* X-70 steel plate finish rolled at 790°C. Contour levels: 1, 2, 3, 4, 5.

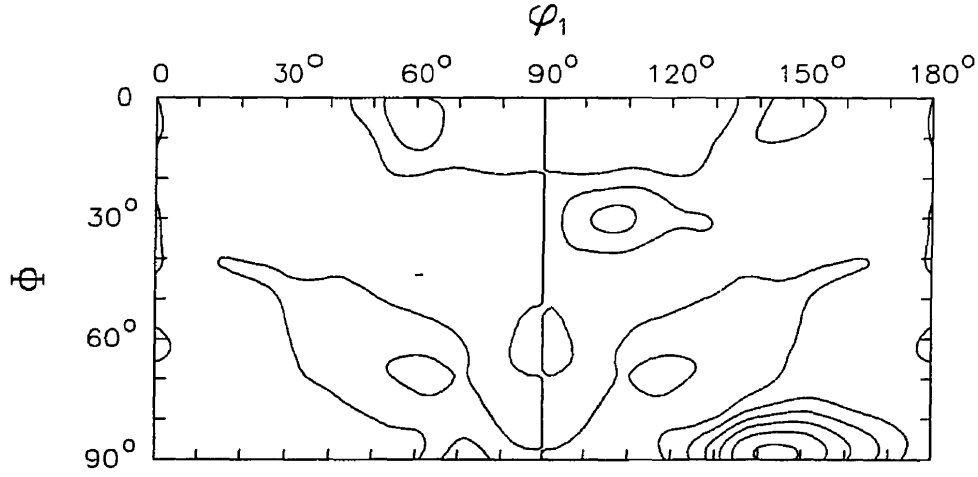

Max= 6.3

(a) R=0

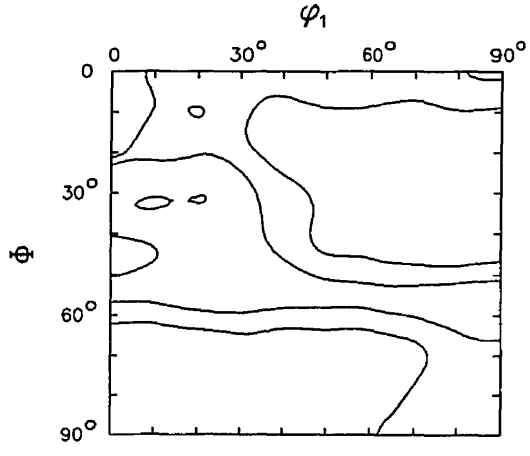

Max= 3.0

(b) R=1/6

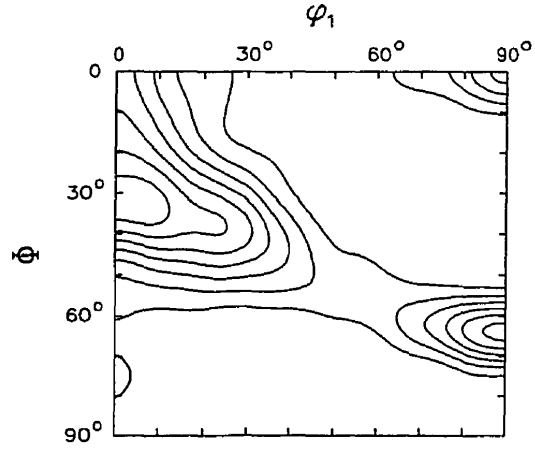

Max= 7.7

(c) R=1/3

Figure 5.6 $\varphi_2 = 45°$ ODF sections of a *rapidly cooled* X-70 steel plate finish rolled at 790°C. Contour levels: 1, 2, 3, 4, 5, 6.

5.2.2 High Niobium Steel

The $\varphi_2 = 45°$ ODF sections pertaining to the X-80 plates described in Tables 3.7 to 3.10 are illustrated in Figs 5.7 to 5.10. The corresponding RD, TD, and ND fibre intensities are plotted in Figs. 5.11 to 5.14. In all these figures, the presence of strong RD and TD fibre transformation textures is clearly evident. However, the intensities of the texture components depend on the processing conditions. Generally, accelerated cooling sharpens the textures of all plates, irrespective of the preceding controlled rolling conditions.

When the plates with high reheat temperatures are finish rolled in the unrecrystallized austenite region, accelerated cooling results in a very high density TD fibre, with a highest intensity of 9 in comparison to 4 for the air cooled sample, Fig. 5.7. The intensity of the RD fibre is also increased by accelerated cooling, although to a lower degree from almost 6 (in the air cooled sample) to 10. A similar trend is observed in the samples reheated to the lower temperature and finish rolled above the Ar_3, Figs. 5.8 and 5.12, although the sharpness of the texture is generally increased as well. From these two figures, it appears that there is no significant difference between the samples rapidly cooled at 40 or 20 °C s^{-1}. By contrast, it seems that the cooling interruption temperature has a greater effect on the transformation texture. In most cases, a moderate cooling interruption temperature of around 520 °C leads to the highest maximum intensity, Figs. 5.7, 5.8, 5.11, and 5.12.

It is apparent that the TD fibre is always sharpened at {332}<113>. In rapidly cooled samples finish rolled in the γ region, it is also evident that by decreasing the cooling interruption temperature to below 520 °C, the contour lines are attracted toward {112}<131>, Fig. 5.1, and form a circle. In the sample interrupted cooled at the lowest temperature in this study, Fig. 5.8 (f), this effect was accompanied by a depletion of the orientations near the RD fibre. This shows a very clear effect of accelerated cooling, and in

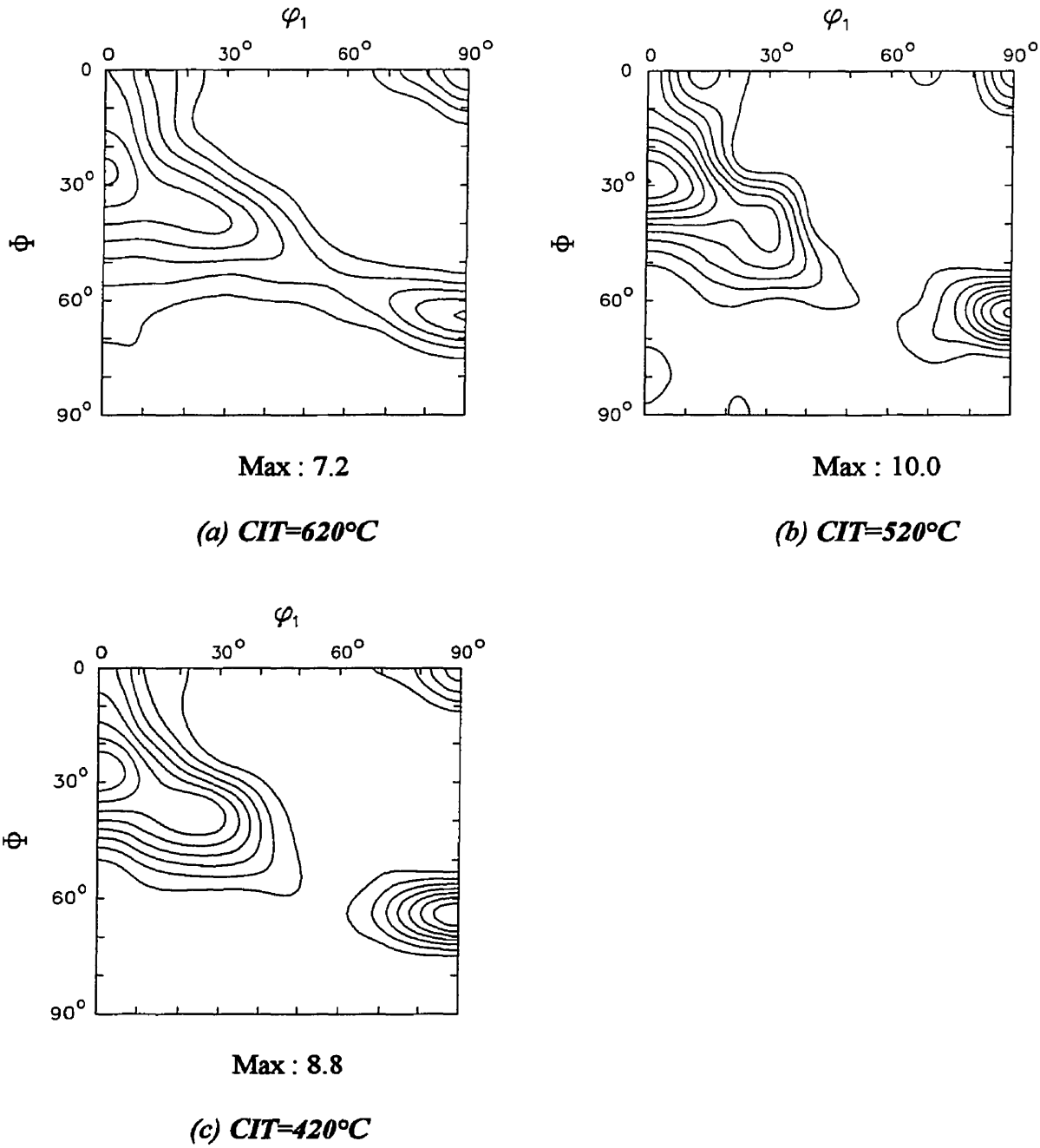

(a) CIT=620°C

(b) CIT=520°C

(c) CIT=420°C

Figure 5.7 $\varphi_2 = 45°$ ODF sections of the X-80 plates reheated at **1275 °C** and finish rolled at **780 °C**; *(a)* to *(c)* CR=40°C s^{-1},

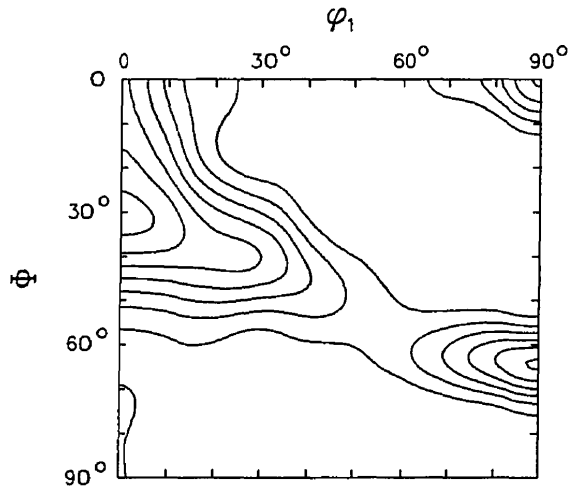

Max : 7.4

(d) CIT=620°C

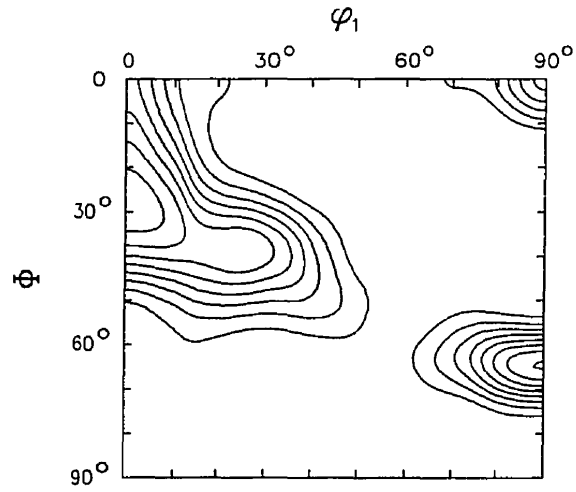

Max : 8.7

(e) CIT=520°C

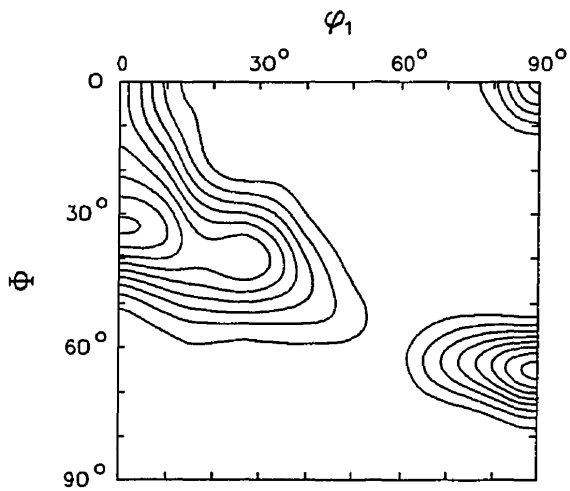

Max : 9.1

(f) CIT=420°C

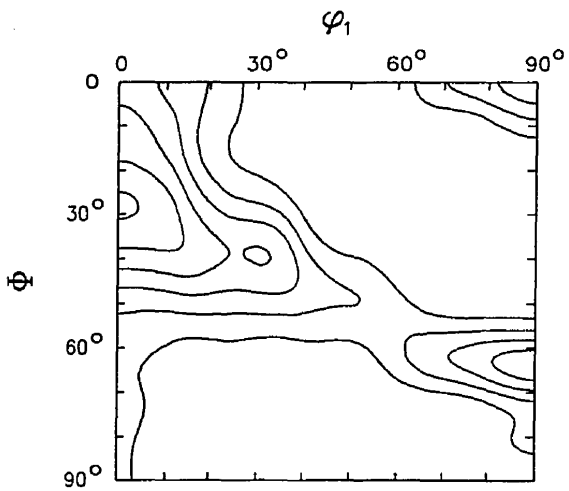

Max : 6.2

(g) Air Cooled

Figure 5.7 (continued) *(d)* to *(f)* CR=20°C s^{-1}, and *(g)* air cooled. Contour levels: 1, 2, 3, 4, 5, 6, 7, 8, 9, 10.

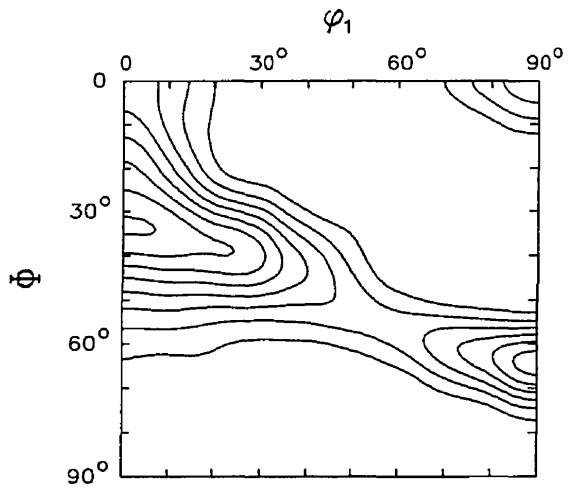

Max : 8.1

(a) CIT=620°C

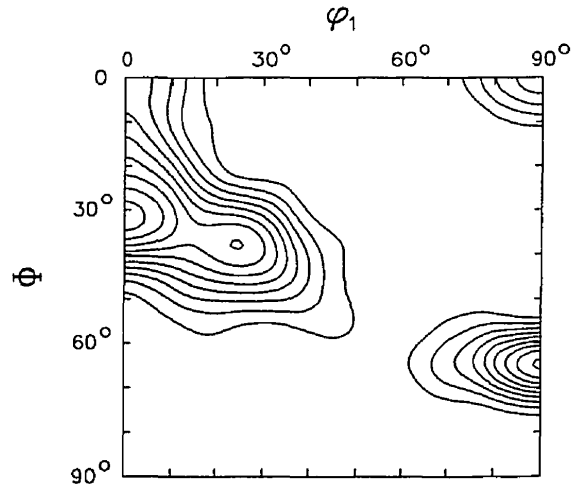

Max : 10.6

(b) CIT=520°C

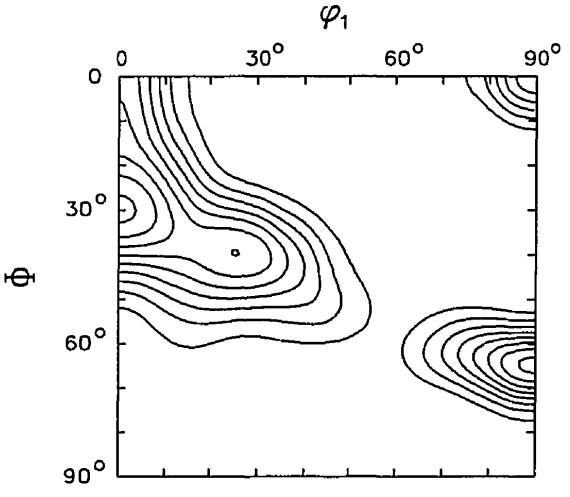

Max : 9.3

(c) CIT=420°C

Figure 5.8 $\varphi_2 = 45°$ ODF sections of the X-80 plates reheated at **1150 °C** and finish rolled at **780 °C**; *(a)* to *(c)* CR=40°C s^{-1},

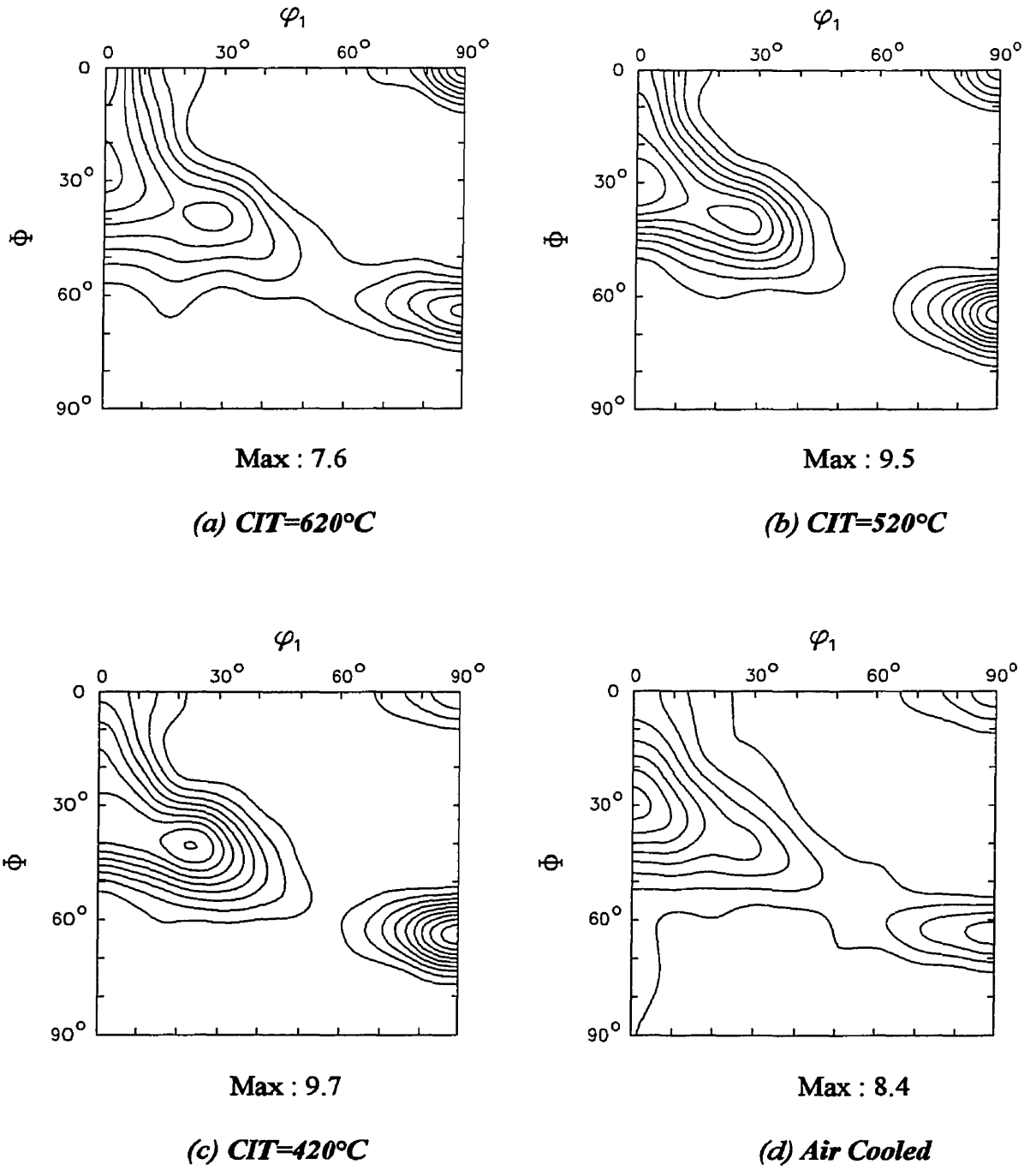

Figure 5.8 (continued) *(d)* to *(f)* CR=20 °C s^{-1}, and *(g)* air cooled. Contour levels: 1, 2, 3, 4, 5, 6, 7, 8, 9, 10.

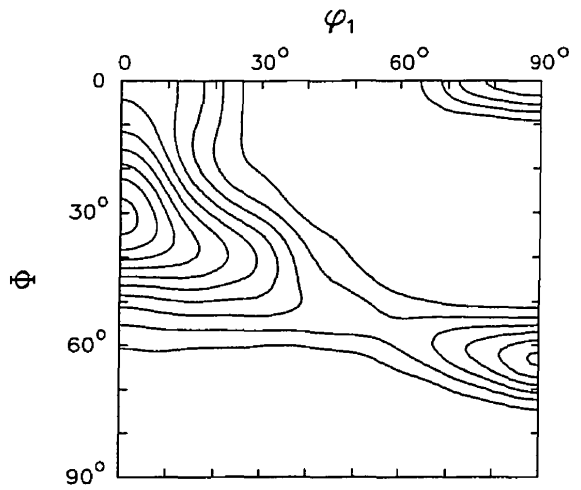

Max : 10.4

(a) CIT=620°C

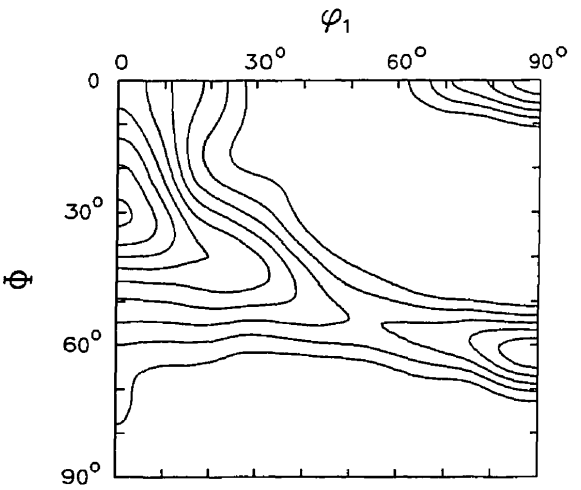

Max : 9.2

(b) CIT=520°C

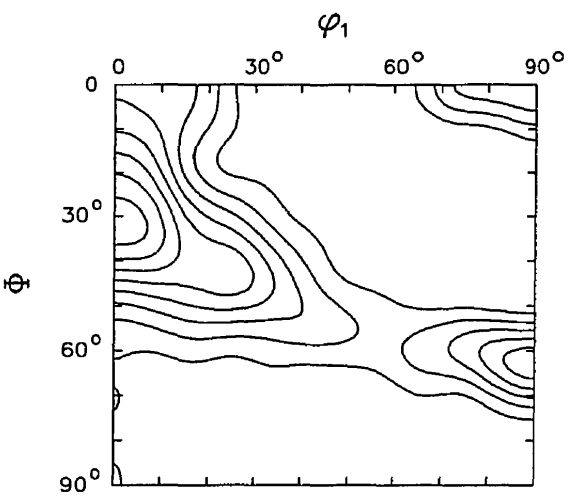

Max : 8.6

(c) CIT=420°C

Figure 5.9 $\varphi_2 = 45°$ ODF sections of the X-80 plates reheated at **1275 °C** and finish rolled at **690 °C**; *(a)* to *(c)* CR=40 °C s^{-1},

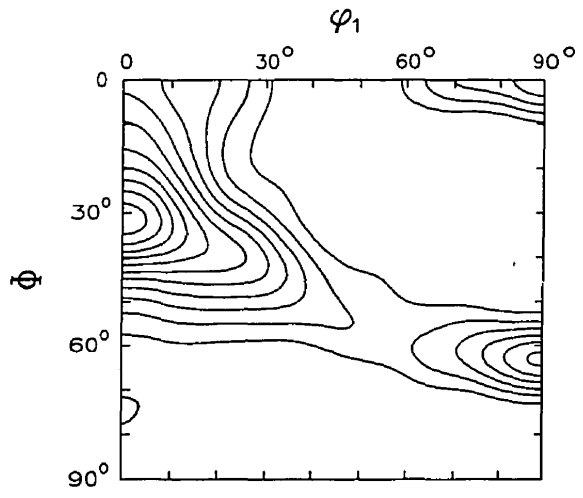

Max : 11.6

(d) CIT=620°C

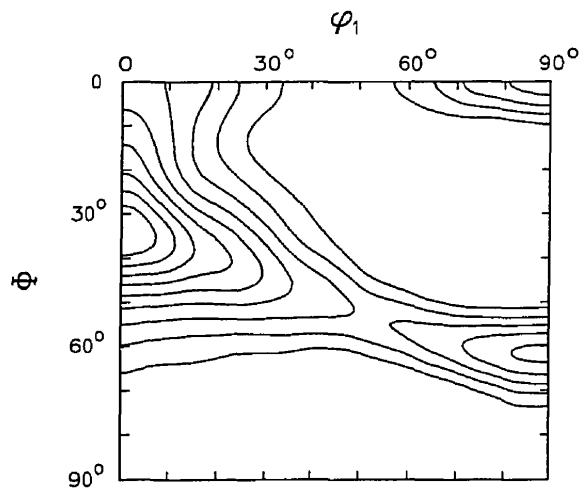

Max : 10.0

(e) CIT=520°C

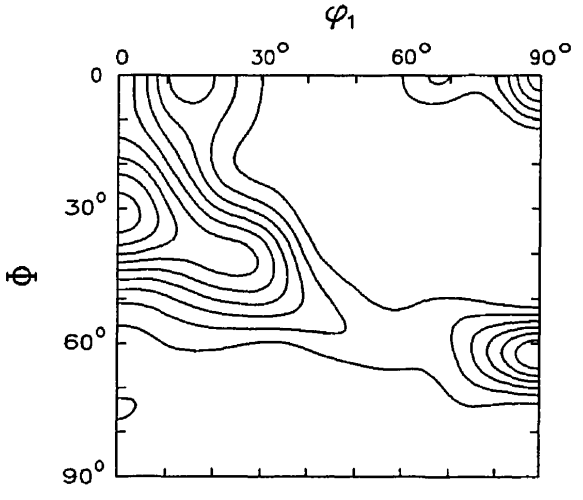

Max : 9.5

(f) CIT=420°C

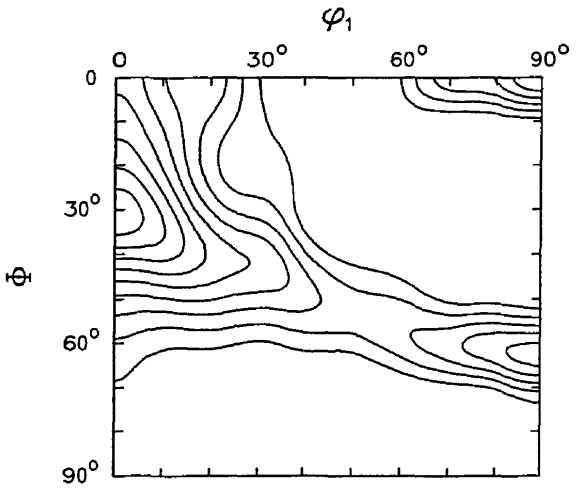

Max : 9.7

(g) Air Cooled

Figure 5.9 (continued) *(d)* to *(f)* CR=20 °C s^{-1}, and *(g)* air cooled. Contour levels: 1, 2, 3, 4, 5, 6, 7, 8, 9, 10.

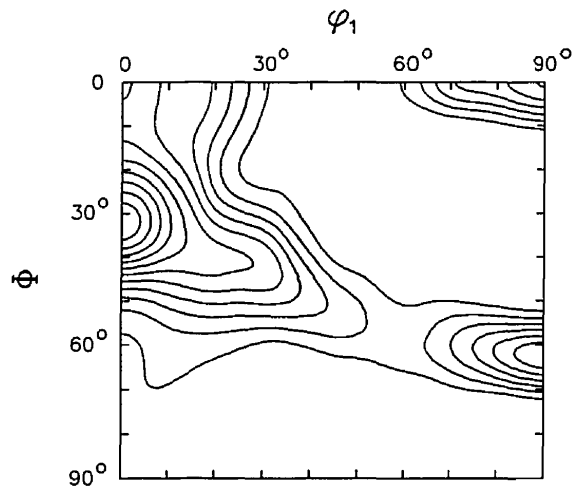

Max : 11.8

(a) CIT=620°C

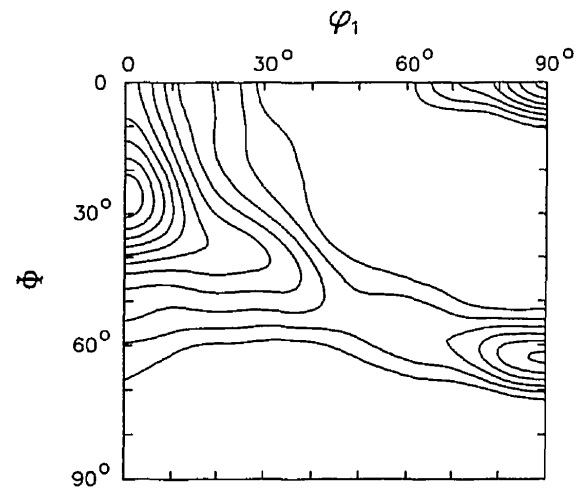

Max : 11.7

(b) CIT=520°C

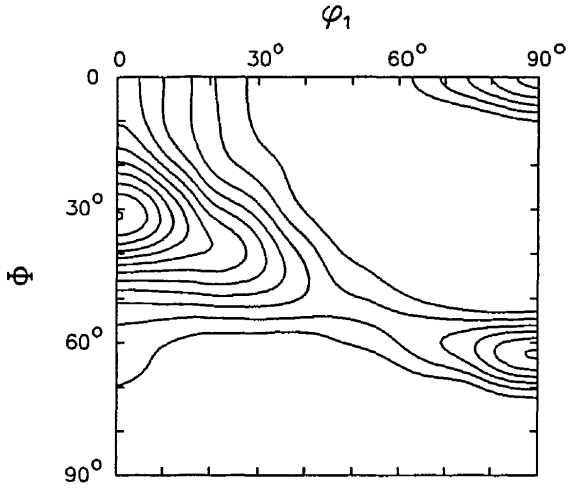

Max : 12.0

(c) CIT=420°C

Figure 5.10 $\varphi_2 = 45°$ ODF sections of the X-80 plates reheated at **1150 °C** and finish rolled at **690 °C**; *(a)* to *(c)* CR=40 °C s^{-1},

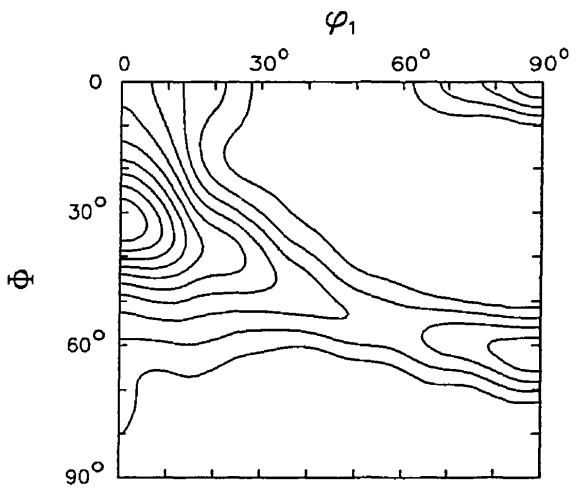

Max : 10.9

(d) CIT=620°C

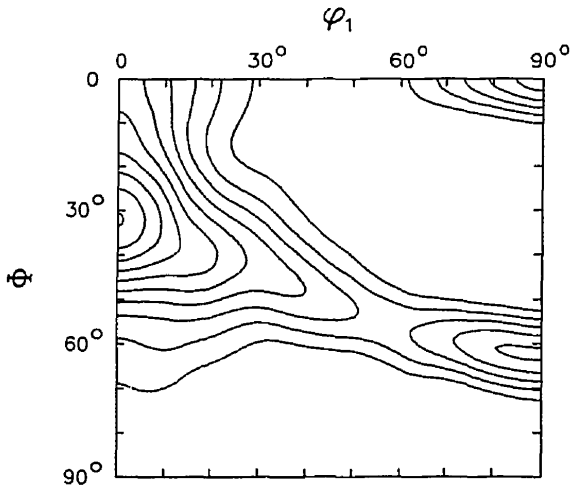

Max : 10.1

(e) CIT=520°C

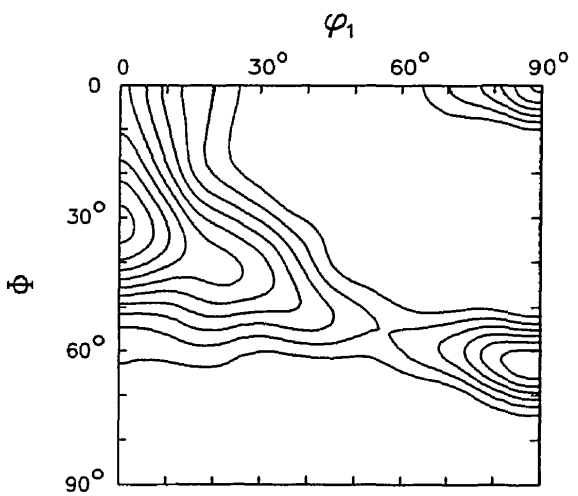

Max : 10.3

(f) CIT=420°C

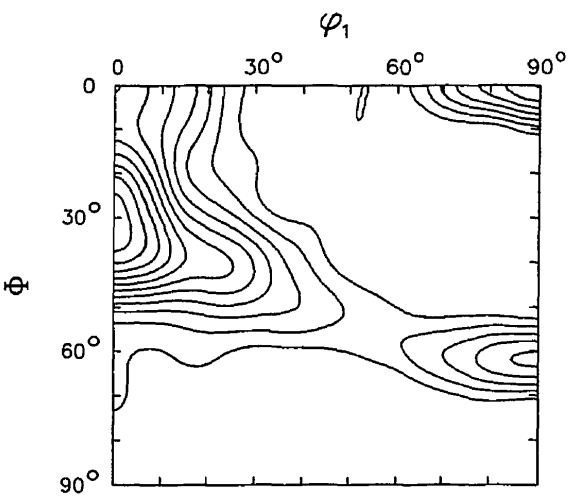

Max : 11.6

(g) Air Cooled

Figure 5.10 (continued) *(d)* to *(f)* CR=20 °C s^{-1}, and *(g)* air cooled. Contour levels: 1, 2, 3, 4, 5, 6, 7, 8, 9, 10.

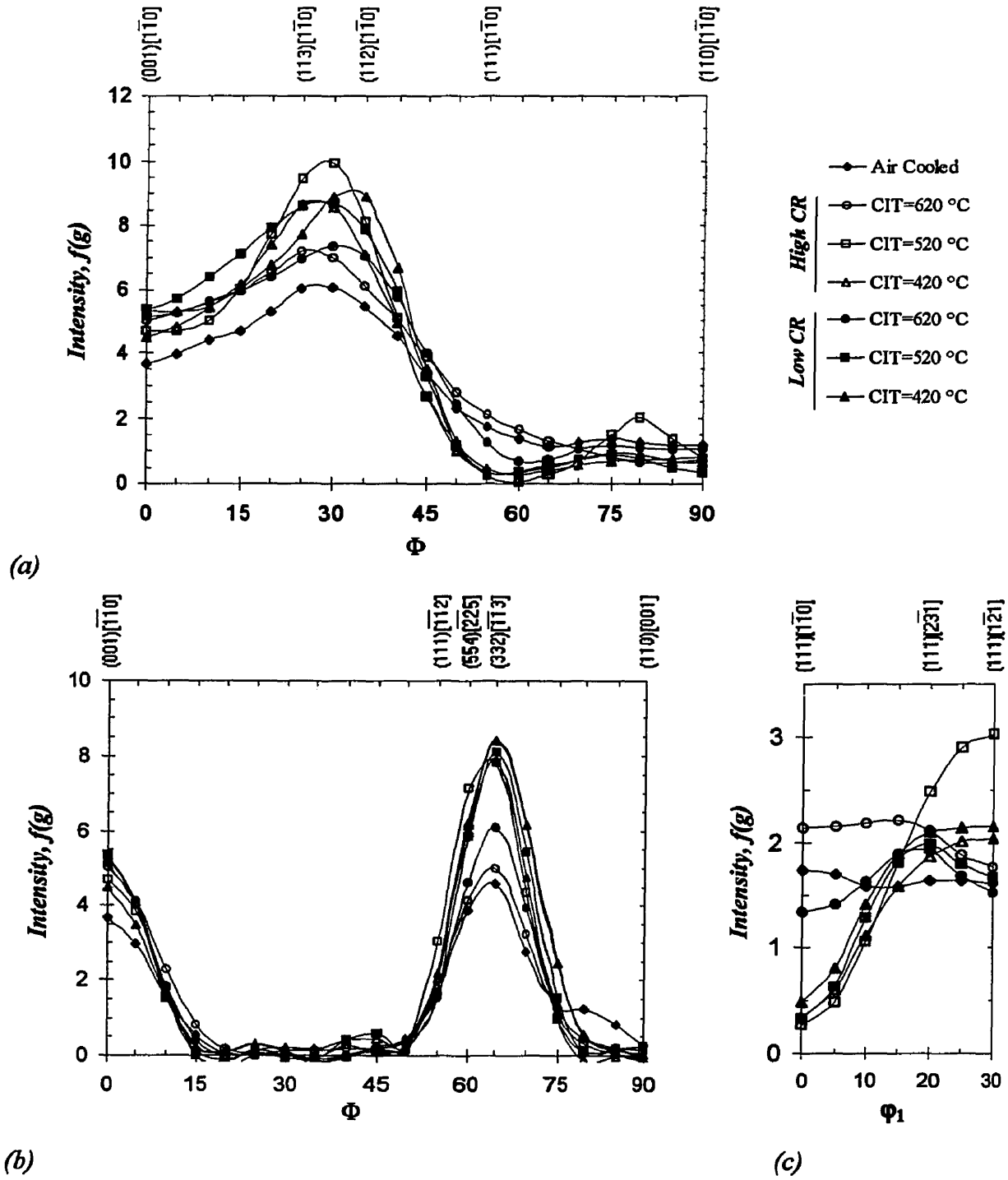

Figure 5.11 Intensity curves of the *(a)* RD, *(b)* TD, and *(c)* ND fibres for the X-80 plates reheated at 1275 °C; and finish rolled at 780 °C.

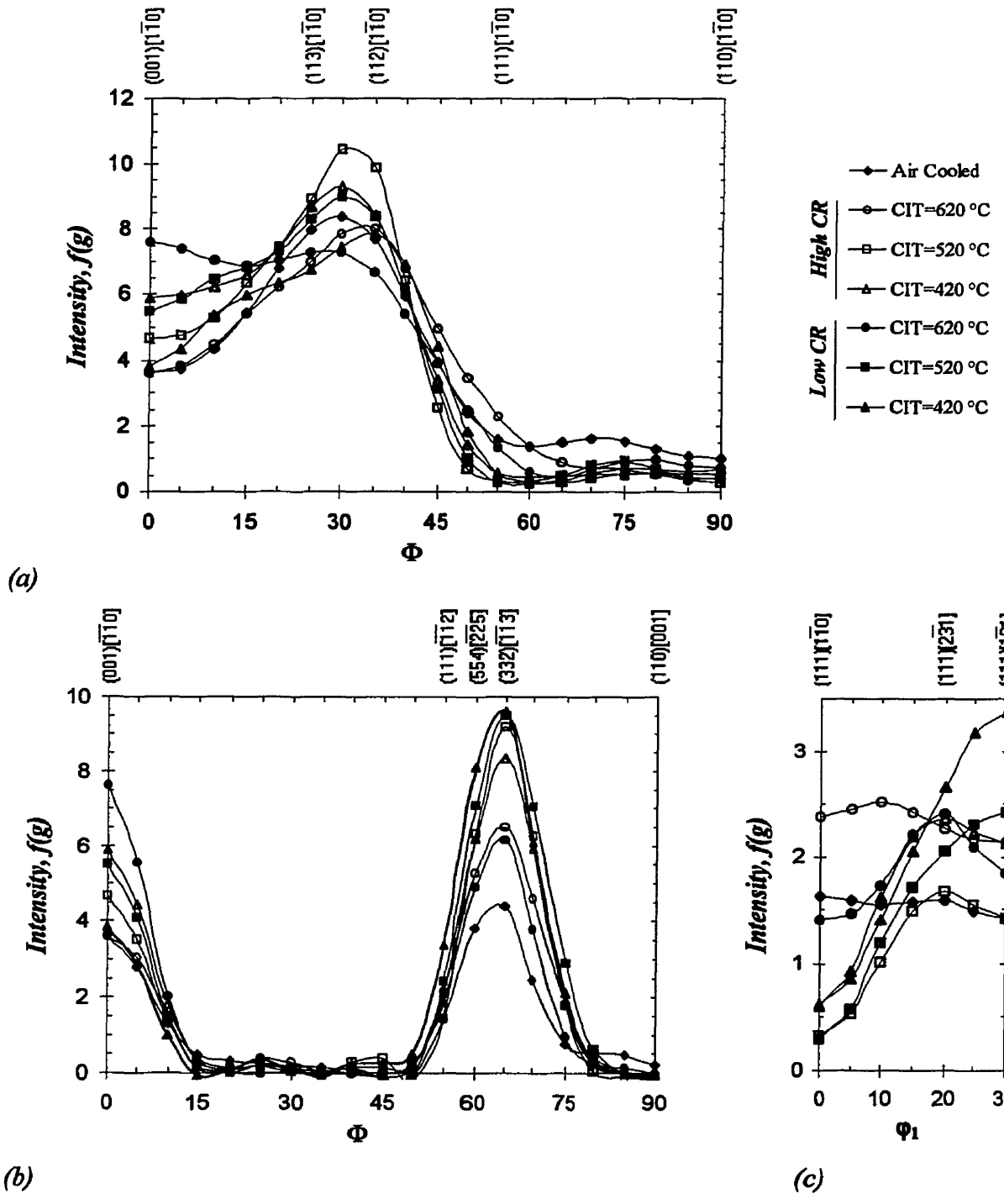

Figure 5.12 Intensity curves of the *(a)* RD, *(b)* TD, and *(c)* ND fibres for the X-80 plates reheated at **1150 °C**; and finish rolled at **780 °C**.

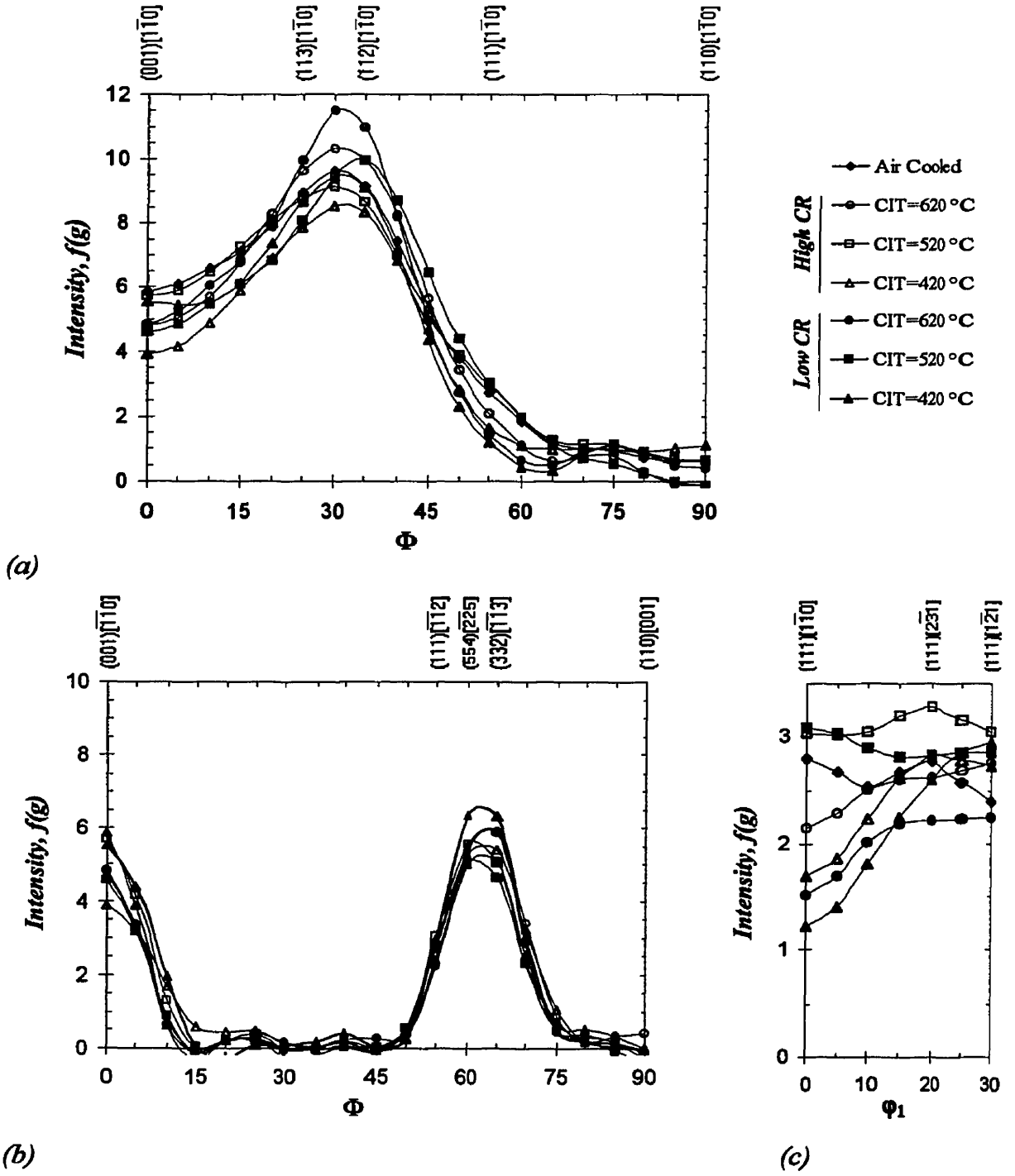

Figure 5.13 Intensity curves of the *(a)* RD, *(b)* TD, and *(c)* ND fibres for the X-80 plates reheated at **1275 °C**; and finish rolled at **690 °C**.

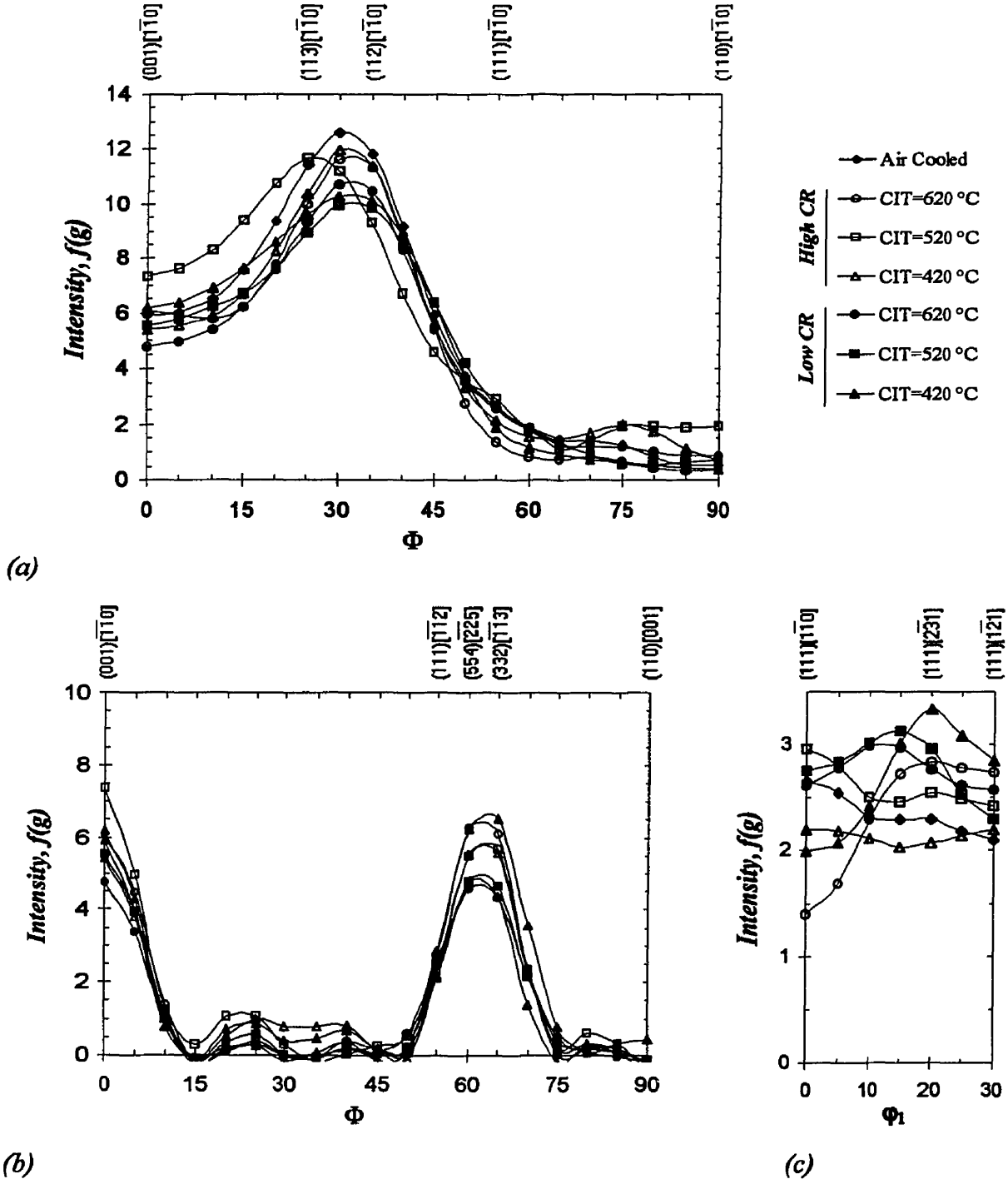

Figure 5.14 Intensity curves of the *(a)* RD, *(b)* TD, and *(c)* ND fibres for the X-80 plates reheated at **1150 °C**; and finish rolled at **690 °C**.

particular of the cooling interruption temperature, on the distribution of the fibers of the transformation texture.

In the samples finish rolled below the A_{r3}, Figs. 5.9, 5.10, 5.13, and 5.14, the textures are sharper than in the corresponding cases in Figs. 5.7 and 5.8, where a higher finish rolling temperature was employed. However, sharpening of the texture mainly involves the high density RD fibers developed under these conditions and here the TD fibre is less intense than in the high FRT samples. It can also be seen that the intensities of the ND fibre components are increased to 3 in these samples. Accelerated cooling again results in the trend described for the high FRT samples, where the {111}<112> is sharpened at the expense of the {111}<110>.

It is of interest to note that in the samples finish rolled in the intercritical region, Figs. 5.9, 5.10, 5.13, and 5.14, air cooling results in a high RD fibre intensity. In the case of the low reheat temperature, it is evident that this is even higher than the peak intensity of the RD fibre in some rapidly cooled plates, Fig. 5.12. This simply implies that the RD fibre texture components are more influenced by the pancaking strain of the austenite before transformation than by the cooling conditions during transformation. This issue will be discussed in greater detail in the Discussion section.

5.3 Discussion

In this section, the relations between the characteristics of the austenite before the transformation and the ferrite texture, which is influenced by the cooling conditions during the transformation, are analyzed and discussed.

5.3.1 Texture Index

To represent the texture without considering the details of the distribution of the orientations, the integral of the square of the texture function was calculated using *eq.* (5.2) [3, 130], which was obtained by substitution of the series expansion for *f(g)* in *eq.* (5.1). This value, *J*, is known as the texture index.

$$J = \int [f(g)]^2 dg \tag{5.1}$$

$$J = \sum_{l,\mu,\upsilon} \frac{1}{2l+1} \left| C_l^{\mu\upsilon} \right|^2 \tag{5.2}$$

The texture index permits characterization of the severity of the texture by a single parameter, which is also considered to be a good measure of how the orientations of the transformed grains differ from a random distribution. In Figs. 5.15 to 5.17, the texture indices calculated for the X-70 and X-80 samples are illustrated for all processing conditions.

In the low niobium steel (X-70), the use of a low finishing temperature led to a decrease in the texture index. This can be due to the lower pancaking strain applied to the austenite before transformation, Table 4.5. It can also be observed that accelerated cooling

increased the severity of the texture, which is certainly due to variant selection during the transformation.

In the X-80 plates, generally, the texture indices of the low FRT samples are higher than those of the high FRT plates, which means that sharper textures developed in the samples finish rolled in the two phase region. Accelerated cooling of the high FRT samples, however, led to increases in the texture indices, whereas in the low FRT plates, the texture indices of the rapidly cooled samples are lower than in the corresponding air cooled sample.

It has been shown by numerous workers [21, 128, 130, 131] that the greater the pancaking strain applied to the austenite, the sharper is the texture developed in the ferrite. As was shown in the previous chapter, greater pancaking strains were applied to the austenite in the low FRT samples than in the high FRT ones. This certainly justifies the high texture indices of the low FRT air cooled plates.

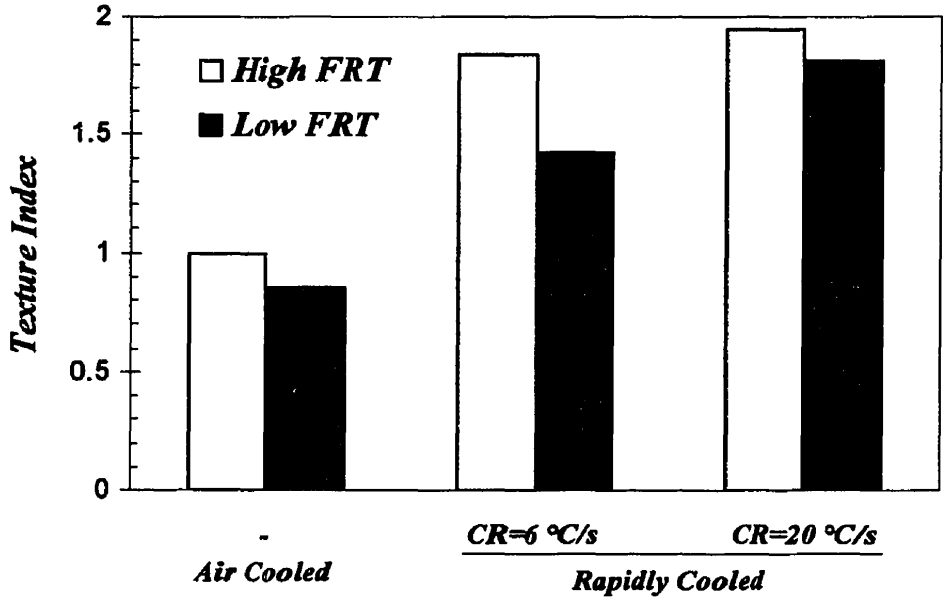

Figure 5.15 Texture indices of the X-70 steel.

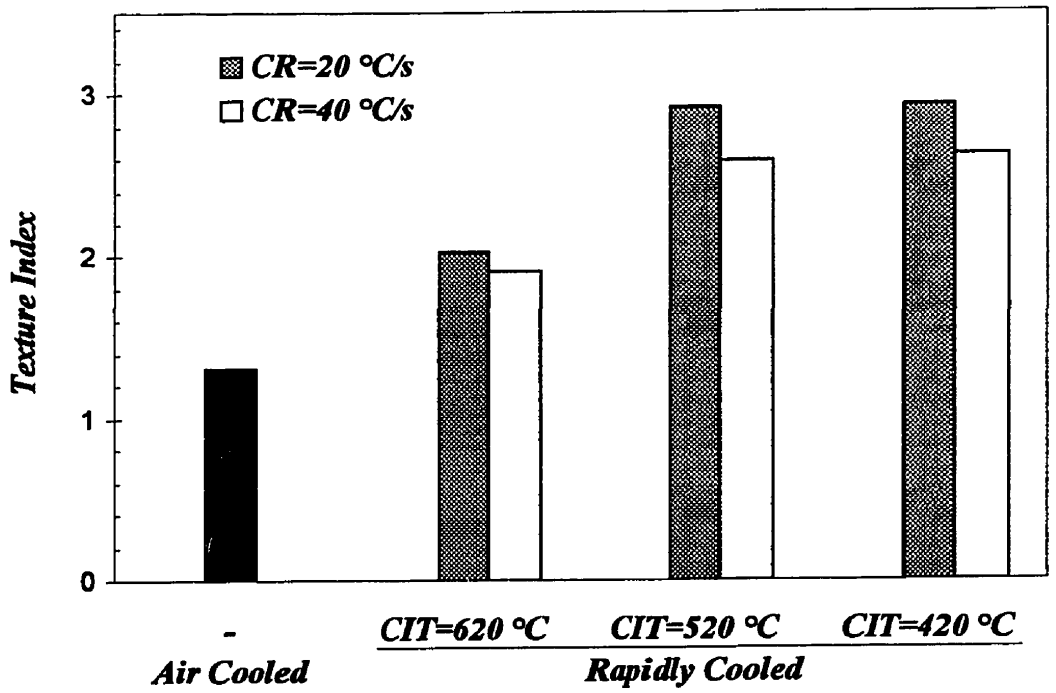

(a)

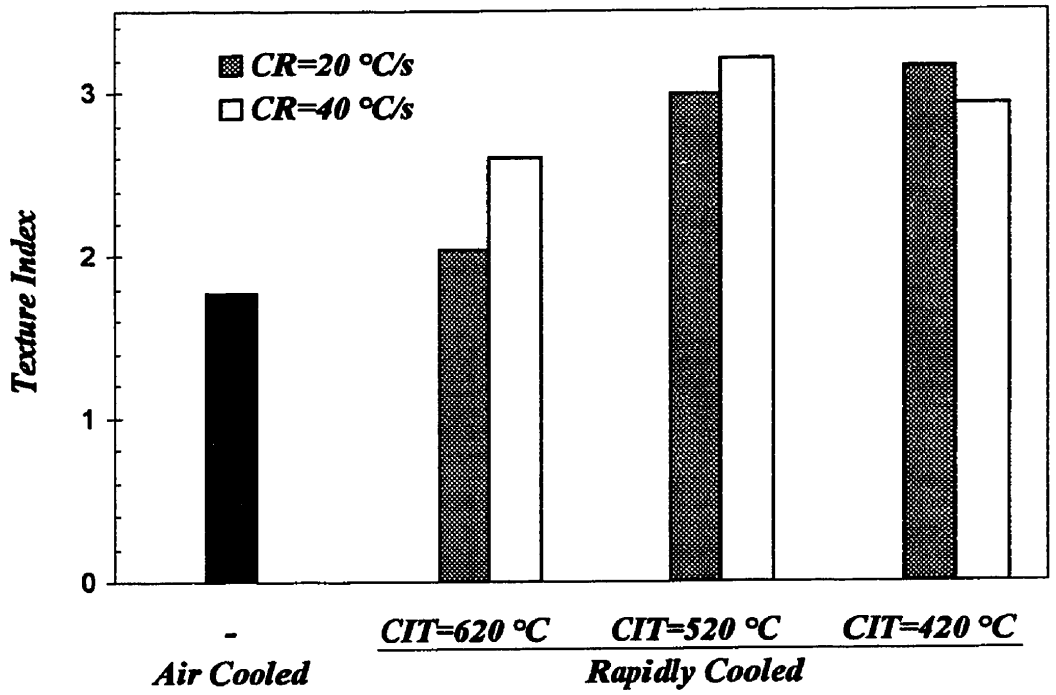

(b)

Figure 5.16 Texture indices of the X-80 steels finish rolled *above* the Ar_3; *(a)* RT=1275 °C and *(b)* RT=1150 °C.

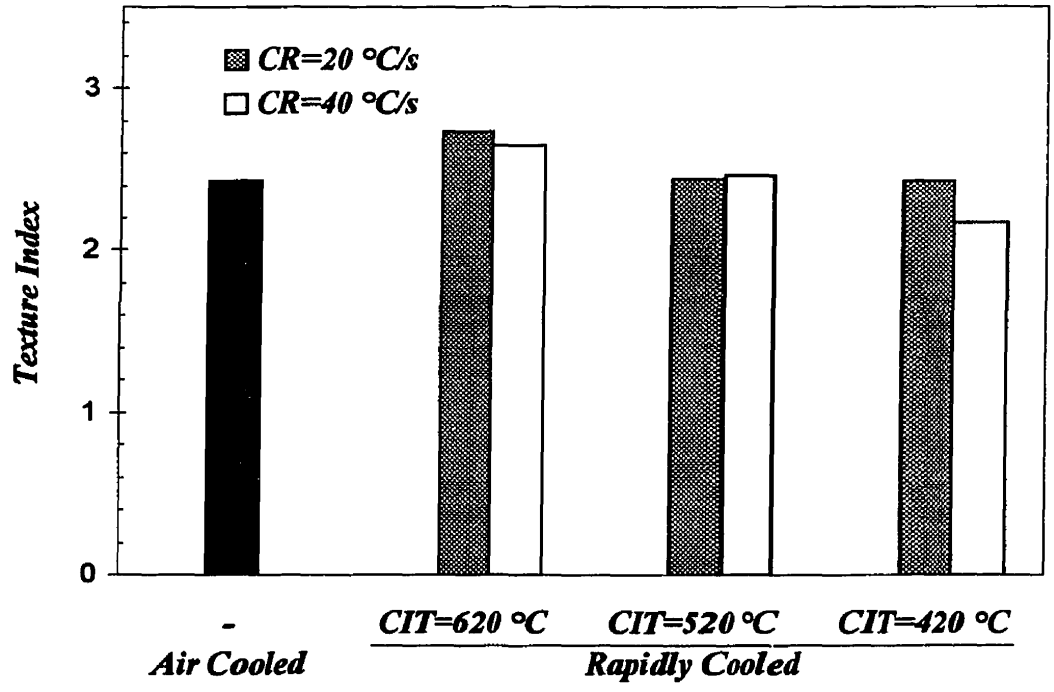

(a)

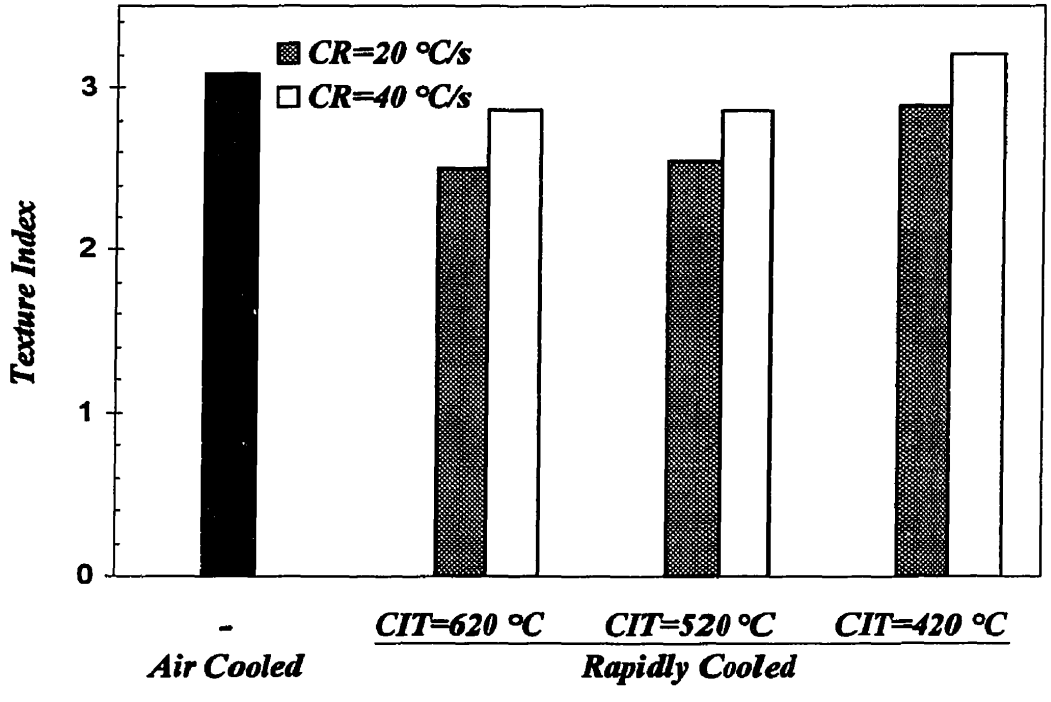

(b)

Figure 5.17 Texture indices of the X-80 steels finish rolled *below* the Ar_3; *(a)* RT=1275 °C and *(b)* RT=1150 °C.

However, the plates associated with the low reheat temperature develop sharper textures than those reheated at the high temperature, although the pancaking strain was either equal (for the high FRT plates) or even lower than the corresponding high RT samples, Table 4.5. Since the amount of pancaking strain applied to the ferrite was the same for the low FRT samples with different reheat temperatures, this increase in the sharpness of the texture cannot be because of ferrite rolling. On the other hand, the same trend is observed in the samples finish rolled above the Ar_3 without any ferrite rolling. Therefore, the main cause of this difference is likely to be the general characteristics of the austenite (e.g. finer grain size) before the transformation.

The characteristics of the austenite include its grain size as well as the amount of pancaking strain applied below the T_{nr}. As discussed in the previous chapter, an equation for the effective interfacial area of the austenite, S_V, developed by Ouchi [91], can be used to take into consideration the grain size of the austenite together with the pancaking strain, ε_P. The amount of shear banding is also considered in the S_V parameter, *eq.* 4.12. Fig. 5.18 illustrates the change in S_V according to the amount of reduction (or pancaking strain) applied below the T_{nr} for all the austenite grain sizes developed under the controlled rolling conditions employed in this work.

This parameter accounts for the severity of the austenite texture before transformation as well as for the fineness of the grain size. In this way, it allows for the effect of grain boundaries on sharpening the rolling texture of pancaked austenite. In cold rolled ferrite, such effects are influenced by the shapes, sizes, and orientations of the neighboring grains [57, 133]. Inagaki, for example, showed that grain boundary constraints play larger roles in fine grained specimens and lead to larger orientation changes in the grain boundary regions [133].

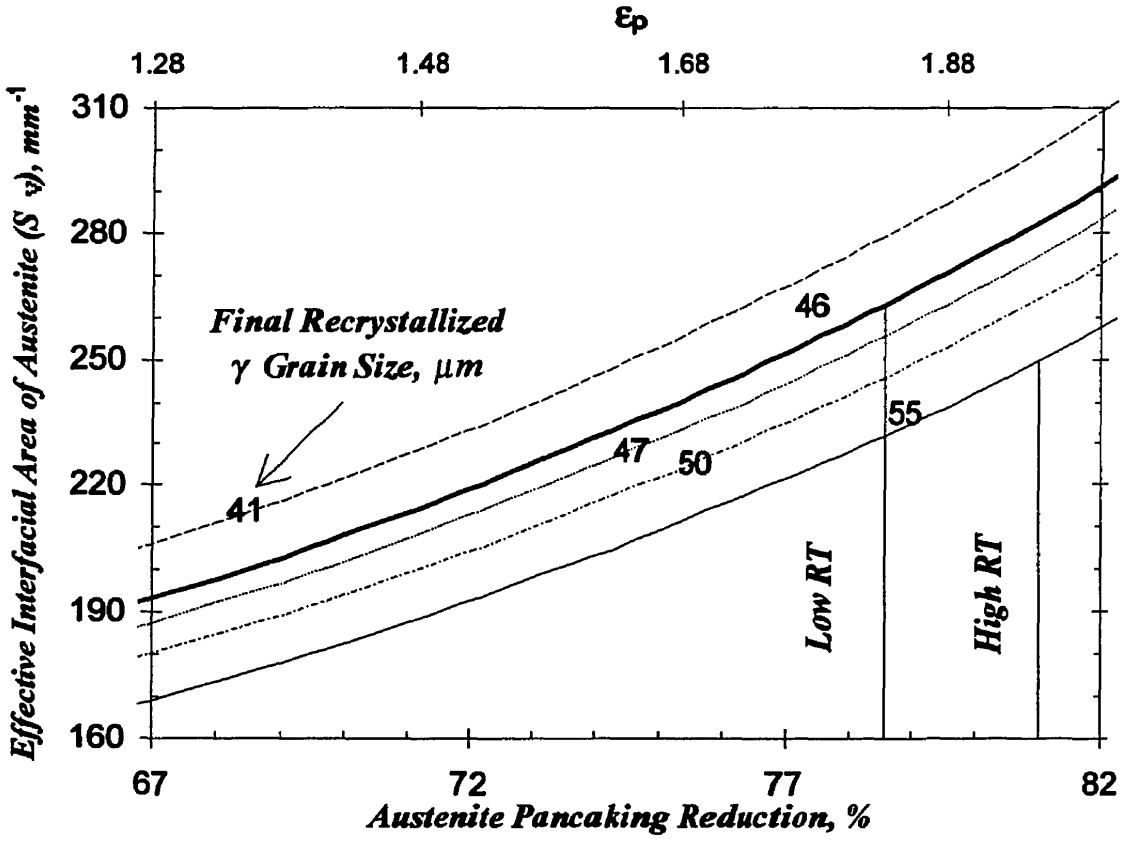

Figure 5.18 Effective interfacial area versus the amount of pancaking reduction applied to the austenite.

The S_V parameter is a useful predictor of the transformation texture in two ways; *i*) it can forecast the sharpness of the austenite texture, and *ii*) it gives a measure of the slip distribution and of the number of active slip systems. While the former involves the intensity of the texture, the latter is concerned with the possibility of nucleation on the austenite slip systems [37, 132].

The S_V parameter and pancaking strain of the austenite are plotted against the texture index for comparable air cooled and rapidly cooled X-70 and X-80 plates in Figs. 5.19a and 5.19b, respectively. It can be seen that, for both the air cooled and rapidly cooled samples, the severity of the texture increases with the S_V parameter, Fig. 5.19b, whereas there is no direct relation between the pancaking strain and the texture index, Fig. 5.19a.

In the low niobium steel, the texture indices of the air cooled and rapidly cooled samples finish rolled below the Ar_3 are lower because of the associated lower S_V parameter. In fact, the sharp textures of the samples processed with high FRT's can be attributed to the sharpnesses of the austenite texture before transformation (i.e. high values of S_V). This effect is not overcome by the texture sharpening due to ferrite rolling, which increases the hardness of the low FRT samples, Fig. 4.16.

In the X-80 steels, it is apparent that higher S_V values in the low RT samples account for the high texture indices of these samples compared to the high RT samples. This cannot be explained in terms of the effect of pancaking strain alone because, as can be seen in Fig. 5.19a, the pancaking strains of the X-80 samples finish rolled above the Ar_3 were equal for high and low RT's. For the samples finish rolled below the Ar_3, again sharper textures were developed in the low RT samples, in comparison with those associated with high RT's in spite of the lower pancaking strains. As can be seen in Fig. 5.19b, here also the higher texture indices of the low RT samples can be attributed to the higher values of the S_V parameter in contrast with the values applicable to the high RT plates.

It is of interest to note that the small increase in the texture index of the rapidly cooled X-80 sample reheated at 1150 °C and finish rolled above the Ar_3 can be attributed to the higher cooling interruption temperature of 650 °C (see Table 3.7) instead of 620 °C.

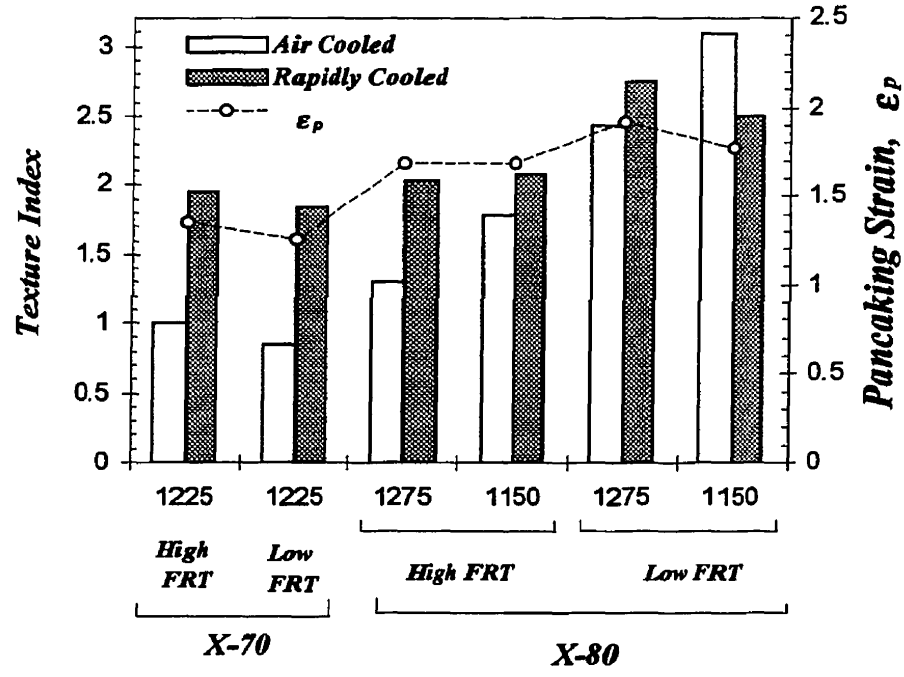

(a)

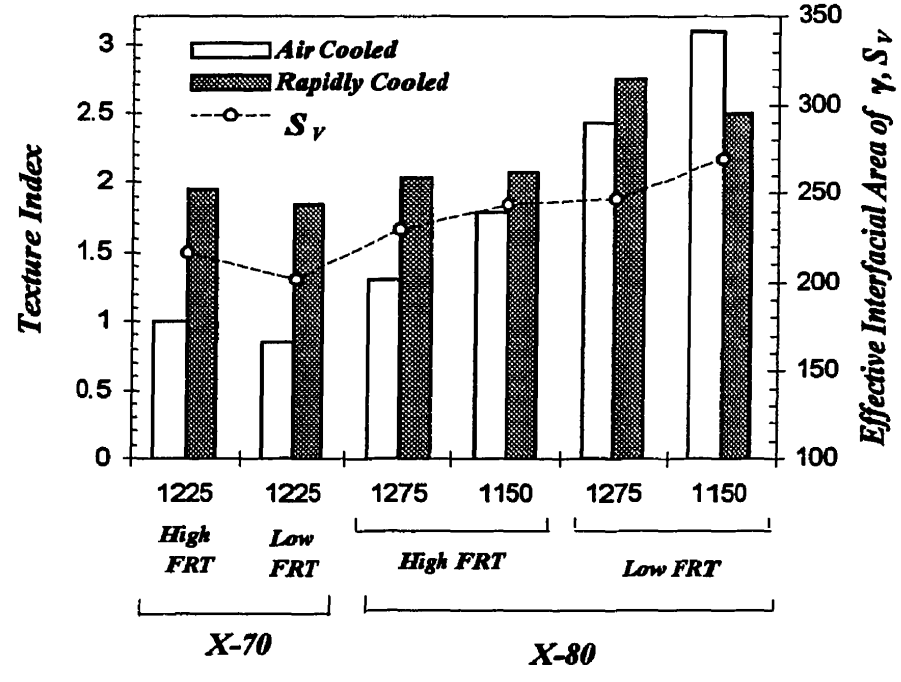

(b)

Figure 5.19 *(a)* Pancaking strain of the austenite and *(b)* S_V parameter versus the texture index in the X-70 and X-80 plates. Accelerated cooling was performed at a CR= 20 °C s^{-1} and CIT= 620 °C.

Similarly, the low texture index of the rapidly cooled X-80 sample reheated at 1150 °C and finish rolled below the A_{r3} is probably due to its low cooling rate of 9 °C s^{-1}, Table 3.7.

It can be seen from Fig. 5.19b that the difference between the sharpnesses of the air cooled and rapidly cooled samples decreases when the S_V parameter increases. This is probably because of the changing relative influence of the pancaking strain and the grain size. This will be further discussed in the next section.

5.3.2 Transformation Texture

Here, the effects of the processing conditions on the three distinct fibres (i.e. the RD, TD, and ND fibres) are discussed by carrying out a more detailed analysis of the transformation textures.

5.3.2.1 Effect of Chemical Composition of the Steels

The intensities of the three ideal fibers in the X-70 and X-80 steels are compared to each other in Figs. 5.20 and 5.21. It is evident that in all cases the RD and TD fibres are more intense in the X-80 plates than in the X-70's. This is consistent with the findings of many other investigators [21, 130, 131] who have shown that the addition of Nb sharpens the texture in microalloyed steels by increasing the intensity of the RD fibre.

As was shown in the previous chapter, the higher niobium content of the X-80 steel increased the T_{nr} by about 40 degrees Centigrade compared to that in the X-70. Since similar rolling schedules were employed for both steels, Table 3.5, the increase in the T_{nr} led to higher pancaking strains for the X-80 samples before transformation. Comparison of the final recrystallized austenite grain sizes in the two steels, Table 4.5, indicates that the S_V parameter is greater in the higher niobium steel. This can, in turn, sharpen the transformation texture either directly by increasing the sharpness of the austenite texture or indirectly by increasing the extent of slip on the active slip systems. This will be taken up again in the section on variant selection below.

The TD fibre intensities of the X-80 plates are also higher than those of the X-70s when they are air cooled. This may again be because of the sharpening effect on the austenite texture of the increased pancaking strain and the higher value of S_V. Inagaki [22] reported that higher Mn levels in samples with the same parent rolling texture before

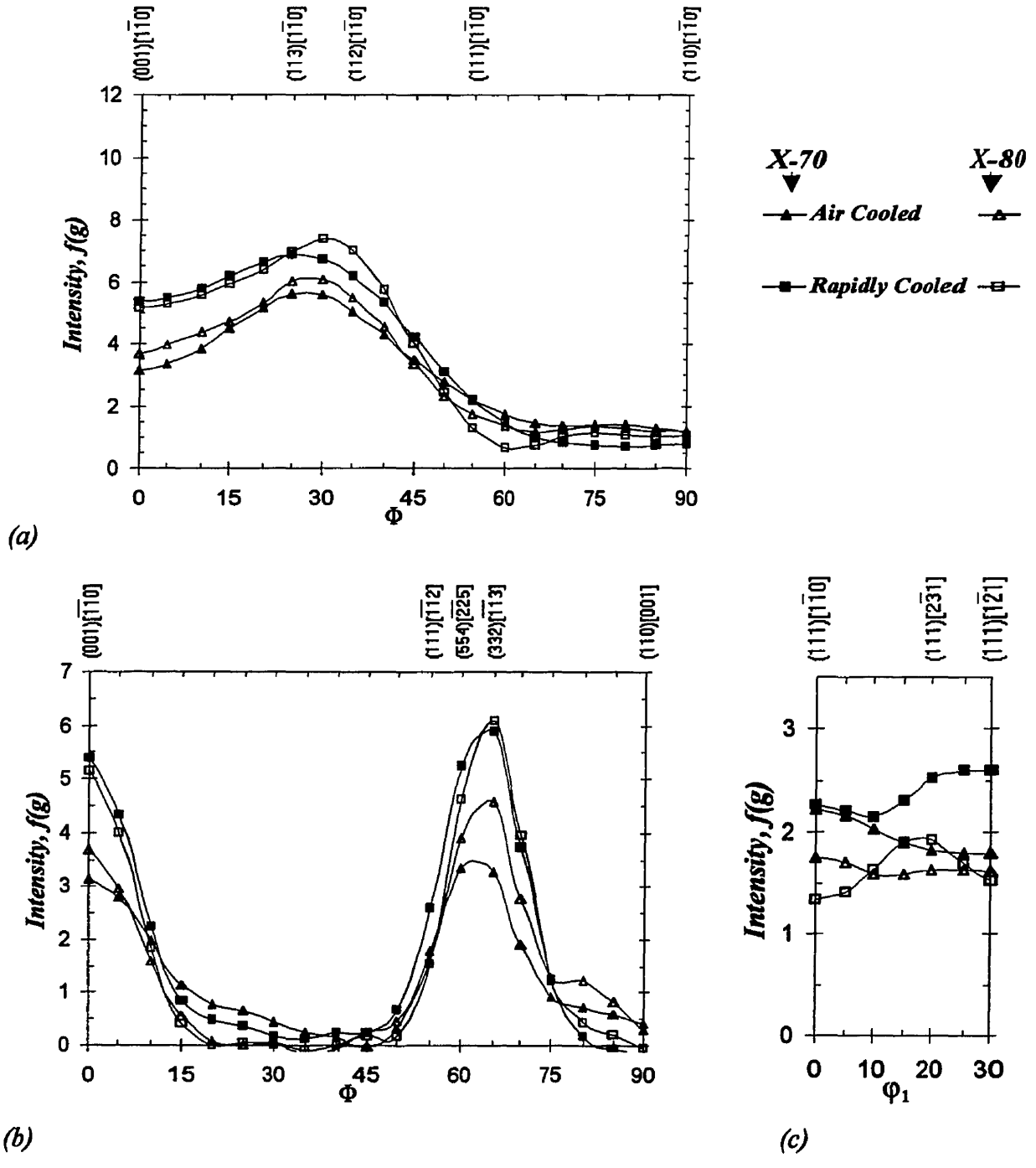

Figure 5.20 Comparison between the *(a)* RD, *(b)* TD, and *(c)* ND fibres of the X-70 and X-80 samples finish rolled *above* the Ar_3. Accelerated cooling was interrupted at 620 °C after cooling at 20 °C s^{-1}.

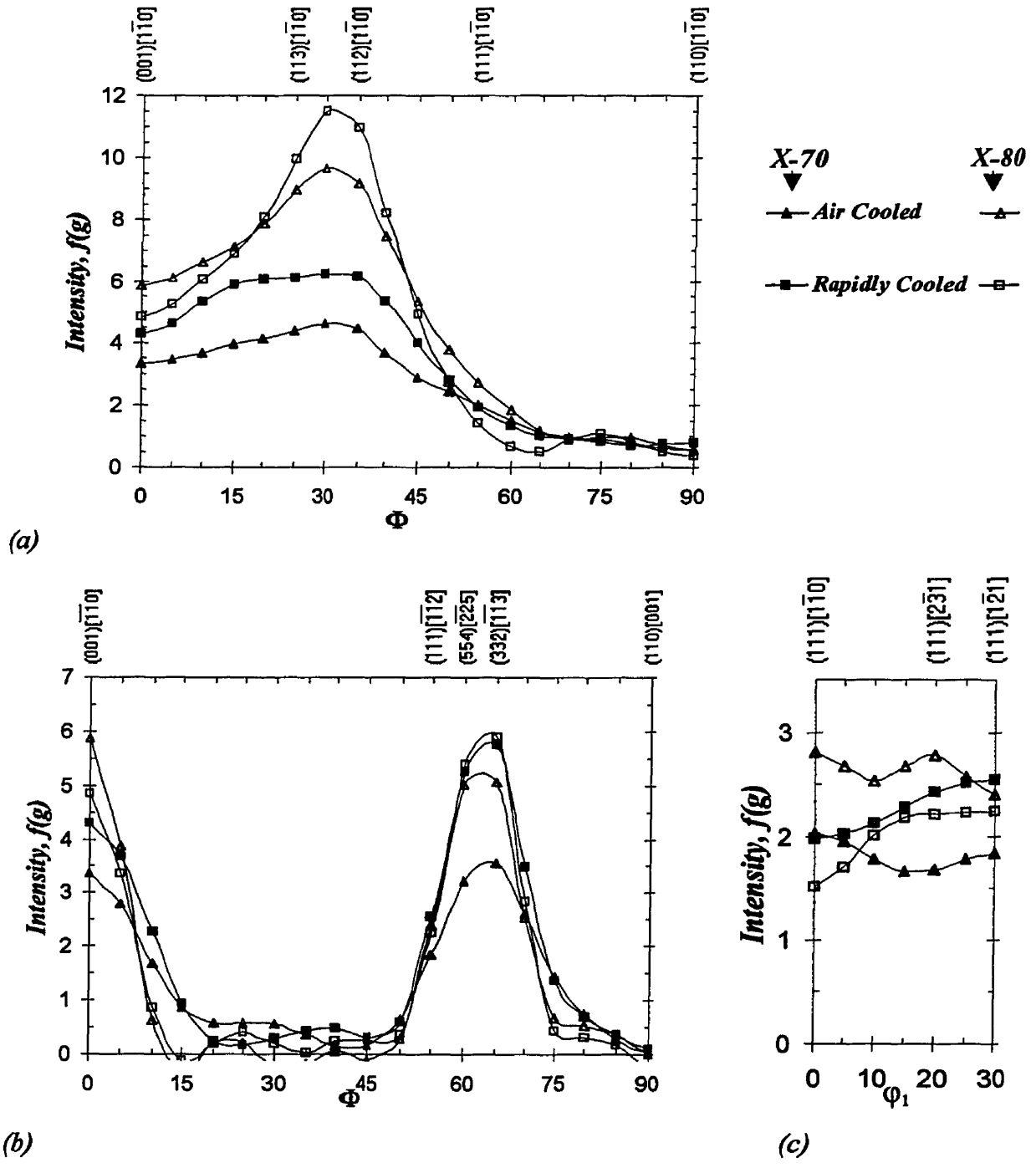

Figure 5.21 Comparison between the *(a)* RD, *(b)* TD, and *(c)* ND fibres of the X-70 and X-80 samples finish rolled *below* the Ar_3. Accelerated cooling was interrupted at 620 °C after cooling at 20 °C s^{-1}.

transformation also increased the intensity of the TD fibre. This was attributed to the occurrence of selective growth in the high Mn steel at the low transformation temperature that resulted from the austenite stabilizing effect of Mn. Such an effect is similar to that of cooling rate in decreasing the transformation temperature and, therefore, in limiting the growth of nuclei.

It can be seen from Figs. 5.20 (b) and 5.21 (b) that accelerated cooling led to the same intensities of the TD fibre in both steels when they were finish rolled above the Ar_3. This clearly implies that the cooling conditions (or the dislocation density) have a greater effect on the TD fibre than the state of the austenite at the transformation, so that it can compensate for the intensity differences between the air cooled samples. In fact, the higher intensity of the TD fibre in the X-80 air cooled sample is more likely to be due to the austenite stabilizing effect of Mn or even Nb and selective growth, as was concluded by Inagaki [22].

It is known that the TD fibre components are formed exclusively from the fcc brass component, i.e. the {110}<112>. Table 4.5 shows that there was a relatively large difference (1.68 versus 1.35) between the pancaking strains applied to the X-80 and X-70 steels when they were finish rolled above the Ar_3. This difference was even higher (1.91 in the X-80 versus 1.25 in the X-70) for samples finish rolled below the Ar_3. Nevertheless, the intensity of the TD fibre was almost the same in the two samples. It can therefore be concluded that the intensity of the brass component was approximately the same in the two steels before transformation, despite the differences in the amount of pancaking strain.

5.3.2.2 Effect of Thermomechanical Processing Parameters

The RD, TD, and ND fibres of the air cooled X-80 samples finish rolled above and below the Ar_3 are illustrated in Fig. 5.22.

RD fibre

In the skeleton diagram of Fig. 5.22 (a), the same texture index trends shown in Fig. 5.19 are observed. That is, the greater the value of S_V, the higher the intensity of the RD fibre. This is probably associated with an increase in the intensity of the copper ({112}<111>) component of the fcc texture before transformation.

Jonas et al. [38] considered the grain aspect ratio of the pancaked grains as a measure of the possibility of growth along the rolling direction as opposed to the TD or ND directions. However, as described in the previous section, the S_V parameter, in which the grain size of the austenite is also taken into consideration can explain all the features of the experimental textures. For instance, the intensity of the RD fibre in the air cooled sample finish rolled below the Ar_3 and reheated at the higher temperature is lower than that of the corresponding sample with the lower reheat temperature, Fig. 5.22, even though its grain aspect ratio (or the pancaking strain applied to the austenite) is greater, Fig. 5.19a.

By contrast, Figs. 5.18 and 5.19a show that, despite the high grain aspect ratio in this sample, the S_V parameter is smaller due to the larger recrystallized austenite grain size. The same explanation pertains to the samples finish rolled above the Ar_3, where the intensity of the RD fibre is higher in the low RT samples, despite the equal grain aspect ratios.

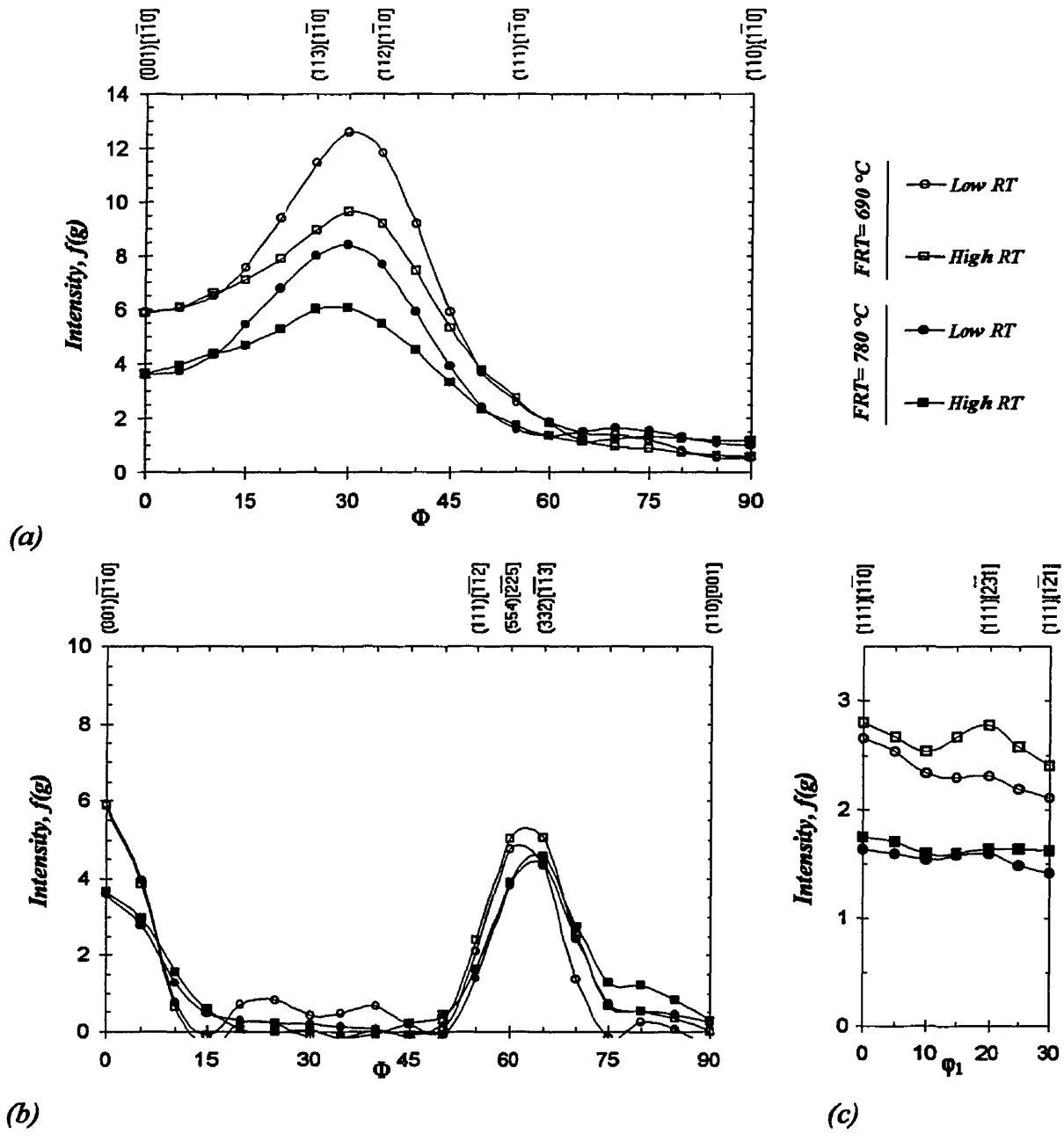

Figure 5.22 *(a)* RD, *(b)* TD, and *(c)* ND fibres in the air cooled X-80 plates.

TD fibre

Small differences between the peak intensities of the TD fibres in samples finish rolled above and below the Ar_3 are evident in Fig. 5.22 (b). This indicates that the TD fibre is much less influenced by the pancaking strain or the S_V parameter. On the other hand, the higher intensity of the {554}<225> component in samples associated with the low FRT implies that the increase in the sharpness of the TD fibre is probably due to ferrite rolling, which has been shown to increase the intensity of this component by rotation of the {332}<113> component towards the {554}<225> and {111}<112> [23, 58].

ND fibre

The ND fibre is more intense in samples finish rolled below the Ar_3, Fig. 5.22 (c). Although this is certainly because of the increase in the sharpness of the austenite textures prior to transformation, it is also partly influenced by the use of ferrite rolling.

5.3.2.2.1 Effect of Cooling Rate and Cooling Interruption Temperature

The three fibres for the samples rapidly cooled at 20 °C s^{-1} and then subjected to interrupted cooling at 620 °C, 520 °C, and 420 °C are plotted in Figs. 5.23 through 5.25. The equivalent fibres for the samples cooled at 40 °C s^{-1} are illustrated in Figs 5.26 to 5.29.

RD fibre

Comparison of Figs. 5.23a, 5.24a, and 5.25a with Fig. 5.22a shows that, generally, accelerated cooling decreased the intensities of the RD fibres in the low FRT samples, whereas it increased the sharpnesses of the RD fibres of the high FRT plates. Samples rapidly cooled at 40 °C s^{-1} display the same trend, Fig. 5.26 to 5.28. The differences between the RD fibre intensities were small despite appreciable differences in the austenite morphologies before transformation. These small differences decreased still further when

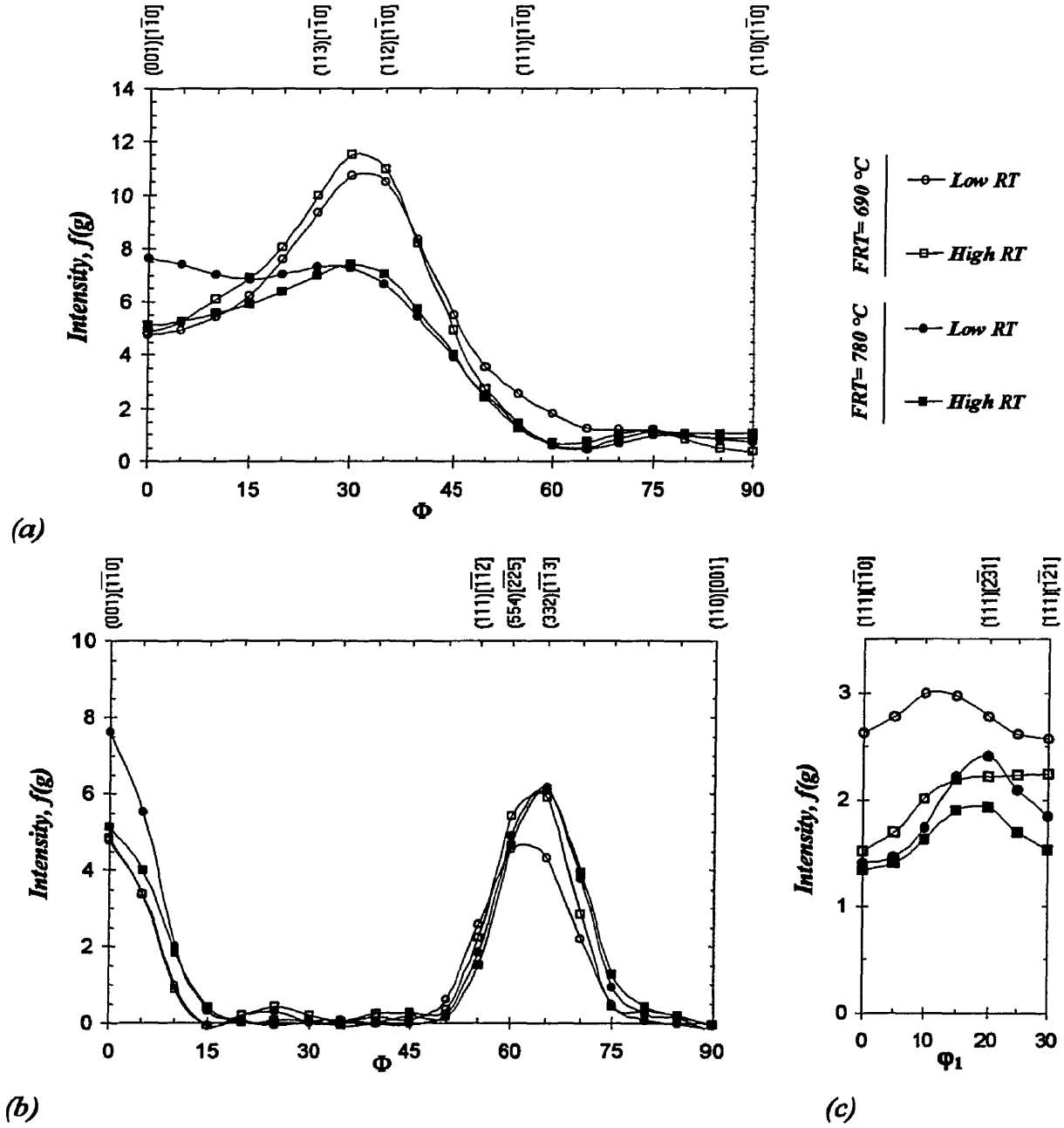

Figure 5.23 *(a)* RD, *(b)* TD, and *(c)* ND fibres in the rapidly cooled X-80 plates; CR= 20 °C s^{-1} and CIT= 620 °C.

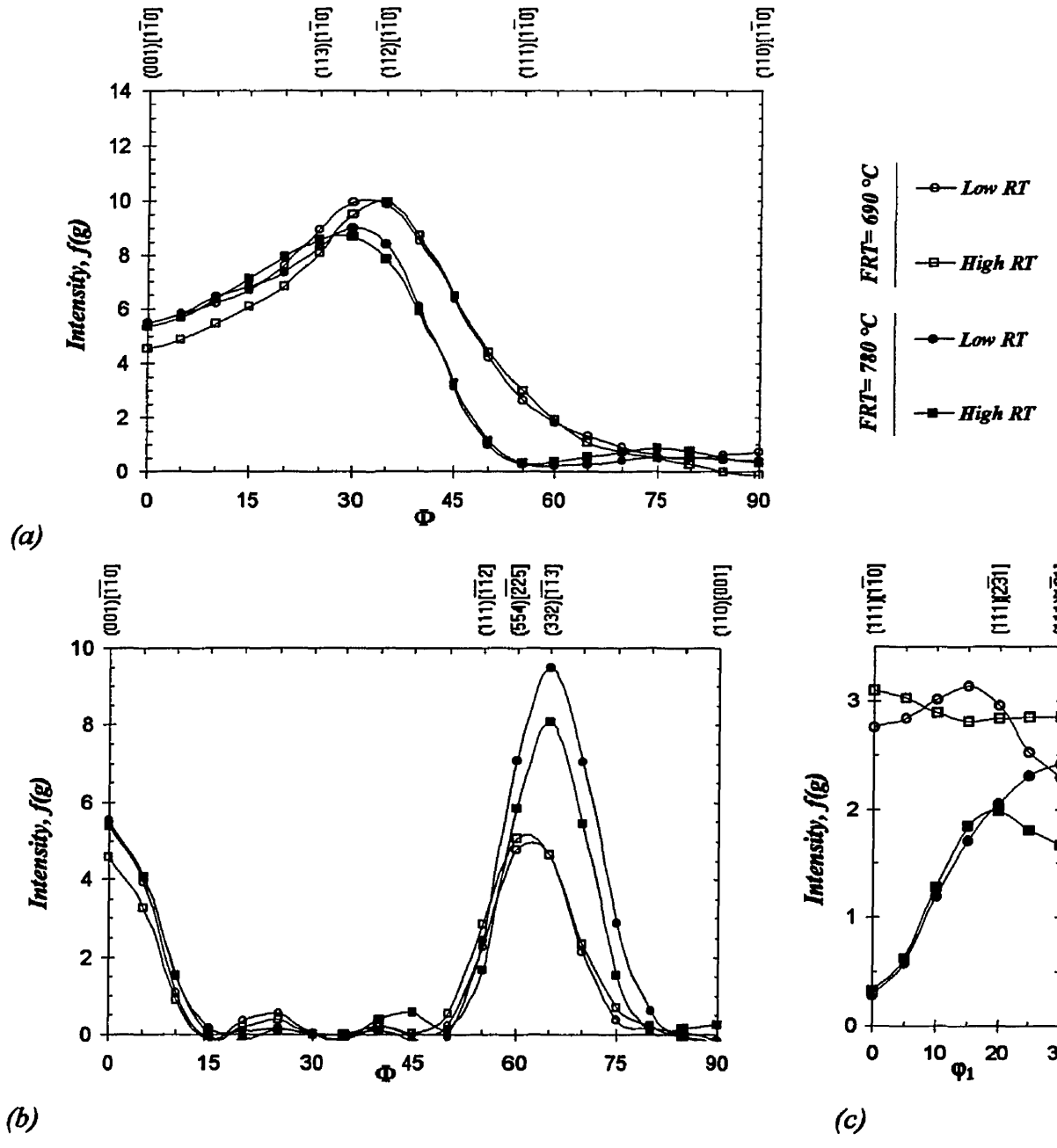

Figure 5.24 *(a)* RD, *(b)* TD, and *(c)* ND fibres in the rapidly cooled X-80 plates; CR= 20 °C s^{-1} and CIT= 520 °C.

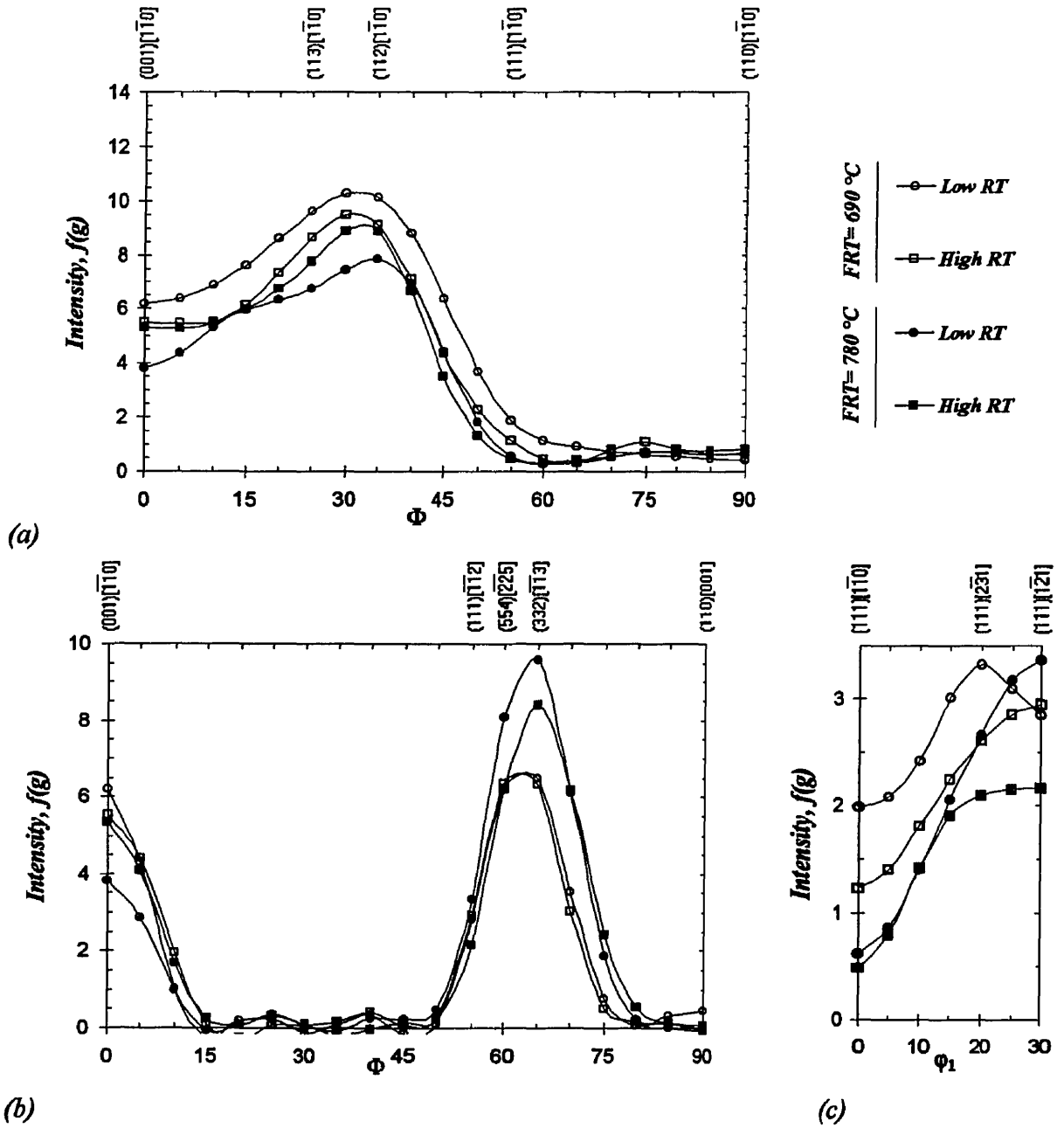

Figure 5.25 *(a)* RD, *(b)* TD, and *(c)* ND fibres in the rapidly cooled X-80 plates; CR= 20 °C s^{-1} and CIT= 420 °C.

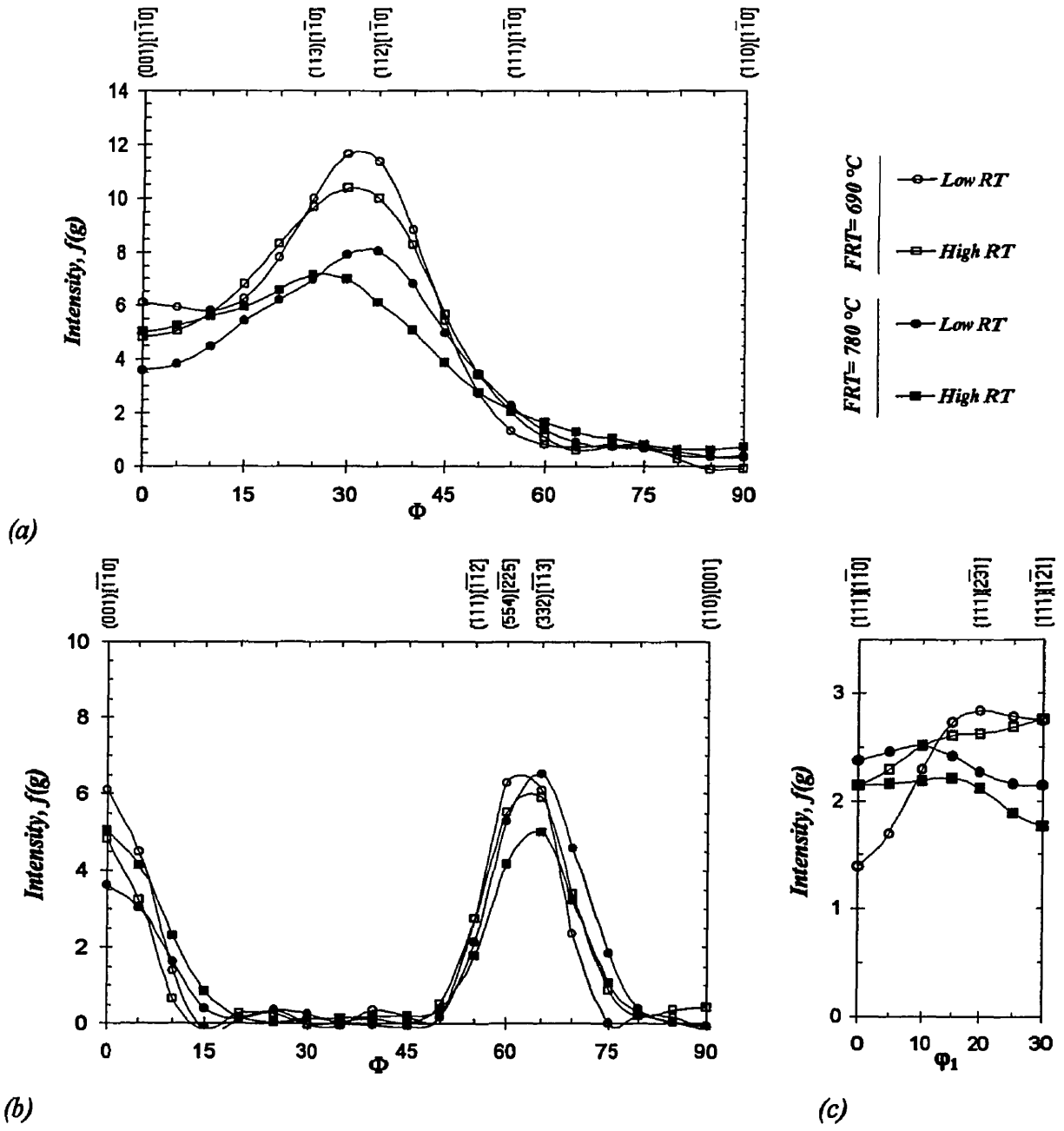

Figure 5.26 *(a)* RD, *(b)* TD, and *(c)* ND fibres in the rapidly cooled X-80 plates; CR= 40 °C s^{-1} and CIT= 620 °C.

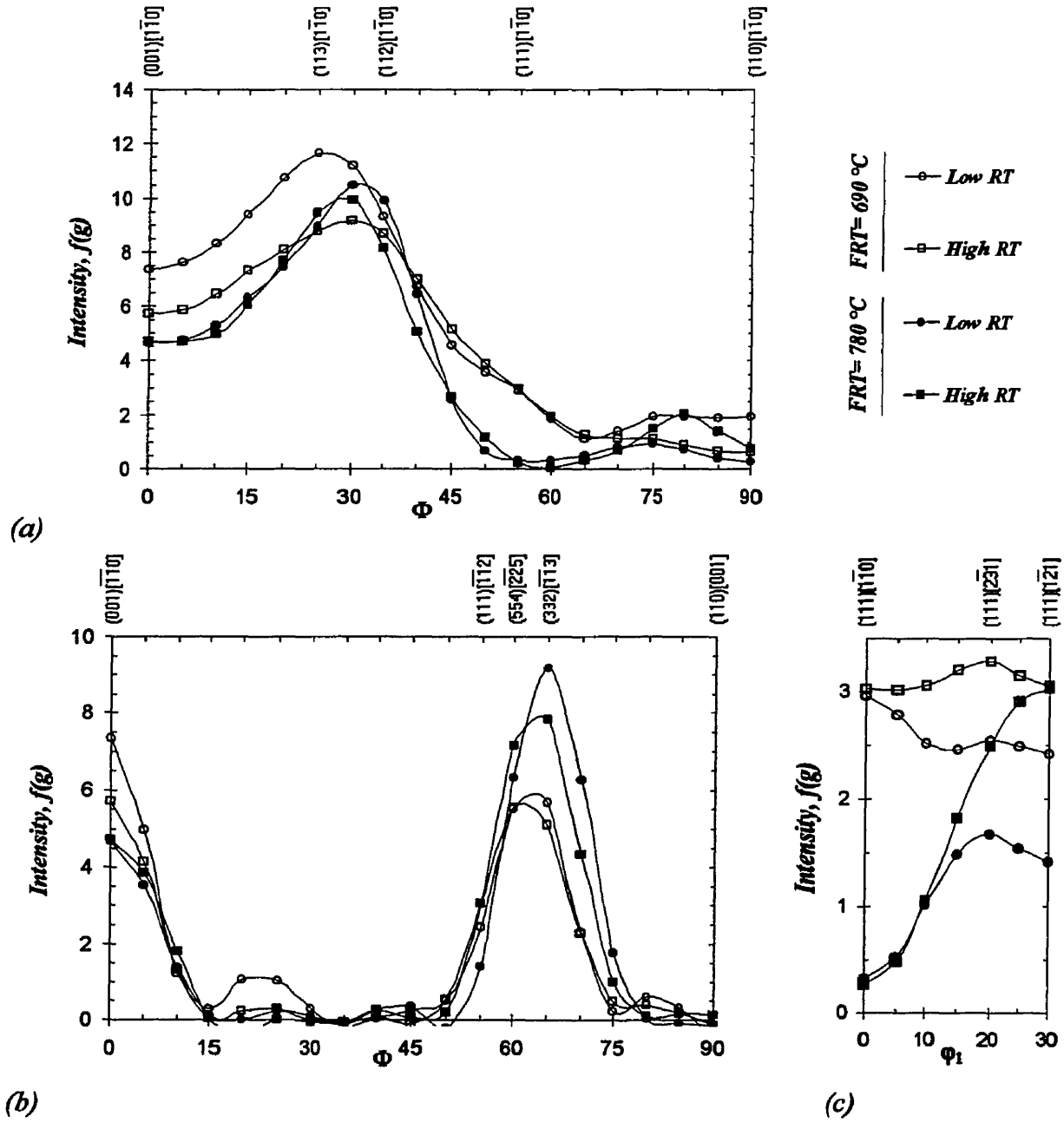

Figure 5.27 *(a)* RD, *(b)* TD, and *(c)* ND fibres in the rapidly cooled X-80 plates; CR= 40 °C s^{-1} and CIT= 520 °C.

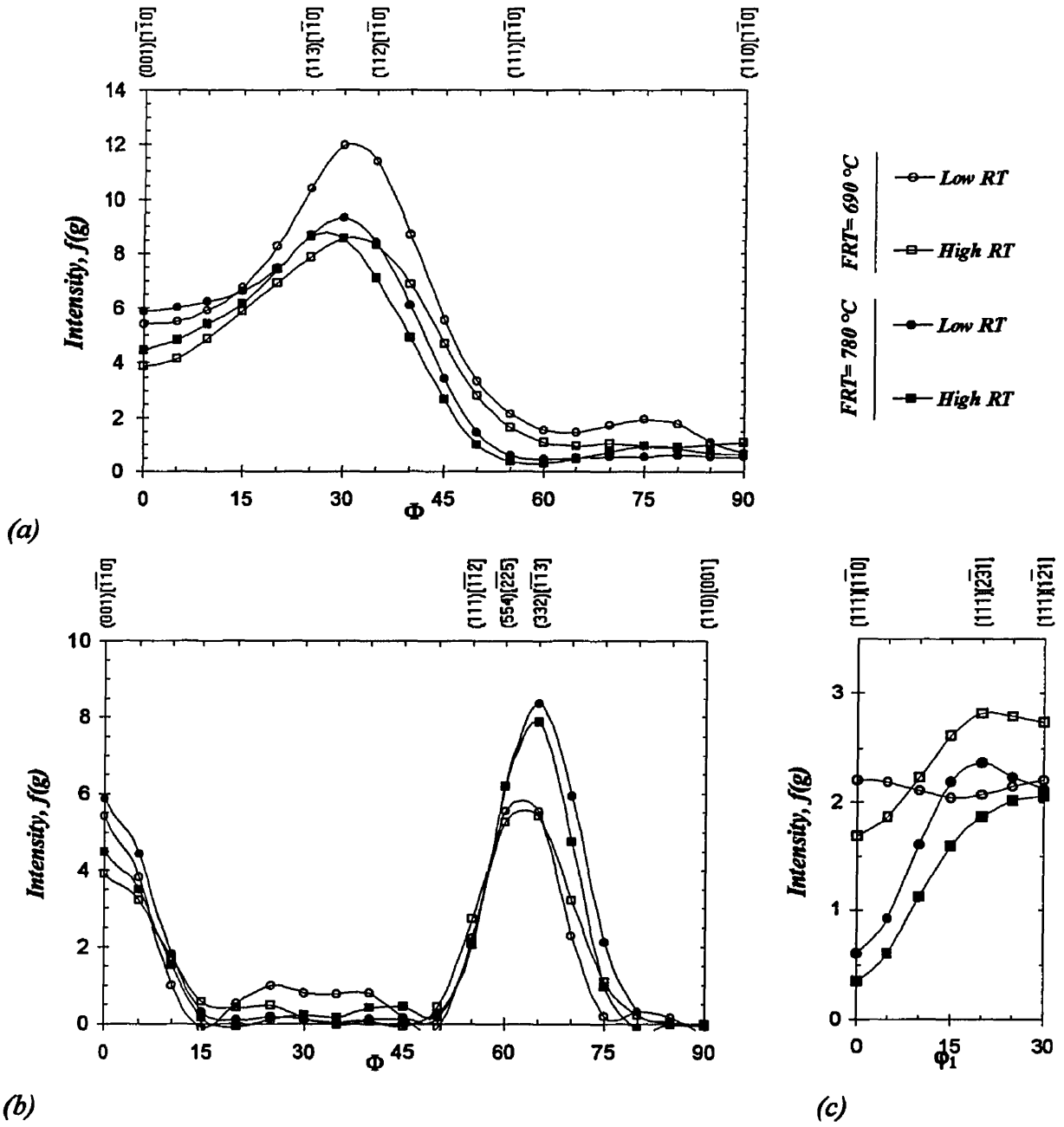

Figure 5.28 *(a)* RD, *(b)* TD, and *(c)* ND fibres in the rapidly cooled X-80 plates; CR= 40 °C s^{-1} and CIT= 420 °C.

the lower cooling interruption temperatures were employed. This indicates that the nucleation rate of the product phase during transformation is influenced to a greater extent by the amount of supercooling than by the morphology of the austenite.

Fig. 5.23a provides very good evidence for the effect of the cooling conditions on the RD fibre. The intensity of the low FRT sample reheated at the lower temperature is less than that of the one reheated at the higher temperature. This is opposite to the behaviour of the air cooled samples displayed in Fig. 5.22. This can be explained in terms of the lower cooling rate (9 °C s^{-1}) of the low RT sample and the higher cooling rate (28 °C s^{-1}) of the high RT sample even though they both had the same nominal cooling rate of 20 °C s^{-1}.

It should be noted that the particularly high intensity of the {100}<110> orientation in the sample associated with a high FRT and a low RT in Fig. 5.23a may have been caused by the unusually high cooling interruption temperature of 650 °C in this case.

The sample associated with the high FRT and low RT in Fig. 5.25a displays a low RD fibre intensity. This may have been caused by the unusually low cooling interruption temperature of 390 °C, see Table 3.7. The higher intensities of the RD fibre in the low RT and low FRT samples, Figs. 5.27a and 5.28a, can again be attributed to their higher cooling interruption temperatures of 550 °C and 445 °C, respectively, Table 3.9.

These observations indicate that the cooling conditions, i.e. cooling rate and cooling interruption temperature, have distinct effects on the intensities of the RD fibre components. Because it is difficult to estimate the frequency of heterogeneous nucleation during continuous cooling, this problem is not discussed further here. Nevertheless, the qualitative explanations advanced above seem to account reasonably well for the experimental results. For instance, Figs. 5.24a and 5.27a show that the moderate cooling interruption temperature results in higher RD fibre intensities in the samples finish rolled above the Ar_3.

This can perhaps be explained by the higher nucleation rate that is likely to prevail at a moderate cooling interruption temperature, as was postulated in the previous chapter.

TD fibre

As is evident from the *(b)* diagrams in Figs. 5.23 to 5.28, the intensities of the TD fibres are increased by the accelerated cooling of samples finish rolled in the austenite region. The highest TD fibre intensities are observed at lower cooling interruption temperatures, i.e. at 520 °C and 420 °C, and also in the samples associated with the low reheat temperature. Accelerated cooling decreases the transformation temperature and at the same time retains the high dislocation densities present in deformed materials. Consequently, it can act so as to promote the type of variant selection that is associated with dislocation character and slip activity.

A recent variant selection model has shown that the TD fibre variants that form from the {110}<112> (brass) component are those associated with the most active slip systems during the final stages of pancaking deformation [38, 132, 133]. As discussed in the previous chapter, acicular ferrite forms from austenite by a shear displacive mechanism. Thus, less loss of dislocations by recovery is likely to occur when accelerated cooling is used. This in turn increases the possibility that product grains will be nucleated on the more active slip planes.

It is evident that use of the moderate cooling rate of 20 °C s^{-1} and medium cooling interruption temperature of 520 °C promotes a higher density of the TD fibre, Figs. 5.24b and 5.27b. Again this can be attributed to the possibility that the optimum nucleation rate, which is associated with moderate cooling rates and cooling interruption temperatures, is accompanied by the highest dislocation densities on the slip systems due to less recovery.

When the plates were finish rolled in the intercritical range, the TD fibre intensities increased gradually with cooling rate and with decreasing cooling interruption temperature. This is because almost 20 percent of the transformation had occurred before the beginning of accelerated cooling. Nevertheless, in most cases, the peak intensities along the TD fibres are less than 80 percent of those observed in the high finishing temperature materials. Since there was less than five seconds of delay in initiating accelerated cooling, see Tables 3.6 to 3.9, this cannot be due to the decrease in the volume fraction of austenite before rapid transformation. Instead, it is possible that the high pancaking strains applied to these samples led to a decrease in the volume fraction of the brass component in the austenite before transformation.

ND fibre

Generally, the higher ND fibre intensities developed as a result of ferrite (warm or intercritical) rolling, Fig. 5.22c, are also observed in the case of the rapidly cooled (as opposed to the air cooled) plates. However, accelerated cooling decreases the intensity of the {111}<110>, especially in the samples finish rolled above the Ar_3. This clearly shows that this component is not selected during transformation. This issue will be discussed further in the variant selection section.

5.3.2.3 Transformation Fibre

A continuous orientation spread along the line between {225}<110> and {332}<113> on the φ_2 = 45° ODF section is introduced here and referred to as the *transformation fibre*. This fibre includes the orientations that normally have the highest intensities in the transformation texture.

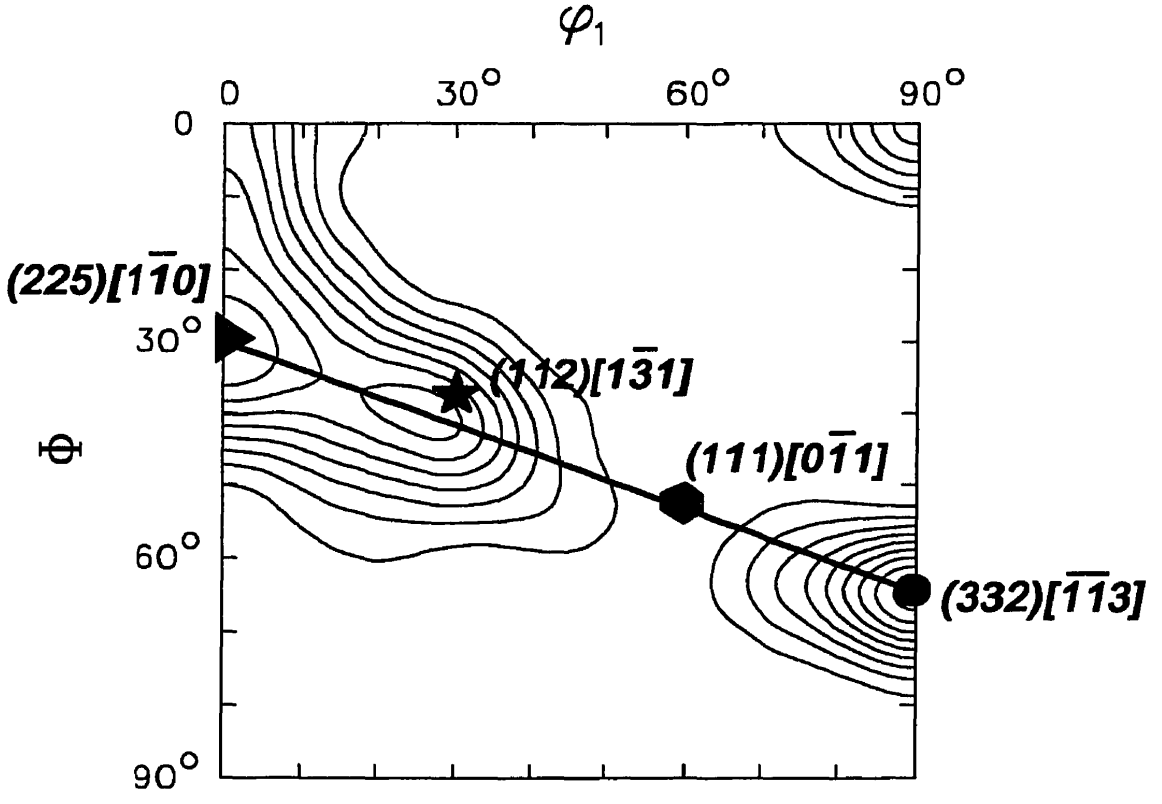

Figure 5.29 Schematic representation of the transformation (TR) fibre in the φ_2 = 45° ODF section showing the ideal orientations along this fibre.

The {225}<110> orientation, which is located between {113}<110> and {112}<110> at $\Phi = 30°$, is an RD fibre component represented in the TR fibre. In most of the ODF's presented in this work, this orientation is located at the peak intensity of the RD fibre. The peak intensity of the TD fibre, i.e. the {332}<113>, also lies on the TR fibre. As was shown in the previous sections, accelerated cooling has a strong effect on the {111}<110> orientation, which is less than 1 degree away from the TR fibre and forms part of the ND fibre.

The exact position of the {112}<131> orientation, which forms from the brass {110}<112> and S {123}<634> fcc components, is nearly 5 degrees away from this fibre. However, as can be seen on Fig. 5.29 (a typical $\varphi_2 = 45°$ ODF section of the rapidly cooled samples in this study), the local peak is located at $\varphi_1 = 30°$ and $\Phi = 42°$ on the TR fibre. Nevertheless, this orientation is generally referred to as (112)[131] because this is the nearest low index orientation.

There is another component ({112}<295>) on the TR fibre at $\varphi_1 = 15°$, $\Phi = 35.26°$, which is generally located on a high intensity plateau. This orientation is also strongly affected by accelerated cooling, as will be discussed in more detail below.

5.3.2.3.1 Effect of Cooling Conditions on the TR Fibre

Cooling Rate

The skeleton lines of the TR fibres in the air cooled and rapidly cooled X-70 and X-80 samples are plotted in Fig. 5.30. The intensities of the (112)[131] in the air cooled samples gradually increased with S_V, as illustrated more generally in Fig. 5.19b. The (225)[110] and (332)[113] also appeared to follow the same trend as S_V. However, the intensity of the (112)[131] increased to about 5 in all samples irrespective of the niobium

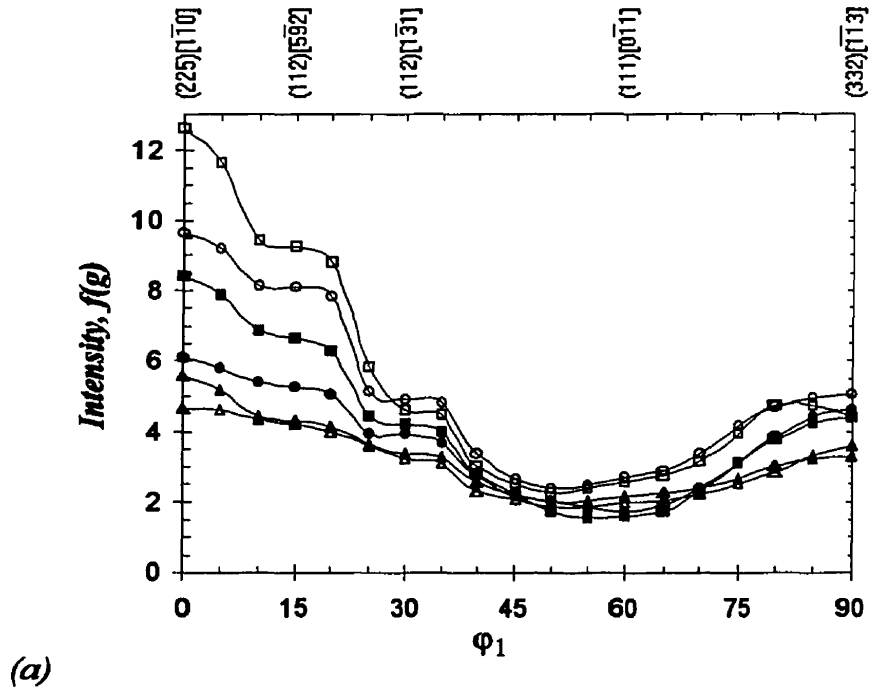

Figure 5.30 Transformation (TR) fibres of the X-70 and X-80 samples; *(a)* air cooled and *(b)* rapidly cooled with CR= 20 °C s^{-1} and CIT= 620 °C.

content and controlled rolling conditions, when they were rapidly cooled. As for the (332)[113], this component is very sensitive to cooling rate and cooling interruption temperature. It can be seen that a cooling rate of 9 instead of 20 °C s^{-1} in the sample associated with the low RT and low FRT led to a decrease in the intensity of the (112)[131] component as well as in that of the (332)[113].

The intensities of some ideal orientations are plotted against S_V in Fig. 5.31. It can be seen in Fig. 5.31a that the intensities of the two RD fibre components {113}<110> and {112}<110> in the air cooled samples increase with S_V. This indicates that the intensity of the copper {112}<111> orientation in the austenite prior to transformation increased with S_V. Thus, given that S_V=265 in this case, the present results reveal that the other fcc orientations rotate towards the copper and the copper-S as the {113}<110> and {112}<110> bcc orientations form mainly from these fcc components.

Rolling texture simulations in fcc materials carried out by Zhou et al. [138] revealed that copper is, in fact, the stable end orientation, Fig. 5.32. These simulations for various boundary conditions, such as full constraints, lath and pancake compression, showed that the intensity of this component increases with the level of strain.

One can therefore imagine that the higher pancaking strains associated with the greater S_V parameter led to increases in the intensities of the copper and copper-S components before transformation. Nevertheless, as the S_V includes both the amount of pancaking strain and the austenite grain size, it can be argued that the finer grain sizes associated with greater S_V values also resulted in sharpening the austenite texture due to more constraining effect of the grain boundaries [133].

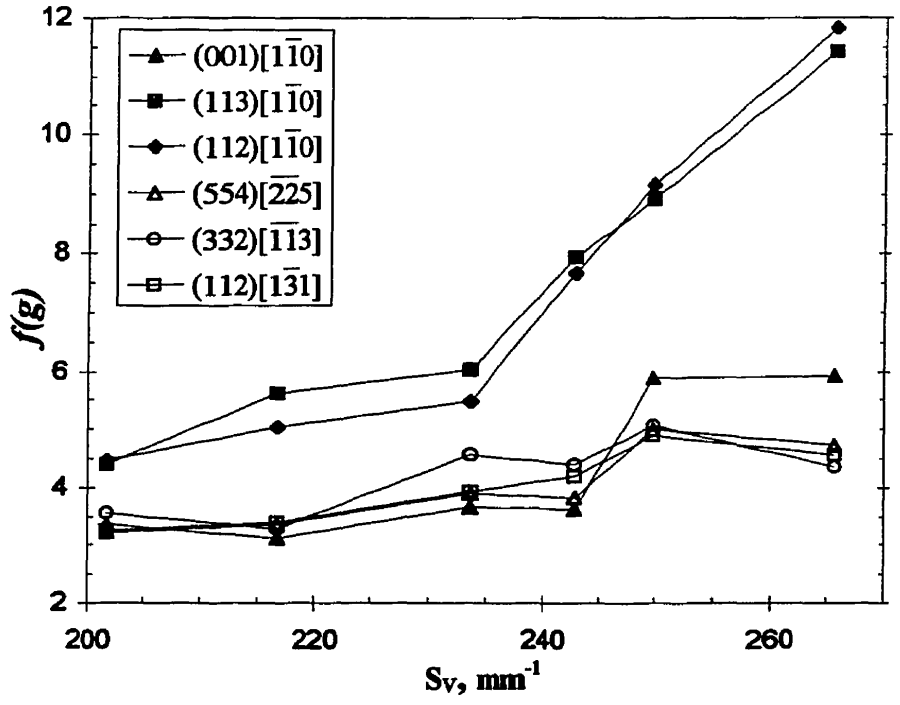

(a)

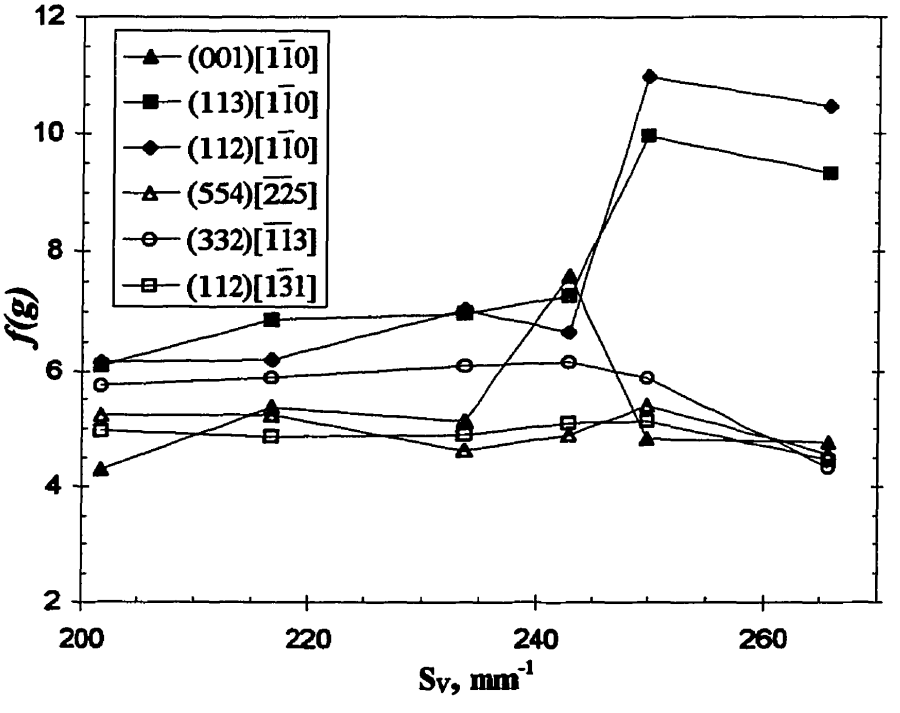

(b)

Figure 5.31 Intensities of the ideal orientations of the ferrite texture versus S_V for *(a)* the air cooled and *(b)* the rapidly cooled samples.

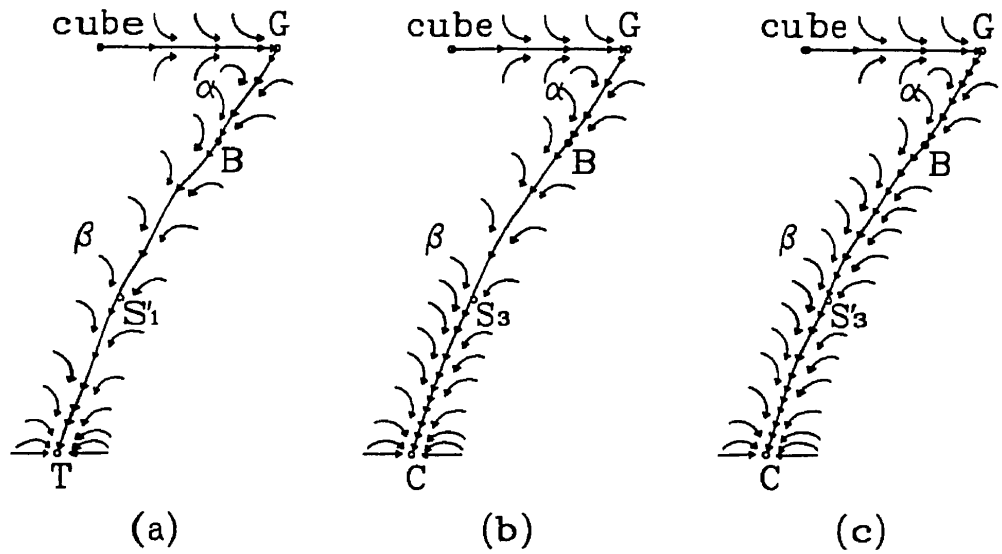

Figure 5.32 Orientation development in fcc materials during: *(a)* plane strain compression (full constraints), *(b)* lath compression, and *(c)* pancake compression; after Ref. [138].

It has been argued in the literature that the grain split-up produced by the formation of shear bands results in the randomization of the deformation texture in aluminum [139, 140]. This phenomenon has been used to explain the sharper textures present in samples containing lower amounts of banding during the warm rolling of steel [141]. It is also known that there is less banding in fine grained microstructures. Thus, when high pancaking strains are applied, it is possible that sharper textures develop in the fine grained samples due to the drop in shear banding and the accompanying increase in grain matrix rotation.

Cooling Interruption Temperature

The transformation fibres of the rapidly cooled X-80 material associated with cooling interruptions at 620 °C, 520 °C, and 420 °C are illustrated in Figs. 5.33, 5.34, and 5.35, respectively. It can be seen that the intensity of the {112}<131> was increased when accelerated cooling was interrupted at 520 °C and 420 °C, as discussed above for the TD fibre. Again, it can be seen that a moderate cooling rate and a medium CIT of 520 °C result in the highest intensity of the {112}<131>. This supports the previous conclusion regarding the effect of moderate supercooling on optimization of the nucleation rate.

The observation that the intensity of this component is about 5 times random in all the low FRT samples processed with high pancaking strains, Figs. 5.30, 5.33, 5.34, and 5.35, implies that a stable orientation that is not influenced by accelerated cooling was formed in the austenite before transformation. The transformed brass (i.e. the {332}<113>), on the other hand, shows a high sensitivity to the cooling conditions, so that the {332}<113> reaches an intensity of about 10 in the high FRT samples.

It has been shown that the {112}<131> transforms from the brass and S with frequencies of occurrence of 6 and 5, respectively, out of the 24 possible K-S orientations [9]. This orientation may also transform from other minor orientations, such as the {123}<856>, with a frequency of 5 out of 24 [9]. It is therefore possible that high pancaking strains increase the volume fraction of the S and other minor orientations at the expense of the brass; that is, the volume fraction of the brass in austenite is decreased by increasing the pancaking strain.

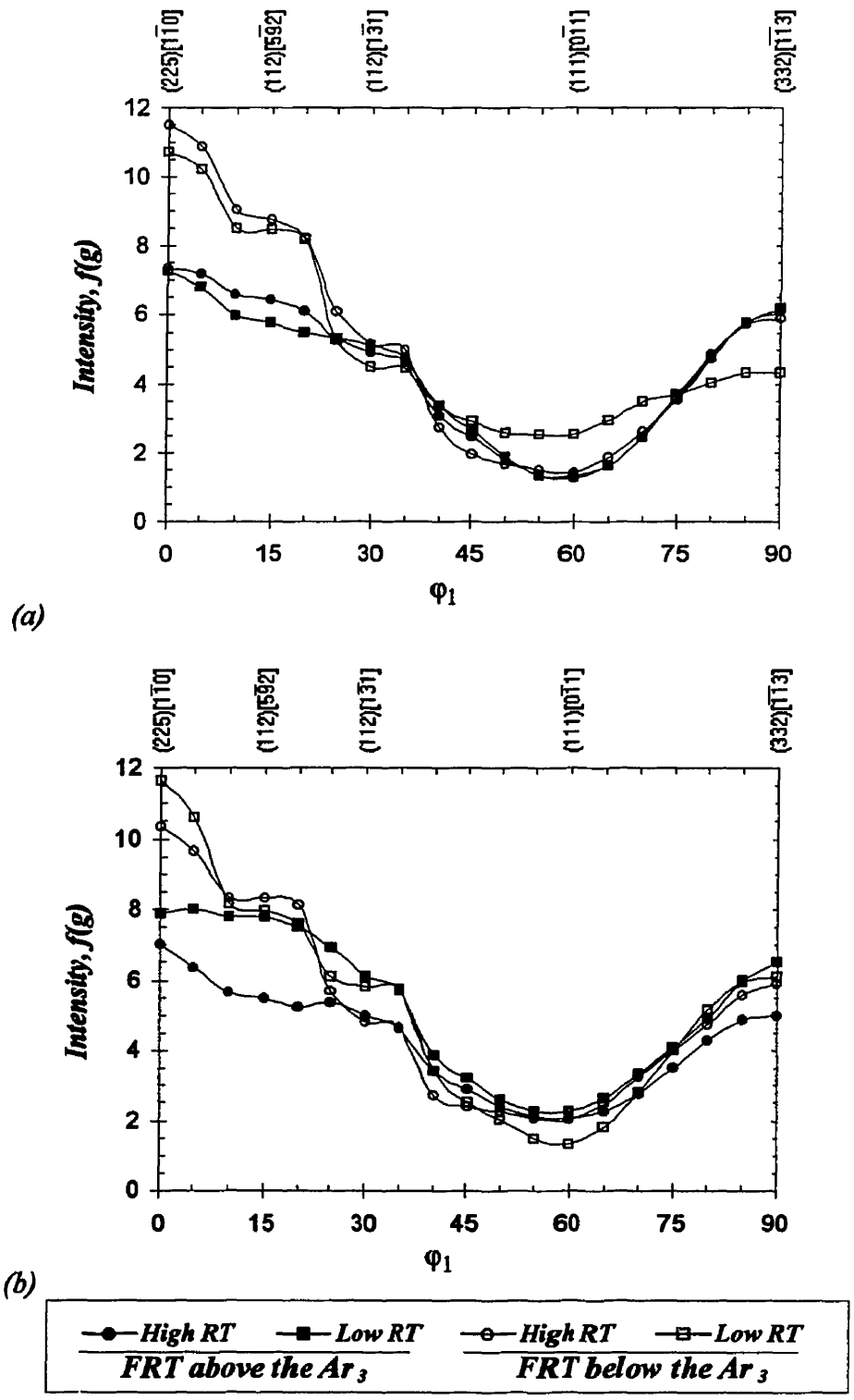

Figure 5.33 Transformation (TR) fibre of the rapidly cooled X-80 steels interrupted at **620 °C**; *(a)* CR= 20 °C s^{-1}, *(b)* CR= 40 °C s^{-1}.

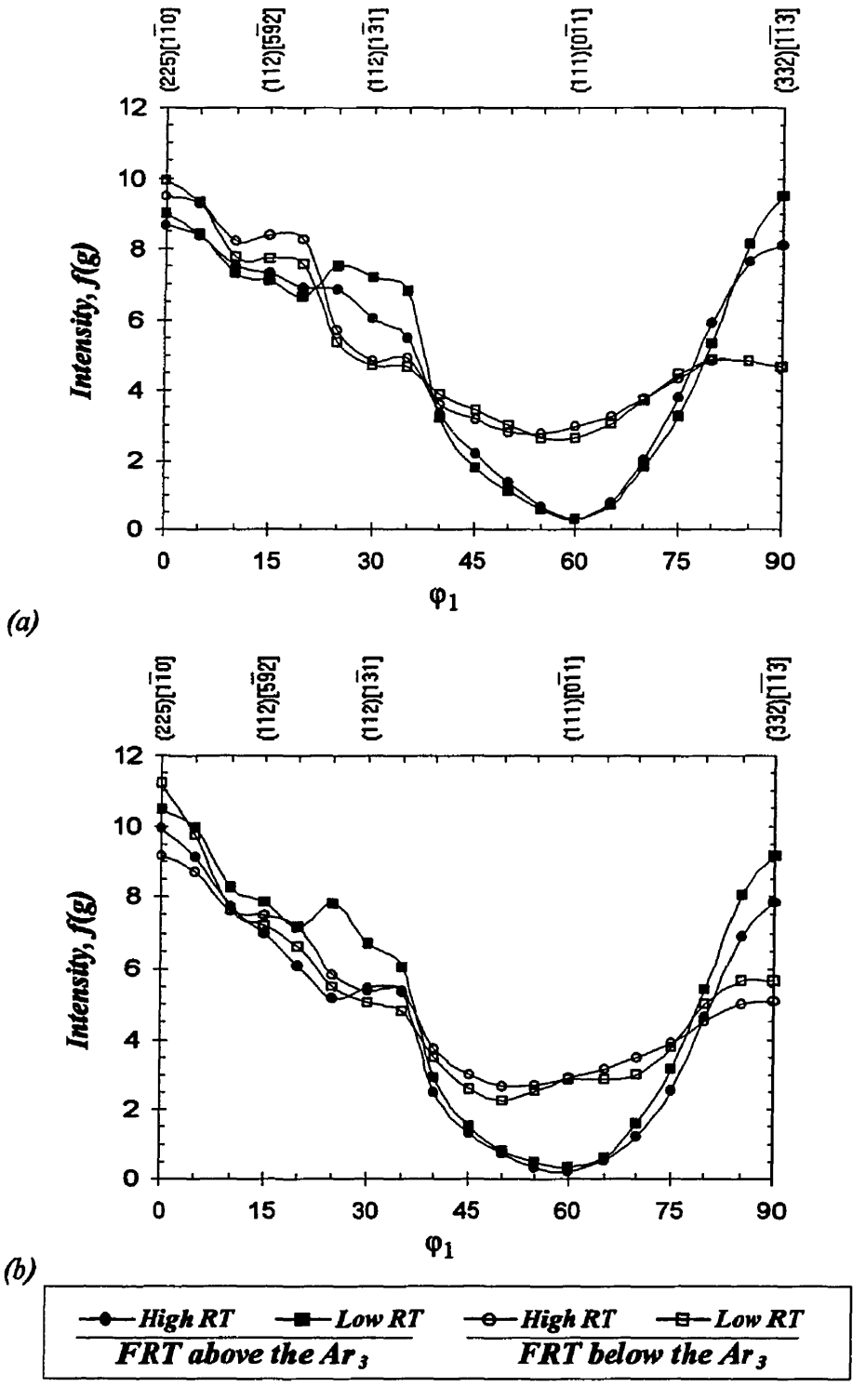

Figure 5.34 Transformation (TR) fibre of the rapidly cooled X-80 steels interrupted at **520 °C**; *(a)* CR= 20 °C s^{-1}, *(b)* CR= 40 °C s^{-1}.

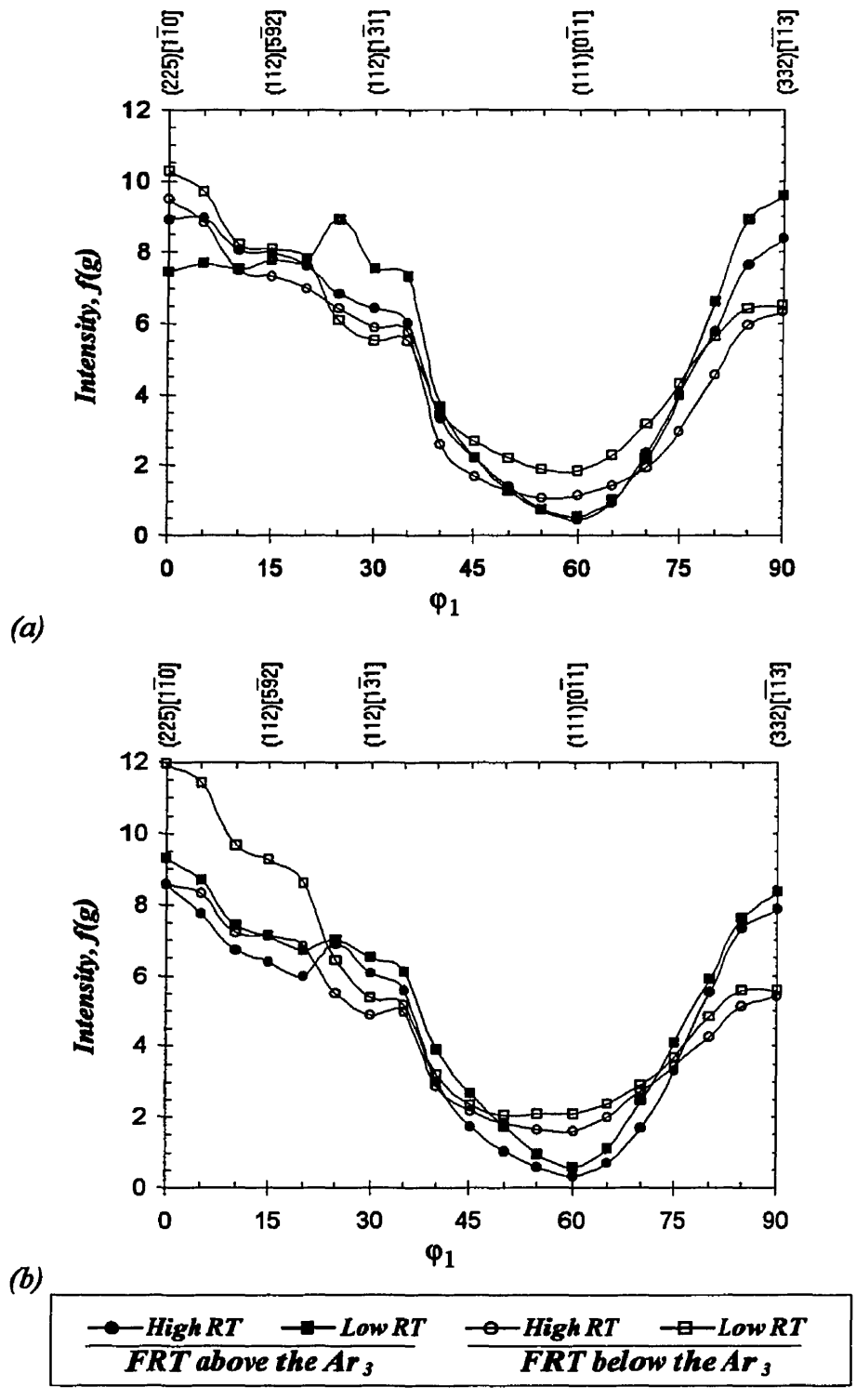

Figure 5.35 Transformation (TR) fibre of the rapidly cooled X-80 steels interrupted at **420 °C**; *(a)* CR= 20 °C s^{-1}, *(b)* CR= 40 °C s^{-1}.

This is evident from Figs. 5.33 to 5.35, where the intensities of the {332}<113> in the low FRT samples are less than 80 percent of those of the high FRT samples. This interpretation is also supported by the rolling simulation results of Zhou et al. [138], Fig. 5.32, which predict an increase in the S intensity at the expense of the brass intensity.

5.3.3 Variant Selection

Understanding variant selection has been an important problem in the subject of transformation textures. Variants are a set of transformed texture components that have some specific orientation relationship with the parent texture components. One set of possible orientation relationships between austenite and ferrite (or martensite, bainite, and acicular ferrite) are the 24 variants defined by Kurdjumov and Sachs [23, 26]:

$$\begin{cases} (111)_\gamma \| (110)_\alpha \\ [1\bar{1}0]_\gamma \| [1\bar{1}1]_\alpha \end{cases}$$

In most cases, experimental textures are both qualitatively and quantitatively different from those predicted by the K-S relationship. In the case of pancaked austenite and/or accelerated cooling, greater differences occur between the measured and predicted textures.

A sharp texture forms in pancaked austenite containing the copper {112}<111>, brass {110}<112>, and S {123}<634> components together with a weaker Goss {110}<100> orientation [134, 135]. To calculate the ferrite texture based on the K-S relation without variant selection, volume fractions of these fcc ideal orientations were chosen according to their intensities in a Ni-30%Co alloy with a stacking fault energy similar to that of austenite [136]. These were normalized by adding a random background of 30%. The volume fractions of the ideal product orientations were calculated from the austenite

ideal orientations using the frequencies of occurrence predicted by the K-S relation taken from Refs. 9 and 35. The results are illustrated in Table 5.1.

Table 5.1 Volume fractions of the ideal orientations calculated from the austenite ideal orientations according to the frequencies of occurrence predicted by the K-S relation.

Ferrite Ideal Orientation	Austenite Ideal Orientation				Volume Fraction of the Product Component, %
	Copper {112} <111>	Brass {110} <112>	S {123} <634>	Goss {110} <001>	
	Volume Fraction, %				
	20	21	25	4	
{100}<110>		4			3.5
{113}<110>	2		2		3.7
{112}<110>	6			8	6.2
{111}<110>				8	1.3
{111}<112>		2			5.3
{111}<123>		4			1.8
{554}<225>		2			5.3
{332}<113>		2			5.3
{112}<131>		6	5		10.6
{100}<001>				8	1.3
{110}<110>				4	0.7

From these discrete orientations, C-coefficients and an ODF were calculated using a Gaussian spread of 11 degrees together with the McGill texture software [105]. The model ODF and two X-80 experimental ODF's are illustrated in Fig. 5.36.

Comparison of the model ODF with the measured ODF's, Fig. 5.36, reveals a number of discrepancies between the calculated and experimental textures. Firstly, the distributions of the intensities of the ideal orientations are different. Secondly, some predicted orientations, such as the cube {100}<001>, are absent in the measured ODF's. The intensities of the orientations derived from the same parent texture components display significant differences in the product ODF's. These observations imply that some type of variant selection among the 24 possible orientations has occurred.

The fact that air cooling and rapid cooling result in textures that differ from the predicted ODF indicates that variant selection is directly influenced by the processing conditions. The greater differences between the model ODF and the ODF diagram of the rapidly cooled sample indicate that variant selection, i.e. a deviation from the KS predictions, is more pronounced when accelerated cooling is employed during transformation. Cooling rate and cooling interruption temperature affect the selection of some variants over others and also change the distribution of the intensities of the product components. The effects of cooling rate and cooling interruption temperature on texture were discussed in the previous sections. In order to determine which orientations are selected during transformation, the predicted volume fractions are compared here with the observed volume fractions of selected ideal orientations.

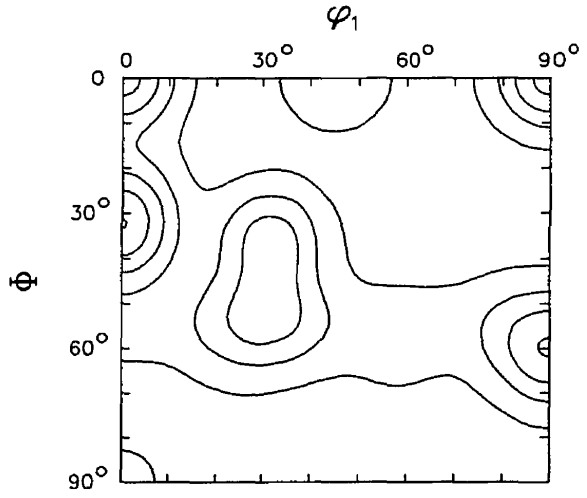

Max=5.0

(a) Model ODF

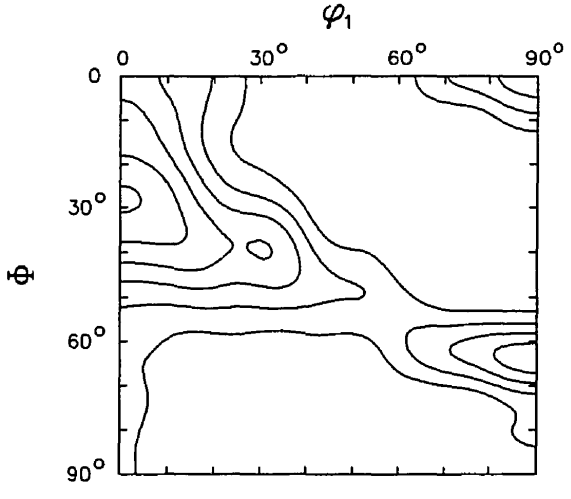

Max=6.2

(b) Air Cooled

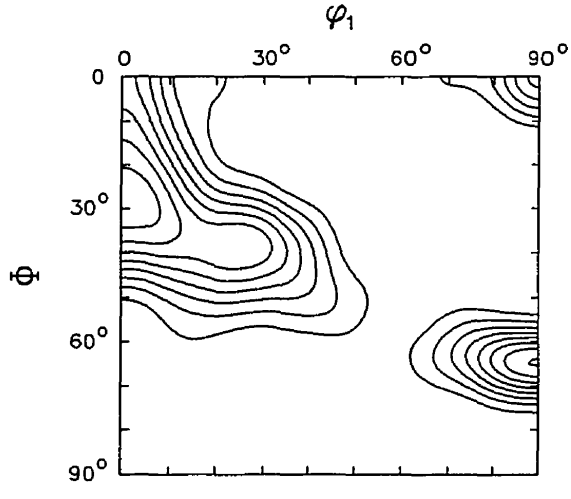

Max=8.7

(c) Rapidly Cooled

Figure 5.36 φ_2 = 45° sections of *(a)* model, *(b)* and *(c)* experimental ODF's. The experimental textures are from the X-80 plates finish rolled in the γ region.

For this purpose, volume fractions of the ferrite texture components were calculated from the experimental ODF's using the software of Ref. 137 for two sets of samples finish rolled in the austenite region. The results of the volume fraction calculations are presented in Tables 5.2 and 5.3 for the samples reheated at high and low temperatures, respectively. The volume fractions of the product components in the predicted ODF, Table 5.1, are compared with those of the measured ODF's, Tables 5.2 and 5.3, in Figs. 5.37, 5.38, and 5.39. The measured ODF's were determined on samples processed at different cooling rates and cooling interruption temperatures.

It can be seen from Fig. 5.37 that the rotated cube {100}<110> has nearly the same volume fraction as predicted by the K-S relation. By contrast, the volume fractions of the two other components, i.e. {112}<110> and {113}<110>, are appreciably higher than the predictions. This is particularly significant for the {113}<110>, which indicates the favouring of this component during both nucleation and growth.

Orientated nucleation and selective growth are two mechanisms that lead to deviations from the K-S predictions. However, the relative contributions of these two mechanisms can vary significantly, depending on the processing parameters. Selective growth is affected by steel chemistry and cooling rate during transformation. In martensite or at low CIT's, oriented nucleation is likely to be the prevailing mechanism, whereas selective growth may also be active in the air cooled or higher CIT samples.

Thus, it seems that the {113}<110> and {112}<110> components form in the air cooled samples by the selective growth mechanism, although the number of nucleation sites is likely to be less than in the rapidly cooled samples. As discussed in Chapter Four, acicular ferrite forms by a displacive growth mechanism without diffusion [123, 125].

Table 5.2 Volume fractions of the ideal orientations in the X-80 *high* RT and high FRTsamples.

TMP Schedule		**Cooling Rate**					
Reheating at 1275°C	**Air**	**20 °C s^{-1}**			**40 °C s^{-1}**		
Finish Rolling at 780°C	**Cooled**	**Cooling Interruption Temperature, °C**					
		620	**520**	**420**	**620**	**520**	**420**
Ferrite Ideal Orientation	**Volume Fraction of the Ideal Orientation, %**						
{100}<110>	2.8	3.2	3.2	3.0	3.5	2.7	2.9
{113}<110>	8.3	9.6	11.2	10.8	9.3	11.9	10.4
{112}<110>	7.8	9.4	10.1	10.8	8.5	10.6	9.3
{111}<110>	3.5	3.6	2.7	2.9	3.8	2.4	2.6
{111}<112>	4.3	5.1	5.8	6.2	5.0	5.7	5.8
{111}<123>	7.8	9.1	9.6	10.2	9.1	8.8	9.4
{554}<225>	5.8	7.2	8.7	9.2	6.9	8.0	8.5
{332}<113>	6.0	7.5	9.3	9.8	7.1	8.2	9.0
{112}<131>	10.3	11.5	13.8	13.7	12.1	11.5	13.7
{100}<001>	0.0	0.0	0.0	0.0	0.0	0.0	0.0
{110}<110>	1.2	1.1	0.3	0.8	0.7	0.3	0.6

Table 5.3 Volume fractions of the ideal orientations in the X-80 *low* RT and high FRTsamples.

TMP Schedule		**Cooling Rate**					
Reheating at 1150°C	**Air**	**20 °C s^{-1}**			**40 °C s^{-1}**		
Finish Rolling at 780°C	**Cooled**	**Cooling Interruption Temperature, °C**					
		620	**520**	**420**	**620**	**520**	**420**
Ferrite Ideal Orientation	**Volume Fraction of the Ideal Orientation, %**						
{100}<110>	2.6	3.1	3.3	2.8	2.7	2.9	3.3
{113}<110>	10.0	9.9	10.7	9.7	9.8	11.3	11.0
{112}<110>	9.8	9.6	10.0	10.1	10.3	10.9	10.2
{111}<110>	3.8	3.0	2.5	3.1	4.3	2.5	2.9
{111}<112>	4.2	6.2	6.5	7.5	5.9	5.8	6.3
{111}<123>	7.9	9.9	10.1	12.0	10.6	9.4	10.5
{554}<225>	5.7	8.7	9.7	10.7	8.4	9.0	9.3
{332}<113>	5.8	9.0	10.3	11.0	8.7	9.8	9.8
{112}<131>	10.5	13.7	14.0	14.5	13.6	14.6	14.0
{100}<001>	0.0	0.0	0.0	0.0	0.0	0.0	0.0
{110}<110>	1.2	1.1	0.3	0.8	0.7	0.3	0.6

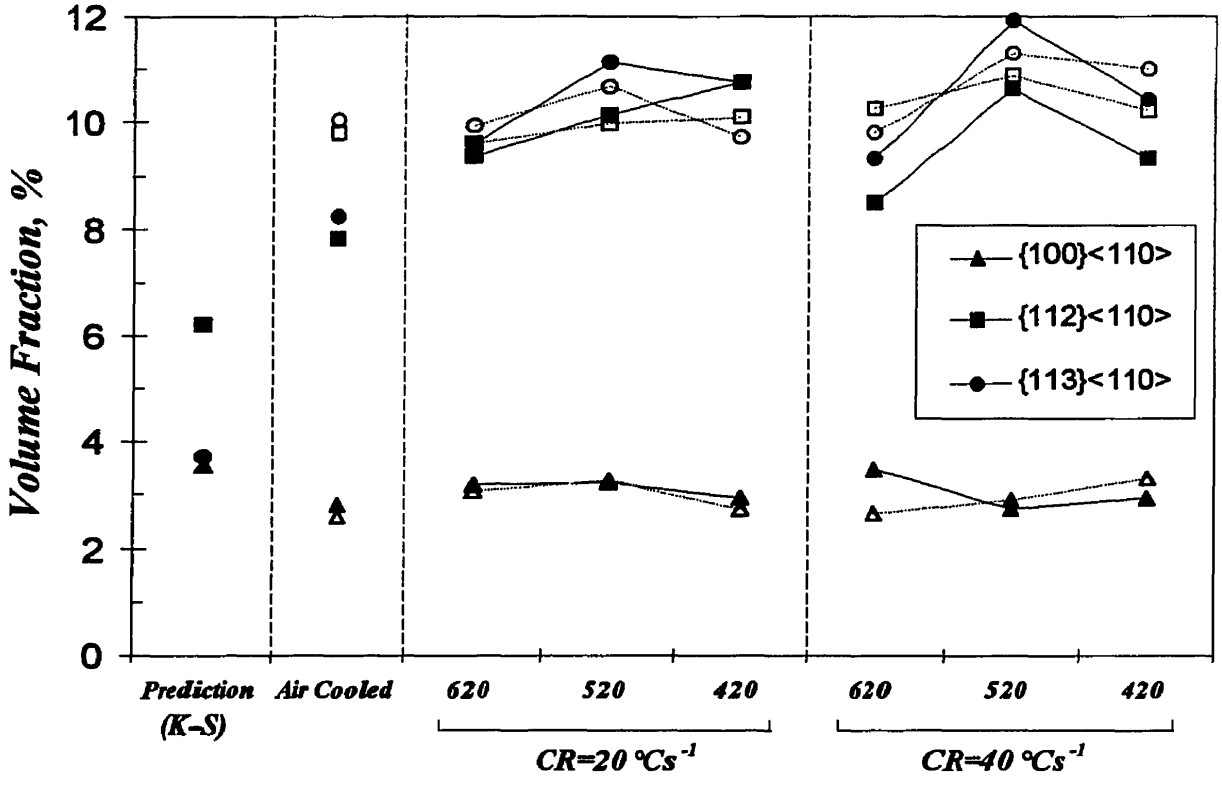

Figure 5.37 Comparison of the predicted and measured volume fractions of the three RD fibre components in the samples reheated at high (solid lines and symbols) and low (dashed lines and open symbols) temperatures, respectively.

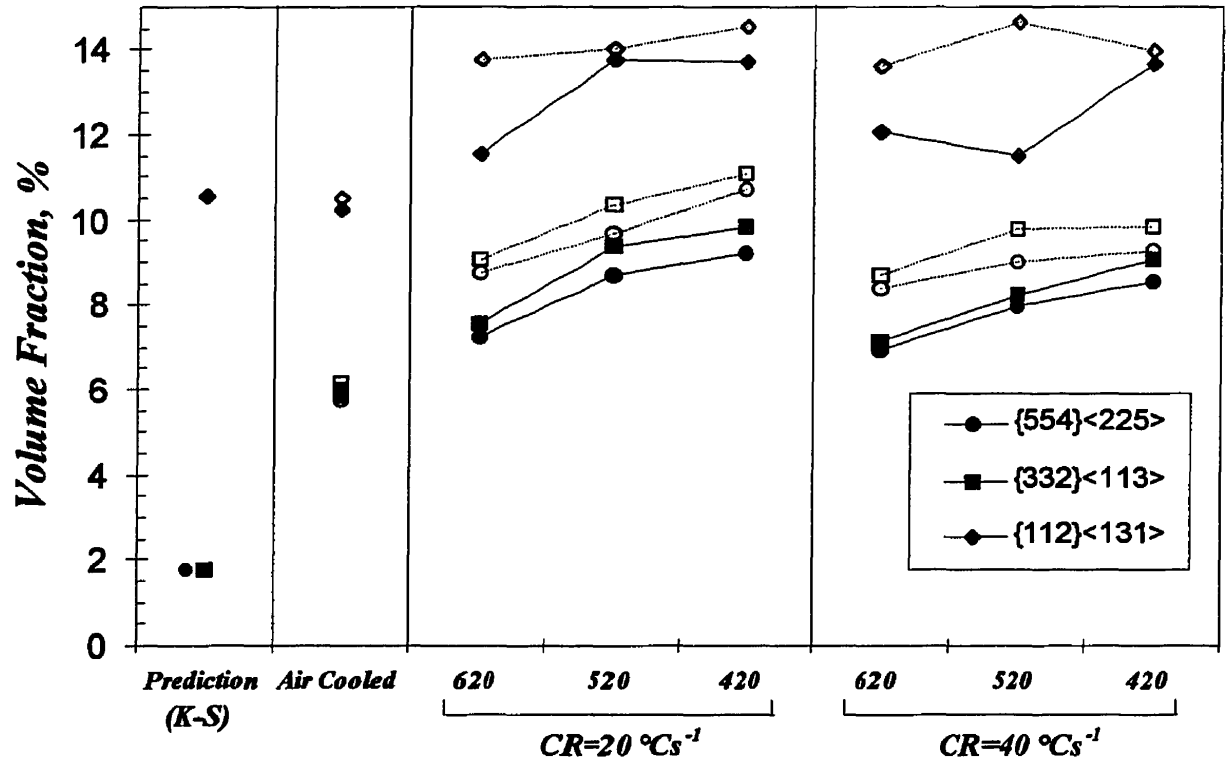

Figure 5.38 Comparison of the predicted and measured volume fractions of the two TD fibre components and the {112}<131> orientation in the samples reheated at high (solid lines and symbols) and low (dashed lines and open symbols) temperatures, respectively.

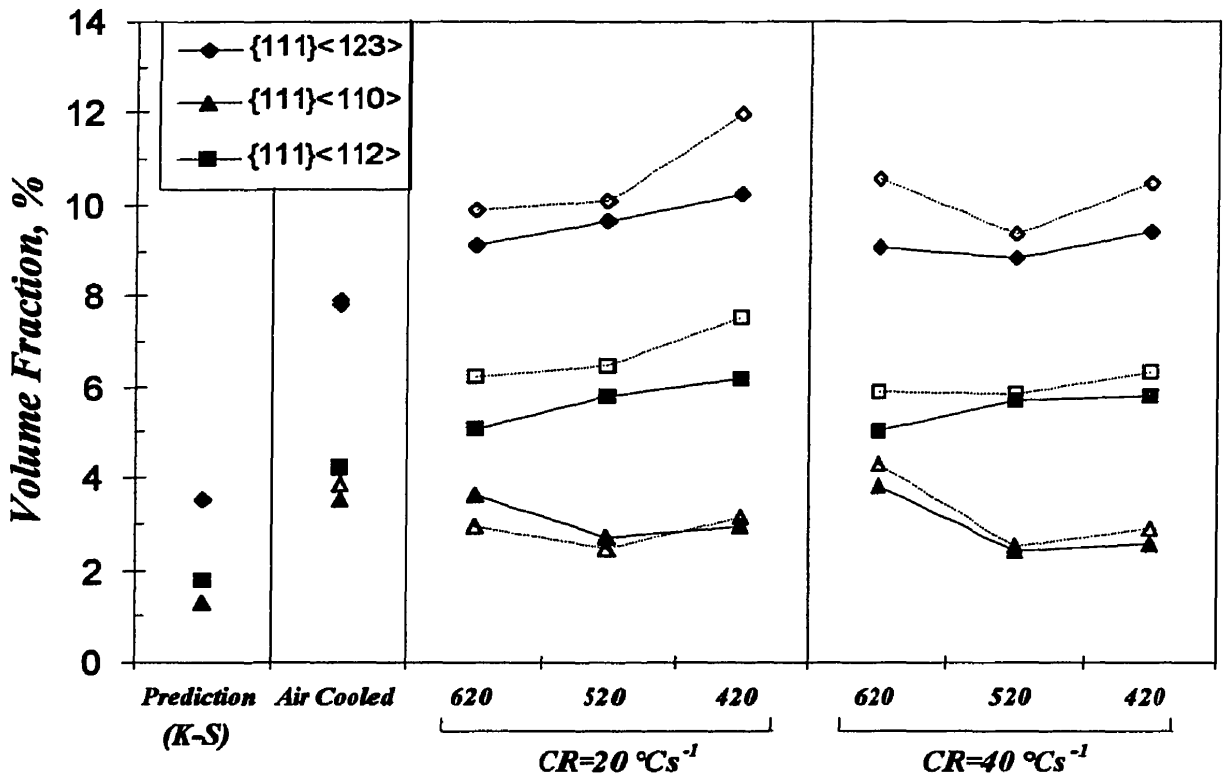

Figure 5.39 Comparison of the predicted and measured volume fractions of the three ND fibre components in the samples reheated at high (solid lines and symbols) and low (dashed lines and open symbols) temperatures, respectively.

It has also been reported that in high manganese (about 3%) steels, similar textures developed in the air cooled acicular ferrite and rapidly cooled martensitic microstructures [29]. This is despite the expected differences in the nucleation textures (and in the number of nucleation sites); these observations imply that selective growth can result in textures that are just as sharp as the nucleation textures.

It is evident from Fig. 5.37 that the volume fractions of {112}<110> and {113}<110> are the greatest in the case of the medium cooling interruption temperature of 520 °C. Assuming a 'nucleation texture" for the rapidly cooled samples, it can be concluded that the nucleation rate of the product phase, i.e. the acicular ferrite as discussed in the previous chapter, was highest at 520 °C. This supports the view advanced above that the optimum nucleation rate occurs at moderate cooling rates and medium cooling interruption temperatures.

The intensities of the other ideal orientations, such as the {332}<113>, {554}<225>, and {112}<131>, are much higher than the predicted values, Fig. 5.38, even in the case of the air cooled samples. This implies that oriented nucleation has taken place or that selective growth occurred in these cases. However, accelerated cooling led to more variant selection, especially at the moderate cooling rate of 20 °C s^{-1} and the low CIT of 420 °C. These ferrite components can thus be considered as primarily oriented nucleation orientations.

The greater differences between the volume fractions of {112}<131> in the low RT samples and in the predictions, as compared with the high RT samples, are probably related to the intensities of the parent texture components, i.e. the S in this case, than to variant selection. As discussed in the previous section, greater S_V values lead to higher volume fractions of S, whereas the brass component is either unchanged or even decreased by increasing S_V.

The volume fractions of the ND fibre components are higher than the predicted values, Fig. 5.39. The volume fractions of these components are close in the air cooled and rapidly cooled samples, which implies that selective growth may also have been an effective mechanism, in addition to oriented nucleation. This is evident from the lower volume fractions of the {111}<110> in the rapidly cooled samples than in the air cooled ones, Fig. 5.39.

CHAPTER 6

Planar Anisotropy of Yield Strength

6.1 Introduction

The deformation behaviour of a polycrystal is an average of that of the individual grains. Because single crystals are intrinsically anisotropic, preferred crystallographic orientations or textures are the essential cause of the anisotropy of mechanical properties in metals. Since the work of Lankford et al. [142], r-value has been related to preferred grain orientations. Many researchers [143-146] have subsequently studied the "planar anisotropy" of flat products by correlating the characteristics of crystallographic slip to the texture.

Modified versions of the Taylor approach have been proposed, such as the relaxed constraint models, in which certain components of the strain rate tensor are relaxed in the grains. All relaxed constraint models are based on the observation that the grains are not equiaxed, but rather flattened (pancaked) or elongated (lath-shaped).

For the manufacture of spiral welded pipe from skelp, it is desirable to have higher strengths in the hoop rather than in the longitudinal direction, see Fig. 6.1. For this purpose, knowledge of the influence of processing parameters on the anisotropy of mechanical properties is required. In fact, all the processing parameters affecting the texture, as described in the previous chapter, influence the planar anisotropy of the plates.

In this chapter, the effects of the processing parameters, described in Chapter Three, on the anisotropy of the strength will be discussed. The relations between texture, presented in Chapter Five, microstructure, described in Chapter Four, and the plastic anisotropy of the yield strength will also be considered. The experimental results of the tensile tests are compared with models for predicting the anisotropy in the last section. Experimental data obtained on the anisotropy of the *fracture* properties will not be presented here due to a lack of space, but will be described in a separate publication [147].

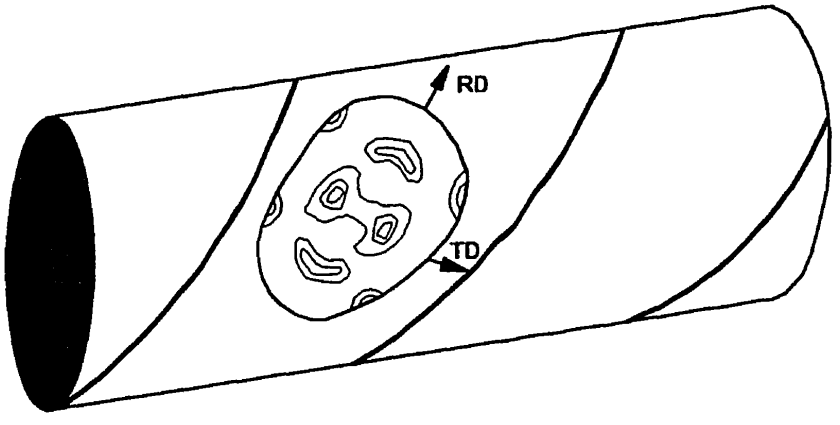

Figure 6.1 Schematic representation of spiral welded pipe.

6.2 Tensile Test Results

As described in Chapter Three, tensile tests were performed on plates processed under various TMP conditions. The yield strength anisotropy was examined by measuring the yield strength of each plate along five directions with inclinations of 0°, 22.5°, 45°, 67.5°, and 90° with respect to the rolling direction. The results of tensile testing (the proof stress and the ultimate tensile strength) of the X-70 and X-80 plates are presented in the following sections. The values of yield strength displayed in these figures are the averages of three to five tensile samples for each direction. Experimental errors of ±2 % (±12 MPa) from the average value are associated with these values. However, in most cases, the error was less than ±5 MPa.

6.2.1 Low Niobium Steel

The yield and ultimate tensile strengths of the X-70 plates (processed under the TMP conditions described in Tables 3.5 and 3.6) are illustrated in Fig. 6.2. Two distinct differences are evident in this figure. Firstly, the yield strengths vary over a larger range, i.e. about 150 MPa, than the ultimate tensile strengths, with a 100 MPa difference between the highest and lowest values. In other words, the ratio of yield stress to UTS along the transverse direction changes from $r_1 = 0.76$ in the air cooled sample with a high FRT to $r_1 = 0.85$ in a rapidly cooled plate with a low FRT. This indicates the effect of grain refinement of the ferrite on the yield strength, either by intercritical rolling or by accelerated cooling. By contrast, the ultimate tensile strength, which is mostly affected by the work hardening rate, displays less scatter, indicating that the dislocation densities in these plates are probably similar.

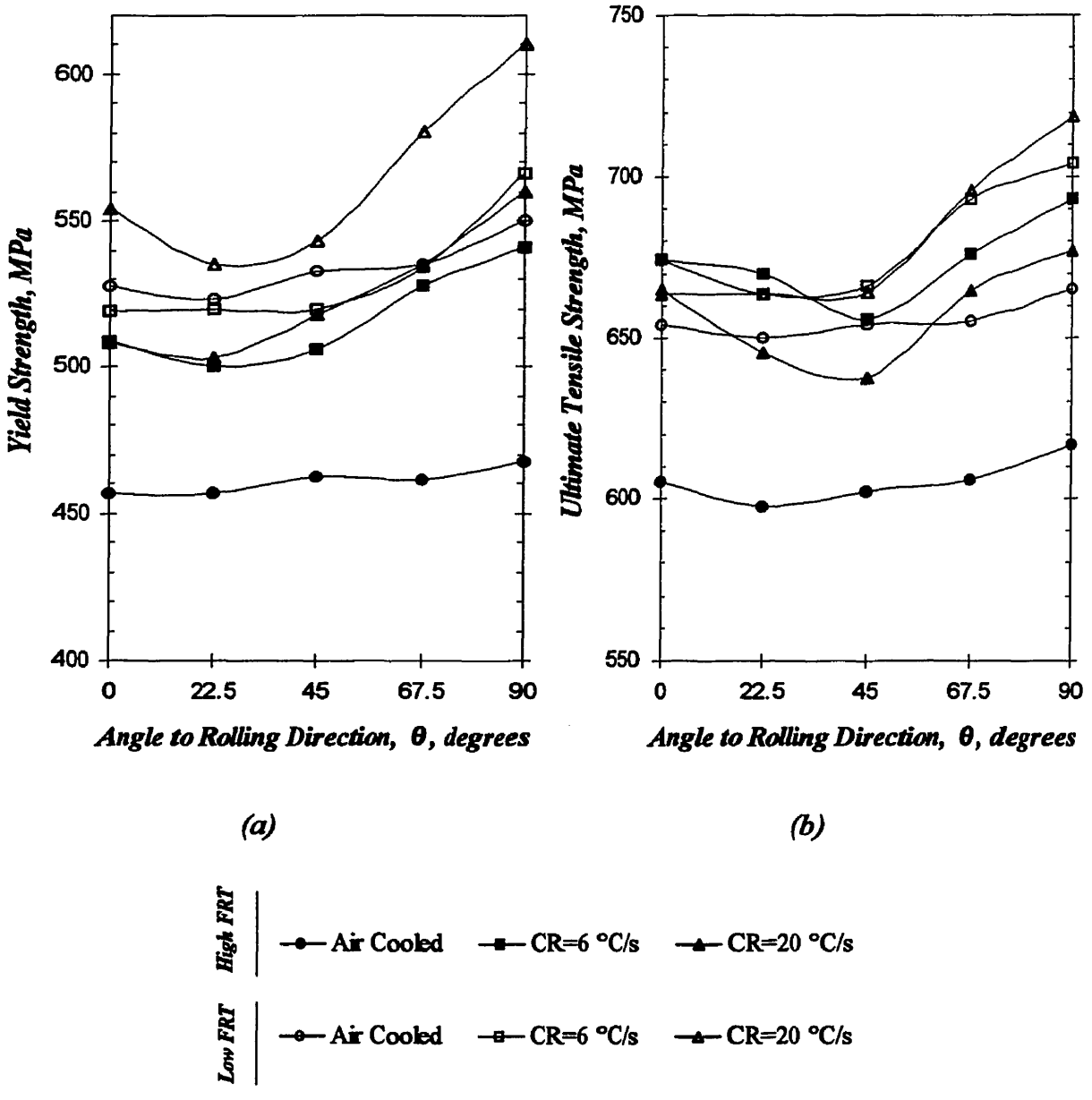

Figure 6.2 Measured values of the *(a)* yield strength and *(b)* ultimate tensile strength at various inclinations to the rolling direction for the X-70 plates reheated at 1225 °C.

Secondly, the ratios of transverse to longitudinal yield strength are greater (with the highest values displayed by the samples rapidly cooled at 20 $°C\ s^{-1}$) than the ratios of the corresponding UTS's, which increase more smoothly from the rolling to the transverse direction. As will be seen in the Discussion section below, the main causes of this difference can be linked to the textures of the plates and to the morphologies of the grains.

The very low strength of the air cooled sample finish rolled in the austenite region, Fig. 6.2, was probably because of the high degree of recovery at 790 °C, which also resulted in the low hardness of the ferrite, Fig. 4.16. By contrast, ferrite rolling increased the yield strength along the transverse direction by 70 MPa (from 470 MPa in the sample with a high finishing temperature to 540 MPa) due to work hardening of the ferrite. Air cooling also resulted in the lowest anisotropy of both the yield strength and the ultimate tensile strength as compared to accelerated cooling.

6.2.2 High Niobium Steel

The yield and ultimate tensile strengths measured along different inclinations to the rolling direction are illustrated in Figs. 6.3 to 6.6 for the X-80 samples processed under the TMP conditions described in Tables 3.7 to 3.10.

The air cooled samples display lower yield and ultimate tensile strengths than the rapidly cooled samples. By contrast, higher strengths and greater transverse to longitudinal strength ratios are produced by accelerated cooling. The high strengths can be attributed to the higher dislocation densities present in the acicular ferrite and bainitic microstructures produced by rapid cooling, as well as to the greater grain refinement applicable to acicular ferrite compared to polygonal ferrite. The higher anisotropy ratios indicate that texture and grain morphology are very effective in this respect. These factors are considered in greater detail in the Discussion section below.

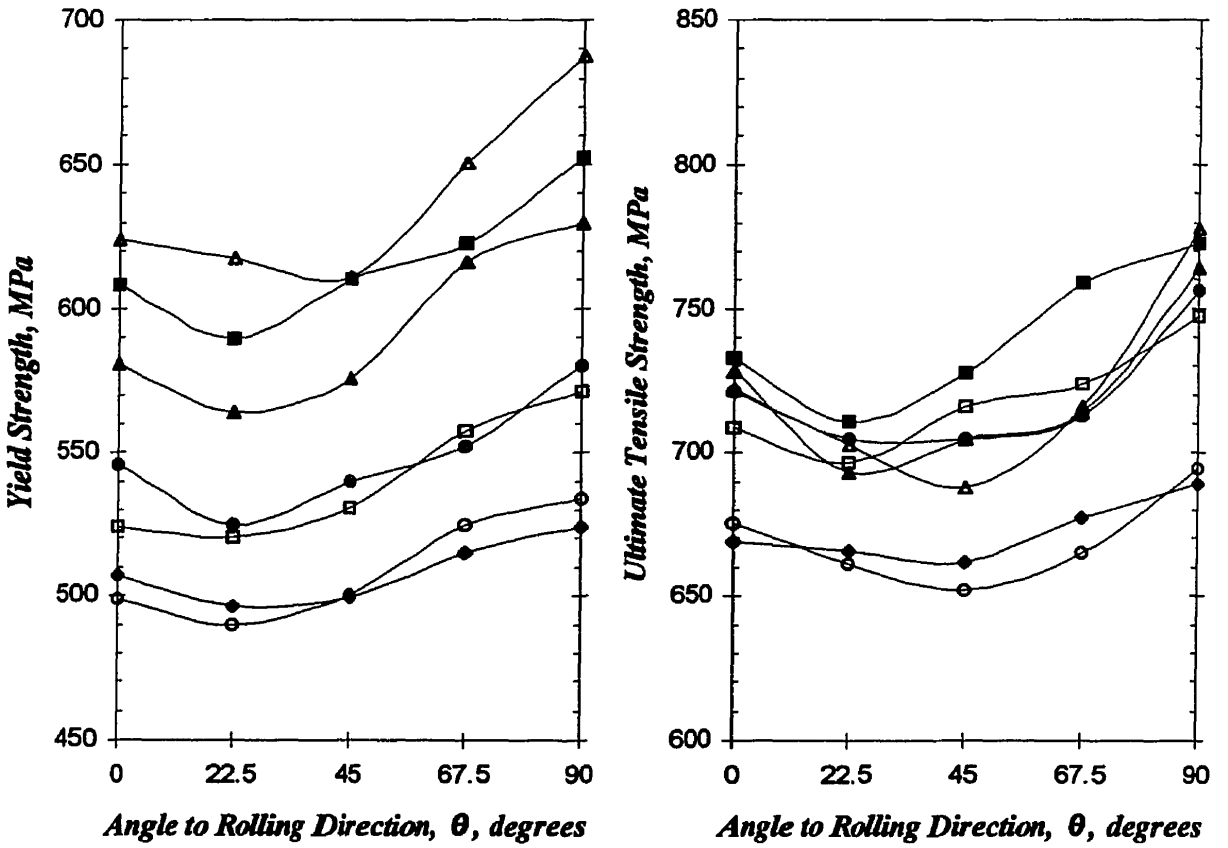

Figure 6.3 Measured values of the *(a)* yield strength and *(b)* ultimate tensile strength at various inclinations to the rolling direction for the X-80 plates reheated at **1275 °C** and finish rolled at **780 °C**.

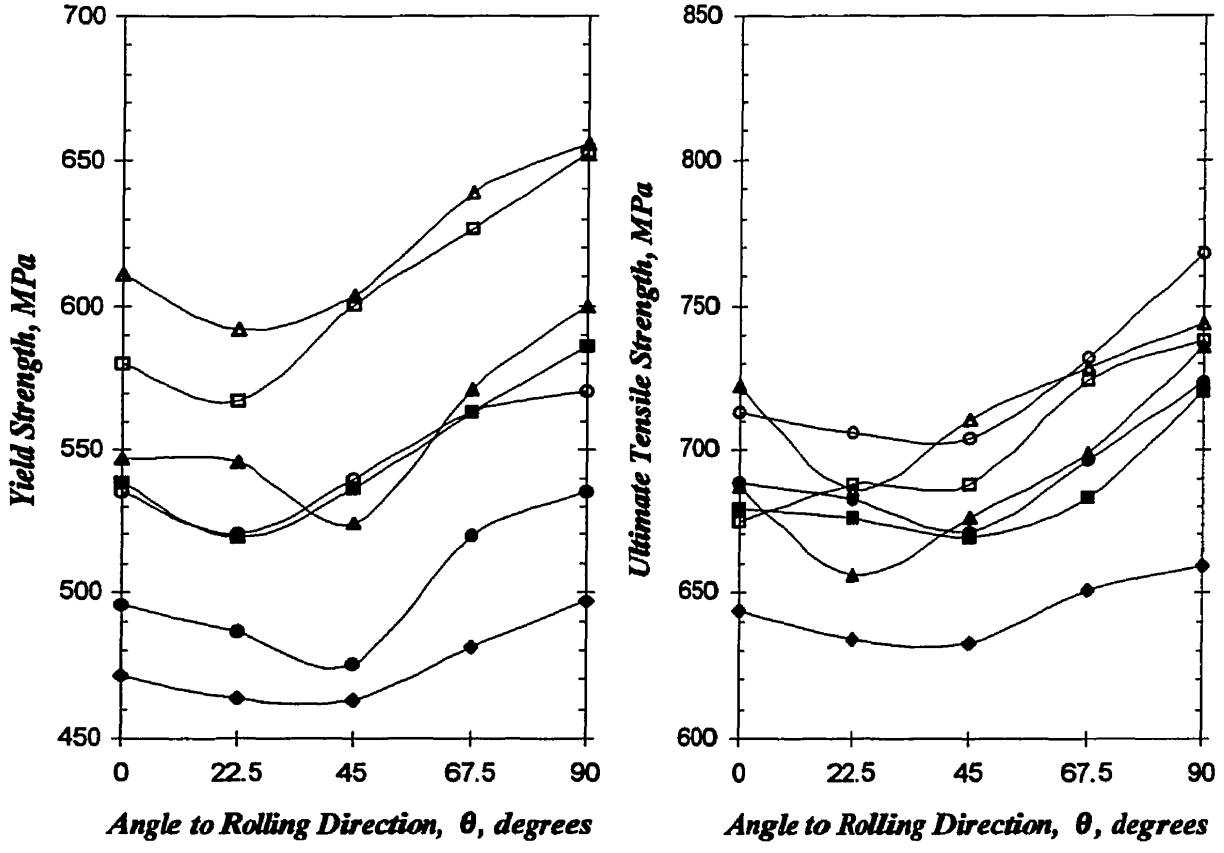

Figure 6.4 Measured values of the *(a)* yield strength and *(b)* ultimate tensile strength at various inclinations to the rolling direction for the X-80 plates reheated at **1150 °C** and finish rolled at **780 °C**.

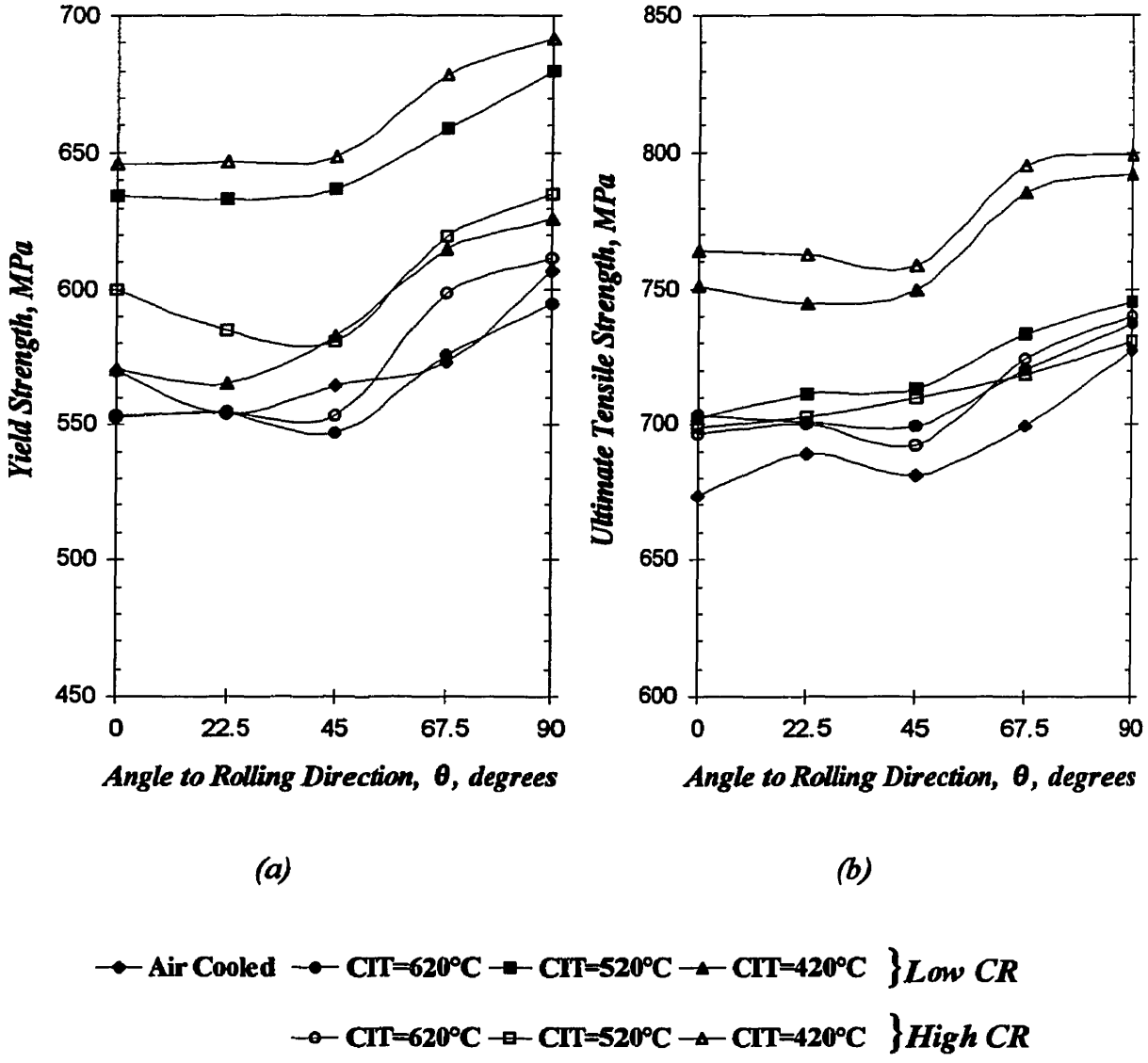

Figure 6.5 Measured values of the *(a)* yield strength and *(b)* ultimate tensile strength at various inclinations to the rolling direction for the X-80 plates reheated at **1275 °C** and finish rolled at **690 °C**.

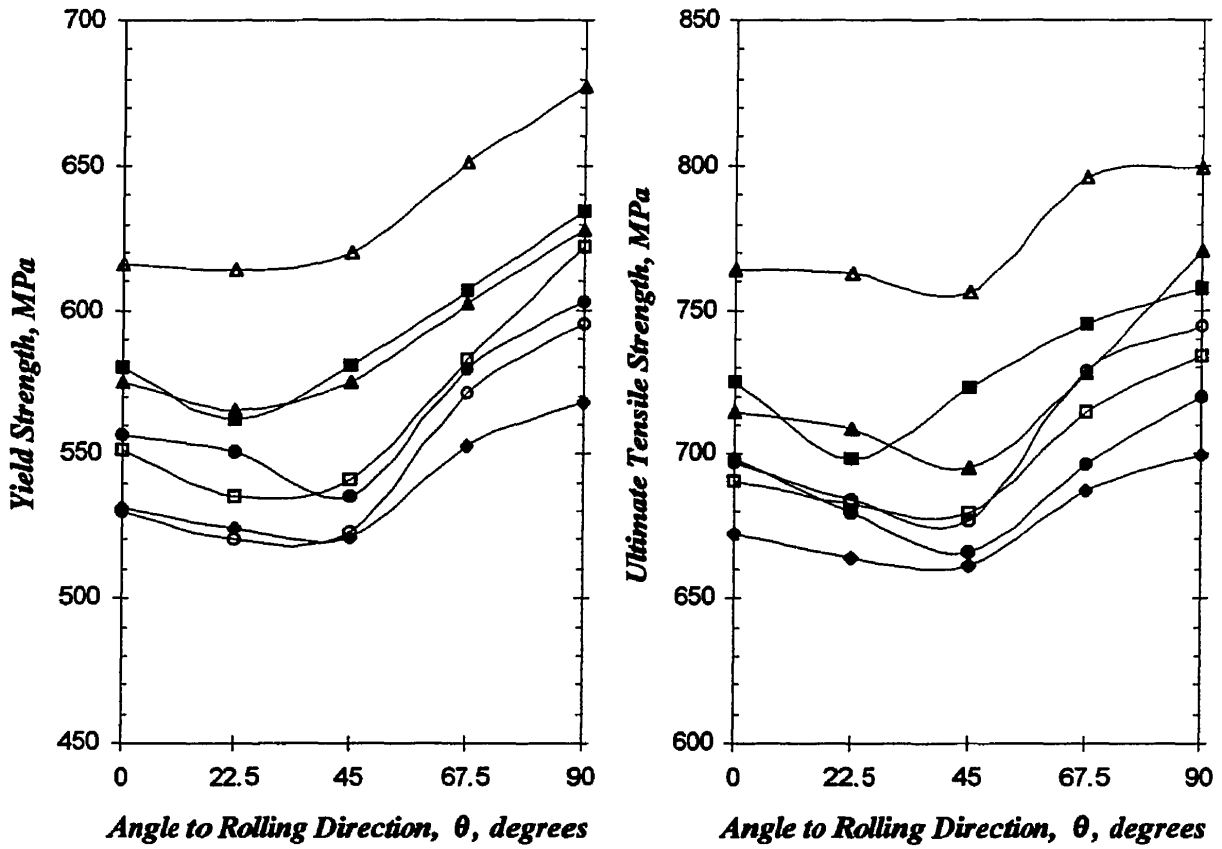

Figure 6.6 Measured values of the *(a)* yield strength and *(b)* ultimate tensile strength at various inclinations to the rolling direction for the X-80 plates reheated at **1150 °C** and finish rolled at **690 °C**.

Generally, higher strengths are produced by employing ferrite intercritical rolling, Figs. 6.5 and 6.6. This can be attributed to the high dislocation densities introduced by ferrite rolling. The ratios of proof stress to UTS, however, do not increase as opposed to those displayed by the samples finish rolled above the Ar_3. This is evident in both the air cooled and rapidly cooled plates, indicating that work hardening of the ferrite during rolling may result in an effect comparable to that of accelerated cooling after rolling.

As depicted in Figs. 6.3 and 6.4, the variation in the yield strength along the transverse direction is as much as twice that of the ultimate tensile strength (200 MPa versus 100 MPa). Here, the ratio of yield stress to UTS along the transverse direction increases from $r_1 = 0.76$ in the air cooled sample to $r_1 = 0.88$ in a rapidly cooled sample subjected to the higher RT, Fig. 6.3, and from $r_1 = 0.76$ to $r_1 = 0.87$ in the lower RT sample, Fig. 6.4.

Four sets of typical stress–strain curves of air cooled and rapidly cooled samples are displayed in Fig. 6.7 for plates finish rolled above the Ar_3 and reheated at the higher and lower temperatures. As can be seen in this figure, the rapidly cooled samples display continuous yielding due to their fully acicular ferrite microstructures. By contrast, in the air cooled samples, the presence of polygonal ferrite led to less prominent continuous yielding and even to some evidence for yield drops and Luders propagation. This occurred even though there was less carbon and nitrogen in solution in the slowly cooled materials.

It is evident from Fig. 6.7 that, despite the higher initial work hardening rates ($d\sigma/d\varepsilon$) displayed by the rapidly cooled samples, their ultimate tensile strengths are close to those of the air cooled plates. This is due to the higher initial dislocation densities (and yield stresses) of the rapidly cooled samples, which in turn led to the earlier satisfaction of the Considere criterion [148].

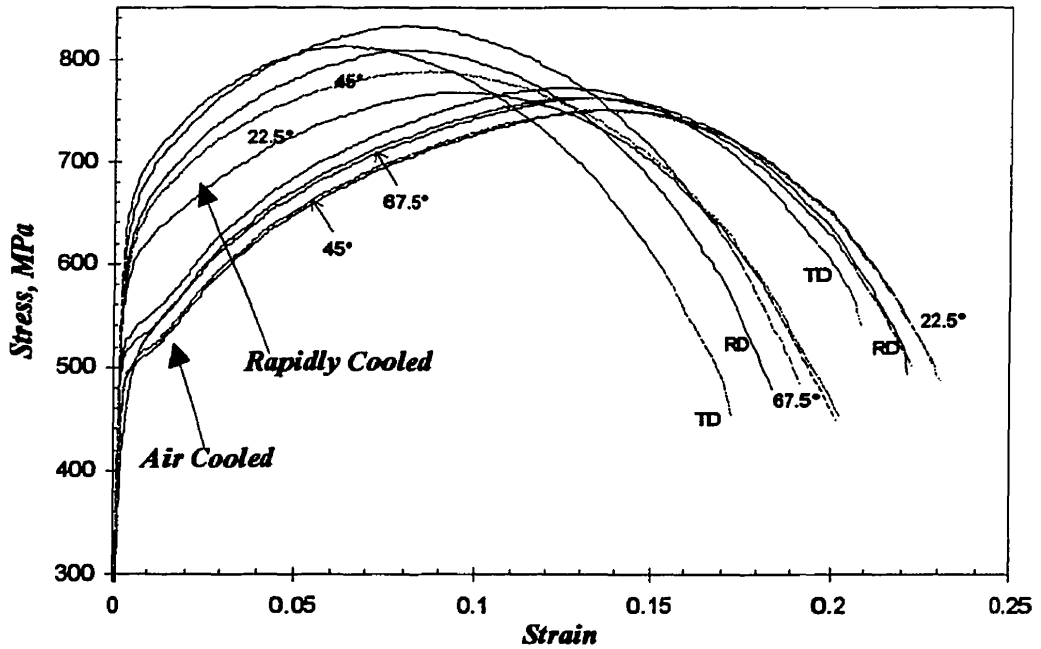

(a)

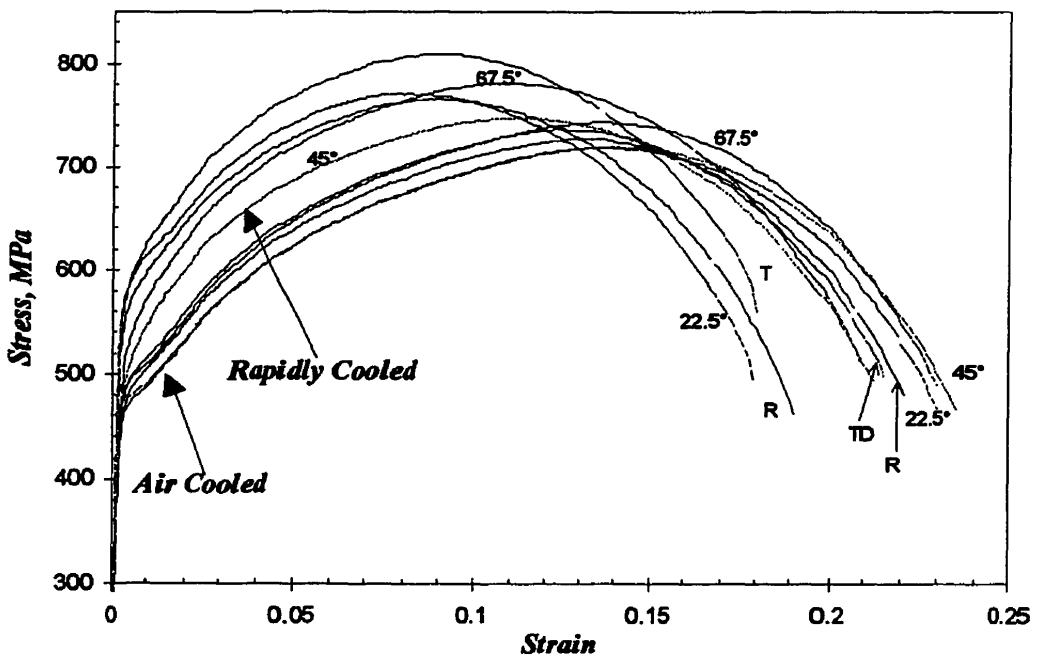

(b)

Figure 6.7 Typical stress– strain curves of air cooled and rapidly cooled (CR= 20 °C s^{-1} and CIT= 520 °C) samples finish rolled above the Ar_3; *(a)* RT= 1275°C and *(b)* RT= 1150°C.

6.3 Discussion

In order to quantify the average strength of a rolled plate, a $\overline{\sigma}$ parameter is introduced here, *eq.* 6.1, which is defined as the average of the yield strengths measured along the various directions of inclination to the rolling direction. This is similar to the definition of the $\overline{r}$ value from the angular variation of $r(\theta)$ [149].

$$\overline{\sigma} = \frac{2}{\pi}\int_0^{\pi/2}\sigma(\theta)d\theta = \frac{1}{8}\left(\sigma_0 + 2\sigma_{22.5} + 2\sigma_{45} + 2\sigma_{67.5} + \sigma_{90}\right) \qquad (6.1)$$

The following parameter is also defined as it permits the planar anisotropy of the yield strength to be quantified:

$$\Delta\sigma = \frac{2}{\pi}\int_0^{\pi/2}\left(\left|\overline{\sigma} - \sigma(\theta)\right|\right)d\theta$$

$$= \frac{1}{8}\left(\left|\overline{\sigma} - \sigma_0\right| + 2\left|\overline{\sigma} - \sigma_{22.5}\right| + 2\left|\overline{\sigma} - \sigma_{45}\right| + 2\left|\overline{\sigma} - \sigma_{67.5}\right| + \left|\overline{\sigma} - \sigma_{90}\right|\right) \qquad (6.2)$$

In the following sections, the average yield strengths and planar anisotropies of the yield strength (values obtained from *eqs.* 6.1 and 6.2) of the X-70 and X-80 plates are compared with the other characteristics of the samples.

6.3.1 Effect of Chemical Compositions

The average yield strengths ($\overline{\sigma}$) of the air cooled and rapidly cooled X-70 and X-80 plates are compared in Fig. 6.8 to the ferrite grain sizes measured on the air cooled samples. It is evident that in nearly all cases the yield strengths were higher when the plates were rapidly cooled after rolling.

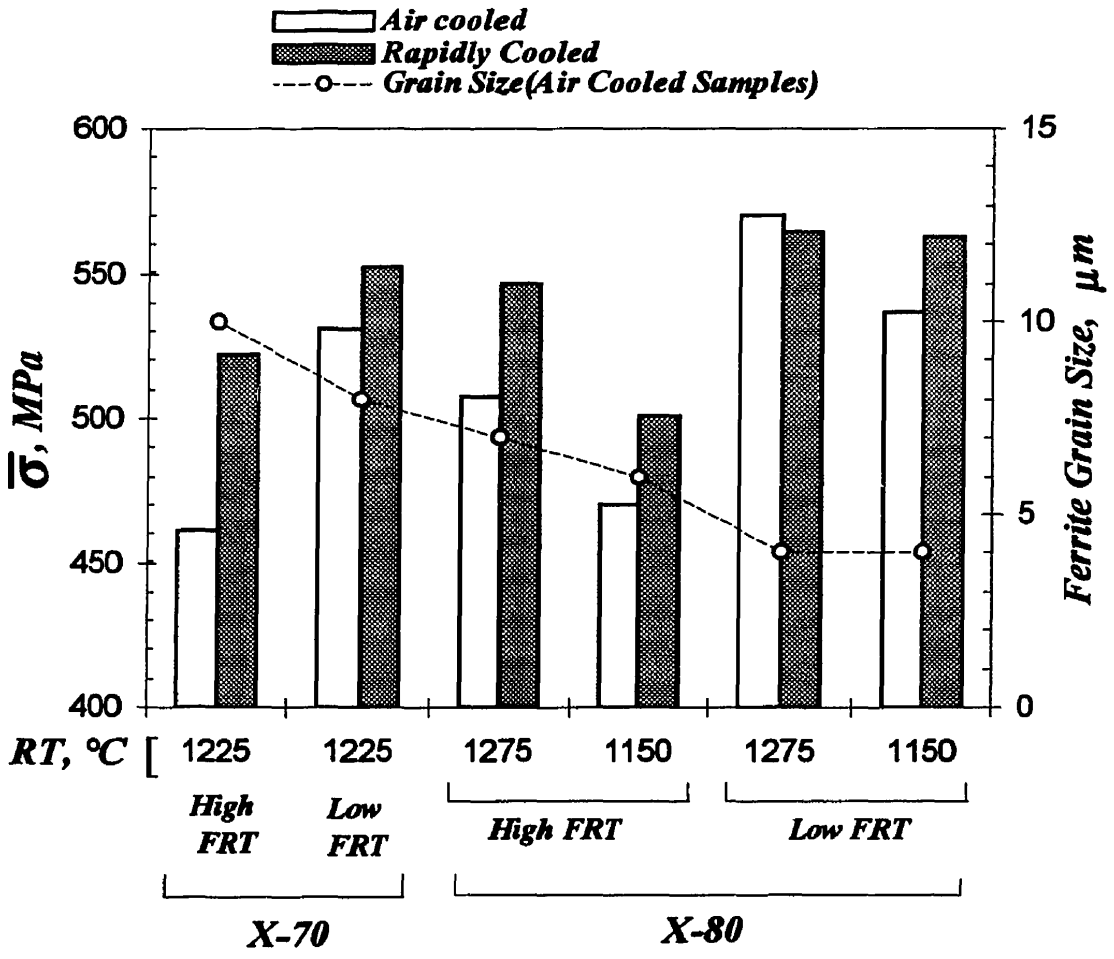

Figure 6.8 Average yield strengths ($\bar{\sigma}$) of the air cooled and rapidly cooled X-70 and X-80 plates together with the ferrite grain sizes measured on the air cooled samples. Accelerated cooling was interrupted at 620 °C after cooling at 20 °C s^{-1}.

As can be seen in this figure, the yield strengths of the air cooled X-80 samples finish rolled above and below the Ar_3 are higher than the corresponding values for the X-70 plates. This can be attributed to both the finer ferrite grain sizes, as is evident in Fig. 6.8, and to more hardening by Nb precipitation in the X-80 steel. These two factors were the main causes of the high yield strengths of the X-80 samples, as opposed to the low Nb steel (X-70) samples, Fig. 6.8.

The air cooled X-80 sample associated with the lower RT and higher FRT displays a higher yield strength than the higher FRT X-70 plate. However, the $\overline{\sigma}$ of the lower FRT X-70 sample is increased by ferrite rolling to a level higher than that of the X-80 plates finish rolled above the Ar_3. This is despite the coarser ferrite grain size of the X-70 sample. This clearly indicates that ferrite rolling results in such a high dislocation density in this case that it compensates for the effect of both the finer grain size and of more precipitation hardening in the higher Nb steel.

Accelerated cooling resulted in a similar variation of the average yield strength. The lower strength of the rapidly cooled X-80 sample associated with the lower RT and higher FRT, as compared to the X-70 plate with the higher FRT, was probably due to the higher cooling interruption temperature (650 °C instead of 620 °C). This is consistent with the slightly higher Vickers hardness of this sample in comparison with the X-70 sample, see Tables 4. 3 and 4.4. These results indicate the effect of cooling interruption temperature on the characteristics of the acicular ferrite, as discussed in Chapter Four, and consequently on the yield strength, as discussed in the next section.

6.3.2 Effect of Cooling Conditions on the Yield Strength Anisotropy

Low Niobium Steel (X-70)

As can be seen in Fig. 6.9, both accelerated cooling and intercritical rolling increased the yield strengths of the X-70 plates by grain refinement and by increasing the dislocation density, respectively. These increases are always accompanied by increases in the hardnesses of the plates with the direct proportionality specified in the literature [103].

Accelerated cooling, which results in higher yield strength, was associated with greater yield strength anisotropy as well, as compared to air cooling, Fig. 6.10. However, ferrite rolling, which also increases the yield strength, does not contribute to the anisotropy of the yield strength in this case. As can be seen in Fig. 6.10, the yield strength anisotropy of the air cooled samples is within the experimental error (±2 %), indicating that there is almost no anisotropy in these samples.

As discussed in the previous chapter, accelerated cooling promotes variant selection and changes the orientation distribution of the ferrite transformation products; it also increases the severity of the fibre textures. The deformation behaviours of individual grains as single crystals depend on their crystallographic orientations, so that processing parameters such as cooling rate and cooling interruption temperature can contribute to the anisotropy of mechanical properties. Figure 6.10 shows that the highest yield strength anisotropies occurred in the samples cooled at 20 °C s^{-1}. As was shown in Chapter Five, similar textures were developed in the X-70 plates rapidly cooled at 6 °C s^{-1} and 20 °C s^{-1} . It can therefore be concluded that the morphology of the acicular ferrite (or bainite) also contributes to the yield strength anisotropy. This issue is discussed in the next section.

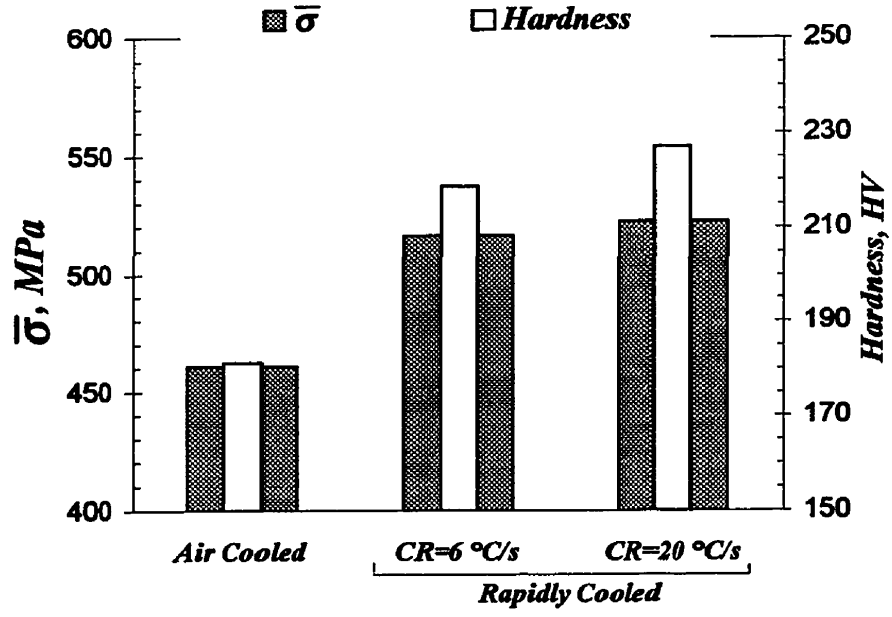

(a)

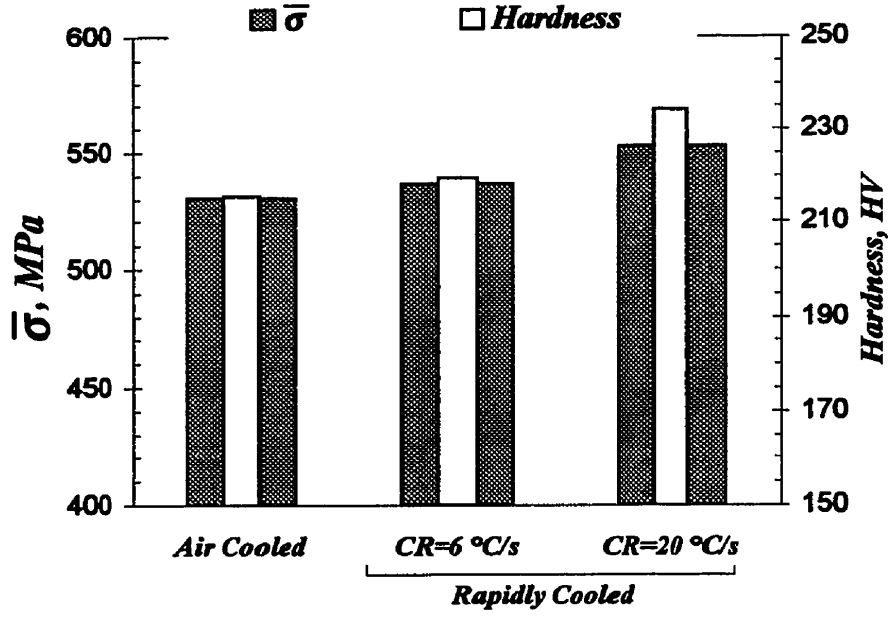

(b)

Figure 6.9 Yield strength versus microhardness in the X-70 samples finish rolled *(a) above* and *(b) below* the Ar_3.

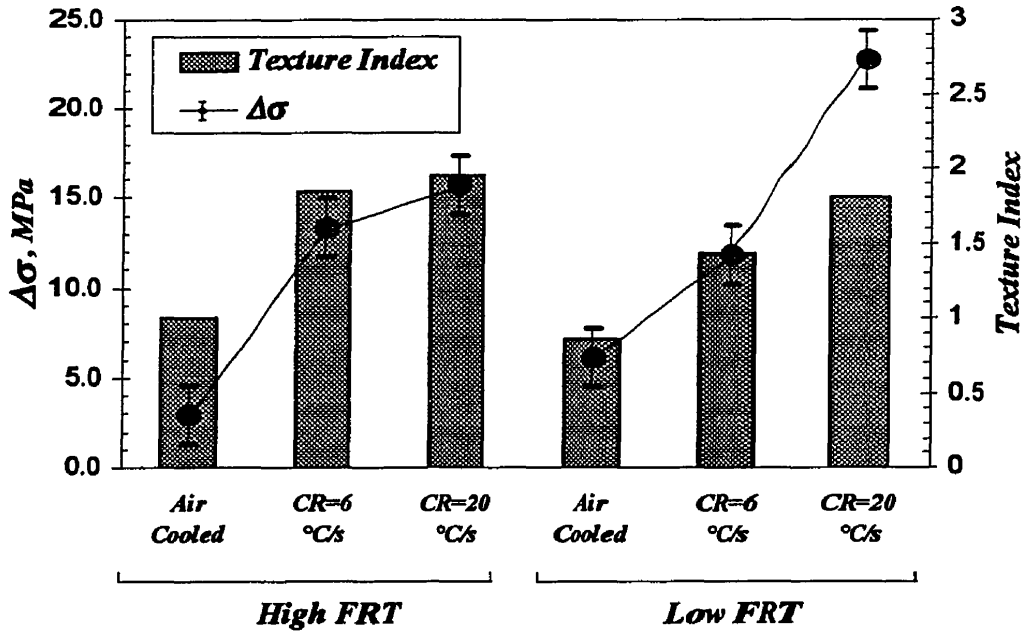

Figure 6.10 Yield strength anisotropy ($\Delta\sigma$) of the X-70 samples.

High Niobium Steel (X-80)

As was shown in Chapter Four, accelerated cooling of the X-80 plates produced a fine microstructure of acicular ferrite or bainite. Air cooling of the X-80 plates developed a mixture of polygonal ferrite and acicular ferrite microstructures. The bainitic ferrite that grows from deformed austenite is known to contain a greater density of dislocations [150]; this is expected from the displacive mechanism of bainite formation, in which ferrite can inherit the dislocations present in the parent austenite [151]. However, such inheritance is more effective during accelerated cooling as the amount of recovery is limited. Tsuzaki et al. [152] demonstrated that much smaller aspect ratios of the bainite sheaves are adopted by transformation from deformed austenite, leading to a finer ferrite grain size.

As discussed in Chapter Four, greater values of the effective interfacial area of the austenite (S_V), which represent the degree of austenite deformation before transformation, provide more nucleation sites for acicular ferrite or bainite, leading to finer microstructures. This is evident from Fig. 6.11, where samples associated with low FRT's (with greater S_V values) have higher yield strengths.

There is extensive evidence that dislocations are predominantly generated at grain boundaries at low strains [153-156]; such generation has even been observed at stresses below the yield stress [157]. It can therefore be postulated that the higher S_V's of the samples associated with the lower FRT's were responsible for the higher dislocation densities. The other source of dislocation production in these samples could be work hardening of the ferrite during intercritical rolling.

The degree of supercooling during accelerated cooling is another effective grain refinement parameter as it increases the ferrite nucleation rate. As was shown in Chapter Four, an intermediate cooling rate employed in conjunction with an intermediate cooling interruption temperature resulted in more grain refinement which, in turn, led to higher strength, as can be seen in Fig. 6.11.

It is apparent from Fig. 6.11 that, when the higher cooling rate was employed, higher yield strengths were produced in the samples associated with the lower RT and higher FRT than the corresponding higher RT plates. This implies that, despite the reduced precipitation hardening (due to less Nb in solution), greater grain refinement and higher dislocation densities were developed in these plates. By contrast, the strengths of the lower RT air cooled and moderately cooled (20 °C s^{-1}) samples were *lower* than the corresponding higher RT samples. This is despite the higher S_V values (i.e. possible finer grain sizes) in these plates, and indicates the effect of supercooling on grain refinement and on increasing the dislocation density.

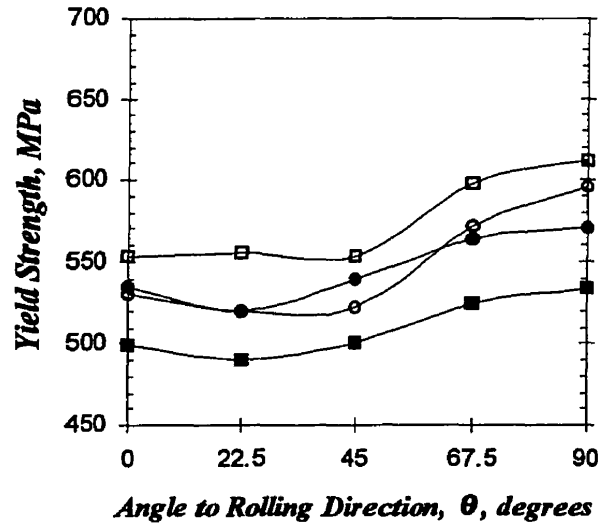

(a) CIT=620°C

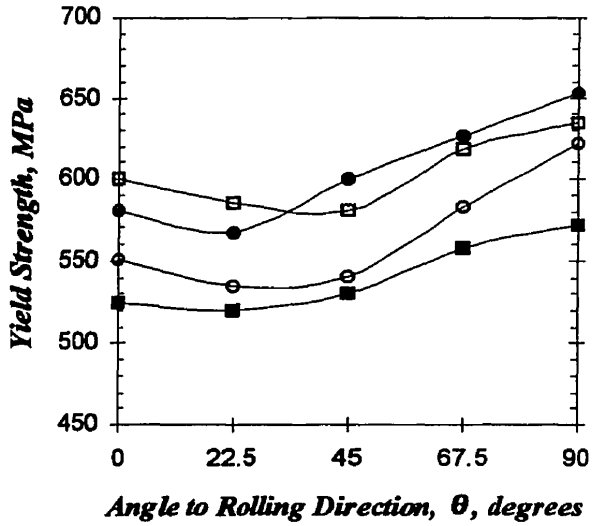

(b) CIT=520°C

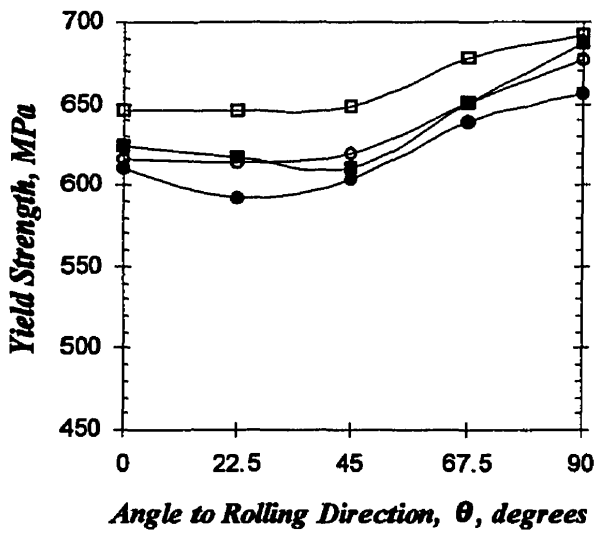

(c) CIT=420°C

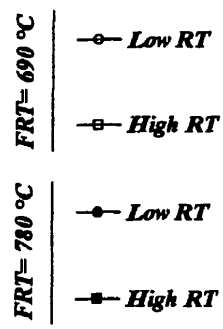

Figure 6.11 Effects of cooling rate and cooling interruption temperature on the yield strength anisotropy of the X-80 plates; *(a)* to *(c)* CR=40°C s^{-1},

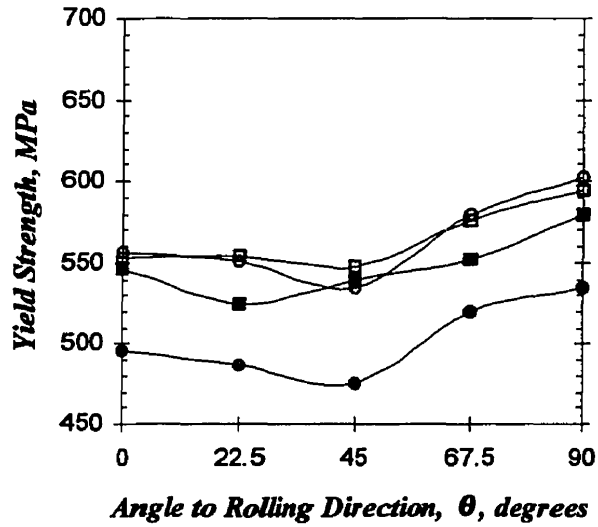

(d) CIT=620°C

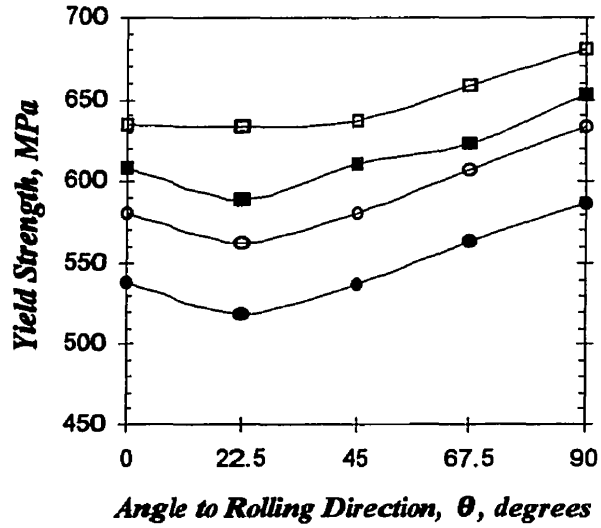

(e) CIT=520°C

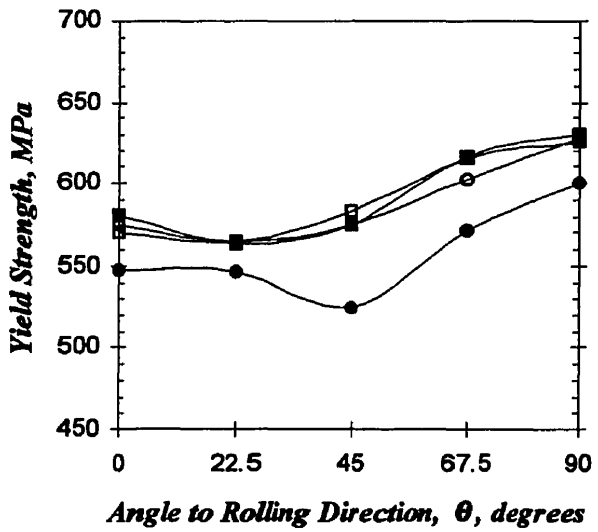

(f) CIT=420°C

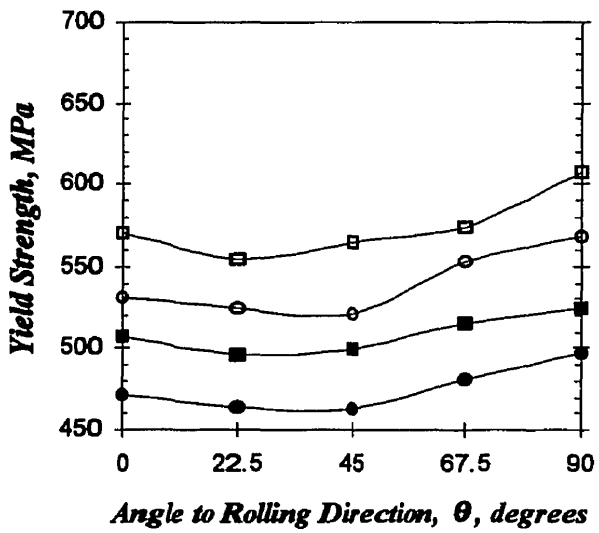

(g) Air Cooled

Figure 6.11 (continued) *(d)* to *(f)* CR=20°C s^{-1}, and (g) air cooled.

The yield strengths of all the X-80 samples presented in Fig. 6.11 are compared with their hardnesses in Figs. 6.12 to 6.14. As can be seen in these figures, there is reasonable agreement between the hardnesses and yield strengths of the plates. This again confirms the conclusions about the effect of cooling rate and cooling interruption temperature on the yield strength by refinement of the acicular microstructure and raising the dislocation density.

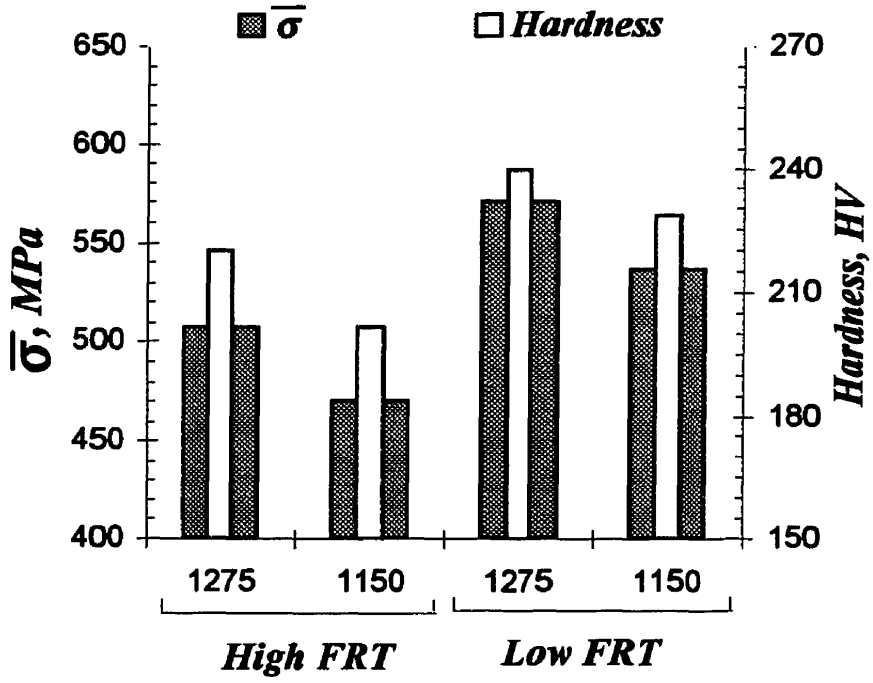

Figure 6.12 Yield strength versus hardness in the air cooled X-80 plates.

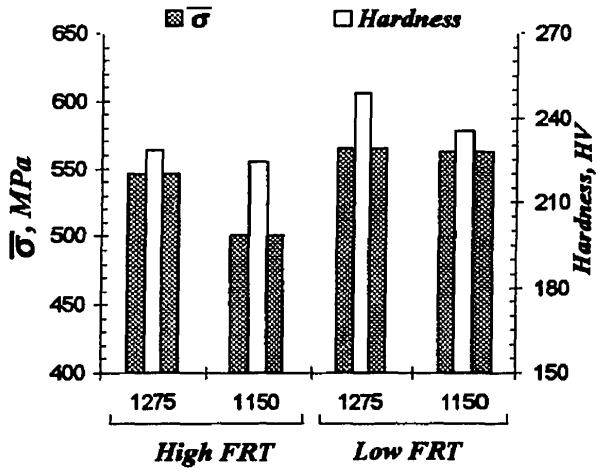

(a) CIT= 620 °C

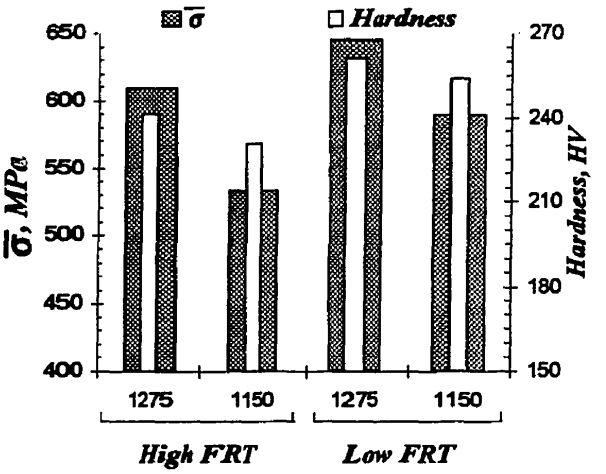

(b) CIT= 520 °C

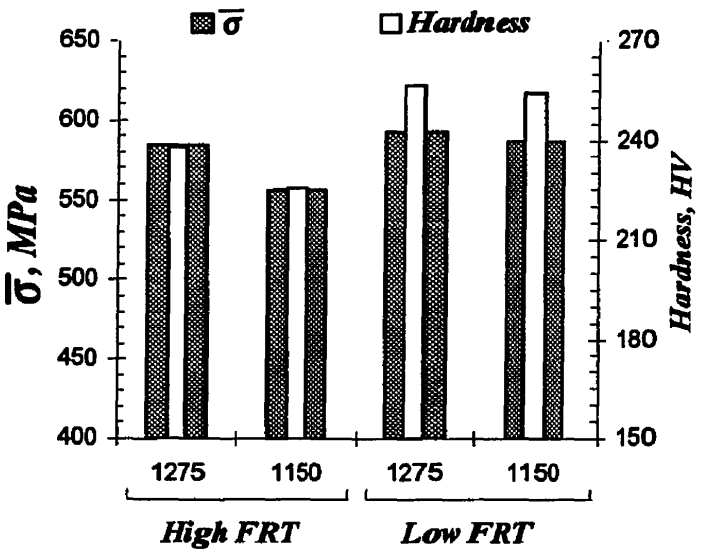

(c) CIT= 420 °C

Figure 6.13 Yield strength versus hardness in the X-80 plates rapidly cooled at 20 °C s^{-1}.

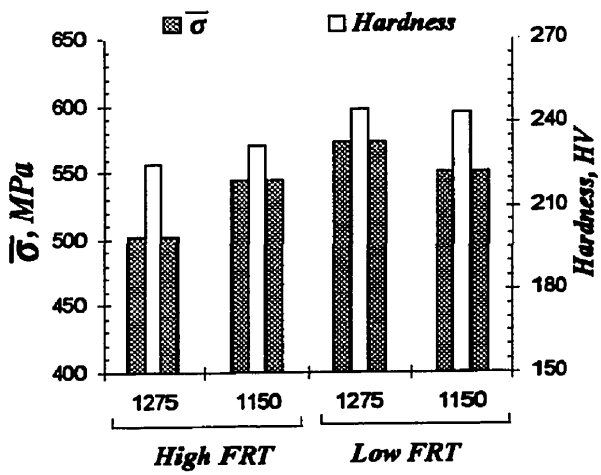

(a) CIT= 620 °C

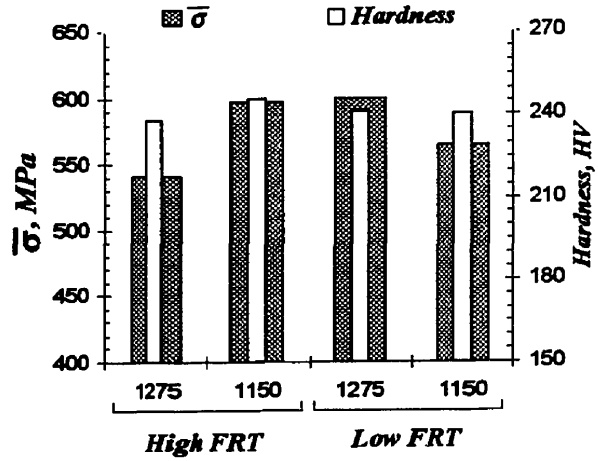

(b) CIT= 520 °C

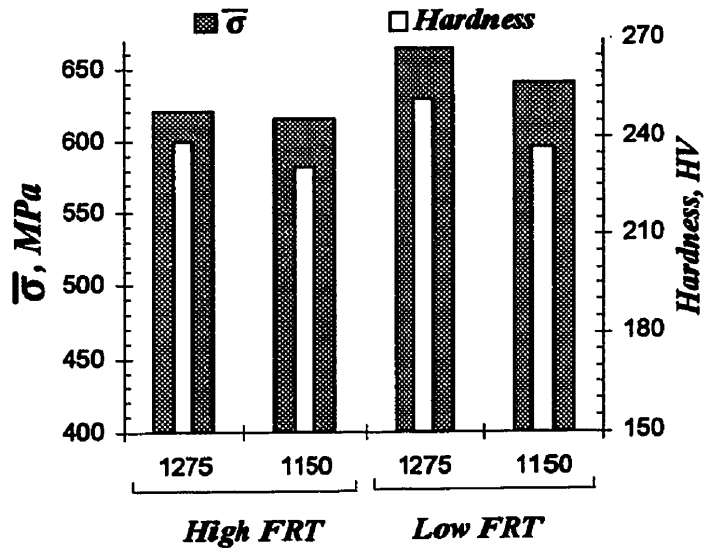

(c) CIT= 420 °C

Figure 6.14 Yield strength versus hardness in the X-80 plates rapidly cooled at 40 °C s^{-1}.

6.3.3 Planar Anisotropy of the Yield Strength

The planar anisotropies of the X-80 yield strengths were calculated using equation 6.2. These values are illustrated in Figs. 6.15 and 6.16 for the samples finish rolled above and below the Ar_3, respectively, together with the corresponding texture indices calculated from eq. 5.2.

It is evident from Figs. 6.15 and 6.16 that lower degrees of yield strength anisotropy were developed in the air cooled samples. It was shown in the previous chapter that an increase in the severity of the texture (texture index) in these samples was accompanied by increases in the RD and TD fibre intensities. Here, no direct relations between the intensities of these fibres and the yield strength anisotropies were detected. However, as can be seen in Fig. 6.15, the anisotropies of the rapidly cooled samples finish rolled in the austenite region generally increased with the relevant texture indices.

More scatter of the yield strength anisotropy was observed in the samples finish rolled in the two phase region so that the correlation between the anisotropy of the rapidly cooled samples and their texture indices, Fig. 6.16, is not quite as good. Nevertheless, it is evident that the low RT samples, with sharper textures (i.e. higher texture indices), have more planar anisotropies. The fact that there is more scatter in the results for the rapidly cooled and low FRT samples implies that the grain morphology (acicular ferrite in the rapidly cooled plates and/or pancaked ferrite in the low FRT samples) and the dislocation distribution may also play roles in determining the planar anisotropy.

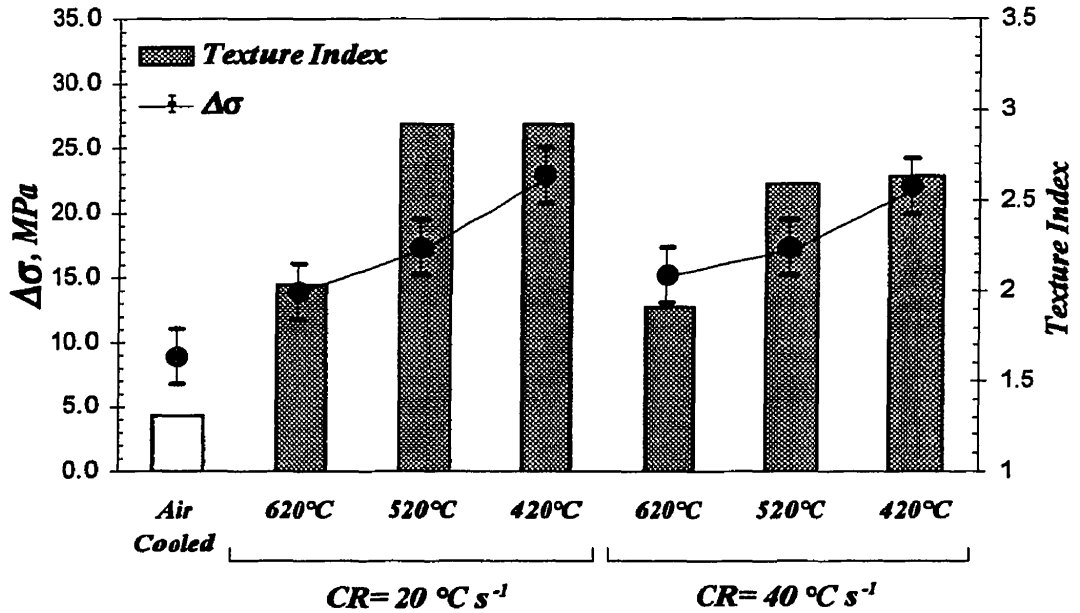

(a)

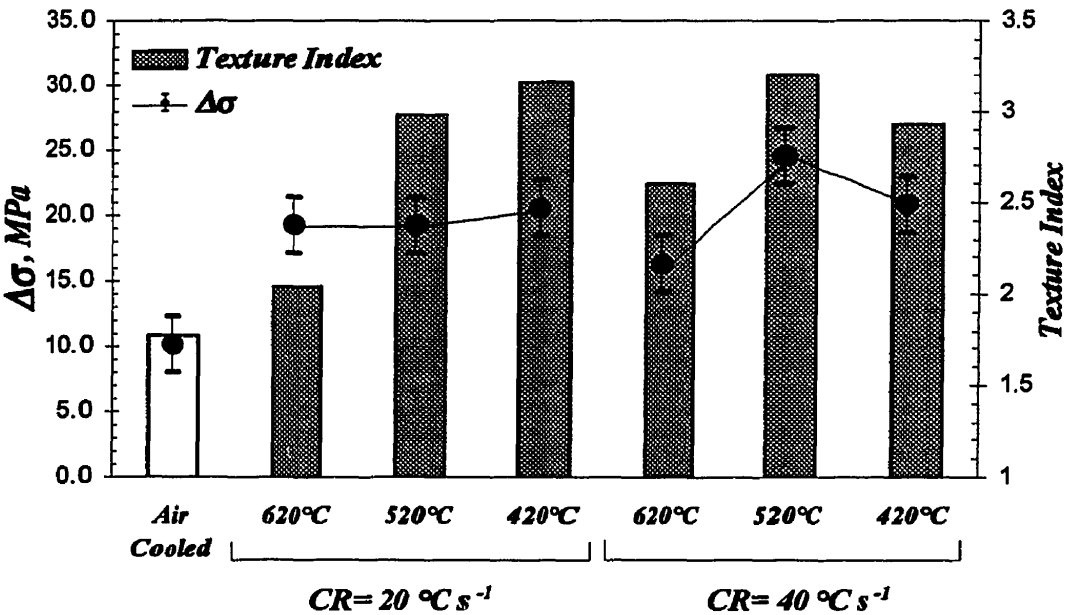

(b)

Figure 6.15 Anisotropy of yield strength of the X-80 steels finish rolled *above* the Ar_3; *(a)* RT=1275 °C and *(b)* RT=1150 °C.

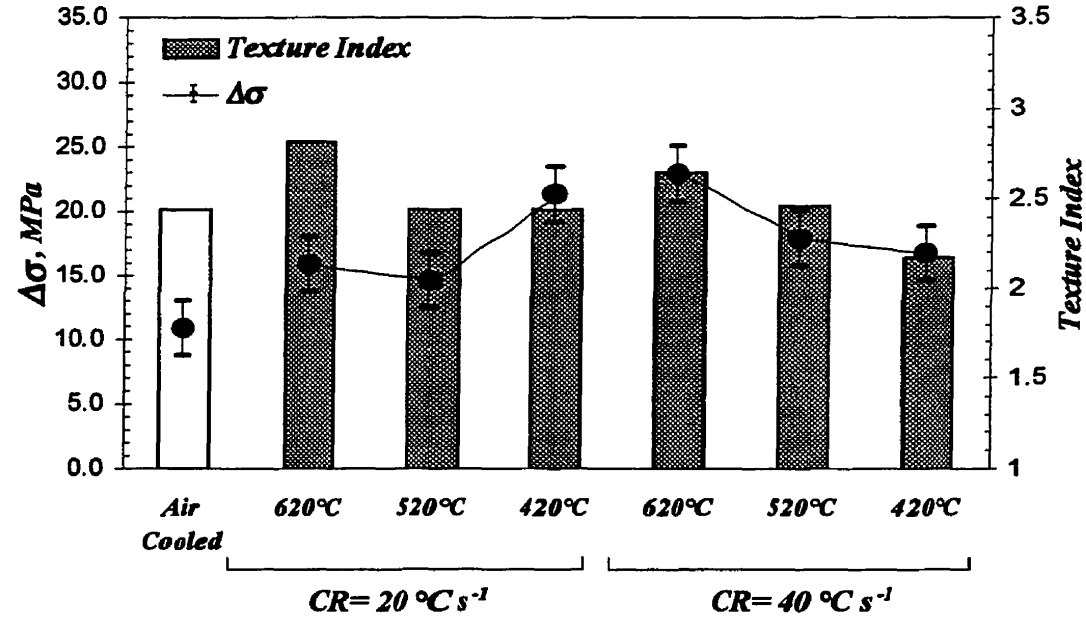

(a)

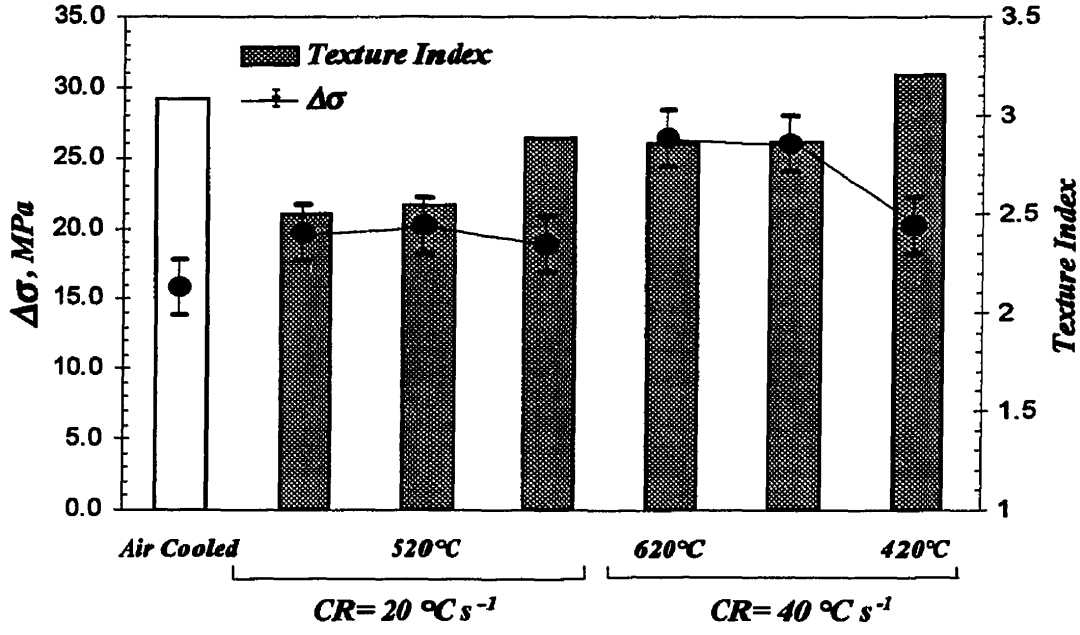

(b)

Figure 6.16 Anisotropy of yield strength of the X-80 steels finish rolled *below* the Ar_3; *(a)* RT=1275 °C and *(b)* RT=1150 °C.

6.3.4 Model Predictions of Yield Strength Anisotropy

There are several models that can be used to calculate the properties of polycrystals from their textures. In this investigation, the relaxed constraint methods were employed together with the full constraint model for calculation of the normalized yield stress ratio ($\sigma(\theta)/\sigma(0)$). The relaxed constraint models take into consideration the grain morphology by relaxing some of the shear components; this leads to a decrease in the number of active slip systems from five in the full constraint model to four (lath model), three (pancake model), and two (RC2 model), respectively.

The angular variation of normalized yield stress ($\sigma(\theta)/\sigma(0)$) was simulated using a gaussian orientation distribution for each texture component. The order of truncation was 22 (l_{max} = 22), and a gaussian spread of ω_0 = 15° was employed together with a background of 30% random orientations. Here, the ratios of the critical resolved shear stresses (CRSS) on the {110} and {112} slip planes, as defined by eqs. 2.16 and 2.17, were chosen to be $\alpha_S = \alpha_H = 0.95$. Predictions for the ideal texture components obtained in this way are presented in Fig. 6.17.

As can be seen in these figures, the behaviours of the ND fibre components (i.e. {111}<110>, {111}<123>, and {111}<112>) predicted by the relaxed constraint and FC models display opposite trends. Considerable differences are also observed between the angular variations of the other orientations called for by the FC and relaxed constraint models. For instance, more anisotropy of the {113}<110> and {112}<110> is predicted by the RC models than the FC. This shows that the choice of plastic anisotropy model has a strong effect on the predicted yield strength anisotropy.

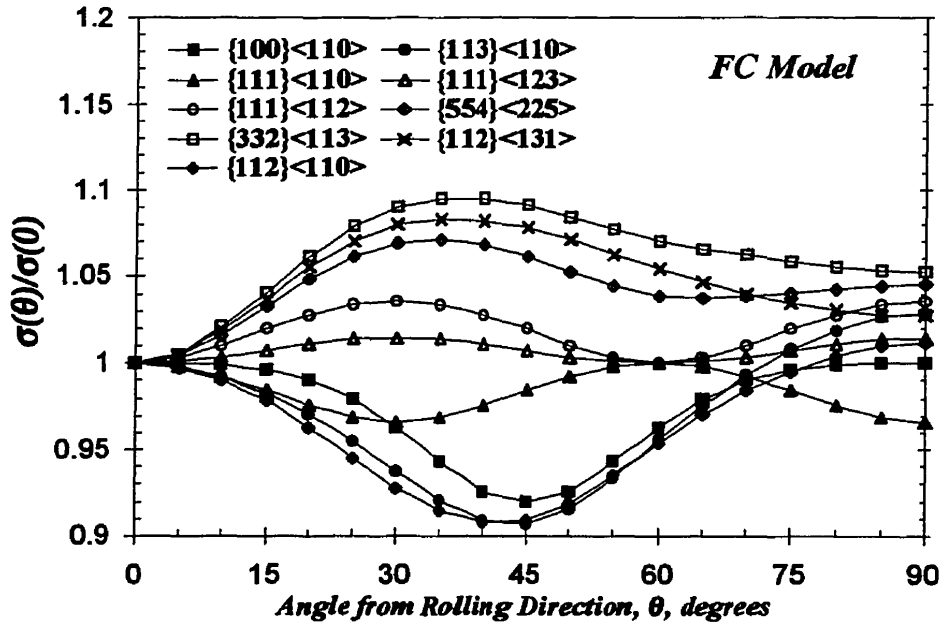

(a)

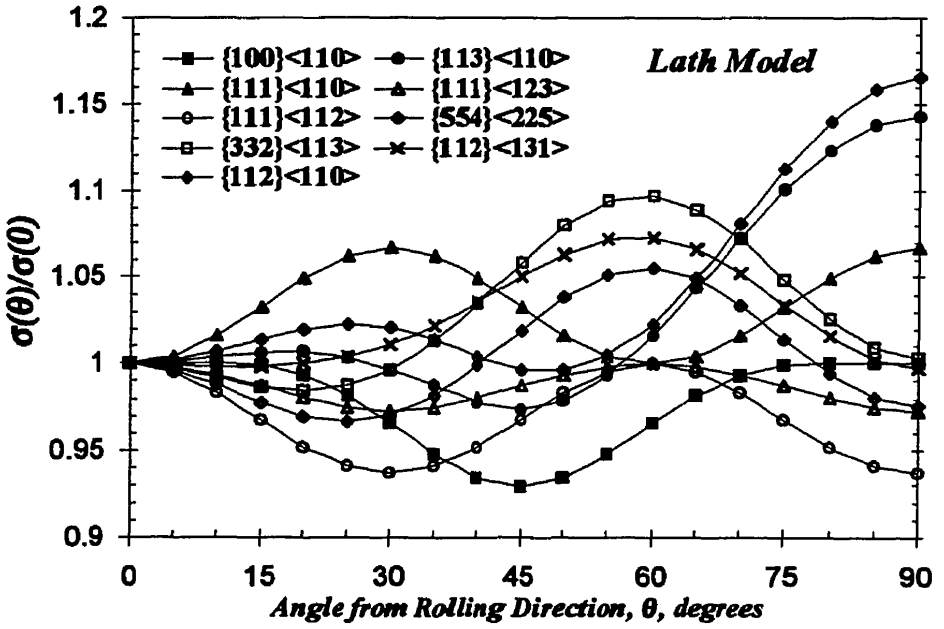

(b)

Figure 6.17 Angular variation of the yield stress ratio for selected ideal orientations; *(a)* full constraint (FC) and *(b)* lath model.

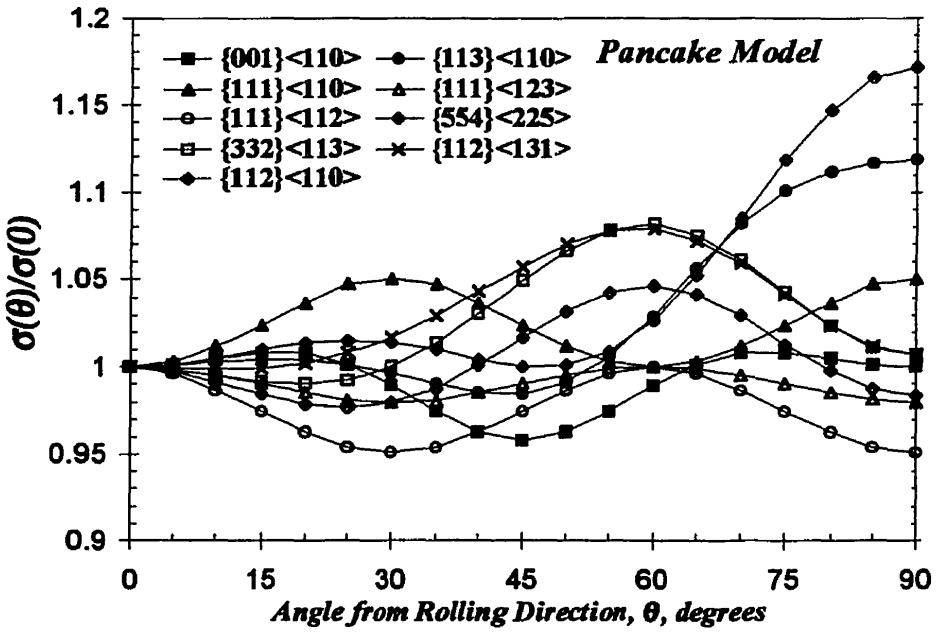

(c)

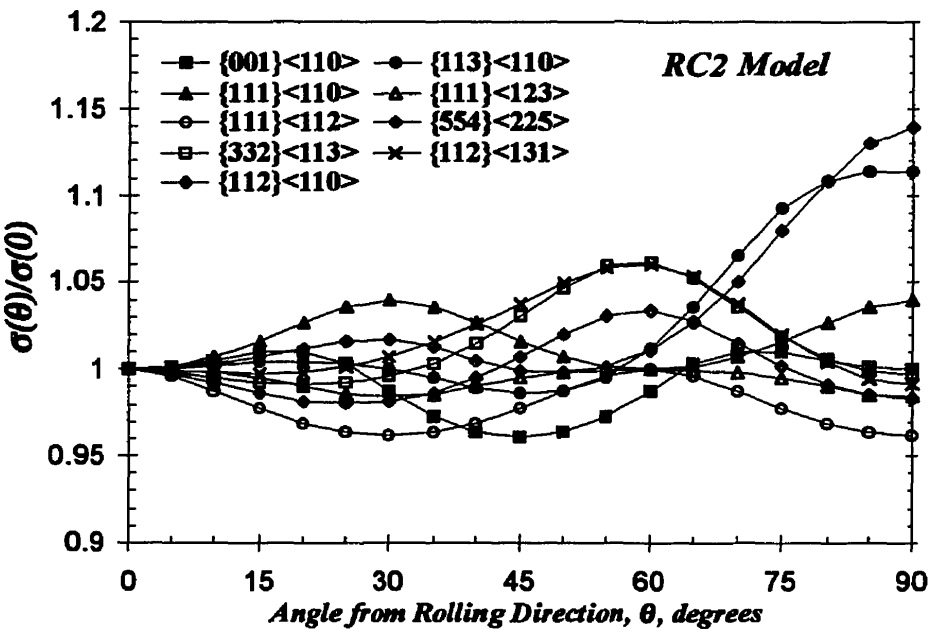

(d)

Figure 6.17 (continued) *(c)* pancake (RC3) and *(d)* RC2 model.

Substituting $K(\theta)$ for $\sigma(\theta)/\sigma(0)$ the anisotropy of the yield stress ratio (ΔK) can be defined using eqs. 6.3 and 6.4, leading to the dependences shown in Fig. 6.17 for the ideal orientations considered above.

$$\bar{\sigma} = \frac{2}{\pi}\int_0^{\pi/2}\sigma(\theta)d\theta = \frac{2}{\pi}\int_0^{\pi/2}\sigma(0)K(\theta)d\theta = \frac{\sigma(0)}{8}\left(K_0 + 2K_{22.5} + 2K_{45} + 2K_{67.5} + K_{90}\right)$$

$$= \sigma(0)\cdot\bar{K} \qquad (6.3)$$

$$\Delta\sigma = \frac{2}{\pi}\int_0^{\pi/2}\left(\left|\bar{\sigma} - \sigma(\theta)\right|\right)d\theta = \frac{2}{\pi}\int_0^{\pi/2}\left(\left|\sigma(0)\bar{K} - \sigma(0)K(\theta)\right|\right)d\theta$$

$$= \frac{\sigma(0)}{8}\left(\left|\bar{K} - K_0\right| + 2\left|\bar{K} - K_{22.5}\right| + 2\left|\bar{K} - K_{45}\right| + 2\left|\bar{K} - K_{67.5}\right| + \left|\bar{K} - K_{90}\right|\right)$$

$$= \sigma(0)\cdot\Delta K \qquad (6.4)$$

The planar anisotropies (ΔK) associated with various crystallographic orientations predicted by the different models are displayed in Fig. 6.18. As can be seen, the lath and pancake models call for higher planar anisotropies than the other two models, the greatest values pertaining to the RD fibre components. According to the predictions of the models employed, the ND fibre components are associated with the lowest anisotropies. The TD fibre components, especially the {332}<113>, also display relatively high anisotropies of the yield stress ratio when the lath and pancake models are employed.

Calculations based on the method described above were carried out for two combinations of ideal orientations, leading to the results presented in Fig. 6.19. For this purpose, two RD ({113}<110> and {112}<110>), two TD ({332}<113> and {554}<225>), and two ND ({111}<123> and {111}<112>) fibre components were selected, together with the transformed S ({112}<131>) orientation.

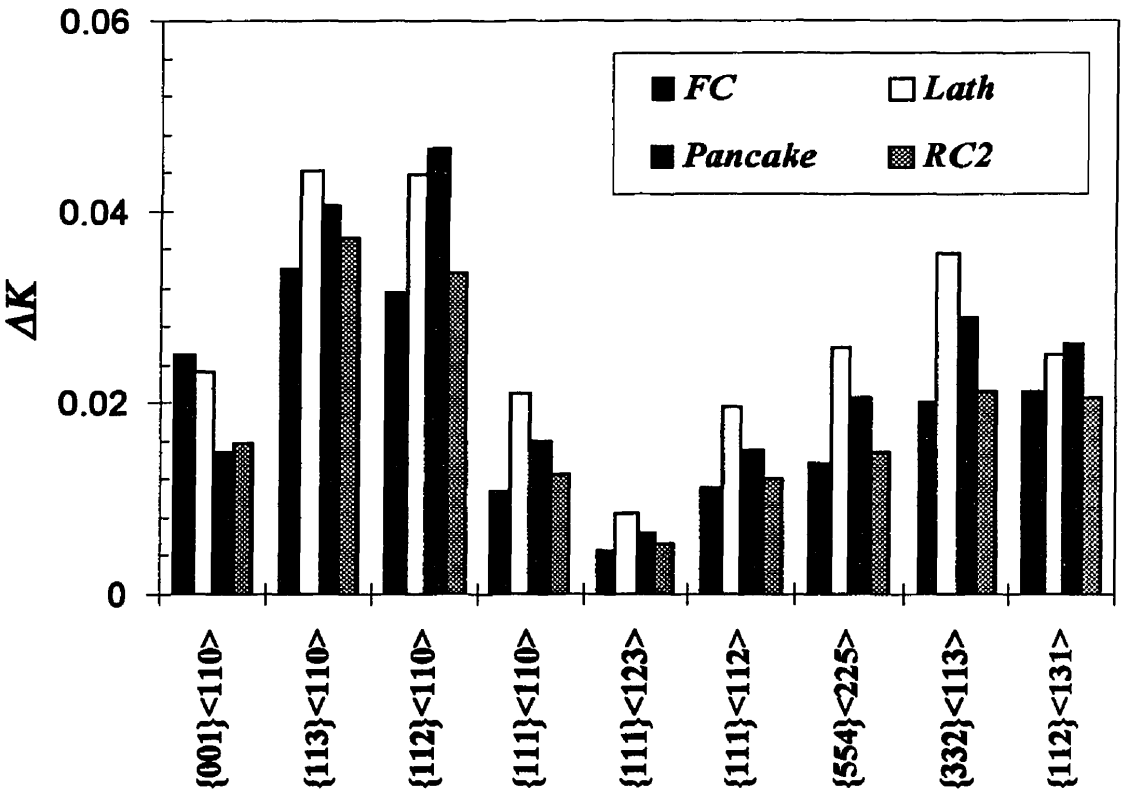

Figure 6.18 Anisotropy of the yield stress ratio (ΔK) predicted by different models for the ideal orientations considered here.

When equal fractions of these orientations are combined, it appears that a higher yield stress ratio is called for by the FC than by the pancake and RC2 models, Fig. 6.19a. It is therefore evident that the yield strength anisotropy depends largely on the choice of plastic anisotropy model. By contrast, when the volume fractions of the two RD fibre components are about twice those applicable to each of the remaining components, the transverse yield stress ratios predicted by the pancake and RC2 models increase, Fig. 6.19b.

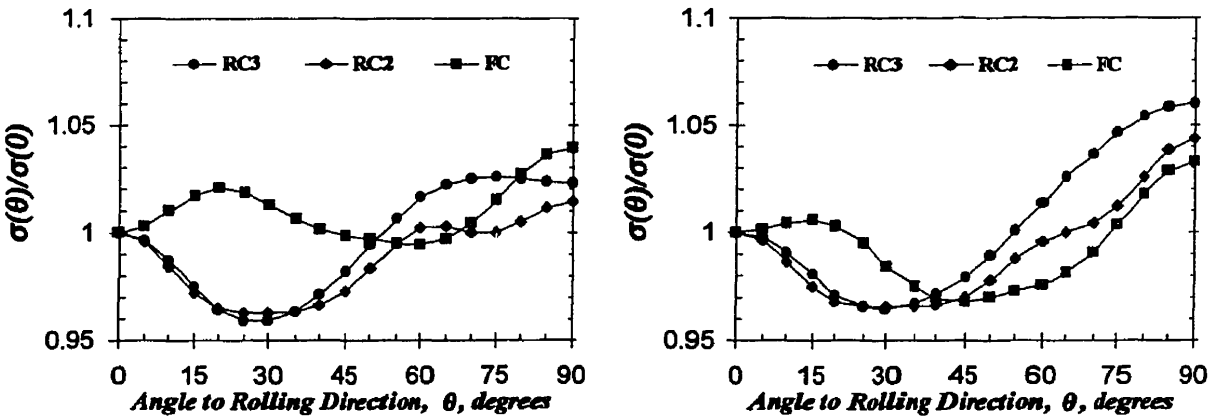

Figure 6.19 Angular variation of the yield stress ratio for *(a)* equal volume fractions of the texture components considered and *(b)* double the intensities of the {113}<110> and {112}<110> components. The latter change leads to an increase in the transverse yield stress ratio (solid circles).

In the case of the measured textures, however, the similarities in the intensities of the fibre components of the samples processed under different TMP conditions make the choice of model more difficult. Nevertheless, it can be seen from Fig. 6.20a that the calculated transverse yield stress ratio (according to the pancake model) increases with the intensity of the {112}<110> component in the high FRT samples. Similar remarks apply to the low FRT samples, Fig. 6.20b, despite the errors that apply to X-ray measurements, and the generally higher intensity levels.

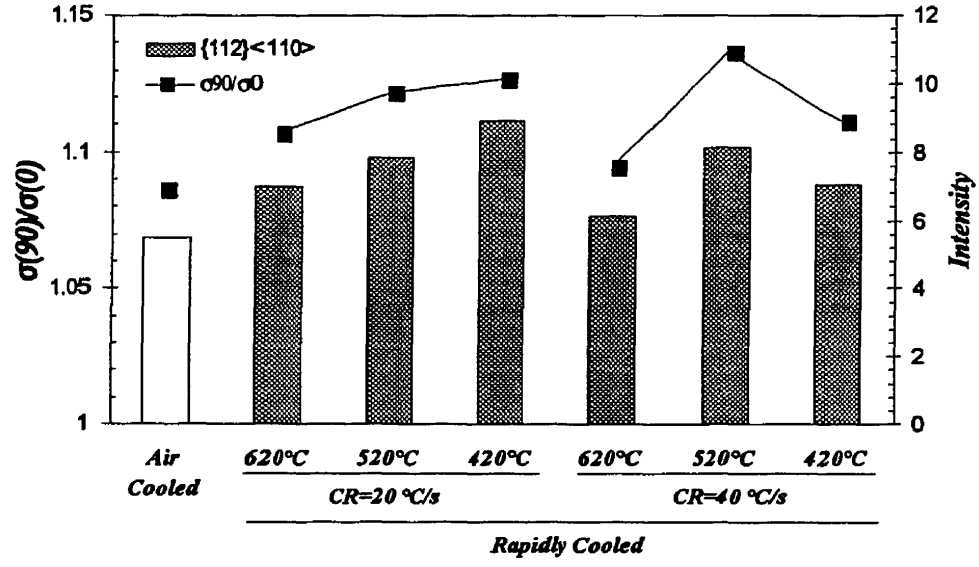

(a)

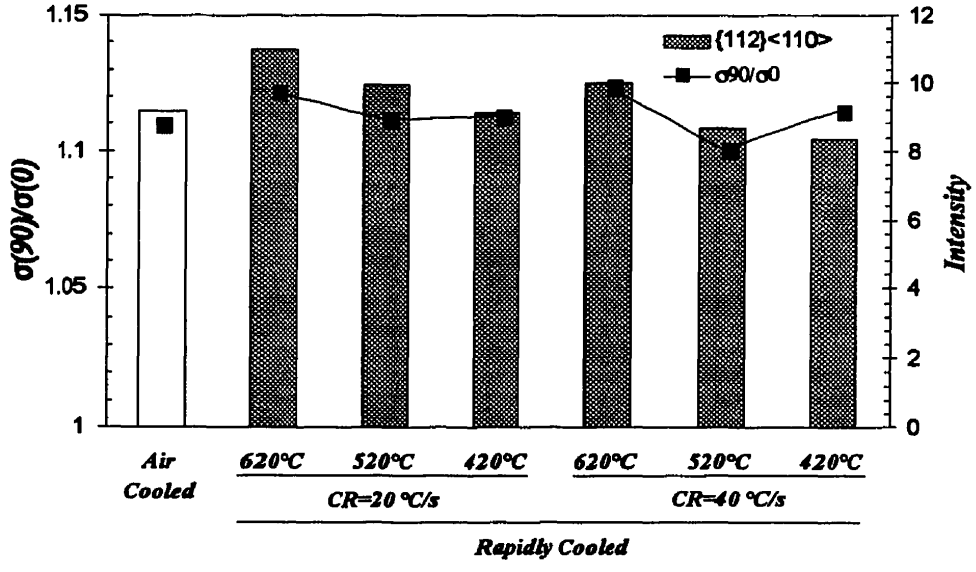

(b)

Figure 6.20 Transverse yield stress ratios predicted using the pancake model and the intensities of the {112}<110> component in the X-80 samples reheated at 1275 °C and finish rolled *(a) above* the Ar_3 and *(b) below* the Ar_3.

6.3.5 Comparison between Yield Stress Anisotropy Predictions and Experimental Results

The measured yield strength anisotropies of the X-70 samples are compared with the model predictions in Figs. 6.21 and 6.22. The equivalent diagrams for the X-80 plates are displayed in Figs. 6.23 through 6.26. The predictions are based on the four models described in the previous section. The experimental errors associated with the measured yield strengths are shown with the aid of error bars.

As can be seen in Figs. 6.21 and 6.22, there is reasonable agreement between the model predictions and the experimental results up to 67.5 degrees. Somewhat greater deviation from the RC predictions is observed along the transverse direction, particularly for the air cooled materials. The planar anisotropies of the yield strength, which were quantified as $\Delta\sigma = \sigma(0)\Delta K$, are compared for the X-70 samples in Table 6.1 with the measured values. This table shows that the planar anisotropies of the air cooled samples are close to the full constraint predictions. Nevertheless, it is evident from Figs. 6.21 and 6.22 that the samples generally display behaviours consistent with the RC models.

As was shown in Chapter Four, a duplex microstructure of bainite and polygonal ferrite developed in the air cooled samples. It was also shown, Chapter Five, that the TD fibre components are more intense in the rapidly cooled samples, an increase that is accompanied by increases in the volume fraction of the bainite phase. It can be therefore concluded that the proportion of the RD fibre components is higher in the polygonal ferrite grains. According to the angular variations of the yield stress ratio presented in Fig. 6.17 for the various texture components, low transverse stress ratios are called for by the FC model for the RD fibre components. As the FC model is appropriate for polygonal ferrite, this can explain the decrease in the transverse stress ratios of the air cooled samples.

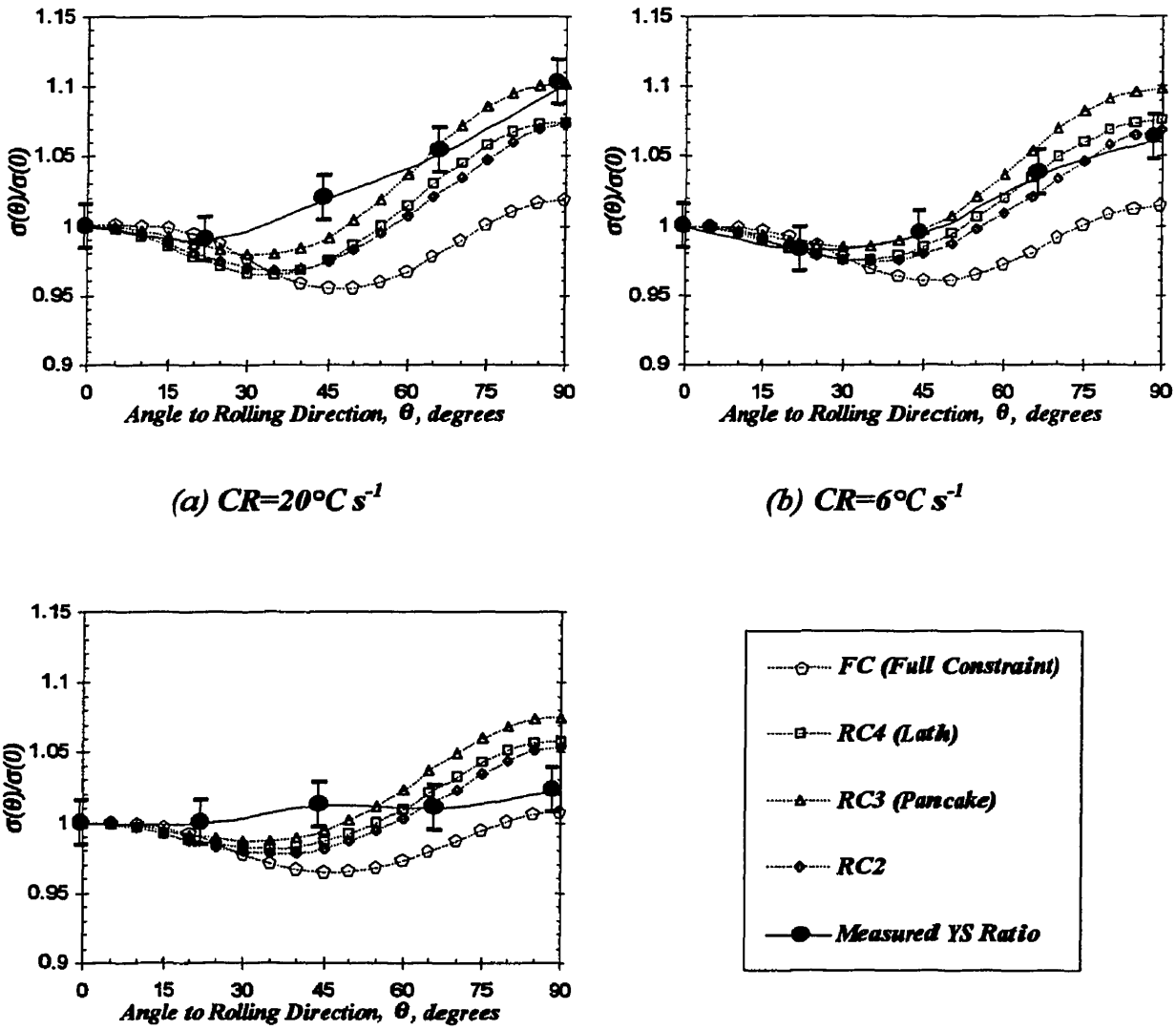

Figure 6.21 Comparison between the experimental observations and model predictions of the yield strength anisotropy of the X-70 plates reheated at 1225 °C and finish rolled at 790 °C; accelerated cooling was interrupted at 620°C.

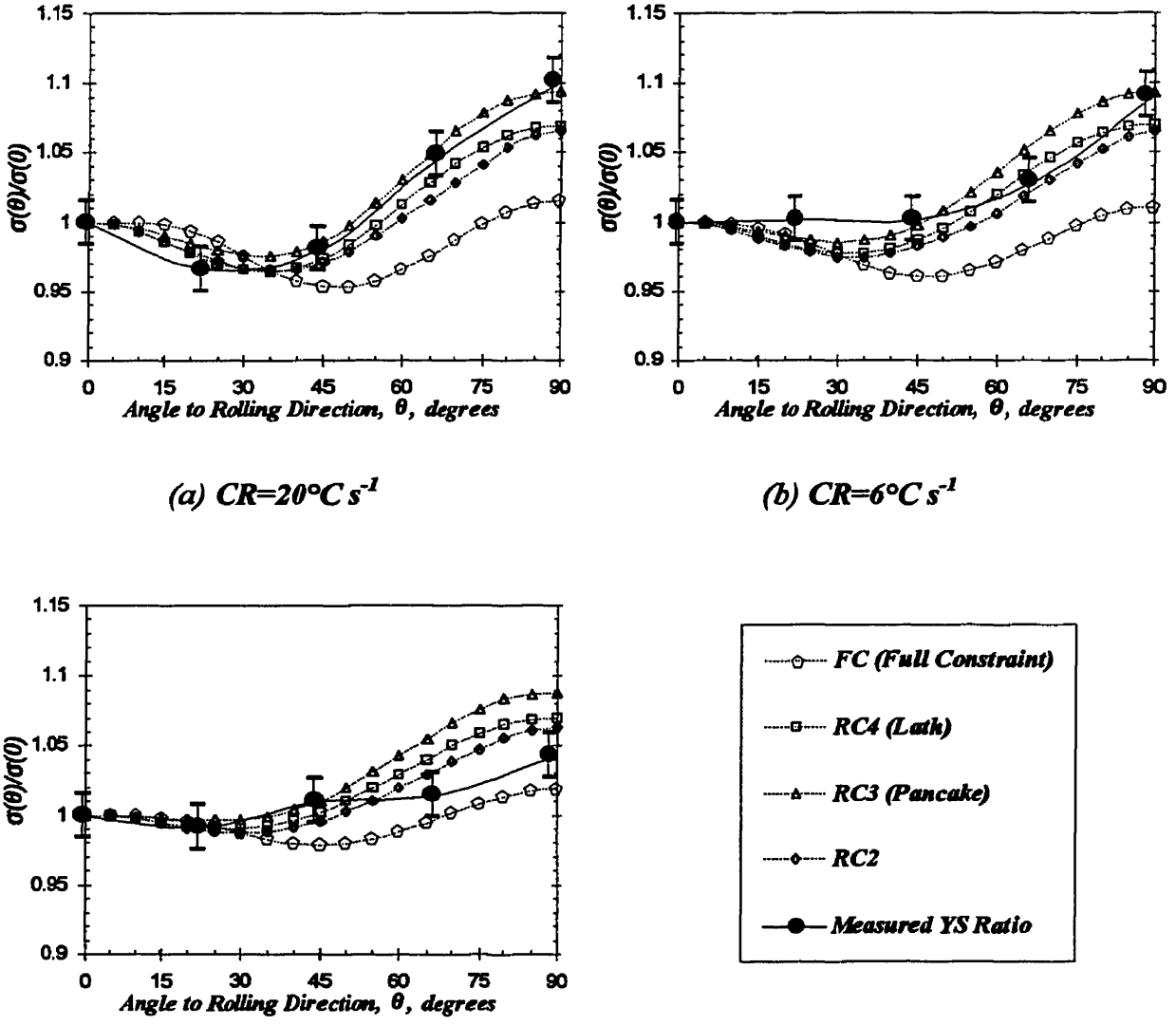

Figure 6.22 Comparison between the experimental observations and model predictions of the yield strength anisotropy of the X-70 plates reheated at 1225 °C and finish rolled at **730 °C**; accelerated cooling was interrupted at 620°C.

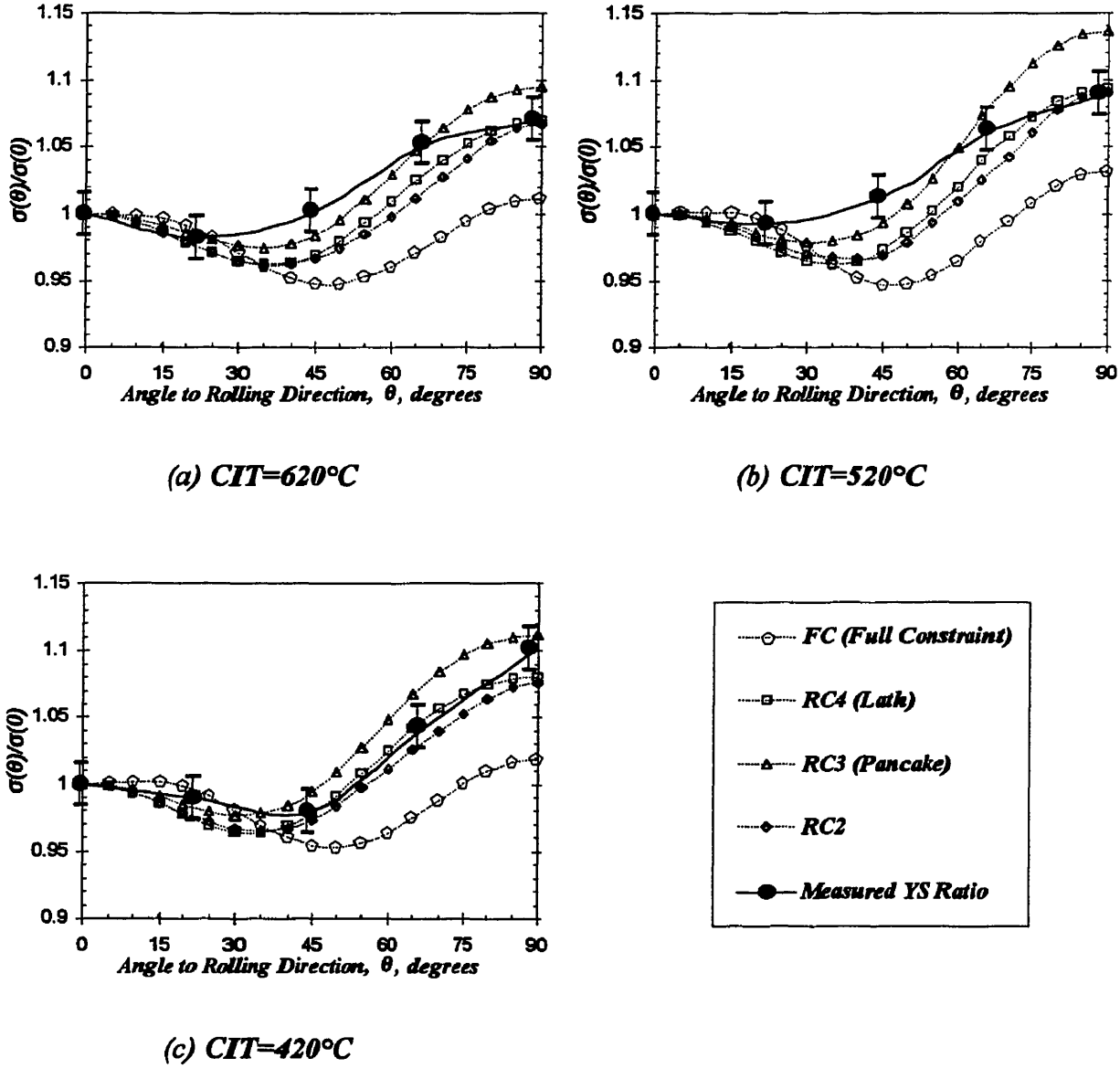

(a) CIT=620°C

(b) CIT=520°C

(c) CIT=420°C

Figure 6.23 Comparison between the experimental observations and model predictions of the yield strength anisotropy of the X-80 plates reheated at **1275 °C** and finish rolled at **780 °C**; *(a)* to *(c)* CR=40°C s^{-1},

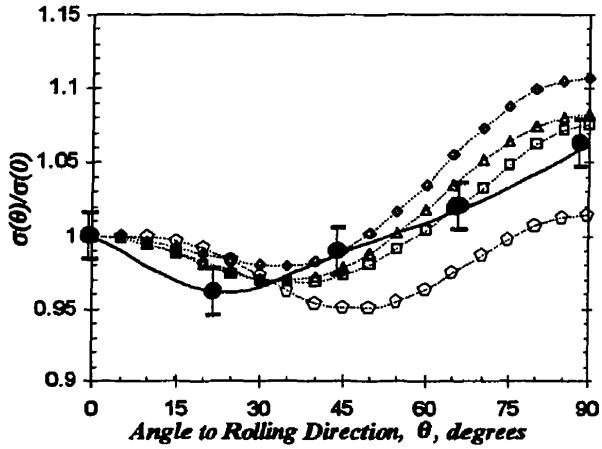

(d) CIT=620°C

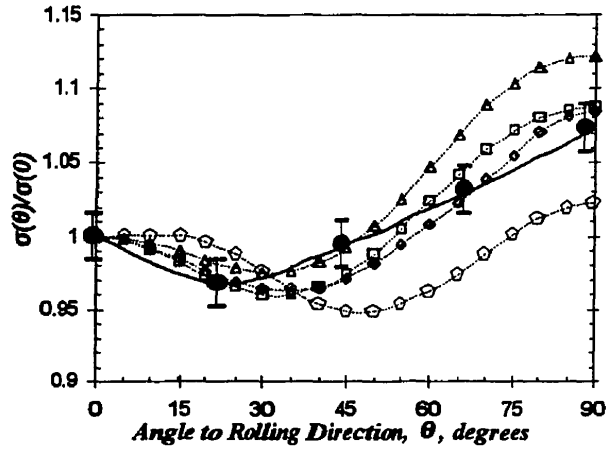

(e) CIT=520°C

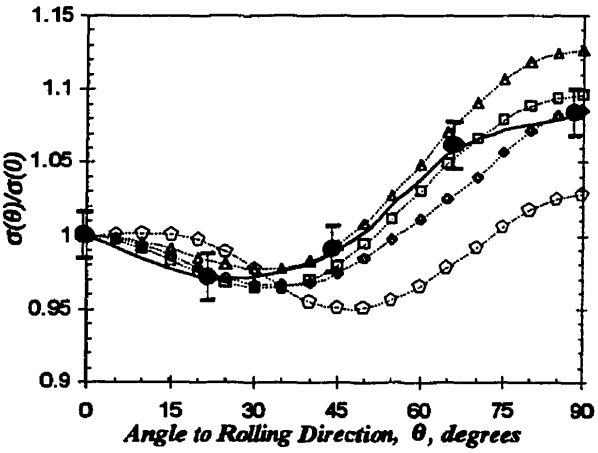

(f) CIT=420°C

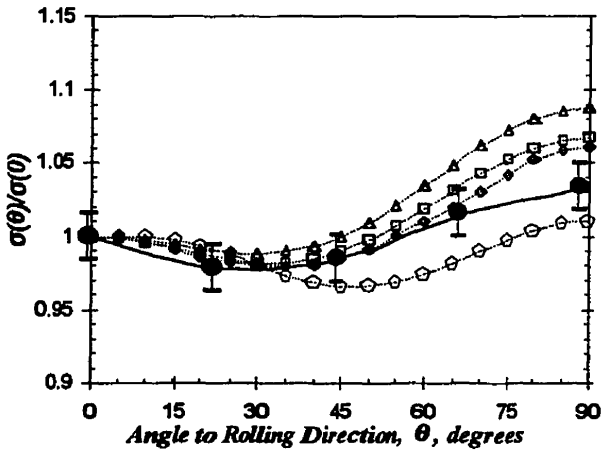

(g) Air Cooled

Figure 6.23 (continued) *(d)* to *(f)* CR=20°C s^{-1}, and (g) air cooled.

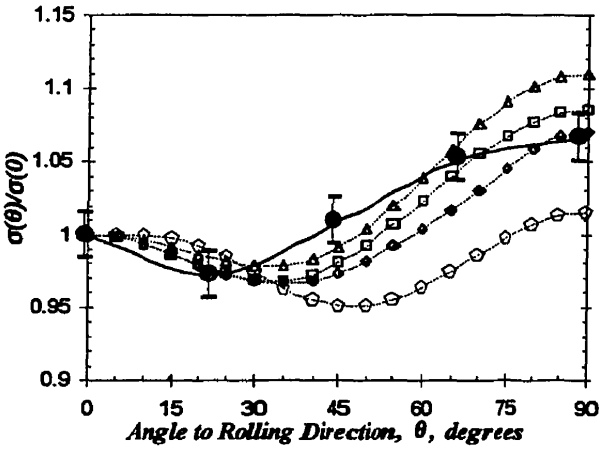

(a) CIT=620°C

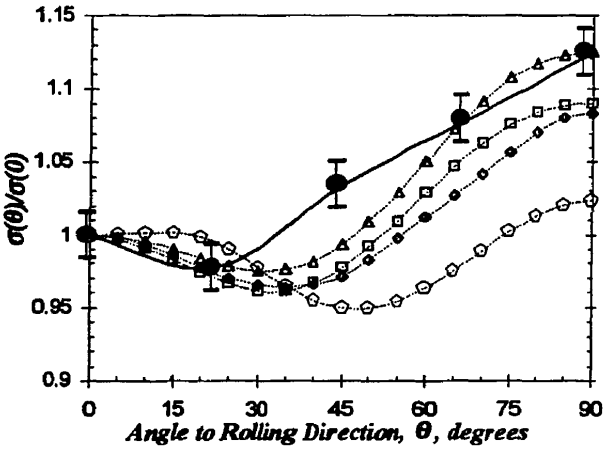

(b) CIT=520°C

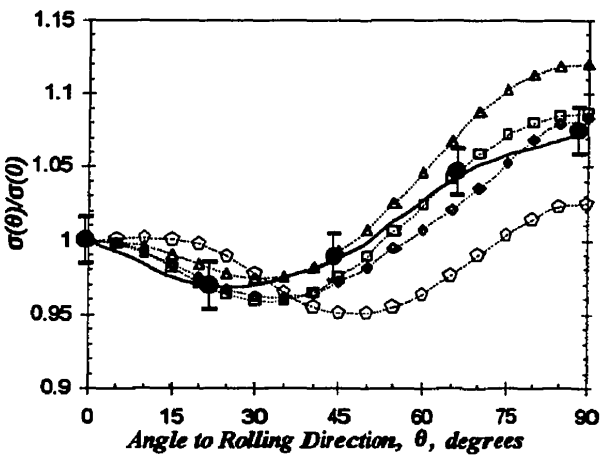

(c) CIT=420°C

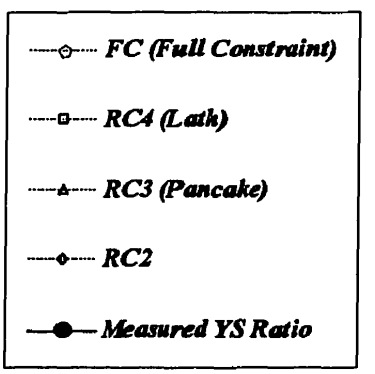

Figure 6.24 Comparison between the experimental observations and model predictions of the yield strength anisotropy of the X-80 plates reheated at **1150 °C** and finish rolled at **780 °C**; *(a)* to *(c)* CR=40°C s^{-1},

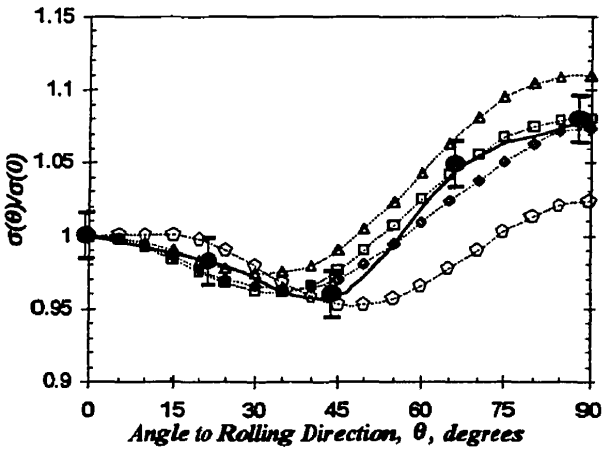

(d) CIT=620°C

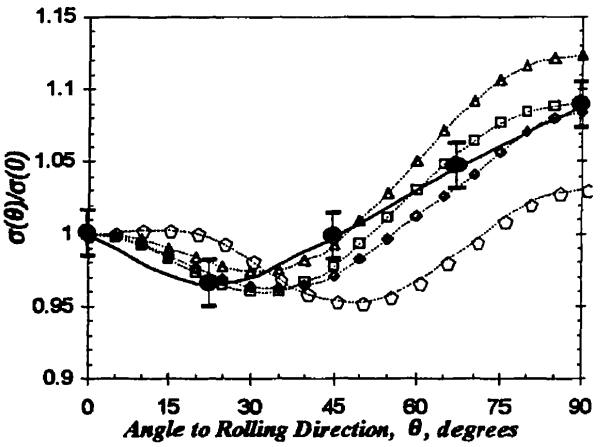

(e) CIT=520°C

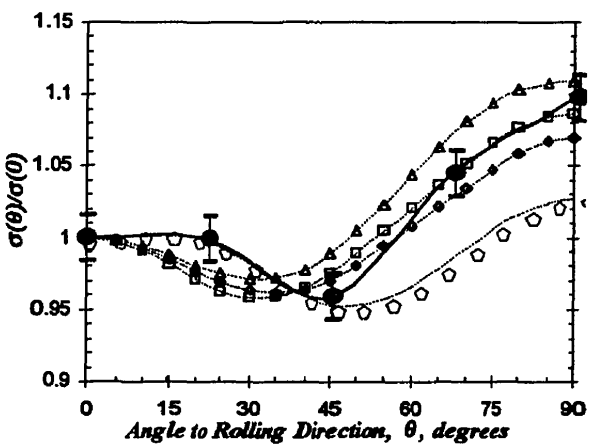

(f) CIT=420°C

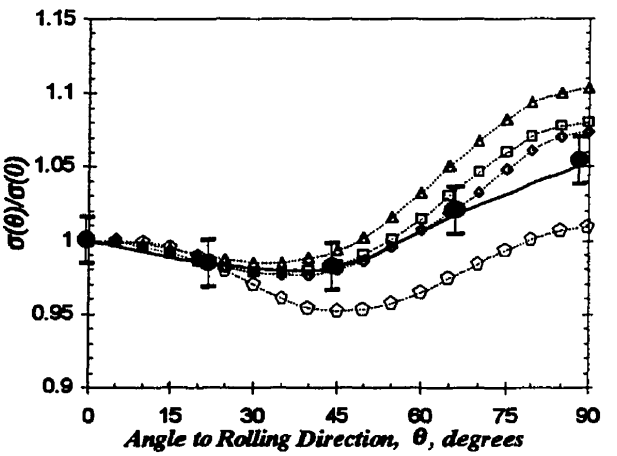

(g) Air Cooled

Figure 6.24 (continued) *(d)* to *(f)* CR=20°C s^{-1}, and (g) air cooled.

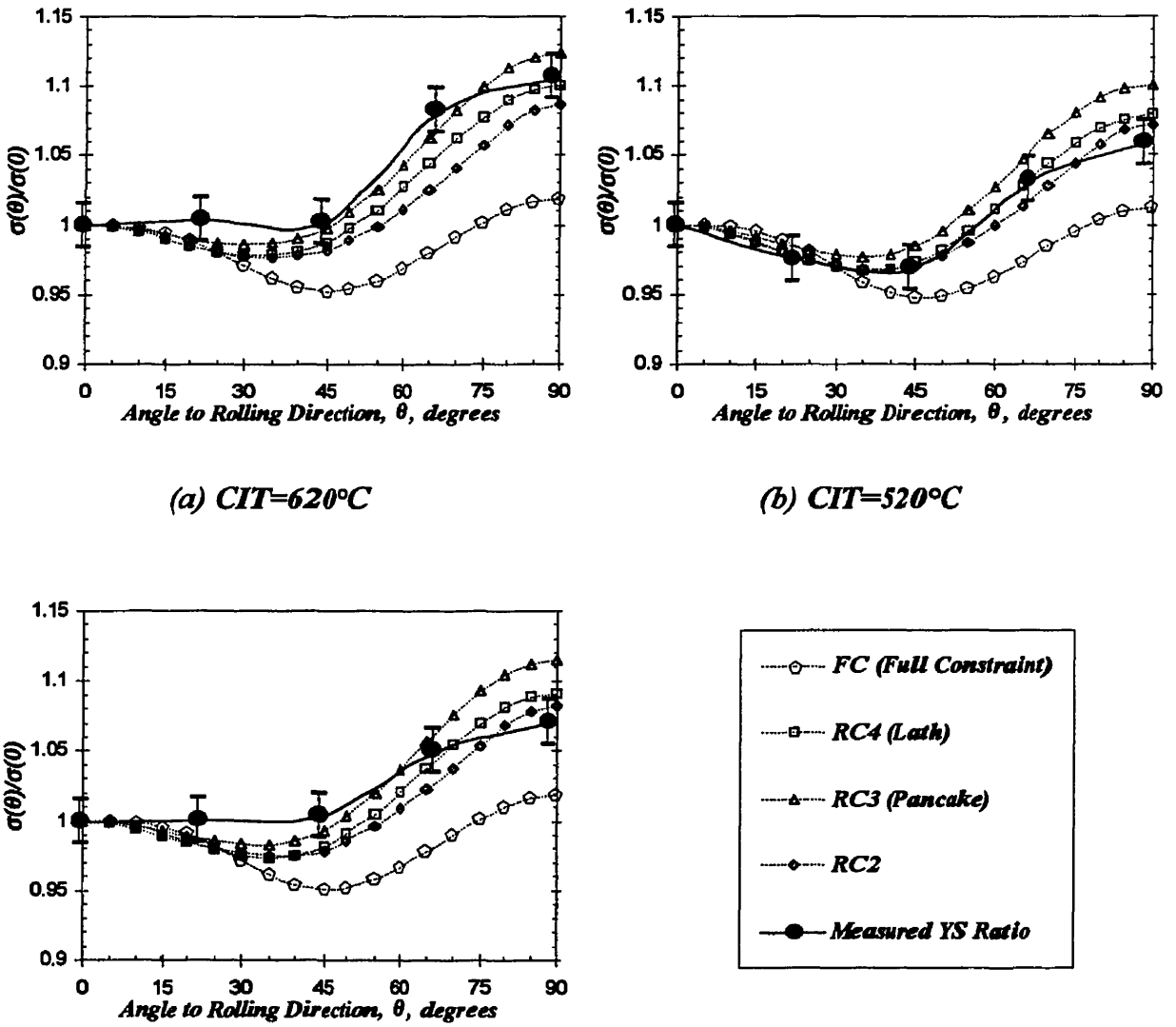

Figure 6.25 Comparison between the experimental observations and model predictions of the yield strength anisotropy of the X-80 plates reheated at **1275 °C** and finish rolled at **690 °C**; *(a)* to *(c)* CR=40°C s^{-1},

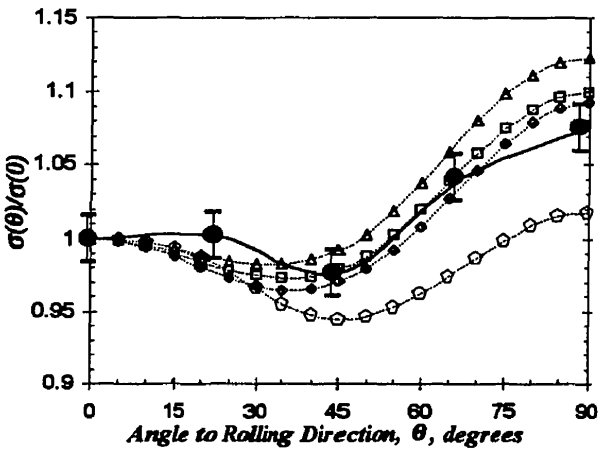

(d) CIT=620°C

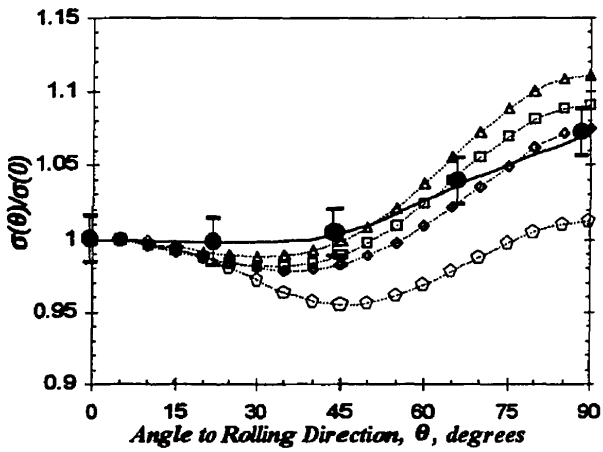

(e) CIT=520°C

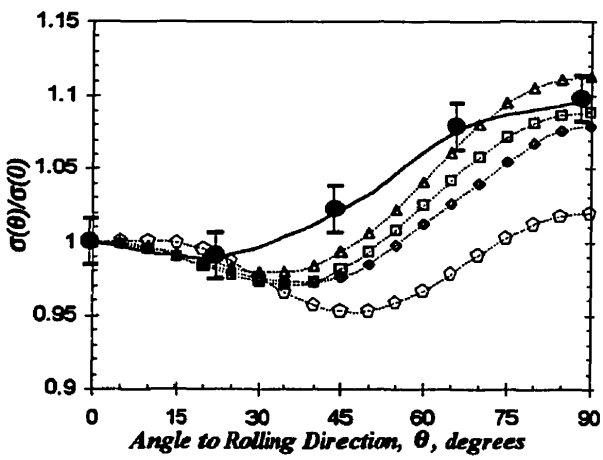

(f) CIT=420°C

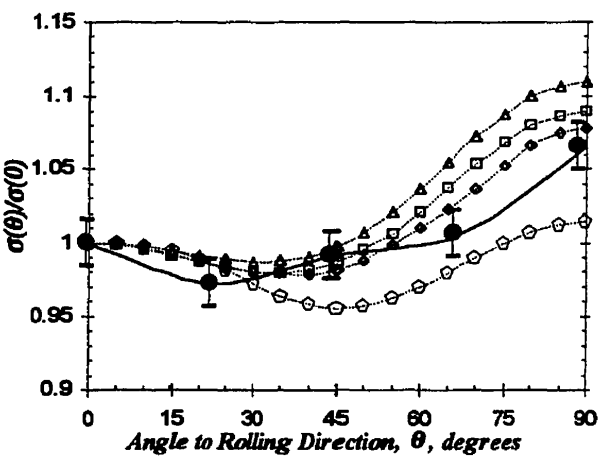

(g) Air Cooled

Figure 6.25 (continued) *(d)* to *(f)* CR=20°C s^{-1}, and (g) air cooled.

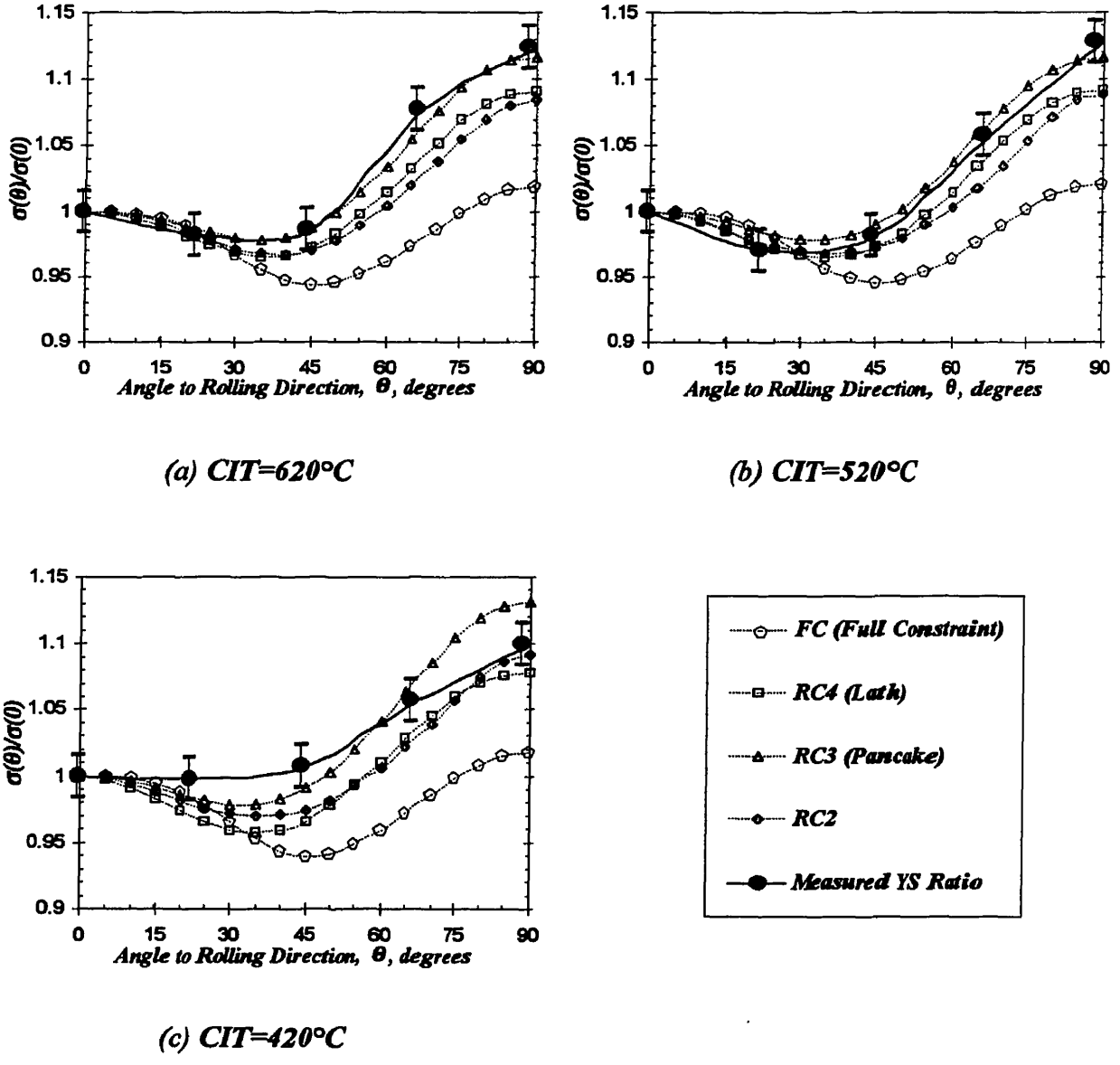

Figure 6.26 Comparison between the experimental observations and model predictions of the yield strength anisotropy of the X-80 plates reheated at **1150 °C** and finish rolled at **690 °C**; *(a)* to *(c)* CR=40°C s^{-1},

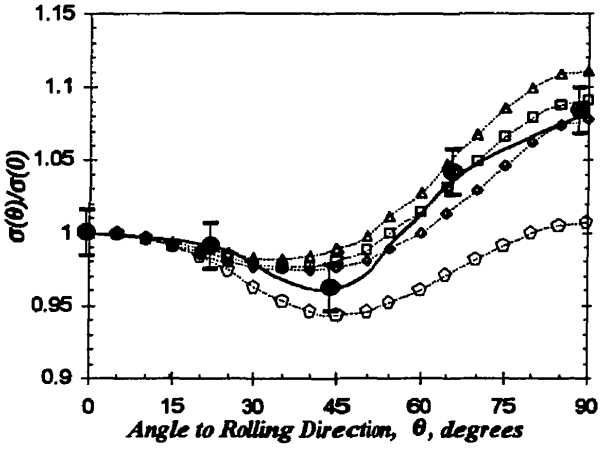

(d) CIT=620°C

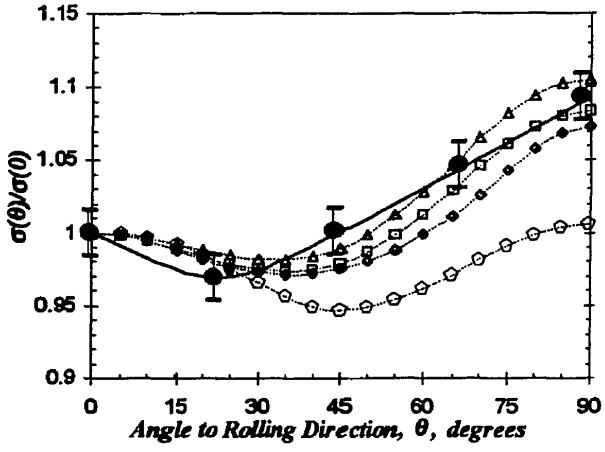

(e) CIT=520°C

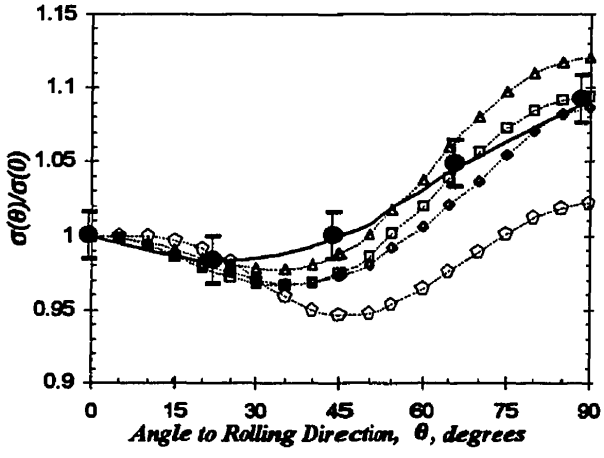

(f) CIT=420°C

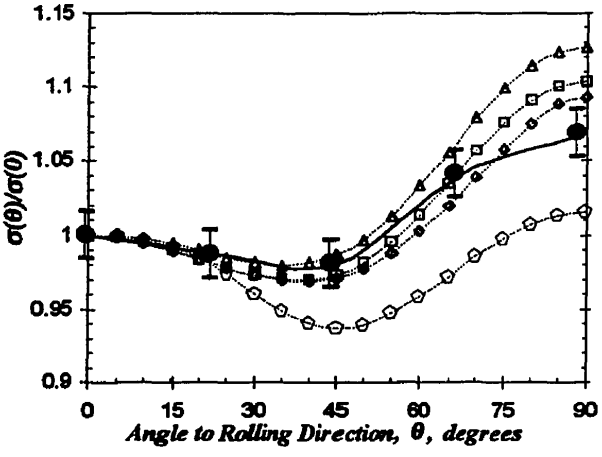

(g) Air Cooled

Figure 6.26 (continued) *(d)* to *(f)* CR=20°C s^{-1}, and (g) air cooled.

Table 6.1 Comparison between the experimental results and model predictions of the yield strength anisotropies ($\Delta\sigma$'s) for the X-70 plates.

		Yield Strength Anisotropy, $\Delta\sigma$, MPa				
		Experimental Results	**Model Predictions**			
FRT, °C	**CR, °C s^{-1}**		**FC**	**Lath**	**Pancake**	**RC2**
790	**Air Cooled**	2.9	5.8	10.0	12.4	9.0
	6	13.2	7.7	15.3	18.3	13.0
	20	15.6	9.1	16.2	19.6	14.2
730	**Air Cooled**	6.0	5.2	13.4	16.2	11.8
	6	11.7	7.6	14.6	17.7	12.4
	20	22.7	9.9	16.7	20.4	14.5

The above discussion also applies to the X-80 air cooled samples, Figs. 6.23 to 6.26. As can be seen in these diagrams, the transverse yield stress ratios increased in the X-80 air cooled samples compared to the X-70's. Accordingly, there is a better agreement between the model predictions and experimental results. This is because of the increased proportion of the bainite or acicular ferrite phase, which leads to a decrease in that of polygonal ferrite. The higher volume fraction of bainite has already been shown above to produce higher transverse yield stress ratios for a given intensity of the RD fibre components.

Once again, the models systematically overestimate the effect of texture on the yield strength anisotropy associated with the transverse direction. This is more pronounced in the samples finish rolled above the Ar_3, Figs. 6.21 , 6.23, and 6.24. As was shown in Chapter Five, the TD fibre intensities of these samples were very high compared to the samples finish rolled below the Ar_3, especially in the rapidly cooled plates. The above discussion again applies to these cases, where the high intensities of the TD fibre components decrease the transverse yield stress ratio, Figs. 6.17b, 6.17c, and 6.17d. In the low FRT samples, the pancaked ferrite grains also behave in the manner called for by the RC models, leading to an increase in the transverse stress ratios.

It is evident from Figs. 6.21 to 6.26 that, in some cases, the values measured at 45 degrees to the rolling direction are higher than the model predictions. As can be seen in Fig. 6.17, these differences appear to result from the respective volume fractions of the TD and RD fibre components.

The measured and predicted yield strength anisotropies ($\Delta\sigma$) for the X-80 samples are presented in Tables 6.2 and 6.3. The rapidly cooled samples display higher anisotropies, and therefore behaviours closer to those called for by the RC models; thus it seems that the lath and RC2 models provide the most accurate predictions for these samples.

Table 6.2 Comparison between the experimental results and model predictions of the yield strength anisotropies ($\Delta\sigma$'s) for the X-80 plates finish rolled *above* the Ar_3.

			Yield Strength Anisotropy, $\Delta\sigma$, MPa				
FRT = 780 °C			**Experimental Results**	**Model Predictions**			
RT, °C	**CR, °C s^{-1}**	**CIT, °C**		**FC**	**Lath**	**Pancake**	**RC2**
1275	**Air Cooled**	-	8.8	6.4	13.0	15.9	11.4
		620	13.8	10.2	18.0	21.7	15.1
	20	**520**	17.2	12.6	23.2	28.3	19.6
		420	22.9	12.1	23.4	27.6	18.6
		620	15.1	9.5	15.1	18.5	13.5
	40	**520**	17.2	11.7	19.9	26.2	17.4
		420	22.0	11.6	22.1	27.2	18.9
1150	**Air Cooled**	-	10.0	8.1	14.0	17.2	12.1
		620	19.1	9.6	17.9	21.5	15.0
	20	**520**	19.1	11.0	21.5	25.7	17.7
		420	20.4	10.9	20.1	24.1	16.0
		620	16.2	10.0	18.7	21.9	14.5
	40	**520**	24.4	12.0	22.9	27.8	19.0
		420	20.8	12.5	23.5	28.2	19.3

Table 6.3 Comparison between the experimental results and model predictions of the yield strength anisotropies ($\Delta\sigma$'s) for the X-80 plates finish rolled *below* the Ar_3.

			Yield Strength Anisotropy, $\Delta\sigma$, MPa				
FRT = 690 °C			**Experimental Results**	**Model Predictions**			
RT, °C	**CR, °C s^{-1}**	**CIT, °C**		**FC**	**Lath**	**Pancake**	**RC2**
1275	**Air Cooled**	-	10.8	9.4	18.5	21.7	15.3
	20	**620**	15.8	11.3	20.3	23.8	19.2
		520	14.6	10.3	20.7	24.3	16.4
		420	21.3	10.8	20.1	24.0	16.8
	40	**620**	22.9	10.1	20.2	23.7	16.3
		520	17.8	11.3	19.0	22.6	16.0
		420	16.7	12.1	22.2	26.4	18.4
1150	**Air Cooled**	-	15.7	12.0	20.0	23.6	17.0
	20	**620**	19.6	10.7	18.1	21.4	14.8
		520	20.0	10.4	18.1	21.6	14.9
		420	18.8	11.8	21.5	25.4	17.7
	40	**620**	26.3	11.2	19.0	22.5	16.2
		520	25.9	11.5	20.2	23.6	17.2
		420	20.1	13.6	21.1	28.8	19.5

Tables 6.2 and 6.3 show that, in most cases, the lath and RC2 models predict the measured values of the yield strength anisotropy quite well. This indicates that, for the acicular microstructures of these samples, relaxed constraint models such as the lath and RC2, in which one and three shear strain components are relaxed, are accurate.

However, considering the measurement errors of about ±4 MPa associated with the planar anisotropies, the predictions obtained from the different relaxed constraint models are relatively close. This is also evident in Figs. 6.21 to 6.26, in which the curves predicted according to the FC model are far below those obtained from the RC models, especially at angles close to the transverse direction. It can also be seen that the pancake model always predicts the highest transverse stress ratio and the greatest planar anisotropy of the yield stress as well.

CHAPTER 7

Conclusions

In this research, the effects of TMP parameters on microstructure, texture, and the planar anisotropy of yield strength were investigated in two Nb microalloyed linepipe steels. The conclusions of this work are drawn here in three sections, one for each of the three different topics discussed in Chapters Four to Six.

7.1 Microstructural Evolution during Thermomechanical Processing

1- The torsion simulation of rolling schedules led to more accurate predictions of the "critical temperatures" pertaining to steel rolling than the empirical equations because, in this work, the effects of initial austenite grain size and accumulated strain could be determined.

2- The strain accumulated before the T_{nr} in this investigation was well below the minimum required for the initiation of DRX. As a result, it can be concluded that no DRX occurs under the processing conditions of this work.

3- Comparison between measured ferrite grain sizes and calculated S_V's reveals that, generally, finer ferrite grain sizes are associated with higher S_V's.

4- From the higher hardnesses of the samples cooled at the higher rates, it can be concluded that the dislocation density of the acicular phase increases and the packet size decreases with cooling rate.

5- The acicular ferrite sheaves inclined at 45 degrees observed in the samples associated with high pancaking strains before transformation support the displacive mechanism for the growth of acicular ferrite.

6- For the case of finishing in the austenite region, the hardness is at a maximum when a medium CIT (520°C) is employed. This observation can be attributed to the higher nucleation rate applicable to transformation during moderate supercooling; the latter appears to result in finer packet sizes and finer precipitate dispersions in the acicular substructure.

7.2 Texture Development during the γ-to-α Transformation

1- The texture index that was used in this work permits the severity of the texture to be characterized by a single parameter; this is a measure of the extent to which the orientations of the transformed grains differ from a random distribution.

2- In air cooled samples, the higher intensity of the RD fibre associated with higher values of S_V can be attributed to increases in the intensity of the copper ({112}<111>) component of the fcc texture before transformation. Other workers have also shown that copper and S are, in fact, the stabilized end orientations in the fcc materials. By contrast, the small differences observed between the peak intensities of the TD fibres in samples with different S_V's indicate that this fibre is much less influenced by the pancaking strain or the S_V parameter.

3- The observation that a moderate cooling rate and a medium cooling interruption temperature led to the highest intensity of the TD fibre is attributable to variant selection. According to a recent model, higher dislocation densities on the active slip systems (due to less time available for recovery) are responsible for higher intensities of the {332}<113> and {554}<225> components.

4- The peak intensities along the TD fibres of the low FRT samples are less than 80 percent of those observed in the high FRT materials. Thus, it appears that the higher pancaking strains applied to the former samples led to a decrease in the volume fraction of the brass component in the austenite before transformation.

5- The continuous orientation spread along the line between {225}<110> and {332}<113> on the $\varphi_2 = 45°$ ODF section is referred to here as the *transformation fibre*. It includes the orientations that normally have the highest intensities in the transformation texture and shows that, as for the {332}<113>, the converted brass {112}<131> is very sensitive to cooling rate and cooling interruption temperature.

6- The greater difference between the volume fractions of {112}<131> in the low RT samples and in the predictions, as compared with the high RT samples, can be related to the intensities of the parent texture components, i.e. the S in this case, rather than to variant

selection. That is, the greater S_V values lead to higher volume fractions of S, whereas the brass component is either unchanged or even decreased by increasing S_V.

7- It can be also argued that the finer grain sizes associated with greater S_V values resulted in sharpening the austenite texture due to the more constraining effect of the grain boundaries. The sharper textures in the samples associated with higher S_V's (finer grained microstructures) can also be attributed to less shear banding and therefore to less randomization of the texture.

8- The discrepancies between the calculated and experimental textures imply that some type of variant selection occurred during the transformation. Oriented nucleation and selective growth are the two mechanisms that lead to deviations from the K-S predictions. Selective growth is affected by steel chemistry and cooling rate during transformation and appears to be active in the air cooled and higher CIT samples. Under the lower CIT conditions, oriented nucleation appears to be the prevailing mechanism.

9- The high intensities of the {113}<110> and {112}<110> components in the air cooled samples imply that selective growth can result in textures just as sharp as the oriented nucleation textures.

7.3 Planar Anisotropy of the Yield Strength

1- The higher strengths produced by intercritical rolling can be attributed to the high dislocation densities introduced by ferrite rolling. The higher pancaking strains of the samples associated with the lower FRT's are responsible for the higher dislocation densities. Such work hardening of the ferrite during rolling results in strengthening effects comparable to that of the grain refinement attributable to accelerated cooling.

2- An intermediate cooling rate employed in conjunction with an intermediate cooling interruption temperature results in more grain refinement (by increasing the ferrite nucleation rate) which, in turn, leads to higher strength.

3- There is good agreement between the hardnesses and yield strengths of the plates, with the direct proportionality specified in the literature. This confirms the conclusions advanced above regarding the effect of cooling rate and cooling interruption temperature on the yield strength by refinement of the acicular microstructure and raising the dislocation density.

4- The variations in yield strength along the transverse direction are as much as twice those of the ultimate tensile strength. This indicates that the texture and grain morphology have more influence on the planar anisotropy of the yield strength than on that of the UTS.

5- Finer ferrite grain sizes and more hardening by Nb precipitation in the X-80 steel were the main causes of the higher yield strengths of these samples, as opposed to the low Nb steel (X-70) samples.

6- In the X-70 plates, despite the similar textures developed in the samples rapidly cooled at two different rates, the yield strength anisotropy increased with cooling rate. It can therefore be concluded that the morphology of the acicular ferrite (or bainite) also contributes to the yield strength anisotropy.

7- Generally, the planar anisotropy of the yield strength is fairly low when the sample is air cooled; conversely, it exhibits its highest level when the lowest cooling interruption temperature is employed. This is accompanied by an increase in the sharpness of the texture (texture index) in the samples with high FRT's. Nevertheless, in the low FRT samples, it appears that the mixed microstructure of pancaked ferrite and acicular ferrite also plays a role in determining the planar anisotropy.

The TD fibre components, especially the {332}<113>, display somewhat lower anisotropies of the yield stress ratio when the lath and pancake models are employed.

9- The measured yield strength anisotropies are in relatively good agreement with the model predictions. The rapidly cooled samples display higher anisotropies, and therefore behaviours closer to those called for by the RC models than the air cooled samples. For materials containing acicular microstructures, the lath model provides the most accurate property predictions.

Statement of Originality and Contribution to Knowledge

In the series of torsion tests that were carried out in this study, a temperature control program was utilized instead of the interpass time control program, so that each pass deformation was performed at a specific temperature. In this way, the industrial conditions were directly simulated by torsion testing for the first time.

In this Ph.D. program, the effects of TMP conditions such as soaking and finish rolling temperature on the intensities of the texture components were studied in two low-carbon Nb steels. The influence of these parameters on the planar anisotropy of the yield strength, which is a new issue, were determined experimentally and modelled theoretically.

The influence of different cooling rates after rolling on the yield strength anisotropy was determined and described. In this regard, the effect of cooling interruption temperature on the microstructural evolution and texture development during continuous cooling was studied for the first time.

The effects of the cooling conditions (cooling rate and cooling interruption temperature) on the transformation texture were interpreted in terms of the relation between the various γ-to-α transformation products (such as bainite and acicular ferrite) and the texture components that are expected to form on the basis of the Kurdjumov-Sachs relationship.

The concept of a *transformation* (TR) *fibre* was introduced here and defined as a continuous orientation progression along the line between {225}<110> and {332}<113> on

the $\varphi_2 = 45°$ ODF section. This fibre includes the orientations that normally have the highest intensities in the transformation texture.

The effective interfacial area of the austenite (S_V) was shown to be more effective than the pancaking strain with regard to increasing the intensity of the transformation texture in ferrite, particularly that of the transformed copper component.

From the measured ferrite textures, the distribution of the ideal components of the austenite texture was deduced. In this way, it was concluded that greater S_V values lead to higher volume fractions of the copper and S components in the hot rolled austenite, whereas the brass component is either unchanged or even decreased by increasing S_V.

The experimental results indicate that selective growth is active in the air cooled and higher CIT samples, whereas oriented nucleation is the prevailing variant selection mechanism under the lower CIT conditions. In a similar manner, the high intensities of the {113}<110> and {112}<110> components in the air cooled samples suggest that selective growth can result in textures that are just as sharp as the oriented nucleation ones.

Two parameters ($\overline{\sigma}$ and $\Delta\sigma$) were introduced in this work to quantify the average yield strength and planar anisotropy of the yield strength, respectively.

It was demonstrated that the choice of plastic anisotropy model, especially for the duplex microstructures of pancaked ferrite and acicular ferrite in the low FRT samples, affects the yield strength anisotropy predicted from the texture measurements. Of the four models examined, the lath and RC2 models were shown to predict the planar anisotropy of the yield strength in the rapidly cooled samples most accurately.

References

1. H.J. Bunge, in "Directional Properties of Materials", Ed. H.J. Bunge, DGM, Germany, 1988, p. 1.
2. H.J. Bunge, Int. Materials Reviews, 1987, Vol. 32, No. 6, p. 265.
3. H.J. Bunge, "Texture Analysis in Materials Science", Butterworths, London, 1982.
4. C. Esling, H.J. Bunge, M.J. Philippe, and J. Muller, in "Theoretical Methods of Texture Analysis", Ed. H.J. Bunge, DGM, Germany, 1987, p. 105.
5. W. Bleck, R. GroBterlinden, U. Lotter, and C.P. Reip, Steel Research, 1991, Vol. 62, No. 12, p. 580.
6. T. Tanaka, Int. Metal Reviews, 1981, Vol. 26, No. 4, p. 185.
7. H. Inagaki, in Proc. 6th Int. Conf. on "Textures of Materials" (ICOTOM6), The Iron and Steel Institute of Japan", Tokyo, 1981, Vol. 1, p. 149.
8. R.K. Ray, M.P. Butron-Guillen, J.J. Jonas, and G.E. Ruddle, ISIJ Int., 1992, Vol. 32, No. 2, p. 203.
9. M.P. Butron-Guillen, Ph.D. Thesis, McGill University, Canada, 1995.
10. J.D. Jones and A.B. Rothwell, in "Deformation Under Hot Working Conditions", The Iron and Steel Institute, London, 1968, p. 78.
11. J.J. Jonas and I. Weiss, Metal Science, 1979, Vol. 13, p. 238.
12. H.J. Kestenbach, J.A. Rodrigues, and J.R. Dermonde, Materials Science and Technology, 1989, Vol. 5, No. 1, p. 29.
13. U. Dahmen, Acta Metall., 1982, Vol. 30, p. 63.
14. K.H. Yang and W.K. Choo, Acta Metall. Mater., 1994, Vol. 42, No. 1, p. 263.
15. W.F. Hosford and R.H. Zeisloft, Metall. Trans., 1972, Vol. 3, No. 1, p. 113.
16. T. Tanaka, N. Tabata, T. Hatomura, and C. Shiga, in "Microalloying 75", Eds. M. Korchynsky et al, Union Carbide Corporation, New York, 1977, p. 107.
17. T. Terazawa, H. Higashiyma, and S. Sekino, in "Toward Improved Ductility and Toughness", Climax Molybdenum Company, Tokyo, Japan, 1972, p. 101.

18. B.L. Bramfitt and A.R. Marder, in "Processing and Properties of Low Carbon Steel', American Institute of Mining, Metallurgical and Petroleum Engineers, New York, 1973, p. 191.
19. E.L. Brown, A.J. DeArdo, and J.H. Bucher, in "Hot Deformation of Austenite", Ed. John Ballance, American Institute of Mining, Metallurgical and Petroleum Engineers, New York, 1977, p. 250.
20. G.R. Speich and D.S. Dabkowski, *ibid.*, p. 557.
21. H. Inagaki, Z. Metallkunde, 1983, Vol. 74, No. 11, p. 716.
22. H. Inagaki, Trans. of ISIJ, 1977, Vol. 17, p. 166.
23. R.K. Ray and J.J. Jonas, Int. Materials Reviews, 1990, Vol. 35, No. 1, p. 1.
24. H. Inagaki, in Proc. 5th Int. Conf. on "Textures of Materials" (ICOTOM5), Eds. G. Gottstein and L. Lucke, Aachen, Germany, 1978, Vol. 1, p. 157.
25. R.K. Ray, Ph. Chapellier, and J.J. Jonas, Textures and Microstructures, 1990, Vol. 12, p. 141.
26. G. Kurdjumov and G. Sachs, Z. Phisik., 1930, Vol. 64, p. 325.
27. A. Jones and B. Walker, Metal Science, 1974, Vol. 8, p. 397.
28. K. Haslam, T. Coleman, D. Dulieu, and I.L. Dillamore, in Proc. "Deformation and Recrystallization Textures in Metals and Their Industrial Applications", Soc. Franc. Met., Nancy, France, 1973, p. 369.
29. T. Yutori and R. Ogawa, Proc. ICOTOM 6 (see Ref. 7), Vol. 2, p. 669.
30. A. Akbarzadeh, L.E. Collins, M. Kostic, and J.J. Jonas, Proc. of the 36th Conf. on Mechanical Working and Steel Processing, ISS, Baltimore, USA, 1994, Vol. XXXII, p. 337.
31. J.S. Kallend, P.P. Morris, and G.J. Davies, Acta Metall., 1976, Vol. 24, p. 361.
32. G.J. Davies, Proc. ICOTOM 6 (see Ref. 7), Vol. 1, p. 132.
33. J. Savoie, R.K. Ray, M.P. Butron-Guillen, and J.J. Jonas, Acta Metall. Mater., 1994, Vol. 42, p. 2511.
34. R.K. Ray, J.J. Jonas, M.P. Butron-Guillen, and J. Savoie, ISIJ Int., 1994, Vol. 34, No. 12, p. 927.

35. M.P. Butron-Guillen, J.J. Jonas, and R.K. Ray, Acta Metall. Mater, 1994, Vol. 42, No. 11, p. 3615.
36. C.S. Da Costa Viana, M.P. Butron-Guillen, and J.J. Jonas, Textures and Microstructures, 1996, Vol. 27, No. 1-4, p. 599.
37. M.P. Butron-Guillen, C.S. Da Costa Viana, and J.J. Jonas, in Proc. 11th Int. Conf. on "Textures of Materials", Xian, China, 1996, Vol. 1, p. 132.
38. J.J. Jonas, M.P. Butron-Guillen, C.S. Da Costa Viana, in Proc. 11th Int. Conf. on "Textures of Materials", Xian, China, 1996, Vol. 1, p. 126.
39. H.I. Aaronson, T. Furuhara, J.M. Rigsbee, W.T. Reynolds, and J.M. Howe, Metall. Trans., 1990, Vol. 21A, p. 2369.
40. F.B. Pickering, Proc. of "Microalloying 75" (see Ref. 16), p. 9.
41. T. Gladman, D. Dulieu, and I.D. McIvor, Proc. of "Microalloying 75",(see Ref. 16), p. 32.
42. W.E. Duckworth, R. Phillips, and J.A. Chapman, Iron Steel Institute, 1965, Vol. 203, p. 1108.
43. G.J. Davies, J.S. Kallend, and P.P. Morris, Acta Metall., 1976, Vol. 24, p. 159.
44. J. Pospiech, J. Jura, and M. Maciosowski, in Proc. "Deformation and Recrystallization Textures in Metals and Their Industrial Applications", Soc. Franc. Met., 1973, Nancy, France, p. 117.
45. R.E. Hook and H. Nyo, Metall. Trans., 1975, Vol. 6A, p. 1443.
46. H. Watanabe, Y.E. Smith, and R.D. Pehlke, in "Hot Deformation of Austenite", Ed. John Ballance, American Institute of Mining, Metallurgical and Petroleum Engineers, New York, 1977, p. 140.
47. R. Coladas, J. Masounave, and J.P. Bailon, in "Hot Deformation of Austenite" (see Ref. 19), p. 341.
48. T. Tanaka, in Proc."Microalloying 95", ISS, Pittsburgh, PA, 1995, p. 165.
49. E.J. Palmiere, C.I. Garcia, and A.J. DeArdo, Metall. and Mater. Trans., 1994, Vol. 25A, No. 2, p. 277.
50. Y.C. Liu and G.A. Alers, Metall. Trans., 1973, Vol. 4, p. 1491.

51. T. Coleman, D. Dulieu, and A. Gouch, "The Microstructure and Design of Alloys", The Metals Society, London, 1974, Vol. 1, p. 70.
52. T. Tanaka, "Hot Deformation of Steels", The Iron and Steel Institute of Japan, Tokyo, 1979, p. 55.
53. H. Hu and J.S. Kallend, Proc. of ICOTOM 6 (see Ref. 7), Vol. 1, p. 164.
54. I. Kozasu, C. Ouchi, T. Sanpei, and T. Okita, in "Microallying 75" (see Ref. 16), p. 136.
55. A.T. Davenport, R.E. Miner, and R.A. Knott, in "Hot Deformation of Austenite" (see Ref. 19), p. 186.
56. H. Inagaki, Z. Metallkunde, 1983, Vol. 74, p. 716.
57. H. Inagaki and T. Suda, Texture, 1972, Vol. 1, p. 129.
58. L.S. Toth, J.J. Jonas, D. Daniel, and R.K. Ray, Metall. Trans., 1990, Vol. 21A, p. 2985.
59. T. Tanaka, Proc. of "Accelerated Cooling of Rolled Steel", Eds. G.E. Ruddle and A.F. Crawley, Canadian Institute of Mining and Metallurgy, 1987, p. 187.
60. C. Ouchi, Proc. of Int. Conf. on HSLA steels, Wollongong, Australia, 1984, p. 17.
61. J.D. Baird and R.R. Preston, in "Processing and Properties of Low Carbon Steel", Ed. J.M. Gray, American Institute of Mining, Metallurgical and Petroleum Engineers, New York, 1973, p. 1.
62. C.H. Young and H.K.D.H. Bhadeshia, Mat. Science. and Tech., 1994, Vol. 10, No. 3, p. 209.
63. G. R. Speich, L.J. Cuddy, C.R. Gordon, and A. J. DeArdo, in "Phase Transformations in Ferrous Alloys", Eds. A.R. Marder and J.I. Goldstein, TMS-AIME, 1984, p. 341.
64. A.P. Coldren, Y.E. Smith, and R.L. Cryderman, in "Processing and Properties of Low Carbon Steel", Ed. J.M. Gray, American Institute of Mining, Metallurgical and Petroleum Engineers, New York, 1973, p. 163.
65. G. Tither and M. Lavite, Journal of Metals, 1975, Vol. 27, No. 9, p. 15.
66. W.C. Leslie, The Physical Metallurgy of Steels, McGraw Hill, New York, 1981.
67. W.A. Backofen, in "Deformation Processing", Addison Wesley, 1972, p. 57.

68. M.A. Meyers and K.K. Chawla, in "Mechanical Metallurgy", Prentice Hall, NJ., 1984, p. 383.
69. S. Mishra and C. Darmann, Int. Metall. Rev., 1982, Vol. 27, No. 6, p. 307.
70. W.B. Hutchinson, Int. Metall. Rev., 1984, Vol. 29, No. 1, p. 25.
71. R. K. Ray, J.J. Jonas, and R.E. Hook, Int. Materials Review, 1994, Vol. 39, No. 4, p. 129.
72. B.L. Bramfitt and A.R. Marder, Metall. Trans., 1977, Vol. 8A, No. 8, p. 1263.
73. H. Inagaki, Z. Metallkunde, 1985, Vol. 76, p. 85.
74. H. Inagaki, K. Kurihara, and I. Kozasu, Trans. ISIJ, 1977, Vol. 17, p. 75.
75. C. M. Vlad and H.J. Bunge, Proc. of ICOTOM 6 (see Ref. 7), Vol. 2, p. 649.
76. U. Lotter and L. Meyer, Metals Technology, 1977, Vol. 4, No. 1., p. 27.
77. D.N. Hawkins; Metals Technology, 1976, Vol. 3, No. 3, p. 417.
78. J.M. Rosenberg and H.R. Piehler, Metall. Trans., 1971, Vol. 2, p. 257.
79. P. Franciosi, Acta Metall., 1983, Vol. 31, p. 1331.
80. P. Van Houtte, Proc. of ICOTOM 5 (see Ref. 24), Vol. 2, p. 347.
81. G. Sachs, Z. Verein Deut. Ing., 1928, Vol. 72, p. 734.
82. G. Taylor, J. Inst. Met., 1938, Vol. 62, p. 307.
83. J.F.W. Bishop and R. Hill, Phil. Mag., 1951, Vol. 42, p. 414.
84. D. Daniel, Ph.D. Thesis, McGill University, Montreal, Canada, 1990.
85. D. Daniel and J.J. Jonas, in Proc. 8th Int. Conf. on "Textures of Materials" (ICOTOM 8), New Mexico, 1987, p. 1079.
86. H. Honeff and H. Mecking, Proc. of ICOTOM 5 (see Ref. 24), Vol. 1, p. 265.
87. P. Van Houtte, Proc. of ICOTOM 6 (see Ref. 7), Vol. 1, p. 428.
88. U.F. Kocks and H. Chandra, Acta Metall., 1982, Vol. 30, No. 3, p. 695.
89. C. Tavard and F. Royer, in Proc. Int. Conf. on "Textures of Materials" (ICOTOM 7), Eds. C.M. Brakman et al., Netherlands, 1985, p. 145.
90. R. Barbosa, F. Boratto, S. Yue, and J.J. Jonas, Proc. of Int. Symposium on "Processing, Microstructure and Properties of HSLA Steels", Ed. A. J. DeArdo, TMS-AIME, Warrendale, PA, 1988, p. 51.

91. C. Ouchi, T. Sampei, and I. Kozasu, Trans. ISIJ, 1982, Vol. 22, p. 214.
92. F. Boratto, R. Barbosa, S. Yue, and J.J. Jonas, Proc. of Int. Conf. on "Physical Metallurgy of Thermomechanical Processing of Steels and Other Metals" (THERMEC' 88), Ed. I. Tamura, Tokyo, Japan, 1988, p. 383.
93. S. Yue and J.J. Jonas, Materials Forum, 1990, Vol. 14, p. 245.
94. H.L. Andrade, M.G. Akben, and J.J. Jonas, Metall. Trans., 1983, Vol. 14A, p. 1967.
95. C.R. Mackenzie and R.W. Young, J. Iron Steel Inst., 1971, Vol. 209, p. 918.
96. Y.E. Smith and C.A. Siebert, Metall. Trans., 1971, Vol. 2, p. 1711.
97. A.Z. Hanzaki, R. Pandi, P.D. Hodgson, and S. Yue, Metall. Trans., 1993, Vol. 24A, p. 2657.
98. T. Tanaka and N. Tabata, Tetsu-to-Hagane, 1978, Vol. 9, p. 1353.
99. I. Weiss, J.J. Jonas, and G. E. Ruddle, Proc. of ASM Symposium on "Process Modelling Tools", ASM, Metals Park, Ohio, 1980, p. 97.
100. G.E. Ruddle, B. Voyzelle, J.T. Bowker, and L.E. Collins, Proc. of the 34th Conf. on Mechanical Working and Steel Processing, ISS-AIME, 1993, Vol. XXX, p. 19.
101. V.K. Lakshmanan and J.S. Kirkaldy, Metall. Trans., 1984, Vol. 15, p. 541.
102. K.J. Irvine, F.B. Pickering, T. Gladman, J. Iron and Steel Inst., 1967, Vol. 205, p. 161.
103. G.E. Dieter, "Mechanical Metallurgy", 3rd edition, McGraw-Hill, New York, 1986.
104. A.F. Crawley, G. Smelsky, C. Galvani, and G.E. Ruddle, Proc. of Int. Symposium on "Accelerated Cooling of Rolled Steel", Eds. G.E. Ruddle and A.F. Crawley, The Metallurgical Society of CIM, Pergamon Press, New York, NY, 1988, p. 159.
105. CANMET Report MTL 89-43, 1989.
106. J.T. Bowker and J.A. Gianetto, CANMET Report MTL 93-50 (CF), 1993.
107. J. Savoie, Texture Menu Software, Metallurgical Engineering Dept., McGill University, Internal Report, 1994.
108. American Standards for Testing of Materials, ASTM, E8M, 1991, USA.
109. D.Q. Bai, Ph.D. Thesis, McGill University, Canada, 1996.
110. D.Q. Bai, S.Yue, W.P. Sun, and J.J. Jonas, Proc. of 34th Mechanical Working and Steel Processig, ISS-AIME, Vol. XXX, 1993, Montreal, Canada, p. 515.

111. T.M. Maccagno, J.J. Jonas, and P.D. Hodgson, ISIJ Int., 1996, Vol. 36, No. 6 , p. 720.

112. K. Minami, F. Siciliano Jr., T.M. Maccagno, and J.J. Jonas, ISIJ Int., 1996, Vol. 36, No. 12, p. 1507.

113. J.G. Williams, C.R. Killmore, and G.R. Harris, Proc.of THERMEC'88 (see Ref. 92), ISIJ, Tokyo, p. 224.

114. C.M. Sellars, Proc. Int. Conf. on "Hot Working and Forming Processes", The Metals Society, London, 1980, p. 3.

115. M. Pietrzyk, C. Roucoules, and P.D. Hodgson, ISIJ Int., 1995, Vol. 35, p. 531.

116. A.J. DeArdo, Proc. Int. Conf. on HSLA Steels, Wollongong, Australia, 1984, p. 210.

117. M. Umemoto, H. Ohtsuka, and T. Tamura, *ibid.*, p. 96.

118. J. D. Verhoeven, Fundamentals of Physical Metallurgy, Wiley, N.Y., 1975.

119. A.J. DeArdo, Proc. Conf. on "Accelerated Cooling of Steel", Ed. P.D. Southwick, AIME, 1985, p. 97.

120. W. Steven and A.G. Hayres, J. Iron Steel Inst., 1956, Vol. 183, p. 349.

121. T. Araki, K. Shibata, and M. Enomoto, Mater. Sci. Forum, 1990, Vols. 55-58, p. 275.

122. S.W. Thompson, D. J. Colvin, and G. Krauss, Metall. Trans. A, 1990, Vol. 21, No. 6, p. 1493.

123. S.S. Babu and H.K.D.H. Bhadeshia, Materials Trans., JIM, Vol. 32, No. 8, 1991, p. 679.

124. H.K.D.H. Bhadeshia, private communication, 1996.

125. A.A.B. Sugden and H.K.D.H. Bhadeshia, Metall. Trans. A, 1989, Vol. 20, No. 9, p. 1811.

126. S.S. Babu and H.K.D.H. Bhadeshia, Materials Science and Eng., A 156, 1992, p. 1.

127. C. Ouchi, T. Okita, and S. Yamamoto, Trans. ISIJ, 1982, Vol. 22, p. 608.

128. G. J. Davies and R.M. Bateman, Proc. of ICOTOM 6 (see Ref. 7), p. 132.

129. G.J. Davies, Proc. of ICOTOM 5 (see Ref. 24), p. 121.

130. G.J. Davies, J.S. Kallend, and P.P. Morris, in "Hot Deformation of Austenite" (see Ref. 19), p. 599

131. C. Ouchi, T. Sanpei, T. Okita, and I. Kozasu, in "Hot Deformation of Austenite" (see Ref. 19), p. 316.

132. M.P. Butron-Guillen, C.S. Da Costa Viana, and J.J. Jonas, Metall. and Mater. Trans., 1997, in press.

133. H. Inagaki, ISIJ Int., Vol. 34, No. 4, 1994, p. 313.

134. R.K. Ray, Ph. Chapellier, and J. J. Jonas, Textures and Microstructures, 1990, Vol. 12, p. 141.

135. Ph. Chapellier, R.K. Ray, and J. J. Jonas, Acta Metall., 1990, Vol. 38, No. 8, p. 1475.

136. R.K. Ray, Acta Metall. Mater., 1995, Vol. 43, No. 10, p. 3861.

137. P. Van Houtte, Texture Software, Catholic University of Leuven, 1992.

138. Y. Zhou, L.S. Toth, and J.J. Jonas, Acta Metall. Mater., 1992, Vol. 40, No. 11, p. 3179.

139. D.A. Hughes and N. Hansen, Proc. Conf. on "Advances in Hot Deformation Textures and Microstructures", Eds. J.J. Jonas, T.R. Bieler, and K.J. Bowman, TMS, Warrendale, PA, 1994, p. 427.

140. D.A. Hughes, Proc. 16th Int. Symp. on "Materials Science", Eds. N. Hansen, D. Juul Jensen, Y.L. Yui, and B. Ralph, Roskilde, 1995, p. 63.

141. M.R. Barnett and J.J. Jonas, ISIJ Int., 1997, in press.

142. W.T. Lankford, S.C. Snyder, J.A. Bauscher, ASM Trans., 1950, Vol. 42, p. 1197.

143. U.F. Kocks, Metall. Trans., 1970, Vol. 1, No. 5, p. 1121.

144. M.A. Przystupa, A.K. Vasudevan, and W.G. Fricke, Proc. of ICOTOM 8 (see Ref. 85), p. 1051.

145. E. Aernoudt, in "Directional Properties of Materials", Ed. H.J. Bunge, DGM, Germany, 1988, p. 157.

146. H.J. Bunge, F. Wagner, P.I. Welch, and P. Van Houtte, J. Physique Letters, 1985, No. 46, p. 1109.

147. A. Akbarzadeh and J.J. Jonas; report to be submitted to Ipsco Inc.

148. A. Considere, Ann. ponts et chaussees, 1885, Vol. 9, p. 574.

149. D.J. Meuleman, Ph. D. Thesis, The University of Michigan, 1980.

150. H.K.D.H. Bhadeshia and D.V. Edmonds, Metall. Trans., Vol. 10A, 1979, p. 895.

151. H.K.D.H. Bhadeshia, Bainite in Steels, The Institute of Materials, London, 1992.

152. K. Tsuzaki, T. Ueda, K. Fujiwara, and T. Maki, Proc. 1st Japan Int. SAMPE Symp. and Exhib. on "New Materials and Processes for the Future", Society for Advancement of Mater. and Process Engineering, Chiba, Japan, 1989, p. 699.

153. D. McLean, Mechanical Properties of Metals, John Wiley & Sons, New York, 1962.

154. J.C.M. Li and Y.T. Chou, Metall. Trans., 1970, Vol. 1, p. 1145.

155. A.W. Thompson, Acta Metall., 1975, Vol. 23, p. 1337.

156. L.E. Murr, Metall. Trans., 1975, Vol. 6A, p. 505.

157. P.J. Worthington and E. Smith, Acta Metall., 1964, Vol. 12, p. 1277.

158. R.H. Edwards and N.F. Kennon, Metall. Trans., 1978, Vol. 9A, p. 1801.

IMAGE EVALUATION TEST TARGET (QA-3)

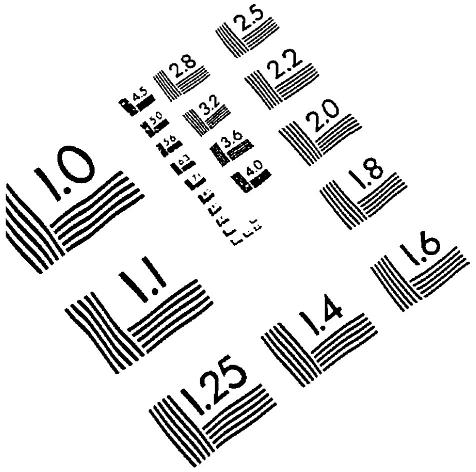

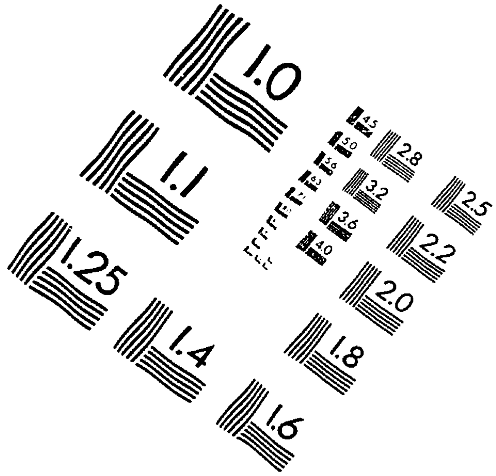

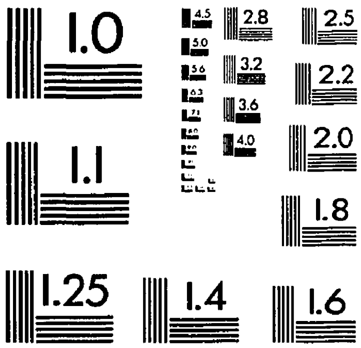

150mm

6″

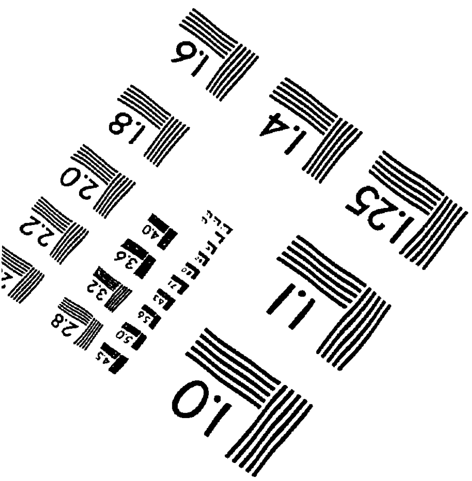

APPLIED IMAGE . Inc
1653 East Main Street
Rochester, NY 14609 USA
Phone: 716/482-0300
Fax: 716/288-5989